



HAL
open science

Constraining the tectonic evolution of extensional fault systems in the Cyclades (Greece) using low-temperature thermochronology

Stéphanie Brichau

► **To cite this version:**

Stéphanie Brichau. Constraining the tectonic evolution of extensional fault systems in the Cyclades (Greece) using low-temperature thermochronology. Applied geology. Université Montpellier II - Sciences et Techniques du Languedoc; Johannes Gutenberg Universität Mainz, 2004. English. NNT : 2004MON20049 . tel-00006814

HAL Id: tel-00006814

<https://theses.hal.science/tel-00006814>

Submitted on 3 Sep 2004

HAL is a multi-disciplinary open access archive for the deposit and dissemination of scientific research documents, whether they are published or not. The documents may come from teaching and research institutions in France or abroad, or from public or private research centers.

L'archive ouverte pluridisciplinaire **HAL**, est destinée au dépôt et à la diffusion de documents scientifiques de niveau recherche, publiés ou non, émanant des établissements d'enseignement et de recherche français ou étrangers, des laboratoires publics ou privés.

Dissertation zur Erlangung des Grades

“DOKTOR DER NATURWISSENSCHAFTEN”

**am Fachbereich Geowissenschaften
der Johannes Gutenberg-Universität Mainz**

THESE

Pour obtenir le grade de
“DOCTEUR DE L’UNIVERSITÉ MONTPELLIER II”

**Discipline: Terre solide, géodynamique
Formation Doctorale: Structure et Evolution de la Lithosphère
Ecole Doctorale: Science de la Terre et de l’Eau**

Presented and publicly defended at Mainz

by

Stéphanie Brichau

June 29th, 2004

Title:

**Constraining the tectonic evolution of extensional fault systems in the
Cyclades (Greece) using low-temperature thermochronology**

JURY

M. Stephen Foley	GP, Mainz	President
M. Michel Faure	IST, Orléans	Reviewer
M. Wolfgang Jacoby	Geophysik, Mainz	Examiner
M. Patrick Monié	LDL, Montpellier	Examiner
M. Uwe Ring	CECM, Mainz	Director
M. Maurice Brunel	LDL, Montpellier	Co-director

Acknowledgements

First I would like to thank my supervisors Uwe Ring and Maurice Brunel for their constant support over the last few years and, in particular, the last months.

My PhD adviser Andy Carter has done his best to teach me the fission track technique at the University College of London while also providing tremendous support, much needed motivation and fast return reading service with the help of Tony Hurford!

I thank specially Wolfgang Jacoby and Stephen Foley who have accepted to be members of the jury for this thesis and P. Monié for the argon dating, despite the caprices of the mass spectrometer, who gave up his time to carry out the last dating and to be examiner of this study .

I thank Michel Faure and Cees Passchier who have accepted to review this thesis.

I am grateful to Ken. Farley and Lindsey Hedges for assistance and forbearance during (U-Th)/He dating at California Institute of Technology and Jean-Marie Dautria at the university of Montpellier II for his help concerning the thin section observations.

Nothing would have been possible without Jean-Patrick Respaut who did my education in geochronology during my Master and my Diploma and has done his best to learn me to like this discipline, thank you again for your constant support over the last six years despite my shouts.

I would like to thank most of the people at the university of Mainz and Montpellier for their friendship/help/encouragement at one time or another. Number of people generously gave up their time in order to help me complete this work, especially those, who offered their proof-reading services in the last mad days before submission. My thanks go to Christine Kumerics for the long discussions about the Greece and her friendship attitude and constant support during the last year, Panos Zachariadis for the nice coffee each morning during the last months (I know that somewhere in Germany a coffee will wait me when I would like...), Hagen Deckert for his jokes about the French, Philippe Turpaut my French colleague, Zuzana Fekiacova for the “afternoon cola break”, Nicolas Walte who has supported me in the office during these three years, Arzu Arslan the nice and friendly “Turkey girl”, Cecile Gautheron my French colleague in US (I hope to work with you in the future...), Delphine Bosch for your good advises in any circumstances, Julie Schneider my best friend since the Diploma, Philippe Vernant for the Kansas (!!!), Anne Renon to give me a critical opinion of non-geologist about the abstract and also the secretaries of the DL lab, Marie-France, Nathalie, Celine, Martine. I wish you all the best for the future...

My family has been forbearing during the course of my education, I don't know where I would have been without them. I appreciate all the sacrifices my family have made because I decided to go in Germany to do my thesis. The success of my education is largely due to their support.

None of this extraordinary odyssey would have been possible without the help of my future husband Cédric Totee who continues to encourage and support me in any endeavor and who tolerates all my caprices.

Contents

- <i>Résumé étendu</i>	9
- <i>Abstract for non-geologists</i>	13
<u>Introduction</u>	15
1. Where and why?	15
2. How?	18
3. Organisation of this thesis	19
I- Methodology	21
I.1 Mineral separation	23
I.1.1 Mineral characteristics	23
I.1.2 Protocol	23
I.2 $^{40}\text{Ar}/^{39}\text{Ar}$ method	25
I.2.1 Introduction to the $^{40}\text{Ar}/^{39}\text{Ar}$ technique	25
I.2.2 Details of $^{40}\text{Ar}/^{39}\text{Ar}$ process used in this study	26
I.3 Fission track method	27
I.3.1 Principles of the FT technique	27
I.3.2 Details of the FT method used in this study	32
I.4 (U-Th)/He method	35
I.4.1 Principles of the (U-Th)/He technique	35
I.4.2 Details of the (U-Th)/He method used in this study	38
I.5 Closure temperature concept	39
I.5.1 Fission Track partial annealing zone	39
I.5.2 Helium partial retention zone	40
I.5.3 The $^{40}\text{Ar}/^{39}\text{Ar}$ closure temperatures	41
I.5.4 Conclusions	41
II- Exhumation processes and tectonic evolution of the Aegean	43
II.1 Exhumation mechanism	45
II.1.1 Ductile flow process	45
II.1.2 Erosion process	45
II.1.3 Normal faulting process	46
II.1.4 Exhumation of metamorphic rocks in the Aegean	47
II.2 Geology of the Aegean	47
II.2.1 Configuration	47
II.2.1.1 High pressure metamorphic sequences	49
II.2.1.2 The Cyclades	50
II.2.1.2.1 Geological setting	50
II.2.1.2.2 Timing of metamorphic events	52
II.2.2 The extensional regime	52
II.3 Palaeogeographic evolution	54
II.4 Implications for this study	55
III- Low-temperature thermochronology: Constraining the cooling history of major extensional detachments in the Cyclades	57
III.1 Samos	59
III.1.1 Geological setting	59
III.1.2 Previous geochronological data	60

III.1.3 Results	61
III.1.4 Discussion	61
III.2 Ikaria	62
III.2.1 Geological setting	62
III.2.2 Previous geochronological data	63
III.2.3 Results	64
III.2.4 Discussion	65
III.3 Tinos	67
III.3.1 Geological setting	67
III.3.2 Previous geochronological data	68
III.3.3 Results	71
III.3.4 Discussion	73
III.4 Mykonos	74
III.4.1 Geological setting	74
III.4.2 Previous geochronological data	75
III.4.3 Results	75
III.4.4 Discussion	77
III.5 Naxos	77
III.5.1 Geological setting	77
III.5.2 Previous geochronological data	79
III.5.3 Results	81
III.5.4 Discussion	83
III.6 Paros	84
III.6.1 Geological setting	84
III.6.2 Previous geochronological data	85
III.6.3 Results	85
III.6.4 Discussion	86
III.7 Serifos	87
III.7.1 Geological setting	87
III.7.2 Previous geochronological data	88
III.7.3 Results	88
III.7.4 Discussion	89
III.8 Ios	89
III.8.1 Geological setting	89
III.8.2 Previous geochronological data	91
III.8.3 Results	91
III.8.4 Discussion	92
III.9 Problematic (U-Th)/He data	94
III.9.1 Ik6 sample from Ikaria	94
III.9.2 T2 sample from Tinos	95
III.9.3 M3 sample from Mykonos	96
III.9.4 Na1 and Na2 samples from Naxos	98
III.9.5 Se2 sample from Serifos	100
IV- Tectonic implications	103
IV.1 Summary of our results and major findings	105
IV.1.1 Dating carried out	105
IV.1.2 Timing, slip rate, cooling story and offset of the extensional fault system	105
IV.1.2.1 Samos	105

IV.1.2.2 Icaria	105
IV.1.2.3 Tinos	109
IV.1.2.4 Mykonos	109
IV.1.2.5 Naxos/Paros	109
IV.1.2.6 Serifos	109
IV.1.2.7 Ios	110
IV.2 Comparisons of the Miocene extensional fault systems in the Aegean	110
IV.2.1 Extensional fault system connections	110
IV.2.2 Timing	111
IV.2.3 Differences and similarities	114
IV.3 Miocene normal faulting and exhumation	116
<u>Conclusions</u>	119
1. Conclusions of this thesis	119
2. Future work and recommendations	121
<i>- Bibliography</i>	123
<i>- Figure captions</i>	139
<i>- Appendices</i>	151
A.I. Deviation of the age equations	153
A.II. Sample characteristics	160
A.III. $^{40}\text{Ar}/^{39}\text{Ar}$ data	161
A.IV. Fission track data	163
A.V. (U-Th)/He data	176
A.VI. Formula listing used for the error calculations of slip and cooling rate and calculation methodology	178
<i>- CV</i>	181

Résumé étendu

Introduction

La zone de subduction Hellénique dans l'Egée, est un des meilleurs exemples au monde de retrait d'une zone de subduction. En raison de ce retrait vers le sud durant le Miocène, les roches de haute pression sont accrétées successivement en position d'avant arc vers une position d'arrière arc. Actuellement en position d'arrière arc, les îles Cycladiques, dans le centre de l'Egée, faisaient partie de l'arc volcanique au Miocène supérieur. Elles sont surtout célèbres pour leurs schistes bleus ainsi que leurs failles de détachement. Il est communément admis que l'exhumation des schistes bleus depuis des profondeurs de l'ordre de 60-50 km a été principalement accomplie par des failles de détachement. Cependant, en Crète, il a été démontré que l'exhumation des roches Miocène de haute pression a été accommodée par le jeu normal de grandes failles quand ces roches étaient en position d'avant arc. La question se pose donc à savoir si l'exhumation des schistes bleus Cycladiques fut ou non principalement accomplie quand les roches étaient encore en position d'avant arc. Pour répondre à cette question, il est indispensable de déterminer: 1) à quel moment ces détachements étaient actifs ainsi que le volcanisme d'arc associé; 2) quelles étaient les vitesses de glissement afin d'estimer le déplacement relatif de chacun de ces détachements; 3) leur contribution dans l'exhumation des schistes bleus.

En utilisant les âges cohérents obtenus par les méthodes traces de fission sur apatite et zircon et (U-Th)/He sur apatite sur des échantillons prélevés selon des profils parallèles à la direction de transport tectonique des principaux détachements de huit îles Cycladiques (Samos, Ikaria, Tinos, Mykonos, Naxos, Paros, Serifos et Ios), j'ai ainsi pu estimer la période d'activité, la vitesse de glissement et la quantité de déplacement relatif à chaque détachement étudié.

1- Résultats

Durant cette thèse quarante cinq échantillons provenant de huit îles grecques ont été collectés. Seulement trente quatre échantillons ont pu être exploités pour la datation. Parmi ces échantillons trente et un ont été datés par la méthode des traces de fission sur zircon, vingt quatre par la méthode des traces de fission sur apatite, dix neuf par la technique (U-Th)/He sur apatite et deux en $^{40}\text{Ar}/^{39}\text{Ar}$ sur hornblende. Donc, soixante seize âges ont été obtenus. Cependant, deux âges (U-Th)/He obtenus sur des échantillons provenant de granites de type S de Naxos (Na1 et Na2) n'ont pas été utilisés. Ainsi, j'ai pu mettre en évidence que les données problématiques en (U-Th)/He peuvent être corrélées à des inclusions de minéraux accessoires dans les apatites (comme par exemple de zircon ou de monazite) et/ou des phénomènes d'implantation et/ou des problèmes analytiques. Dans le cas particulier des échantillons Na1 et Na2 de Naxos, des indicateurs de circulation de fluides ont été reconnus en lame mince (tourmaline) qui peuvent induire des perturbations du système (U-Th)/He. De plus, les faibles concentrations en thorium peuvent être interprétées comme un problème analytique lié à la difficulté de conserver le thorium en solution. Par conséquent quelques données ont été rejetées.

a) Samos

Trois systèmes de faille extensive sont exposés sur Samos: (1) le détachement de Kallithea avec un sens de mouvement vers le nord et qui sépare la nappe de Kallithea de l'unité des schistes bleus Cycladique et de la nappe de Kerketas; (2) le détachement de Kerketas avec un sens de mouvement ENE localise entre la nappe de Kerketas et la nappe superposée d'Ampelos; (3) le système de faille extensive de Selçuk avec un sens de mouvement ENE localisé entre les nappes d'Ampelos et de Selçuk.

L'âge trace de fission obtenu sur zircons provenant d'échantillon de l'unité basale indique que le détachement de Kerketas fonctionnait à $14,1 \pm 0,8$ Ma tandis que l'âge obtenu pour l'unité de Kallithea permet d'estimer que le détachement de Kallithea fonctionnait à $7,3 \pm 0,5$ Ma. De plus, trois échantillons provenant de la nappe d'Ampelos ont permis d'estimer une vitesse minimum de glissement pour le détachement de Selçuk à $8,1 \pm 1,7$ km/Ma et un âge entre ~ 20 - 18 Ma pour ce détachement. Cela implique un déplacement minimum de ~ 18 km pour la période de temps ~ 20 - 18 Ma. Cette vitesse élevée de glissement n'est pas corrélable avec l'intrusion de liquide magmatique dans la zone de faille.

Les contraintes de temps ainsi que la répartition géographique des âges indiquent que les systèmes de faille de Kallithea, Selçuk et Kerketas sont indépendants les uns des autres.

b) Ikaria

Pour le détachement de Messaria, les données obtenues par les thermochronomètres de basse température ont permis d'estimer une vitesse minimum de glissement de $7,6 \pm 0,3$ km/Ma entre ~ 10 - 3 Ma. En utilisant les âges antérieurement obtenus par Altherr et al. (1982) par la méthode K/Ar sur muscovite provenant de la nappe Ikaria, j'ai pu estimer une vitesse de glissement minimum à $8 \pm 0,3$ km/Ma pour la partie ductile du système de faille extensive de Messaria qui aurait fonctionné entre ~ 11 - 10 Ma. L'association de ces résultats permet de déduire une vitesse moyenne minimum à environ 8 km/Ma pour le système de faille extensive de Messaria. Cette vitesse impliquerait un déplacement minimum de ~ 60 km pour la période de ~ 11 Ma à ~ 3 Ma.

De plus, les calculs de vitesse de refroidissement de la granodiorite et des méta-sédiments de la nappe d'Ikaria donnent respectivement ~ 40 et $\sim 25^\circ\text{C}/\text{Ma}$. La vitesse de refroidissement rapide de la granodiorite est probablement due à l'intrusion précoce de ce granite dans l'encaissant froid de la nappe d'Ikaria alors que le cisaillement ductile était actif. Par conséquent, le refroidissement du granite de type I était initialement plus rapide en raison du contexte d'intrusion. Après un refroidissement initialement rapide tectoniquement contrôlé le granite présente une histoire de refroidissement similaire aux roches de l'encaissant. Cette interprétation implique donc que l'âge d'intrusion des granites syn-tectoniques de cette île serait de 11 - 10 Ma.

c) Tinos

Deux détachements sont exposés sur Tinos: le détachement Vari et le détachement de Tinos. Les données ont permis de contraindre une vitesse de glissement à $2,8 \pm 0,5$ km/Ma pour la partie cassante du système de faille extensive de Tinos. Deux âges obtenus par la méthode $^{40}\text{Ar}/^{39}\text{Ar}$ sur hornblende augmente dans la direction du mur de faille indiquant que le système de faille extensive de Tinos était actif à ~ 15 Ma. Ces âges ont permis de calculer une vitesse de glissement pour le détachement de Tinos à $1,8 \pm 0,4$ km/Ma, qui est probablement sous estimée en raison de la température de fermeture plus élevée pour le système $^{40}\text{Ar}/^{39}\text{Ar}$ de l'hornblende (Ketchum, 1996) et du fait que cette vitesse est très mal contrainte avec seulement deux datations. Par conséquent, une vitesse moyenne de glissement minimum pour le détachement de Tinos peut être estimée à ~ 3 - 2 km/Ma entre 15 - 10 Ma, impliquant un déplacement de ~ 15 - 10 km. De plus, les données indiquent un refroidissement rapide du granite de type I de Tinos entre ~ 15 - 10 Ma (de $\sim 550^\circ\text{C}$ à $\sim 80^\circ\text{C}$). Ces nouvelles données démontrent que l'histoire du refroidissement entre $\sim 550^\circ\text{C}$ et $\sim 80^\circ\text{C}$ de cette granodiorite était tectoniquement contrôlée par le système de faille extensive de Tinos, c'est à dire que le granite est bien syn-tectonique.

d) Mykonos

Sur Mykonos, la vitesse de refroidissement du monzogranite a été estimée à minimum $\sim 75^\circ\text{C}/\text{Ma}$ entre 13 - 9 Ma. Ce refroidissement rapide est corrélé au détachement de Mykonos qui contrôlerait l'exhumation du granite. Une vitesse de glissement minimum a été estimée à $6,9 \pm 0,7$ km/Ma ce qui

implique un déplacement minimum de 28 km entre ~13 Ma et ~9 Ma. Ce déplacement ainsi que l'angle de ce détachement à ~30° (Avigad et Garfunkel, 1991; Faure et al., 1991; Lee et Lister, 1992) fournissent les éléments nécessaires qui permettent de calculer une exhumation totale de 14 km pour le mur de faille de ce détachement.

e) Naxos/Paros

Le détachement de Paros est habituellement corrélé au système de faille extensive de Mountsouna exposé sur Naxos (Gautier et al., 1990; Gautier et Brun, 1994). La vitesse moyenne minimum de glissement estimée à $6,4 \pm 0,6$ km/Ma pour le détachement de Paros est plus faible que celle obtenue à $8,4 \pm 0,3$ km/Ma pour la partie cassante du système de faille extensive de Mountsouna sur Naxos. Cette variation peut être interprétée comme étant due à l'intrusion d'un large pluton granodioritique sur Naxos vers 14-12 Ma alors que sur Paros seulement de petites intrusions de granite de type S intrudent le mur de faille. Les données indiquent donc une vitesse de glissement rapide à ~9-8 km/Ma entre 12-9 Ma impliquant un déplacement minimum de ~25 km pour le détachement de Naxos tandis que la vitesse minimum de glissement pour le détachement de Paros est estimée à 7-6 km/Ma pour un déplacement minimum de ~17 km. J'ai également estimé que la vitesse de refroidissement (tectoniquement contrôlée) pour la granodiorite de Naxos était très rapide à minimum ~108°C/Ma entre 300°C et 80°C. Finalement, le système de faille extensive de grande échelle de Naxos/Paros enregistre localement des variations de vitesse de glissement corrélées à des conditions locales spécifiques (intrusion de gros corps granitiques).

f) Serifos

Une vitesse de refroidissement rapide à ~39°C/Ma pour la granodiorite de Serifos a été calculée. Cette vitesse rapide est probablement tectoniquement contrôlée. Par conséquent ce résultat corrobore un modèle extensif d'amincissement crustal par cisaillement ductile et faille normale à faible angle comme étant le processus principal de dénudation du pluton (Graseman et al., 2002). L'histoire du refroidissement du granite semble indiquer que ce granite est synchronique du système de faille extensive de Serifos qui opère au sein de la marge passive de l'unité des schistes bleus Cycladique. De plus, l'âge trace de fission obtenu sur zircon provenant de la granodiorite indique que le détachement de Serifos a commencé à fonctionner vers minimum $11,4 \pm 0,5$ Ma.

g) Ios

Sur Ios, les travaux de terrain antérieurs ont révélé un sens de mouvement vers le sud pour la partie ductile du système de faille extensive exposé sur cette île. En raison de l'absence de critère de déformation cassante, toute direction de transport tectonique pour la partie cassante de ce système de faille extensive est nécessairement spéculative. Dans le cas de cette île, j'ai pu démontrer l'utilité d'appliquer des thermochronomètres de basse température pour contraindre la direction de transport tectonique pour la zone cassante des détachement. En effet, les âges obtenus sur Ios deviennent plus jeunes vers le nord indiquant un sens de mouvement vers le nord pour le détachement responsable de l'exhumation des roches de 300°C à 80°C. De plus les données permettent de calculer une vitesse minimum rapide de refroidissement pour les roches du mur de faille de l'ordre de ~36°C/Ma pour une vitesse de glissement de $3,4 \pm 0,5$ km/Ma entre ~15-9 Ma impliquant un déplacement minimum de 17 km. Des travaux de terrain supplémentaires seraient nécessaire pour identifier précisément le détachement qui cause cette variation d'âge. A l'heure actuelle, je ne peux que spéculer que ce détachement pourrait être le détachement de Ios corrélé à la zone de cisaillement ductile de cette île ou la faille d'André localisée au nord de l'île près du système de faille extensive de Ios ou bien encore la faille Côtière exposée le long de la côte nord de l'île.

2- Implications

Les contraintes de temps apportées sur les zones de cisaillement indiquent que le cisaillement ductile de Selçuk sur Samos était le premier actif avant 21 Ma. Vers ~21-20 Ma, les zones de cisaillement de Tinos et de Naxos/Paros se sont développées tandis qu'entre 15 Ma et 10 Ma, quand la plupart des granites intrudent l'unité des schistes bleus Cycladiques, la majorité des détachements exposés commencent à fonctionner (les détachements de Kerketas sur Samos, de Messaria/Kallithea sur Ikaria/Samos, de Mykonos, de Serifos et de Ios) ou restent actifs (systèmes de failles extensives de Tinos et Naxos/Paros qui deviennent actives dans le cassant). Cette étroite relation des événements entre magmatisme d'arc et détachements extensifs (spécialement pour les détachements Messaria/Kallithea de Ikaria/Samos, de Mykonos, de Serifos et de Ios) a été favorisée par l'existence de forts gradients thermiques et des contraintes extensives provoquées par le retrait de la zone de subduction. Les données thermochronologiques indiquent un refroidissement rapide des murs de faille compris entre $\sim 75^{\circ}\text{C}/\text{Ma}$ et $\sim 25^{\circ}\text{C}/\text{Ma}$ et des vitesses de glissement élevées voisines de 8-7 km/Ma. Aucune organisation particulière des âges des détachements et des vitesses associées n'a été reconnue selon la répartition spatiale des îles dans l'arc égéen.

Cette étude a également mis en évidence que le système de faille extensive exposé sur Naxos est unique dans l'arc Egéen. En effet, le détachement de Naxos présente des vitesses minimum de glissement et de refroidissement légèrement supérieures à $\sim 9\text{-}8$ km/Ma et $\sim 108^{\circ}\text{C}/\text{Ma}$, corrélées à des conditions de température élevée pendant la formation du système de faille. La vitesse de glissement semble augmenter au passage de la transition ductile/cassante de ~ 6 km/Ma (donnée antérieurement publiée) à $\sim 9\text{-}8$ km/Ma. L'intrusion d'une granodiorite massive au voisinage de la zone de faille de Naxos, postérieurement à la formation de la zone de cisaillement ductile augmenterait la vitesse de glissement. Par contre sur Ikaria, la vitesse de glissement sur le système de faille extensive Messaria est constante du ductile au cassant parce que l'intrusion de la granodiorite semble être synchrone de la formation de la zone ductile de cisaillement. De plus, contrairement aux zones de cisaillement des autres îles qui s'enracinent aux environs de la transition ductile/cassante, la zone de cisaillement de Naxos s'enracinerait plutôt dans la croûte inférieure.

Nos données montrent également que les détachements accomplissent des déplacements minimum de l'ordre de ~ 53 km sur Ikaria à 12 km sur Tinos, impliquant une exhumation des schistes bleus d'une profondeur inférieure à 10 km. Par conséquent, les failles normales Miocène des îles Cycladiques ne sont pas responsables d'une exhumation importante des schistes bleus. Ces failles normales à fortes vitesses de glissement ont accommodé l'ouverture de la mer Egée.

Conclusion

Dans un premier temps, cette étude a permis de contraindre à quel moment les différentes zones de failles ont fonctionné. Ainsi, les données ont révélé que la période $\sim 15\text{-}10$ Ma était la principale période de fonctionnement des détachements et d'activité magmatique. Cette étroite relation des événements entre magmatisme d'arc et détachements extensifs a été favorisée par l'existence de forts gradients thermiques et des contraintes extensives provoquées par le retrait de la zone de subduction. De plus, aucune organisation particulière des âges des détachements et des vitesses associées n'a été reconnue selon la répartition spatiale des îles dans l'arc égéen.

Ces failles normales Miocène à forte vitesse de glissement ne sont pas responsables d'une exhumation importante des roches (seulement 15 à 10%) mais sont les principaux agents pour l'accommodation de l'ouverture de la mer Egée ($>160\text{km}$).

Finalement, j'ai pu démontrer l'utilité d'appliquer différents thermochronomètres pour contraindre l'évolution à long terme des systèmes de faille extensive. Cependant pour compléter cette étude, un nombre plus important de datation serait nécessaire dans cette zone. De plus, des travaux de modélisation thermique spécifique à chaque île étudiée seraient extrêmement profitables de façon à contraindre plus finement les vitesses de glissement obtenues.

Abstract for non-geologists

The main objective of this thesis is to estimate the timing and the slip rates of normal faults exposed in the Cycladic islands, Greece. The results will show if there is a significant variation between eight different islands in the Aegean in timing and rate of fault slip.

A fault is a discontinuity in the Earth's crust which induces opposite movements of the two blocks separated by this fault. The block located beneath the fault is called footwall and the overlying block hangingwall. During fault movement rocks in the footwall travel upwards towards Earth's surface (Fig. A1). The samples, which were used for this study, have been collected beneath the faults, from the footwall of eight Greek islands.

To constrain the timing of faulting I have used three different dating methods that record when a sample crossed specific temperatures intervals as the rock travels towards the Earth's surface during (Fig. A2). Therefore, I have obtained three ages per sample indicating the moment when this sample first crossed the 300°C, then 110°C and finally 80°C isotherms (line of same temperature in the crust) (Fig. A2). The age obtained for the temperature 300°C is older than the age obtained for the temperature 110°C which again is older than the age obtained for the temperature 80°C. This process is illustrated in Figure A, where three rock samples labelled A, B, C, and located in the crust at a time t_0 are transported successively to Earth's the surface. The ages obtained for any given dating method will vary according to sample location. Because, A is the first one to reach the surface followed by B and C, the ages obtained for sample A will be older than the ages obtained for sample B which are older than the ages for sample C. The latter will be the last sample which crossed the isotherms and reaches the surface. The samples record different ages and, we constrain the time range when the fault operated.

Furthermore, if we correlated the ages, which we obtained on each sample with the distance to the fault (Fig. A2), we can estimate the slip rate of this fault.

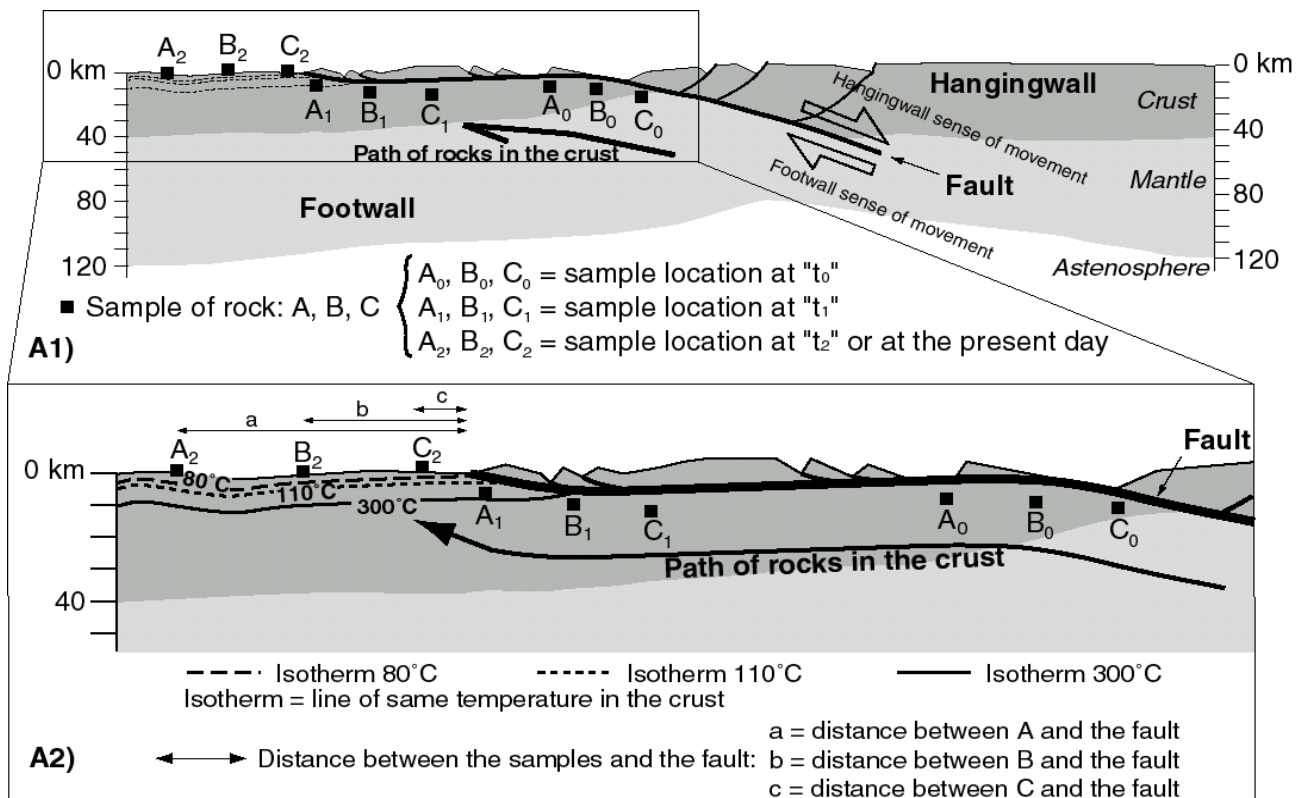


Fig. A (1) Example of the geometry of fault showing rock locations in the time, the path of the rocks in the crust correlated to the footwall and hangingwall senses of movement related to the fault. **(2)** Enlargement of the boxed zone showing the isotherm in the crust related to the methods of dating used and the distance between the samples of rocks collected (A, B, C) and the fault.

The results obtained during this study are summarized in Figure B.

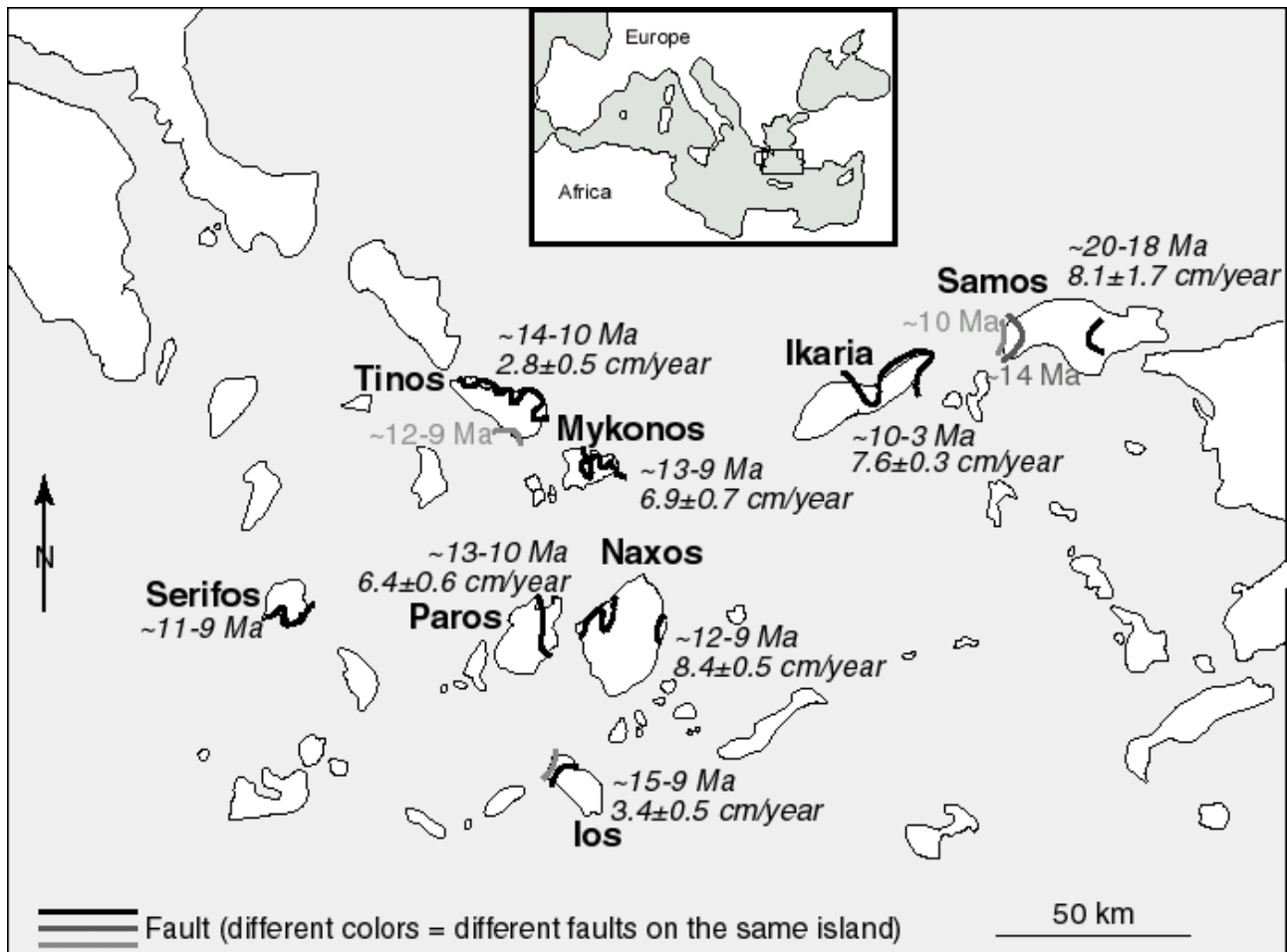


Fig. B Map of the Aegean area showing the studied area and the results obtained from the islands of Samos, Ikaria, Tinos, Mykonos, Naxos, Paros, Serifos and Ios. On Tinos two faults operated at the same time as on Ios, while on Samos three faults with different timing operated (~20-18 Ma, ~14 Ma and ~10 Ma). Ma = Million years.

The result of dating show that Samos Island has the oldest record of fault movement, at around ~20-18 Ma whilst youngest fault movement took place on Ikaria Island between ~10-3 Ma. A major period of faulting activity between 15-9 Ma affected Samos, Tinos, Mykonos, Naxos, Paros, Serifos and Ios islands.

From the results I was able to estimate that the average speed of fault movement, known as slip rates, on Samos, Ikaria, Mykonos and Paros ranged from ~6 to ~8 cm/year, ~3 cm/year on Tinos and Ios and, ~9-8 cm/year on Naxos. On Tinos and Ios the slower slip rate could be explained by several faults operating at the same time and distributed the extension onto several faults.

On Naxos, the slightly higher slip rate is related to the intrusion of a huge granite into the footwall of the fault system when the brittle fault started to operate. This hot granite intrusion increased the weakness of the brittle fault zone and promoted the higher slip rate. On Tinos and Ikaria, granite intrusions occurred as well but slightly before the brittle fault started to operate. Therefore, these intrusions did not increase the slip rate but helped for the fault nucleation.

Although this study has shown that there are differences in the timing and slip rates of fault movement, there is no specific pattern within this part of the Aegean. However a key finding is that between ~15-9 Ma there was major fault activity affecting most of the studied faults.

Introduction

1. Where and why?

After the Pangea supercontinent break-up and the subsequent formation of the Tethys ocean (Late Paleozoic-Early Mesozoic) a series of collisions between continental blocks (mainly, Eurasia with African and Indian plates) have led to the formation of the Alpine-Himalayan mountain chain. This chain is one of the most dramatic manifestations of plate interactions on the Earth's surface. It strikes roughly E-W and runs semi-continuously for more than 15000 km.

The Mediterranean area is located between two main colliding plates, Africa and Eurasia, in the western part of the Alpine-Himalayan chain (Fig. 1).

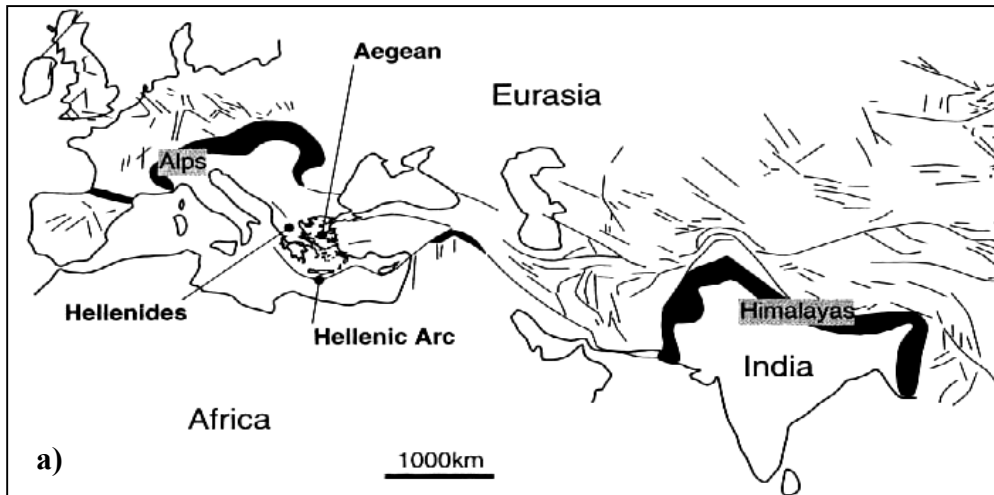
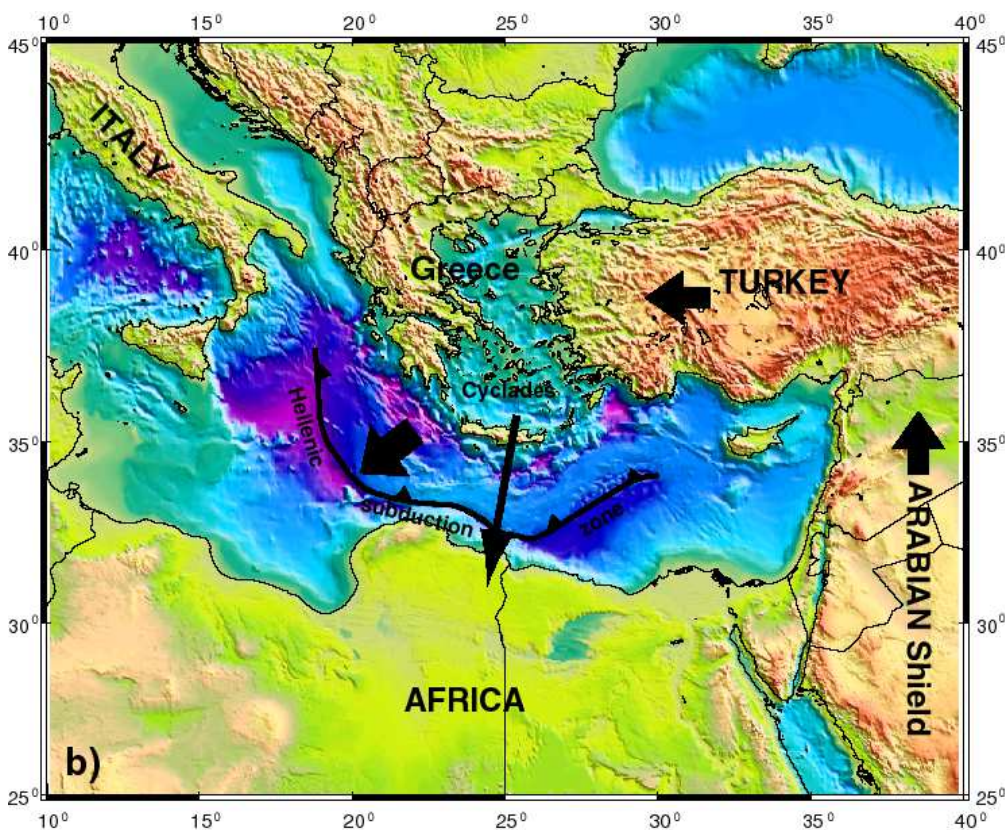


Fig. 1(a) Simplified tectonic map of the Alpine-Himalaya chain (modified after Dewey et al., 1986 and Lips, 1999) showing the dominant linear elements associated with the development of the Alpine-Himalayan system. Black zones characterize main trust belts. **(b)** Topographic map of the Aegean region showing the main relative motions which control the present-day extension.



In the Mediterranean region, the Cyclades in the central Aegean form part of the Apulian-Anatolian plate, which consists of complexly dissected crustal material accreted onto the southern edge of the Eurasian plate (Smith & Woodcock, 1982). Mediterranean sea-floor, which flanks the

northern margin of the African plate, has been subducted beneath the Apulian-Anatolian plate along the Hellenic trench (presently located south of Crete) since late Miocene time (Burchfield, 1980; Robertson & Dixon, 1984) (Fig. 1b).

The Hellenic subduction system is one of the world's best examples of a retreating subduction zone. As subduction retreated with time to the south, accreted high-pressure rocks shifted from a fore-arc position via an intra-arc into a back-arc position. The Cyclades became part of the magmatic arc in the Late Miocene and are now in a back-arc position. The Cycladic islands are famous for their spectacular extensional fault systems (Fig. 2a, 2b) (Lister et al., 1984). These extensional fault systems developed at mid-crustal levels and gradually exhumed from mid to upper crustal levels (Fig. 2b).

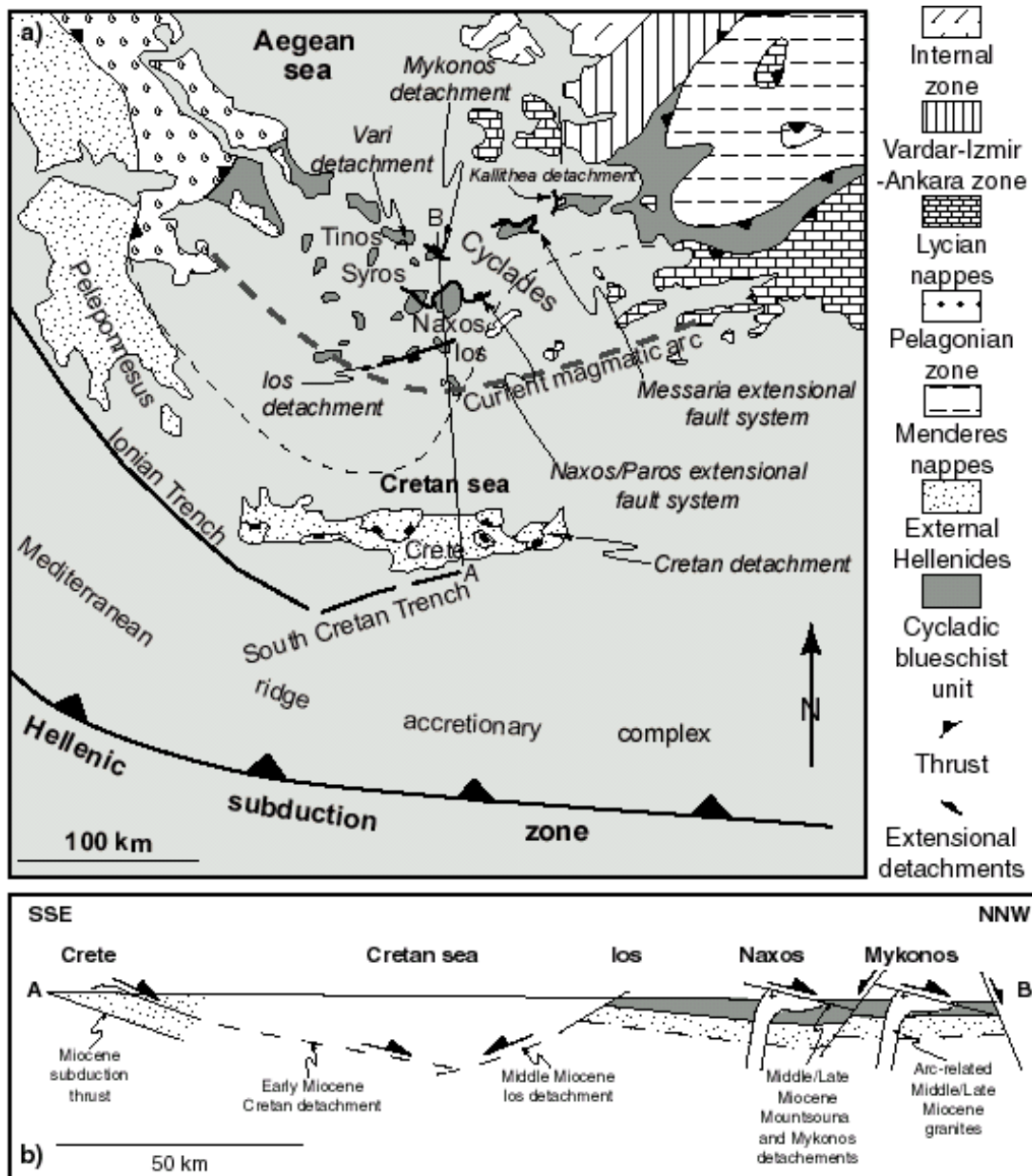


Fig. 2 (a) Generalized tectonic map of the Hellenides showing major tectonic zones, the Cycladic Blueschist Unit, the Cyclades and the subduction zone (modified after Ring et al., 2003). **(b)** Schematic NNW-SSE cross section showing nappe pile and major Miocene detachments in southern Aegean (after Ring et al., 2003); Mountsouna and Mykonos detachment are related top-to-the NNE while the Ios detachment is related top-to-the SSE (Altherr et al., 1982; Buick, 1991; Gautier et al., 1993; Forster & Lister, 1999; Sánchez-Gómez et al., 2002).

The Cyclades blueschists (internal high-pressure belt) formed in the Late Cretaceous and Early Tertiary. It is widely assumed that subsequent exhumation of the blueschist unit was chiefly accomplished by extensional detachment (Lister et al., 1984; Lister and Forster, 1996). Most of this detachment faulting occurred in a back-arc setting, i.e. occurred at a very late stage. However, for the Miocene high-pressure rocks of the external high-pressure belt on Crete, Thomson et al. (1998) showed that ~85-90% of the exhumation was achieved by normal faulting at the Cretan detachment in a fore-arc position. Subsequently, Ring et al. (2001) deduced a displacement of >100 km and a very fast slip rate of >25 km/Myr for the Cretan detachment. These findings raise the question as to whether exhumation of the Cycladic blueschists was mostly accomplished when these rocks were still in a fore-arc setting. To answer these questions we need to know when the detachments exposed in the Cycladic islands, above the blueschists, were active. By constraining the timing of the detachments and arc-related magmatism, we will be able to constrain in detail how much of the exhumation of the Cycladic blueschist unit occurred in an intra/back-arc setting. We can then evaluate the role that fore-arc processes played in the exhumation of the Cycladic blueschists.

From another perspective, several islands have been compared to the extensional Basin and Range province of the western United States which is characterized by high rates of deformation (Lister et al., 1984; Lee & Lister, 1992; Baldwin & Lister, 1994; John & Howard, 1995; Lister & Forster, 1996; Lister and Keay, 1996). Research over the last decade has demonstrated that slip on faults can occur at a range of speeds from <<1 km/Myr up to >20 km/Myr (Table 1). In general these rates are time averaged and do not supply information as to whether the rate of tectonic processes changes systematically over time and across the brittle/ductile transition, which is the major rheologic boundary in the Earth's crust. Unravelling the speed of tectonic processes, and also how the speed of these processes varies over time and across rheologic boundaries, is of primary importance if we are to understand lithospheric deformation. For this reason, it is also interesting to know what the slip rates were on the extensional fault systems. Moreover, the estimation of these slip rates will allow us to constrain the displacement along detachments exposed on the Cycladic islands and when it is possible their contribution to the exhumation of the blueschist. The comparison of the results obtained on each island will permit us to see if a pattern of the extension in the Aegean area exist and to discuss the role of detachment faulting above retreating subduction zones.

Table 1 Slip rates of extensional and strike-slip faults from different areas.

Fault	Reference	Slip rate (km/Myr)
Gressoney extensional shear zone, western Alpine arc	Reddy et al., 1999	3.5
Mountsouna extensional shear zone, Naxos, Greece	John and Howard, 1995	4.7 to 7.6
Vari extensional detachment, Tinos, Greece	Ring et al., 2003	~ 6.5
Cretan extensional detachment, Greece	Ring et al., 2001	20 to 30
Khelmos extensional detachment, Corinth-Patras rift, Greece	Sorel, 2000	~ 15
Catalina extensional detachment, Arizona	Fayon et al., 2000	1.2 to 12
Colorado River extensional corridor, California and Arizona	Foster and John, 1999	3 to 8
Bullard extensional detachment, Arizona	Foster et al., 1993	6 to 8
Buckskin-Rawhide extensional detachment, Arizona	Brady, 2002	4.2 ± 1
Grayback extensional fault, SE Arizona	Howard and Foster, 1996	~1
San Andreas fault, N junction with the San Jacinto fault (strike-slip)	Weldon et al., 2002	20 to 40
Anatolian fault, Turkey (strike-slip)	Westaway, 1994	1.3 to 1.7
Amanos fault, South Turkey (strike-slip)	Yurtmen et al., 2002	1 to 1.6
Naruto-minami fault, Japan (dip-slip)	Nakanishi et al., 2002	~ 1.2
Yangsang fault, SE Korean Peninsula (strike-slip)	Kyung et al., 2002	0.02 to 0.03
Altyn Tagh fault, Tibet (strike-slip)	Yin et al., 2002	9 ± 2
Gowk fault, SE Iran (strike-slip)	Walker and Jackson, 2002	1.5 to 2.4
Dead Sea transform fault, NW Syria (strike-slip)	Meghraoui et al., 2003	6.9 ± 0.1

2. How ?

To estimate the speed of tectonic processes systematic sampling parallel to the movement vector of extensional fault systems has been done on several islands of the Cyclades (Samos, Ikaria, Tinos, Mykonos, Naxos, Paros, Serifos and Ios). The samples have been dated using amphibole and/or white micas and/or biotite $^{40}\text{Ar}/^{39}\text{Ar}$, zircon fission track, apatite fission track and apatite (U-Th)/He methods.

Rates of slip on extensional fault systems may be estimated from the inverse slope of mineral age with distance, in the slip direction, for thermochronological systems that had zero age before extension. When the exhumation of the rocks is controlled by an extensional fault system, thermochronological methods yield older ages in the footwall direction indicating lateral passage of isotherms at the top of the footwall (Foster et al., 1993; John & Foster, 1993; Foster & John, 1999). This approach is most applicable to low-temperature thermochronological data because: (1) it is difficult to determine if higher-temperature thermochronometers yield simple cooling ages, and (2) the effect of thermal pulses on mineral ages is a potential problem at deeper crustal levels. For accurate slip rate estimates the closure isotherm for the thermochronometer must have remained approximately immobile during the interval of slip revealed by the data. Although isotherms may rise owing to heat advection during unroofing, Ketcham (1996) has demonstrated using thermal models that the thermal structure quickly approaches a steady state after the onset of extension. Ketcham (1996) also showed that as the isotherms in the footwall rise in the footwall slip direction, slip rates determined from thermochronological data will underestimate the true slip rate by up to 40%. Also, the underestimation decreases for systems with lower closure temperature and is minimal for slip rates derived from fission track and (U-Th)/He data. However, in several detachment systems the intrusion of granites would have caused an additional thermal perturbation, which may have also affected the low-temperature radiometric systems. Therefore, derived slip rates are minimum estimates. Thus, the minimum slip rates estimated using low-temperature thermochronometers will be used to derive a minimum average slip rate for each detachment fault. This minimum average slip rate will permit estimation of a minimum amount of displacement along each detachment fault during the range of time constrained by the extreme ages obtained with the different low-temperature thermochronometers.

The high closure temperature ($>500^\circ\text{C}$) for the hornblende $^{40}\text{Ar}/^{39}\text{Ar}$ dating experiments will permit constraints to be made on the timing of emplacement of the synkinematic granites associated with extensional faulting in the Cyclades because cooling of granites is fast in footwall of extensional faults (Fig. 3). On the other hand, one of the best-established and most sensitive methods available for reconstructing thermal histories of rocks in the upper crust, over time scale of millions to hundreds of millions of years is fission track thermochronology. However, this method is unable to constrain cooling below $\sim 60^\circ\text{C}$, characteristic of the shallowest structural depths. This limits the ability to close the gap between the deeper subsurface evolution of the rock masses involved and processes acting at surface and near-surface levels. An important technical development in recent years, the advent of (U-Th)/He thermochronometry, provides an exciting and unparalleled opportunity to address this issue directly. Thus, by using a combination of zircon and apatite fission track and apatite (U-Th)/He methods, it will be possible to constrain exhumation in the upper crust ($\sim 1\text{-}7$ km) and to obtain precise temperature-time evolutions (Fig. 3). Moreover, Sibson (1977) showed that the brittle/ductile transition occurs at lowest greenschist-facies conditions at the high end of the zircon fission track partial annealing zone, which is placed between $\sim 300\text{-}200^\circ\text{C}$ (Tagami et al., 1998). For this reason, zircon fission track data allow us to monitor cooling along extensional fault systems roughly at the brittle/ductile transition (Fig. 3). However, several Cycladic islands expose an unusually complete fault systems consisting of a ductile shear zone grading upwards into a brittle detachment (e.g. Naxos, Ikaria and Ios). These fault systems presents an ideal opportunity to constrain slip rates across the brittle/ductile transition. Because slip rates have very rarely been constrained across the brittle/ductile transition, a key aim is

to constrain the temporal evolution of the slip rate in the brittle crust using zircon and apatite fission-track and apatite (U-Th)/He thermochronometry on samples collected across the brittle/ductile transition (particularly the detachments of Naxos and Ikaria). These new data will then be integrated with previously published data to enable detection of any variations in slip rates across the brittle/ductile transition, and shed new light on whether this important rheologic boundary has a significant influence on rates of continental extension.

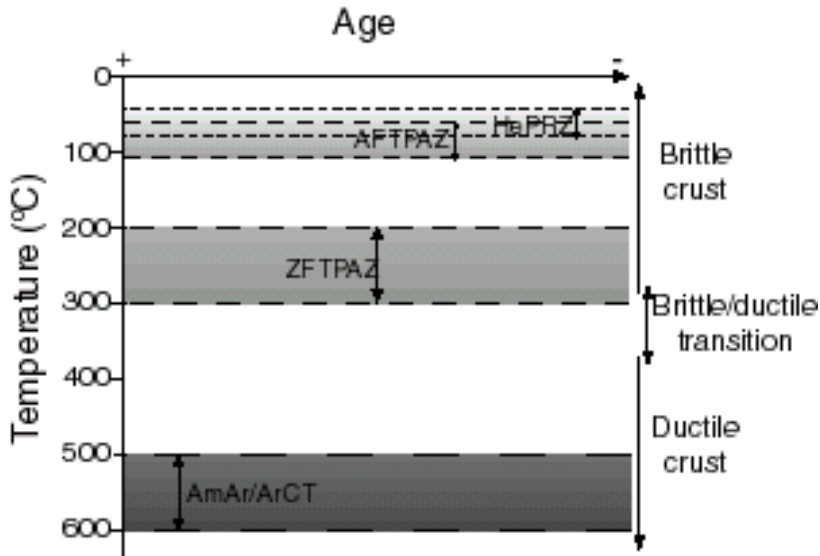


Fig. 3 Closure temperatures of the different chronometers used in this study. The combination of the four methods will allow to constrain the thermal histories of the rock from $\sim 500^{\circ}\text{C}$ to $\sim 40^{\circ}\text{C}$. AmAr/ArCT= closure temperature of the amphibole with the $^{40}\text{Ar}/^{39}\text{Ar}$ method ($550\pm 50^{\circ}\text{C}$); ZFTPAZ= zircon partial annealing zone of fission tracks ($\sim 300\text{-}200^{\circ}\text{C}$); AFTPAZ= apatite partial annealing zone of fission tracks ($\sim 110\text{-}60^{\circ}\text{C}$); HePRZ= partial retention zone of the helium in apatite ($\sim 80\text{-}40^{\circ}\text{C}$).

3. Organisation of this thesis

This thesis is organised into four chapters. The first two chapters provide an introduction to the thermochronological methods used (Chapter I), exhumation processes and the tectonic evolution in the Aegean (chapter II). Chapter I presents a detailed review of the methodology of each dating technique employed in this study and describes the processes that each method records. Chapter II introduces exhumation processes, the geological setting of the Aegean and describes the occurrences of high pressure metamorphic rocks. Chapter III summarises published data and presents the new results obtained from the Cycladic islands along a N-S profile across the Aegean arc (Fig.2). Published results and the new data of this work are considered together for each studied island.

The final chapter (IV) provides an integrated discussion on the possible link between the studied islands and on the geodynamic implications related to the development of the Cycladic area and neighbouring regions.

A concluding chapter summarises the main results and highlights areas for further research.

Chapter I

Methodology

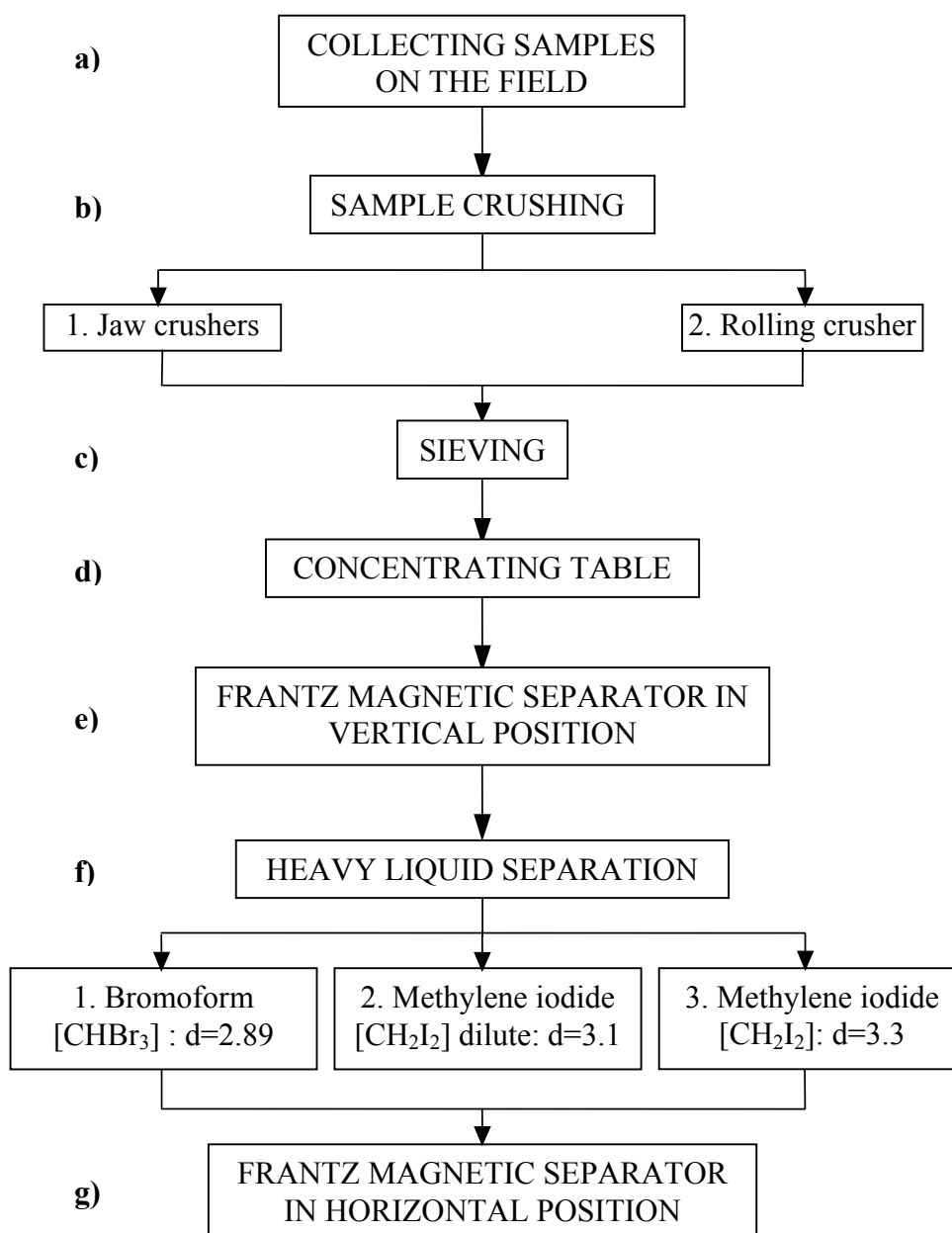
I.1- Mineral separation

The aim of mineral separation is to extract from rock samples individual crystals of amphibole, white mica, biotite, zircon and apatite, for $^{40}\text{Ar}/^{39}\text{Ar}$, fission track and (U-Th)/He dating.

I.1.1 Mineral characteristics

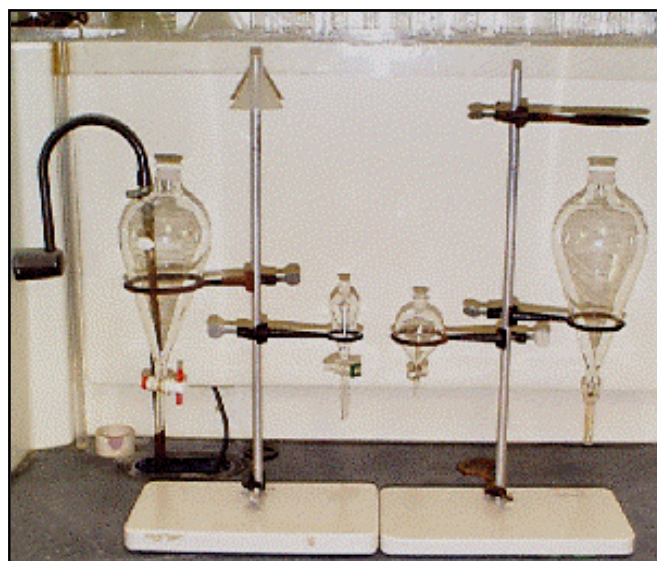
Mineral name	Chemistry	Class	Density	Relative magnetic susceptibility for slope of the Frantz magnetic separator
Hornblende	$\text{Ca}_2(\text{Mg,Fe,Al})_5(\text{AlSi})_8\text{O}_{22}(\text{OH})_2$	Silicates	$2.9 < d < 3.4$	$0.1A < I < 0.8A$
Muscovite	$\text{KA}l_2(\text{AlSi}_3\text{O}_{10})(\text{F,OH})_2$	Silicates	$d \sim 2.8$	Non magnetic
Biotite	$\text{K}(\text{Fe,Mg})_3\text{AlSi}_3\text{O}_{10}(\text{F,OH})_2$	Silicates	$2.9 < d < 3.4$	$0.3A < I < 0.5A$
Apatite	$\text{Ca}_5(\text{PO}_4)_3(\text{OH,F,Cl})$	Phosphate	$3.1 < d < 3.2$	Non magnetic
Zircon	ZrSiO_2	Silicates	$4.6 < d < 4.7$	Non magnetic

I.1.2 Protocol



- Comments:

- a)** Samples for analysis were collected from fresh unweathered outcrops to ensure good quality crystals for dating. This is particularly important for $^{40}\text{Ar}/^{39}\text{Ar}$ dating because weathered minerals, such as partially chloritised biotite, are susceptible to argon loss.
- b)** Large and small jaw crushers are used to reduce the sample size before to put it into the rolling crusher, in the aim to obtain rock powder.
- c)** Sieving was done using an automatic sieve shaker, with two sieves at 500 μm and 80 μm . Grains from within this size interval were used for dating.
- d)** The shaking table uses gravity and water to produce a preliminary separation, removing fine dust particles too small to date. The resultant heavy fraction is then used in the next stage (e)
- e)** The heavy grains from the table are then passed through the magnetic separator in a vertical position at $I=1\text{A}$ to remove ferromagnesian minerals such as biotite and amphiboles. These minerals were kept for hand-picking, under a binocular microscope, for $^{40}\text{Ar}/^{39}\text{Ar}$ dating.
- f)** The non-magnetic fraction from step (e) is then subjected heavy liquid separation using bromoform to remove unwanted quartz and feldspar grains with a density < 2.89 . The minerals that sink in bromoform (Fig. I.2) undergo a second separation using methylene iodide, previously diluted with acetone to a density close to 3.1. To remove grains that have a density close to bromoform, such as composite grains. A final separation using pure methylene iodide (density = 3.3) separate apatite, conodonts and other minerals with density between 3.3 and 3.1 from heavier minerals such as zircon, garnet and sphene.
- g)** The light and heavy fractions from the final methylene iodide separation are run through the Frantz magnetic separator in subhorizontal position at $I=2\text{A}$ to purify the fractions (Fig. I.1) removing unwanted grains such as metamict zircons, garnet or sphene.

**Fig. I.1** Frantz magnetic separator**Fig. I.2** Separatory funnels

I.2- $^{40}\text{Ar}/^{39}\text{Ar}$ method

In order to place temporal constraints on rock formation and exhumation histories, $^{40}\text{Ar}/^{39}\text{Ar}$ analyses of amphibole, white mica and biotite extracted from representative granite samples collected at outcrop in the in the Cyclades Islands was carried out.

I.2.1 Introduction to the $^{40}\text{Ar}/^{39}\text{Ar}$ technique

The $^{40}\text{Ar}/^{39}\text{Ar}$ dating technique is the most commonly used variant of the conventional K-Ar method and is based on the natural decay of ^{40}K to ^{40}Ar (Fig. I.3). A basic underlying assumption is that the relative abundance of the isotopes of potassium are constant in mineral samples.

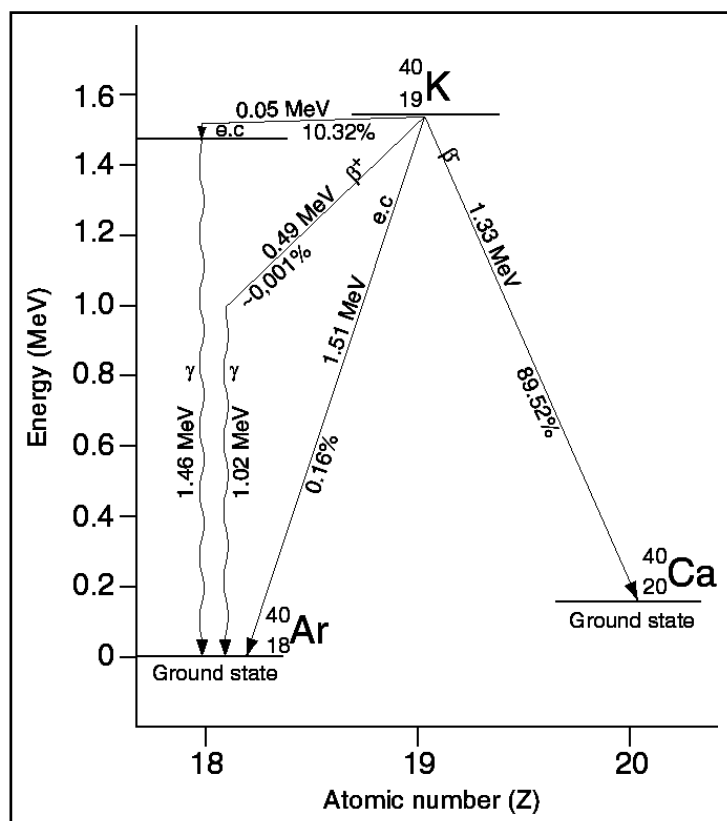


Fig.I.3 Decay scheme for ^{40}K , illustrating the dual decay to ^{40}Ca (85.5%) and the ^{40}Ar (10.5%). Note that the ^{40}K to ^{40}Ar branch is dominated by electron capture (e.c). Adapted from Faure, 1986.

For the $^{40}\text{Ar}/^{39}\text{Ar}$ method the sample to be dated is first irradiated in a nuclear reactor to transform a proportion of the ^{39}K atoms to ^{39}Ar through the interaction of fast neutrons. Following irradiation, the sample is placed in an ultrahigh vacuum system, and the argon extracted from it by fusion is purified and analysed isotopically in a mass spectrometer. Thus, this method has the great advantage that the ratio of daughter ($^{40}\text{Ar}^*$) to parent (^{40}K) is measured in a single isotopic analysis, obviating the need for a separate potassium analysis, overcoming problems of sample inhomogeneity, and, in principle, allowing smaller samples for dating. Another benefit of this approach is that isotope ratios can be measured more precisely, reducing the size of analytical error compared to the conventional K-Ar method.

The major advantage of this technique is that after irradiation a sample can be heated in steps, starting at temperatures below that of fusion. The argon extracted at each step can be analysed isotopically and thus a series of apparent ages determined on a single sample. This approach, known as the incremental heating technique (Merrihue & Turner, 1966), provides a wealth of additional information that can give insights into the distribution of $^{40}\text{Ar}^*$ in the sample. The method relies upon the release of the argon by thermal diffusion processes as the sample is heated at successively higher temperatures. During a step heating experiment $^{40}\text{Ar}^*$ and ^{39}Ar will be released in proportion because of their similar diffusion coefficients, yielding an essentially constant $^{40}\text{Ar}^*/^{39}\text{Ar}_k$ ratio in each gas fraction extracted. A plot of the apparent $^{40}\text{Ar}^*/^{39}\text{Ar}_k$ age for each step against cumulative

proportion of argon released (usually the ^{39}Ar) will yield a flat pattern often termed a plateau. A flat age spectrum of this kind is readily interpreted as indicating that the sample has remained a closed system. However, a sample can lose a proportion of its $^{40}\text{Ar}^*$ after its initial crystallisation, such as during a thermal metamorphism or protracted cooling/exhumation. Such a sample will have sites within its lattice that have different $^{40}\text{Ar}^*/^{40}\text{K}$ ratios, which will be revealed during the step heating experiment and will yield an age spectrum that is not flat. Clearly, the $^{40}\text{Ar}/^{39}\text{Ar}$ total fusion will be intermediate between that of crystallisation and subsequent thermal disturbance.

In the best case, the $^{40}\text{Ar}/^{39}\text{Ar}$ method allows to define a cooling age in relation with the exhumation of the rocks or the age of the last resetting events (details of derivation of the age equations are explained in sections A I.1 and A I.2).

Since mass spectrometers used in $^{40}\text{Ar}/^{39}\text{Ar}$ dating do not normally measure absolute abundances, some standardisation procedure needs to be adopted to calibrate the machine. One standard is atmospheric argon. The isotopic composition of atmospheric argon was measured by Nier (1950) and permits to derive a value of 295.5 for the atmospheric $^{40}\text{Ar}/^{36}\text{Ar}$ ratio as recommended by Steiger and Jäger (1977). Knowledge of the atmospheric argon isotopic composition is essential for successful $^{40}\text{Ar}/^{39}\text{Ar}$ age measurements, as corrections must be made for any contaminating atmospheric argon contained within the sample or contributed from the vacuum system in which the gas is extracted from the sample. (The theory and technique of the $^{40}\text{Ar}/^{39}\text{Ar}$ method are extensively described in the textbook of McDougall & Harrison, 1988).

I.2.2 Details of $^{40}\text{Ar}/^{39}\text{Ar}$ process used in this study

$^{40}\text{Ar}/^{39}\text{Ar}$ dating has been carried out at the University of Montpellier II with the collaboration of Patrick Monié.

The dating has been applied to hornblende, muscovite and biotite separated under the binocular after coarse rock crushing, and cleaning in ethanol and distilled water. All crystals were packed in aluminium foil and irradiated for 70 hours in the McMaster nuclear reactor (Canada) with MMHb hornblende neutron flux monitor dated at 520.4 ± 1.7 Ma (Samson and Alexander, 1987). After irradiation, the single grains were placed on a Cu-holder inside an UHV gas extraction system and baked for 48 hours at 200°C to clean the holder and extract the atmospheric argon potentially retained on the grain surface (Fig. I.4).

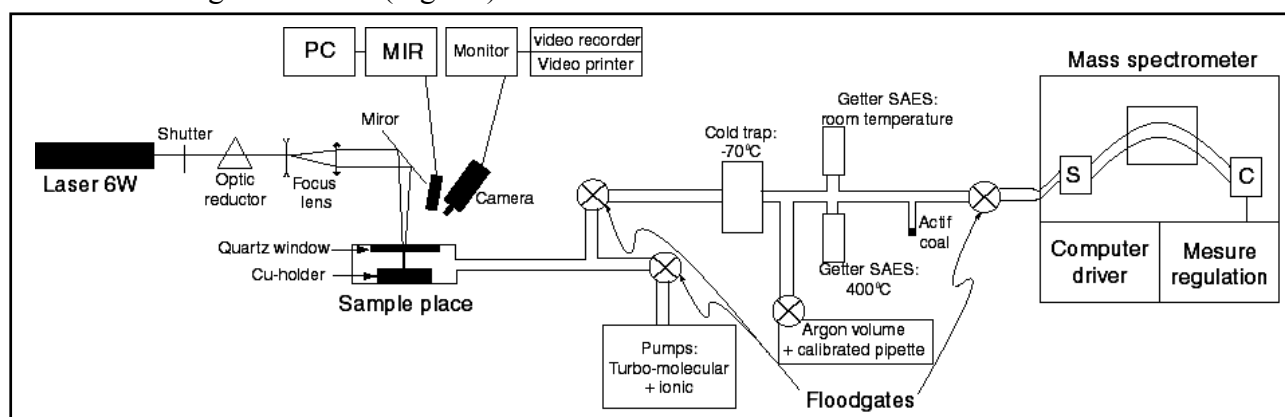


Fig. I.4 Schematic illustration of equipment used during this PhD thesis for Argon measurement at the University of Montpellier II

For each selected sample, single grains of hornblende and/or muscovite and/or biotite were analysed, using a laser probe running in the continuous or semi-pulsed mode depending on the mode of argon extraction: step-heating by increasing progressively the laser power and spot ablation on the grain surface.

The analytical device consists of: 1) a multiline continuous 6 W argon-ion laser; 2) a beam shutter for selection of exposure times, typically 30s for individual steps; 3) divergent and convergent lenses for definition of the beam diameter, which can produce a pit with a size varying

from 50 to 100 μm in diameter for the spot fusion; 4) a small inlet line for the extraction and purification of gases; 5) a MAP 215-50 noble gas mass spectrometer.

Each analysis involved 5 minutes for lasering and gas cleaning and 15 minutes for data acquisition by peak switching from mass 40 to 36, through 10 sets of data. System blanks were evaluated every three analyses and range around $2 \cdot 10^{-12}$ cc for ^{40}Ar and $3 \cdot 10^{-14}$ cc for ^{36}Ar . For each analysis, standard isotope corrections were applied including blanks, mass discrimination radioactive decay of ^{37}Ar and ^{39}Ar and irradiation-induced mass interference. The quoted errors represent one-sigma deviation and were calculated following the procedure of McDougall & Harrison (1988). The raw $^{40}\text{Ar}/^{39}\text{Ar}$ data is provided in section A II.

I.3 Fission track method

Fission track (FT) thermochronology is widely used to reconstruct low-temperature ($<300^\circ\text{C}$) thermal histories of rocks in the upper crust. The method has been successfully used in the Earth Sciences across a range of topics including volcanology, mineral deposits, stratigraphy, basin analysis, tectonics, and impact of extraterrestrial bodies (e.g. Gallagher et al., 1998). The method is ideally suited to constrain the low temperature history of the extensional detachments on islands throughout the Aegean arc.

I.3.1 Principles of the FT technique (Gallagher et al., 1998)

When charged nuclear particles travel through insulating solids, they leave linear trails of disrupted atoms, which reflect intense damage on the atomic scale. Fission tracks are such damage features, and fission track analysis is the study and characterisation of these features in minerals. Natural or spontaneous tracks in geological samples are produced nearly exclusively by spontaneous fission of the isotope ^{238}U .

The currently preferred model for the formation of fission tracks is the ion spike explosion model (Fig. I.5) (Fleischer et al., 1975).

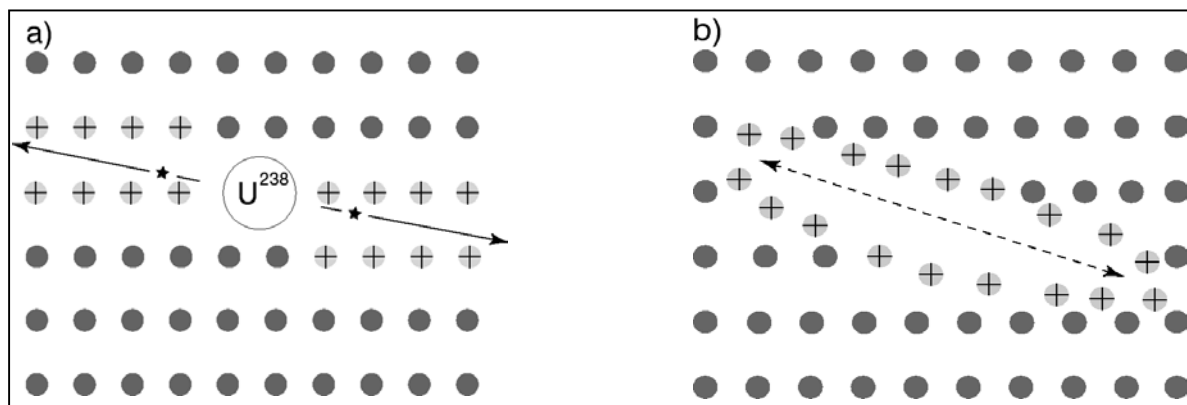


Fig. I.5 Cartoon representation (modified from Fleischer et al., 1975) of the ion spike explosion model and the formation of fission tracks in a mineral. **a)** Spontaneous fission of ^{238}U produces two highly charged heavy particles and releases about 200 MeV of energy. The frequency of fission events is low, about 1 for 2×10^6 α -particle decay events. The highly charged particles recoil as a result of coulomb repulsion and interact with other atoms in the lattice initially by electron stripping or ionisation. This lead to further deformation of the lattice as the ionised lattice atoms repel each other. **b)** As the fission particles capture electrons. They slow down and begin to interact by atomic collisions, leaving a damage trail or fission track.

The application of fission track analysis in a wide variety of fields, including geology, was pioneered in the early 1960s by Fleischer, Price, and Walker (1975). The research was motivated by the first transmission electron microscope observations of latent fission tracks in mica (Silk & Barnes, 1959). The immense progress made by Fleischer et al., was triggered by the discovery that spontaneous fission tracks in natural micas could be observed optically after etching in hydrofluoric

acid. Latent (i.e. unetched) fission tracks, observed with a transmission electron microscope, are generally small but the process of chemical etching opens up the track so that they can be observed optically (Fig. I.6). The etchable width and length of a fission track depends on the actual mineral and the nature of the chemical etchant.

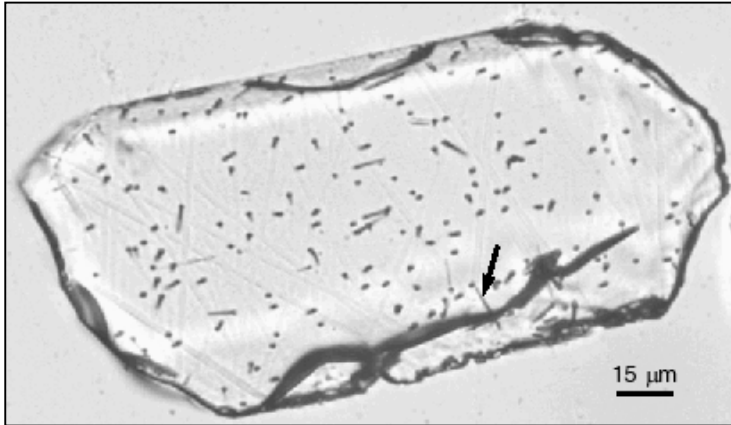


Fig. I.6 Photomicrograph of a polished and etched prismatic section through an apatite crystal (sample M2 from Mykonos), showing etched surface intersecting tracks and a horizontal confined track (narrow). The acid etchant reached the confined track trough a fracture.

Given that fission tracks could be readily observed optically and that the fission process occurs at a statistically constant rate, fission tracks provided a practical method of dating minerals. The major difference between fission track dating and other conventional isotopic dating methods is that the daughter product causes physical damage to the crystal lattice, rather than the production of another isotope. In order to be useful as a dating method, there needs to be a sufficient concentration of parent (i.e. ^{238}U) to produce a detectable number of fission events. On the other hand, too high a concentration of ^{238}U can result in so much fission-induced damage that it is not possible to distinguish individual tracks.

Fission track dating relies on the same general equation as any radioactive decay scheme: it requires an estimate of the relative abundance of the parent and daughter, i.e. the number of ^{238}U atoms and the number of spontaneous fission tracks per unit volume. We count the number of spontaneous fission tracks on a given surface of a mineral grain to quantify how much decay (daughter) has occurred. To determine the ^{238}U abundance (parent) we rely on neutron activation methods to produce a uranium map. Irradiation requires use of a specific energy level of neutrons to induce fission in only ^{235}U rather than ^{238}U . This is because neutron activation of ^{238}U would also cause fission in Th so the map will be a combined U/Th map. Since Th has a long half life all of the tracks observed in natural samples effectively come from the ^{235}U . Provided we monitor the thermal neutron flux, the number of “induced tracks” is indicative of abundance of ^{235}U , and as the ratio $^{235}\text{U}/^{238}\text{U}$ is constant in nature, we can estimate the ^{238}U abundance. The age equation thus becomes;

$$t = \frac{1}{\lambda_d} \ln \left[1 + \frac{\lambda_d \phi \sigma I \rho_s g}{\lambda_f \rho_i} \right]$$

where λ_d , σ , I and λ_f are constants;

λ_d = total decay constant for uranium ($1.55125 \times 10^{-10} \text{ y}^{-1}$);

σ = thermal neutron capture cross section of ^{235}U ($580.2 \times 10^{-24} \text{ cm}^2$);

Φ = neutron fluence, n/cm^2 ;

I = isotope abundance ratio of $^{235}\text{U}/^{238}\text{U}$ (7.2527×10^{-3});

λ_f = spontaneous fission decay constant for ^{238}U ;

g = geometry correction factor. For an internal crystal surface this will be 4π and for an external surface, as in a mica detector will = 2π Thus, for the external detector method $g=0.5(4\pi 2\pi)$;

ρ_s = Density of natural spontaneous fission tracks (daughter product);

ρ_i = Density of induced fission tracks (^{235}U) in a mica detector (surrogate for the parent isotope).

In terms of analytical procedure for age determination, two techniques have been developed: the population and external detector methods.

The population method (Carpéna & Mailhé, 1993 and Wagner & Vanden Haute, 1992) is not widely used as it relies on measuring the spontaneous and induced track densities separately on two aliquots from the same sample. This method implicitly assumes that the uranium distribution is uniform in the grains analysed which is not all the time the case (Fig. I.7).

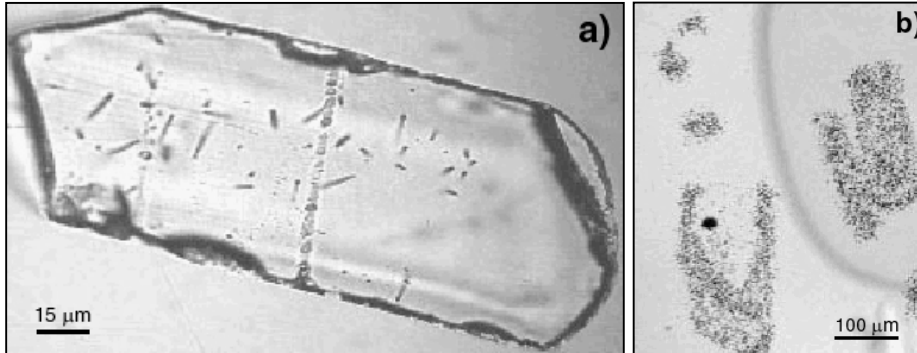


Fig. I.7 Examples of non uniform uranium distribution in grain. **a)** The repartition of the spontaneous tracks in the grain (Naxos sample: Na2) is clearly not uniform with a higher track concentration in the core of the crystal. **b)** Not uniform repartition of the induced tracks in a sample from Paros (P32) with a higher concentration of tracks on the rim.

Moreover, this method neglects the useful geological information contained in distribution of single grain or crystal ages for an individual sample. The external detect method has been applied throughout this study.

For the external detector method (EDM), a single aliquot of sample is used to obtain ρ_s , by counting n crystals to give N_{sj} in an area A_j of the j crystal. The induced track density (ρ_i) is obtained from an external detector, usually mica, that gives a mirror imprint of the uranium variation within each crystal enabling the derivation of N_{ij} from exactly the same area as N_{sj} . This enables any variation within a data-set to be detected and attributed to specific grains. Thus, for the EDM method ρ_s and ρ_i are given by;

$$\rho_s = \frac{\sum N_{sj}}{\sum A_j}; \quad \rho_i = \frac{\sum N_{ij}}{\sum A_j}$$

The external detector method has the distinct advantage that data is recorded on an individual crystal basis such that N_s and N_i are derived from the same concentration of uranium. A major advantage of the external detector method is that grains or crystal can be dated individually (Fig I.8).

A major problem with the age equation is the spontaneous fission decay constant, λ_f . This constant has been difficult to measure and as yet there is no international consensus on a common value. In order to circumvent this and other fundamental problems associated with determination of the neutron fluence (Φ), Hurford and Green (1982), proposed an alternative calibration system based on independently characterised age standards. The resultant 'Zeta' calibration method (Hurford and Green 1983) has become the standard approach to fission track age determination (Hurford 1990) and replaces λ_f , σ and I.

$$\zeta = \frac{[e^{\lambda_d t^{std}} - 1]}{\lambda_d \left[\frac{\rho_s}{\rho_i} g \right]_{std} \rho_d}$$

The neutron fluence (Φ) is represented by the induced track density of a standard uranium glass mica detector (ρ_d). Thus, the age equation becomes;

$$t = \frac{1}{\lambda_d} \ln \left[1 + \lambda_d \zeta \frac{\rho_s}{\rho_i} g \rho_d \right]$$

As well as removing ambiguity concerning the true value of the spontaneous fission decay constant for ^{238}U and determination of the neutron fluence (Φ), Zeta also subsumes, and corrects for, elements of method-based bias that relates to an individual experimenters sample preparation, observation conditions and counting efficiency. Thus, before fission track analysis can begin, an analyst has first to derive his/her own personal zeta calibration value, against a specific standard uranium glass, and for each mineral phase. More details of the age equations are explained in section A I.1 and A I.3.

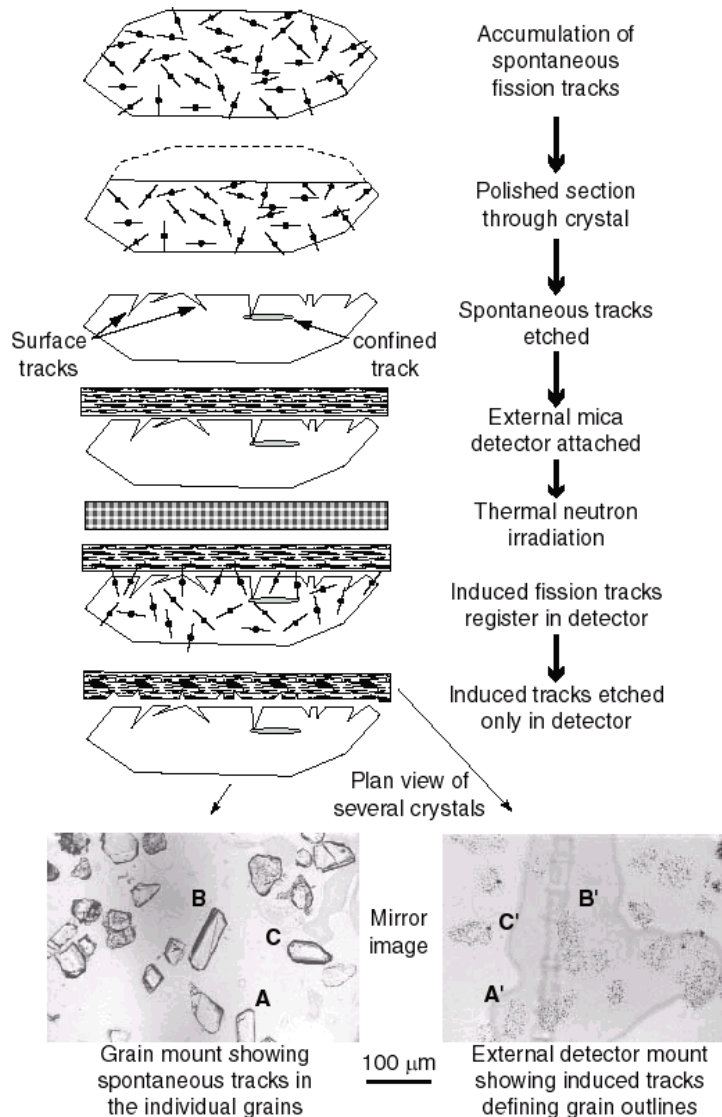


Fig. I.8 The external detector method used in this study, after Hurford & Carter (1991). The surface of a given mineral is polished and etched to reveal spontaneous tracks. Confined tracks can also be revealed if there is a pathway for the etchant. Then an uranium-free detector (muscovite mica) is sealed against this surface and this assembly is sent to irradiation, which will induce fission in ^{235}U . During the fission process, some heavy particles cross the interface between the mineral and the mica, producing a mirror image of the original grain. After, only the mica is etched to reveal the induced tracks. By counting the number of induced tracks in the mica, we estimate the uranium (or parent) concentration of the mineral, whereas by counting the number of spontaneous tracks in the mineral, we estimate the concentration of the daughter product.

For this thesis the zeta calibration factor has been determined using the following age standards; for apatite, Durango from the Cerro de Mercado (iron mountain) Mexico (31.4 ± 0.5 Ma; Steiger & Jäger, 1977), Fish Canyon Tuff from Colorado (27.8 ± 0.2 Ma; Hurford & Hammerschmidt, 1985) and Mont Dromedary Banatite from Australia (98.7 ± 0.6 Ma; Green, 1985). For zircon, I used Fish Canyon, the Tardree Rhyolite from northern Ireland (58.7 ± 1.1 Ma; Hurford & Green, 1983), the Buluk Member Tuff from northern Kenya (16.2 ± 0.6 Ma; Hurford & Watkins, 1987) and Mont Dromedary.

In practice, an individual analyst will undertake a minimum of 15-20 calibrations on different standards to determine his/her own particular ζ value for a given dosimeter and do it regularly to complete his/her own ζ factor. Thus ζ also absorbs some of the vagaries of the observation process.

Typically, the fission track age is reported as some kind of average estimate of the individual single grain age. There are three “mean” age estimates in common use: the mean, pooled, and central ages. The pooled age is simply the sum of the spontaneous counts divided by the sum of the

induced counts, while the mean age is the arithmetic mean of the individual ratios of spontaneous to induced tracks. The central age is a more recent development (Galbraith & Laslett 1993) and is essentially the weighted mean of the log normal distribution of single grain ages. When the variation in the count population is consistent with a Poisson distribution, then all three age estimates are essentially the same. When there is extra-Poissonian variation, due to variable grain composition, provenance (in sedimentary samples), or simply bad experimentation, the central age offers the best measure of the spread in single grain ages.

Having defined an age the next issue is to understand what the age means. Does it record rapid or slow cooling, formation age or resetting? Fission tracks are semi-stable features that react primarily to elevated temperature over time by progressive track shortening (a process of self-repair known as annealing). A decrease in fission track length, causes a reduction in the probability of a track intersecting a mineral surface and this lowers the measured track density, resulting in a reduced or apparent age that has little direct geological meaning. Consequently, to interpret fission track data properly it is essential to know if the measured age reflects a true normal full length distribution or, is an apparent age as a result of track shortening due to exposure to elevated temperatures.

The track length distribution of a sample provides an insight into past thermal history and therefore a means of discriminating between true and apparent ages. Since the length of a fission track is primarily a function of the maximum temperature to which it has been exposed (the duration of heating has a secondary influence), and because tracks are forming continuously, individual tracks will experience and therefore relate to different portions of a sample's thermal history. Since a sample's track length distribution is key to understanding its thermal history and the nature of a measured fission track age it is essential that a suitable approach be adopted for the measurement of track lengths. There are two principal methods. The first, known as projected track lengths, requires measuring all surface tracks that outcrop on a mineral surface. Such lengths are in effect semi-tracks as part of the track will be missing, being either polished or etched away. Although the advantage of using projected or semi tracks is that statistically large data-sets can be rapidly accumulated, mathematical models show that realistically only limited thermal history information can be extracted from such data (Galbraith 1990; Laslett *et al.*, 1994).

The alternative approach to measuring the distribution of track lengths in a sample is to use only horizontal confined tracks which are exposed by etchant passing through either a fracture or cleavage (Tracks IN CLEavage or TINCLES), or, another track (Tracks IN Tracks or, TINTS) (Fig. I.9). Although much rarer than surface tracks, confined track lengths show their full etchable length and can be measured directly requiring no correction for missing section or inclination. Although subject to forms of observation bias, particularly for the shorter tracks, confined track length distributions are more reproducible than semi-or projected lengths and more importantly contain detailed information concerning a samples thermal history (e.g. Laslett *et al.*, 1994).

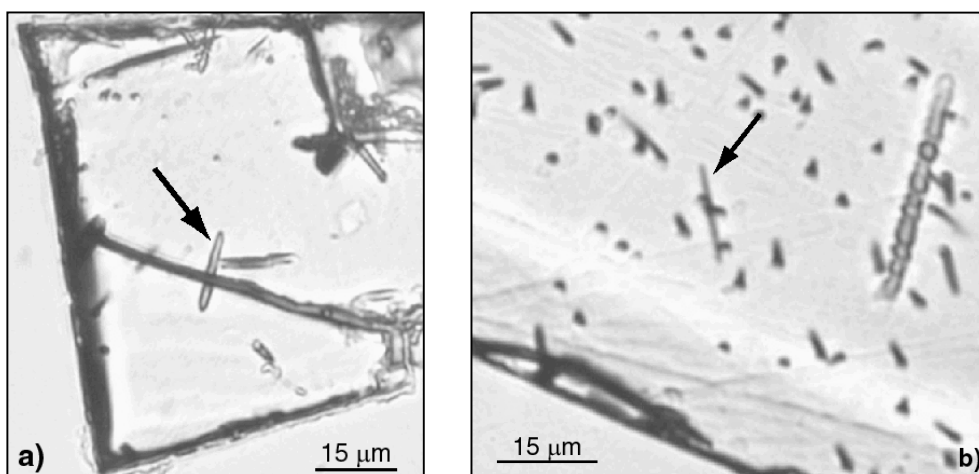


Fig. I.9 Examples of confined tracks (arrows): **a)** Track-IN-Cleavage or TINCLE; **b)** Track-IN-Track or TINT.

As well as measuring the length, it is becoming more common to measure the angle of the track with respect to some reference orientation (Laslett et al., 1982; Green et al., 1986; Galbraith & Laslett, 1988; Galbraith et al., 1990; Donelick, 1991). This is because both the etching and track annealing processes can be anisotropic with respect to the crystallographic axes (Fig. I.10).

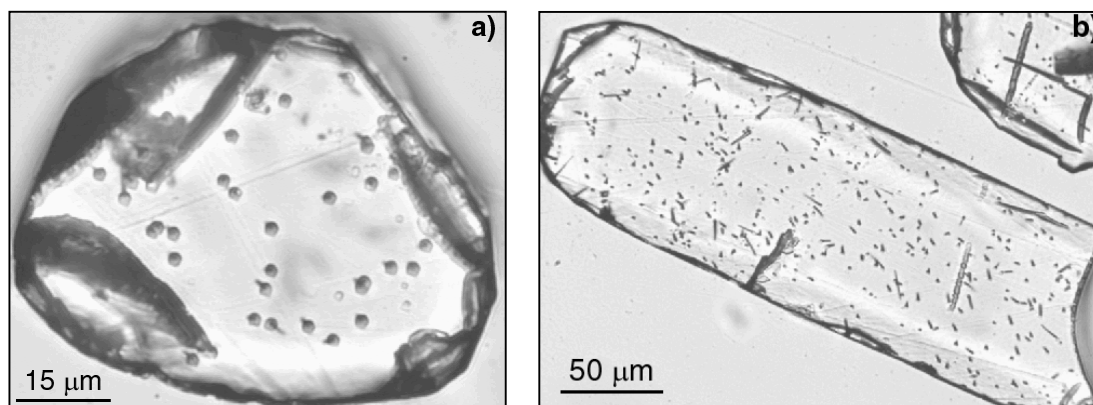


Fig. I.10 Different shapes of fission tracks in apatite crystal according to axis types: **a)** a-crystallographic axis with characteristic fission track shape; **b)** c-crystallographic axis conventionally used for fission track measurement.

Individual confined track length data can be measured to a precision of $\sim 2 \mu\text{m}$ (Green et al., 1986), and 50-150 individual track length measurements are made to obtain a good idea of the real length of the tracks for a given sample. The value and reliability of TINCLE measurements has been debated (Laslett et al., 1984; Carlson et al., 1999; Barbarand et al., 2003) and it appears that different Mean Track Length (MTL) and distributions are found for TINTs and TINCLES in the same sample for all but the longest lengths. For more heavily annealed samples with MTL values $< 12 \mu\text{m}$, TINCLES are substantially longer than TINTs with relatively few short TINCLES at high angles. Measurement of TINCLES effectively masks the anisotropy of annealing. For this reason, it is better to measure the TINTs to reduce the sources of variation between observers and especially for a complex length distribution where the variations can reach $\sim 12\%$ (Barbarand et al., 2003).

The data are reported in terms of the mean standard deviation and a representative length distribution, generally a histogram.

I.3.2 Details of fission track (FT) method used in this study

FT dating has been carried out at the University of Montpellier II and the University College of London with the collaboration of Andrew Carter.

Spontaneous FT were revealed by etching polished apatite grain mounts with 6.5% HNO_3 at 20°C , for 40 seconds while spontaneous FT in zircon were revealed by etching polished grain mounts with a mixture of 33.6g of potassium hydroxide (KOH) and 24g of sodium hydroxide (NaOH) at maximum 225°C during 30 to 45 hours (depending of the sample). Induced FT in mica were revealed by etching with 40% HF, for 40 minutes.

Our samples for Fission track analysis were irradiated with muscovite external detectors, standard samples and Corning dosimeter glass CN-5 and CN-2 (Fig. I.11a. and b.) at the Radiation Center Oregon State University, USA which has a Cd ratio for Au < 200 , under a fluence of $1.10^{16} \text{ n.cm}^{-2}$ for apatite and $8.10^{14} \text{ n.cm}^{-2}$ for zircon.

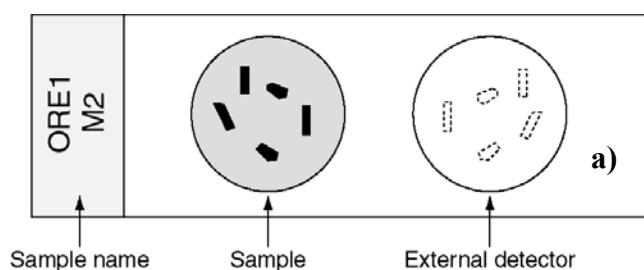


Fig. I.11 (a) Schematic illustration (modified from Jolivet, 2001) of the sample mount for fission track counting.

This fluence is an important parameter which controls the density of tracks in relation with the Uranium concentration in the apatite or zircon grain. Usually, the fluence used for zircon is 1.10^{15} n.cm⁻². However, zircon from our samples has high U contents. After the first irradiation under the conventional fluence it was not possible to make out the fission tracks in the mica owing to the high concentration of tracks. For this reason, the sample have been sent again for irradiation under a lower fluence.

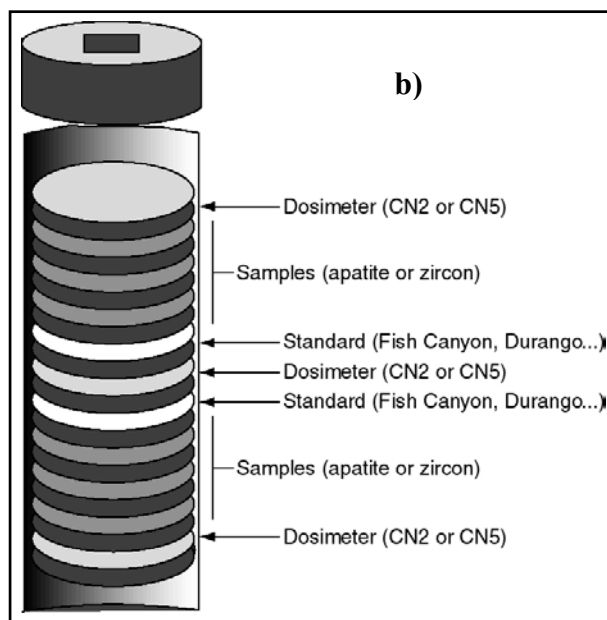


Fig. I.11 (b) Schematic illustration (modified from Jolivet, 2001) of the preparation of the samples for irradiation. Tube of irradiation: a piece of dosimeter is put on top, middle and bottom to define the fluence cross the tube during irradiation (one dosimeter is put in the middle of the tube because between 30 and 40 samples can be put in the tube use at the Radiation center in Oregon). Samples are for the age determination while standards are put regularly in the tube to determinate the zeta number. Dosimeters, samples and standard are cover with external detector (muscovite). The most important is to compress well this sandwich to obtain a good contact between the mount and the external detector. A bad contact induce an ageing of the dating because a part of the induced tracks revealed in the external detector can be lost.

Fission-track densities were measured using an optical microscope at 1250x magnification and a digitising tablet, with a cursor equipped with a high-intensity light emitting diode (LED). By calibration the digitising tablet against a stage micrometer, it is straightforward to measure the length of individual tracks observed under the microscope (Fig. I.12).

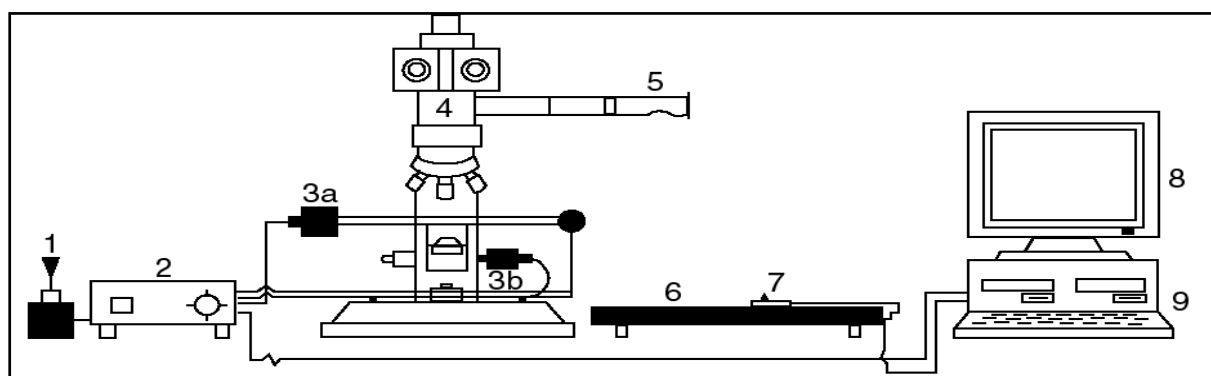


Fig. I.12 Schematic illustration (modified from Wagner & Van der haute, 1992) of equipment used during this PhD thesis for track counting and track size measurements at the University of Montpellier II and University College of London. (1) Tri-axial joystick for manual control of motorised stage; (2) Controlled unit of motorised stage; (3a) Step motors for movement in X, Y direction; (3b) Step motor for movement in the Z direction (focus); (4) Microscope; (5) Drawing tube attachment; (6) High resolution digitising tablet; (7) Cursor with centred LED; (8) and (9) personal computer and monitor connected to tablet and stage controller.

Ages ($\pm 1\sigma$) were calibrated by the zeta method (Hurford & Green, 1983) (Fig. I.9), using a zeta factor of 127.3 ± 4.4 and 332.9 ± 9.7 determined respectively by multiple analyses of zircon and apatite age standards following the recommendations of Hurford (1990) (Fig. I.13 and details of the zeta number determination in section A I.3).

To obtain a good reproducibility of the FT ages only tracks in c-axis have been counted, and we have selected apatite free of impurities, in particular zircon microlites and fluid inclusions while for the zircon the most important criteria are the size and the density of track (Fig. I.14).

The number of measurable tracks lengths for the samples in this study were generally low due to a combination of young FT age and low uranium concentrations.

For this reason, additional sample mounts were prepared for californiating. This involves irradiated the samples with a collimated beam of heavy ions, ^{252}Cf -derived fission fragments for 24 hours (Donelick & Miller, 1991). The exposures were made under vacuum to enable the neutrons to penetrate deeper into the apatite grains increasing the number of intersections with natural confined spontaneous tracks.

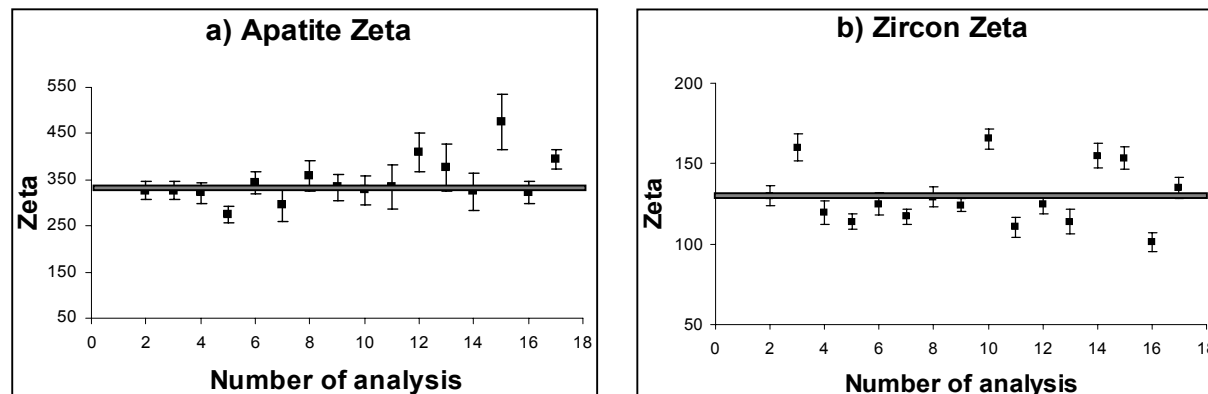


Fig. I.13 Graph of the zeta evolution (Stéphanie Brichau) for apatite and zircon. Grey lines correspond to the weighted mean, i.e. zeta values used in this study (332.9 ± 9.7 for apatite and 127.3 ± 4.4 for zircon). The zeta was determined on Durango, Fish Canyon and Mont Dromedary apatite standards and on Fish Canyon, Tardree, Buluk and Mont Dromedary zircon standards (listing of data are given in section A I.3).

Comparison of unirradiated and Cf-irradiated aliquots suggest an overall deviation of $\sim 3\%$, not exceeding that found for replicate analysis by a single analyst (Barbarand et al., 2003).

Data are reported in this study using the IUGS-recommended approach (Hurford 1990). The track length data are reported in this thesis as mean standard error and standard deviation of the mean. The distribution of lengths are also plotted as a histogram.

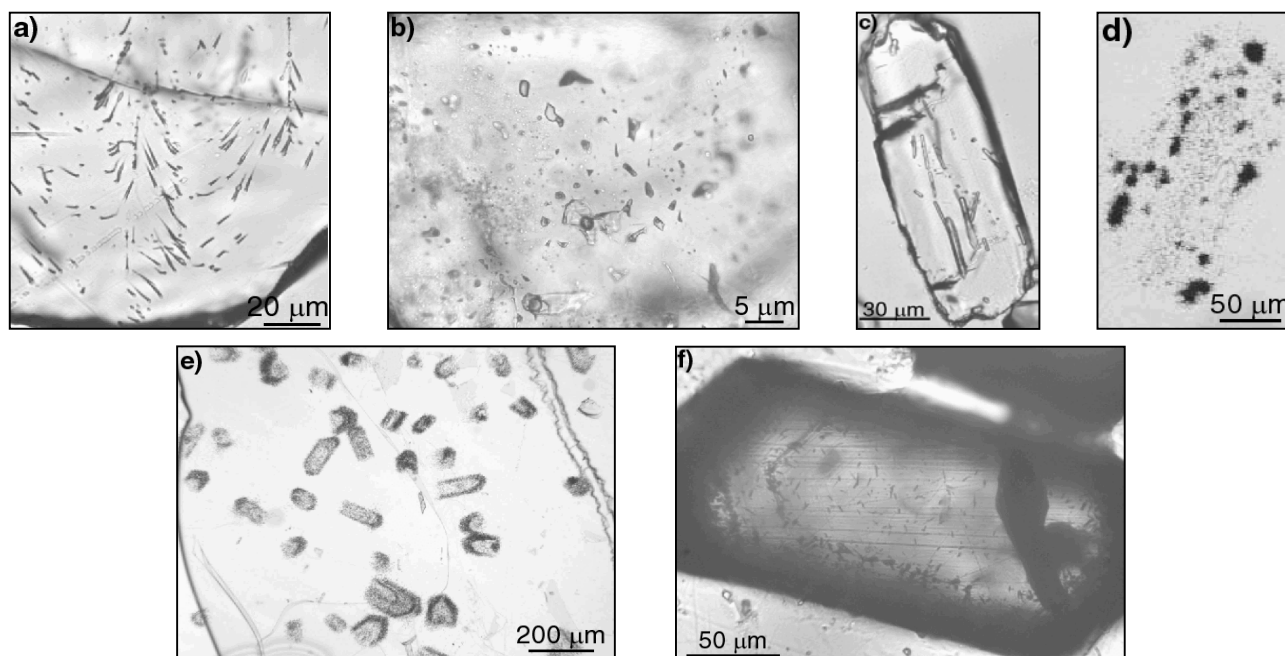


Fig. I.14 Examples of problems encountered during fission track counting. **(a)** *Sample P32*: Sometimes crystal defects can be confused with fission tracks. The repartition of the defects is a good indicator to distinguish them from FT because their repartition is random. **(b)** *Sample P34*: fluid inclusions in this apatite does not allow to count the fission tracks. **(c)** and **(d)** *Sample Na2*: inclusions of zircon in an apatite grain are a problem to count the induced tracks in the mica because the high uranium concentration in the zircon induce a high concentration of tracks (photo d.) and consequently a perturbation of the counting. **(e)** and **(f)** *Sample IK1*: concerning the zircon the most important problem is the strong zonation of the tracks in the grain (photo f.) and the mica (photo e.) in relation with inhomogeneous uranium distribution. Consequently it is difficult to find good grains and/or a large counting area.

I.4 (U-Th)/He method

The low closure temperature of this technique has gained the interest of tectonocists because it is applicable to studies in structural geology across a range of different geodynamic settings. The method is sensitive to temperatures between ~40-80°C and can be used to record small changes in rock uplift not detectable by the FT method. Consequently by combining both FT analysis and (U-Th)/He dating in a single study it is possible to monitor cooling in the top 1-3km of the crust.

I.4.1 Principles of the (U-Th)/He technique

Helium (^4He) is produced within apatite grains as a result of the series decay of ^{238}U , ^{235}U and ^{232}Th and also by decay of ^{147}Sm (details of the age equations are explained in section A I.1 and A I.4). These decay schemes provided the basis for the first attempts at geochronology (Rutherford, 1903). In essentially all minerals the majority of radiogenic helium derives from actinide decay. This assumes no initial ^4He present in the crystal being dated, and this is probably in general a good assumption. For example, while atmospheric argon frequently accounts for a substantial fraction of the ^{40}Ar in a K/Ar or Ar/Ar analysis, the concentration of He in the atmosphere is so low that trapped atmospheric He is unlikely to be important. In some cases fluid inclusions may carry crustal or mantle helium, but for U, Th-rich minerals like apatite or zircon, the He concentration of such fluids and/or the inclusion density would have to be high to affect He ages except when the He ages are young. The presence of helium “inherited” from some prior history, for example due to incomplete degassing of a crystal stopped into a magma chamber, is unlikely given the high diffusivity of He in most solids.

A complication inherent to the He dating method is that α particles of the U and Th series are emitted with sufficient kinetic energy to travel many microns ($20\pm 10\ \mu\text{m}$) through solid matter before coming to rest (Farley et al., 1996). As a result, α decay induces a spatial separation between parent and daughter nuclei. This unavoidably leads to the erroneous appearance of He age heterogeneity within the rock, with some regions or crystal “too old” and “too young”. The effect can be substantial in small crystals and is likely to be the single greatest impediment to high precision He ages in common accessory minerals (Farley et al., 1996).

Each α decay within the U and Th series has a characteristic energy and hence characteristic (Zeitler, 1977) stopping distance within a given material. As a result, an α particle will come to rest on the surface of a sphere centred on the site of the parent nucleus and with a radius equivalent to the stopping distance. There are three relevant outcomes of α decay in a crystal being dated (Fig. I.15). If the parent nucleus is located more than the stopping distance away from the edge of the crystal, the α particle will be retained within the crystal. However, if the parent nucleus lying within one stopping distance of the crystal boundary there is some probability that the α particle will be ejected. It is also important to consider that decay occurring outside of the crystal can lead to implantation into the crystal interest.

The primary observation relating to this phenomenon is that only the outermost $\sim 20\ \mu\text{m}$ of a crystal are affected. This needs to be corrected for a simple solution is either chemical or mechanical removal of the outermost surfaces of the grains to be dated. However, the He diffusion domain in some minerals is the grain itself (Bahr et al., 1994; Reiners and Farley, 1999; Farley, 2000). In this case, removal of the outermost portion will bias the age of the remaining crystal toward erroneously high values. For some applications, such as dating of quickly cooled minerals, this approach may be appropriate (Farley 2003).

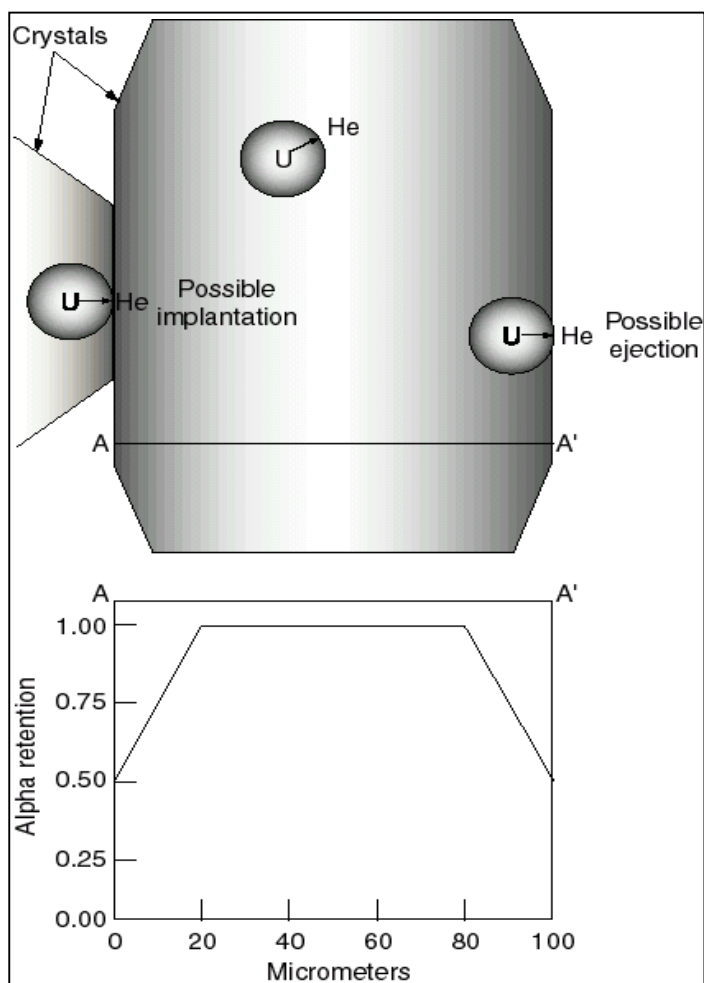


Fig. I.15 Schematic illustration (modified from Farley, 2002) of the effects of long α -stopping distance on He retention. The upper figure illustrates the three relevant possibilities within a schematic crystal: α retention, possible α ejection and possible α implantation. “U” denote the site of the parent U or Th nuclide, and the edge of the shaded sphere labelled He indicates the locus of points where the α particle may come to rest; the arrow indicates possible trajectories. The lower plot shows schematically how α retention changes from rim to core to rim along the path A-A’; exact equations defining the shape of this curve as a function of grain size (Farley et al., 1996).

As an alternative, Farley et al. (1996) developed a quantitative model for correcting He ages for the effect of long α stopping distances based on measured grain geometry and size. Assumptions required for the modelling are:

- the implantation from the surrounding matrix is insignificant because in most minerals used for He dating, the concentration contrast with the host rock.
- ideally, the distribution of U and Th in the crystal should be specified using back scattered, cathodoluminescence (CL) or maps based on neutron activation methods such as induced fission tracks. In most cases the U/Th distribution is assumed to be homogeneous (Fig. I.16).

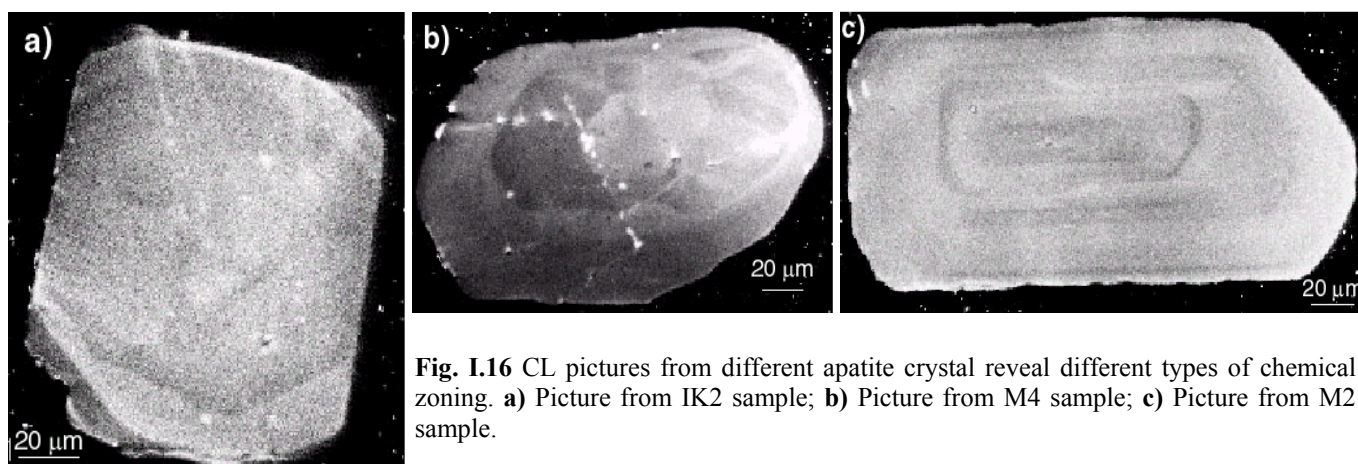


Fig. I.16 CL pictures from different apatite crystal reveal different types of chemical zoning. **a)** Picture from IK2 sample; **b)** Picture from M4 sample; **c)** Picture from M2 sample.

In accordance with these assumptions, Farley et al. (1996) showed how alpha ejection can be corrected for by calculation of a correction factor “ F_T ”, for a particular grain size (section A I.4). Thus, the “ F_T ” parameter is the factor which defines the percentage loss of helium from a grain due to ejection. A corrected age is defined by dividing the measured age by this factor.

To obtain high quality data by the (U-Th)/He dating method the following procedures are used:

Grains to be analysed are selected on the basis of a well defined crystal morphology, homogeneous grain size (not less than 70 μm across) and absence of visible defects such as mineral inclusions and fractures. Hand picking selection is done under a polarising binocular microscope at 125x magnification in ethanol using both transmitted and polarised light. The dimensions of the grains (prism diameter and length in case of apatite) in each aliquot (typically between 1 and 20 grains depending of the analytical accuracy of the spectrometer used and/or the U-Th concentration in the sample) are measured using a reticule in a binocular microscope. Then an F_T value is computed for the grain based on the grain's dimensions and geometry and the α -ejection model (section A I.4). The mean F_T of the entire population of grains is computed, weighting each grain by its mass contribution to the sample. The weighting is based on observed grain dimensions. This weighting implicitly assumes that grains contribute helium in proportion to their mass. If grains of very different sizes have very different U-Th contents, this weighting will be incorrect. Hence the requirement to pick grains of a common size.

The main problem with this approach to α -ejection correction is the assumption of a uniform distribution of parent nuclide. Consider a typical hexagonal apatite crystal. If all of the U and Th is located more than one stopping distance from the grain boundary, then the true fraction of α retained would be more important, and the F_T -corrected age would be greater than the true age. Alternatively, if all of the parent is located on the prism rim, then the fraction of alphas retained would be smaller than predicted by the model and in this case the F_T -corrected age would be underestimated. Farley et al. (1996) considered several different scenarios and concluded that only extreme zonation will produce large error in F_T correction.

Finally, each aliquot of grains are transferred to platinum capsule and outgassed in a vacuum resistance furnace or using a Nd-YAG laser. A laser based approach requires fewer apatite grains than a furnace due to a lower blank associated with a smaller chamber volume. Helium is determined by mass spectrometry while U and Th are analysed by Inductively Coupled Plasma Mass Spectrometry after grains were retrieved from the vacuum system, dissolved in 10 percent HNO_3 , and spiked with ^{230}Th and ^{235}U (The theory and technique of the (U-Th)/He method are extensively described in Farley, 2002).

Based on reproducibility of pure standard gases and aqueous standard solutions, the overall analytical precision of He ages determined by this procedure should be about 2% when ages are well above the blank levels. Most of this uncertainty arises from the He measurement.

The most critical part of the He dating process is grain selection. It is vitally important to avoid selecting apatite grains that contain small mineral inclusions rich in U-Th that can introduce extraneous He into an apatite grain which are then not accounted for during the U/Th analysis, resulting in anomalously older ages. Zircon in particular remains undissolved by standard apatite dissolution protocols. The most common inclusions are zircons but it is possible to encounter monazite, xenotime, quartz, feldspar and pyrite (Fig. I.17). However the three last examples are unlikely to carry sufficient U and Th to be a problem. An indication of the presence of inclusions is poor reproducibility of ages, because the inclusions are not present in equal abundance from one aliquot/grain to another. In many cases inclusions in apatite can be detected during the grain selection process. In rare cases this technique has been found inadequate, usually because the inclusions are oriented parallel to the c-axis (see chapter I.3.1) and are extinct at the same time as the apatite host under crossed-polarised light. In these cases the re-extract test (see section A V) and age irreproducibility are sufficient to identify problem samples.

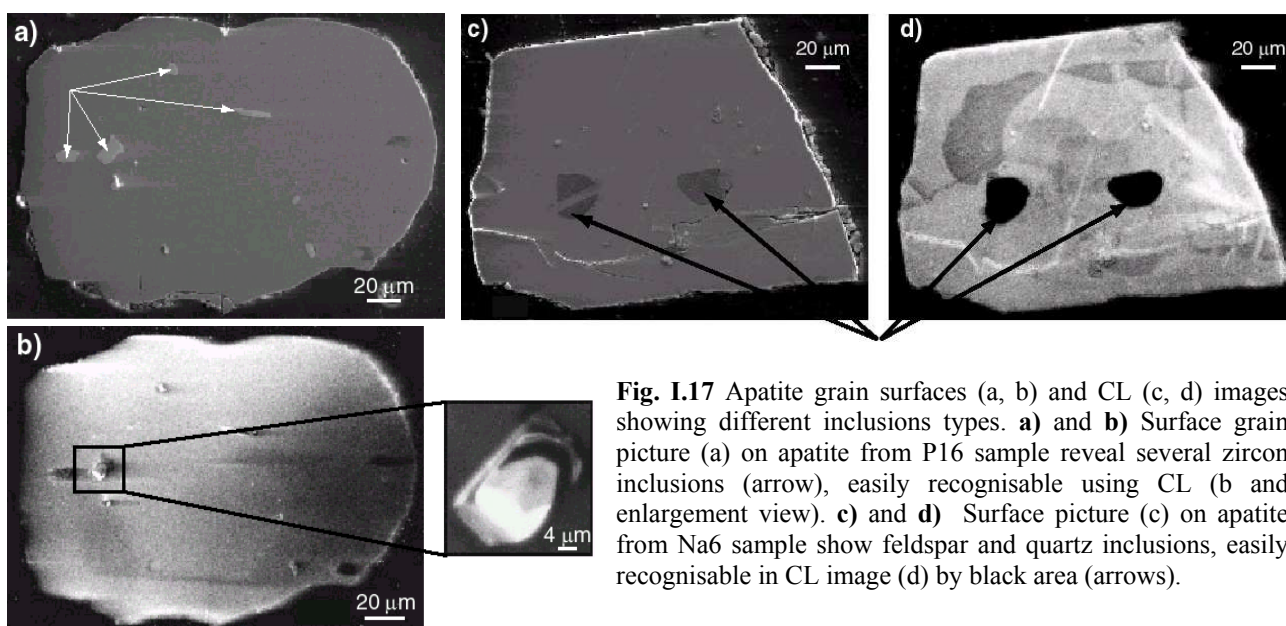


Fig. I.17 Apatite grain surfaces (a, b) and CL (c, d) images showing different inclusions types. **a)** and **b)** Surface grain picture (a) on apatite from P16 sample reveal several zircon inclusions (arrow), easily recognisable using CL (b and enlargement view). **c)** and **d)** Surface picture (c) on apatite from Na6 sample show feldspar and quartz inclusions, easily recognisable in CL image (d) by black area (arrows).

I.4.2 Details of (U-Th)/He method used in this study

The apatite (U-Th)/He thermochronometer (Zeitler et al., 1987) is based on the accumulation of radiogenic ^4He from the decay of ^{235}U , ^{238}U and ^{232}Th series nuclides. Laboratory diffusion experiments of a range of apatites indicate that the helium is partially retained at temperatures between 40°C and 80°C , values which are apparently insensitive to chemical composition and only slightly sensitive to grain size (Wolf et al., 1996a). The depth range that corresponds to this temperature range is termed the partial retention zone (PRZ). At temperatures below 40°C most helium is retained in the apatite crystal, and above 80°C most helium is lost. Details of apatite He age determinations made at the California Institute of Technology are described elsewhere (House et al., 1997). He, U and Th determinations are made on a single aliquot of 4 apatite grains, typically $100\ \mu\text{m}$ in minimum dimension. Evolved helium was spiked with ^3He , cryogenically concentrated and purified, and $4\text{He}/^3\text{He}$ ratio is determined on a quadrupole mass spectrometer after quantitative He degassing of apatites at 1050°C for 5 min with a Nd-YAG laser (House et al., 2000) (Fig. I.18).

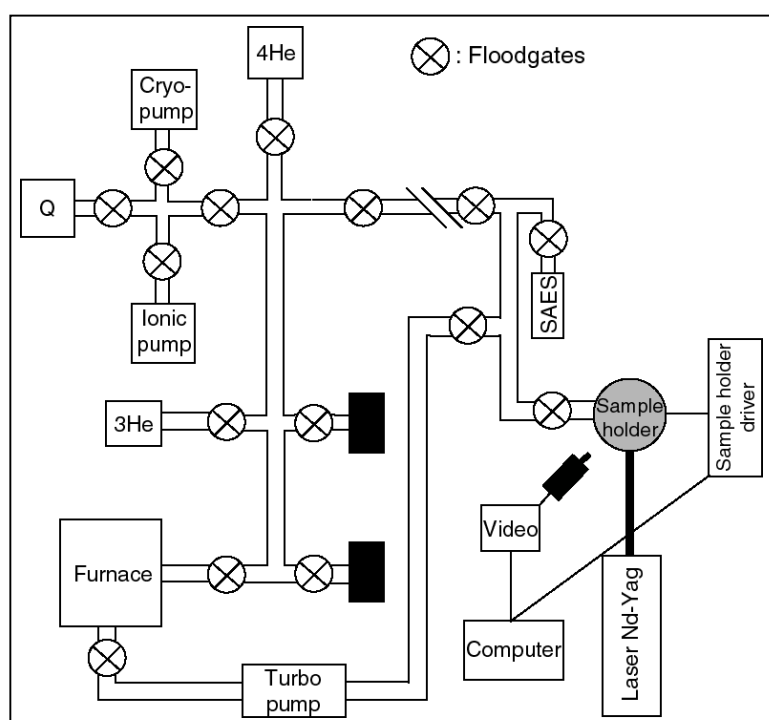


Fig. I.18 Schematic illustration of equipment used during this PhD thesis for Helium measurement at the Caltech. Q = Quatrupole mass spectrometer; SAES = Gas cleanser; Black boxes = Volumes used for diffusion experiments. The Cryo-pump is used to trap the Helium while the ionic and turbo pump are used to clean the line. ^3He is used to spike the sample and ^4He is used only on standard to know the $^3\text{He}/^4\text{He}$ ratio. The laser heat the sample 2 times (for extract and re-extract measurement) during 5 min at 1050°C . The time of analyse per sample is around 15 min. At Caltech, all the system of floodgates (closing and opening), the lasering process and the sample holder driver are controlled by computer.

Grains were retrieved from the vacuum system, dissolved in 10 percent HNO₃, spiked with ²³⁰Th and ²³⁵U, and analysed for U and Th by Inductively Coupled Plasma Mass Spectrometry (ICP-MS).

Reported He ages are corrected for alpha ejection effects based on measured grain dimensions (Farley et al., 1996). Ages are replicated and the mean is reported. The estimated analytical uncertainty for He ages is about 6 percent (1σ), in agreement with the reproducibility observed for most samples.

The listing of the (U-Th)/He data is given in section A V.

I.5 Closure temperatures, FT partial annealing zone and helium partial retention zone

When the absolute age of a sample has been determined by dating experiments it is important to define what the measured age means does it record the time of mineral formation, rapid cooling or more protracted cooling associated with exhumation? In this regard the concept of closure temperature (Dodson 1973) has been widely adopted in geochronology to explain diffusion and the significance of measured ages. The closure temperature is dependent on the activation energy for diffusion, the geometry and size of the diffusion domain and the cooling rate (Dodson, 1973; McDougall & Harrison, 1988). The basic equation used to quantify the closure temperature, T_c , is expressed by the Arrhenius relationship:

$$T_c = R/[E(\ln A\tau D/a^2)] \quad (\text{Dodson, 1973}) \quad (1)$$

Where : R= gas constant; E= activation energy; A= numerical constant related to the geometry and decay constant; τ = time constant with which the diffusion coefficient; D= diminishes related to the cooling rate; a = characteristic diffusion size.

The basic equation (1) shows that the closure temperature is mostly dependent on the activation energy, because it is a linear function of the activation energy for diffusion relative to a dependence on the logarithm of the cooling rate and geometry of diffusion.

The concept of closure temperature is not universally applicable to all geochronological methods and there are problems with the concept. Key issues include i) that it does not allow for variable rates of isotope exchange in the other minerals ii) is applicable only if the cooling interval is short with respect to the half-life of the decay system iii) diffusion rates are affected by lattice damage (radiation /defects) and compositional variation iv) and is vulnerable to the effects of non-uniform cooling rates inherited isotopes, and mineral recrystallization. For the FT and (U-Th)/He methods it is more applicable to consider responses to temperature in relation to partial annealing and partial retention zones. Nevertheless it is often helpful when discussing a range of different methods to discuss resetting temperatures in the context of closure temperatures recognising that in practice it may not be completely valid to do so.

I.5.1 Fission track partial annealing zone

It has been known for some time that fission tracks in apatite are sensitive to comparatively low temperatures and over the last 20 years workers have attempted to describe this on a time-dependence basis through Arrhenius plots initially using track density measurements (e.g. Naeser and Faul 1969), later using confined track length data (Laslett et al., 1982), which provide a more accurate indicator of track annealing. Throughout the 1980's a succession of papers were published that used confined track length data to monitor fission-track annealing in laboratory experiments (Duddy *et al.*, 1988; Green *et al.*, 1986, 1989a,b, Laslett *et al.*, 1987), and in the natural geological environment (Gleadow and Duddy 1981). These resulted in a quantitative predictive model of fission-track annealing, based on the Durango apatite (composition Cl/F ratio of ~ 0.1), which show that for geological time-scales fission tracks partially anneal at temperatures between ~60-110°C.

So the apatite fission track data produced in this study can be used to monitor cooling from $\sim 110^{\circ}\text{C}$ down to $\sim 60^{\circ}\text{C}$. In practice though the apatite fission track data loose resolution below $\sim 70^{\circ}\text{C}$.

The thermal stability of fission tracks in zircon has been less studied than for apatite. So far, there is only one published set of experimental zircon annealing data (Yamada *et al.*, 1995) although these have been subsequently remodelled incorporating new 1000hr data to give an improved annealing algorithm (Tagami *et al.*, 1998). Geological observation that place constraints on the annealing of tracks in zircon are confined to studies in the Vienna gas basin (Tagami *et al.*, 1996), deep boreholes in Russia (Kola Peninsula) and Germany (KTB), exhumed rock in the New Zealand Alps and a contact aureole in Japan. Data from these studies have been used to validate the annealing algorithm and there is now good evidence to suggest that heating durations lasting 10^6 to 10^8 yrs require temperatures of $300\text{-}320^{\circ}\text{C}$ to cause total annealing of all natural spontaneous fission tracks. Below 200°C all tracks in zircon are effectively stable. A zircon partial annealing zone between $200\text{-}300^{\circ}\text{C}$ though is only applicable to zircons that have not accumulated any significant alpha damage causing metamictisation. Metamict zircons anneal at lower temperatures and work is still ongoing to define exactly what these temperatures are.

I.5.2 Helium partial retention zone

Substantial effort is required to measure the He diffusivity parameters in a given phase and to determine how those parameters vary with mineral characteristics such as grain size, shape, chemical composition, and defect and/or radiation damage density.

Zeitler *et al.* (1987) initiated interest in He thermochronometry by demonstrating that apatite has an effective closure temperature of about 100°C (closure temperatures are referenced to a cooling rate of $10^{\circ}\text{C}/\text{Myr}$). More recent efforts (Lippolt *et al.*, 1994; Wolf *et al.*, 1996b; Warnock *et al.*, 1997; Farley, 2000) confirm this approximate closure temperature, and suggest that He diffusion from Durango apatite as well as variety of other apatites, obeys an Arrhenius relationship (eq. (1)), suggesting that He diffusion from apatite is a single-mechanism thermally activated volume diffusion process, at least at temperatures $<300^{\circ}\text{C}$. Moreover, in Durango apatite, the quantity D/a^2 varies with grain size in the manner expected if the diffusion domain is the grain itself, i.e., the quantity “a” is the physical grain dimension. He diffusion from Durango apatite is crystallographically isotropic. The relevant dimension for diffusion is thus the prism radius, as this is the shortest pathway for He loss. Taken together the most precise observations suggest that helium diffusion has an equivalent closure temperature of $\sim 70^{\circ}\text{C}$ in apatites of $\sim 80\text{-}90\ \mu\text{m}$ radius. As described above, the α -ejection rounding of the concentration profile shifts this temperature slightly upward. Variation of the closure temperature with grain size and cooling rate based on the Durango observations is shown in figure I.19.

Several studies have attempted to verify the expected diffusivity behaviour in the natural setting. The most obvious method for verification is to examine the He age distribution in boreholes in which temperature is known as function of depth. In such a setting He ages are expected to decrease rapidly downhole, defining the Helium Partial Retention Zone (HePRZ, Wolf *et al.*, 1998). The position of the HePRZ depends on the thermal history of the crust, but in general lies between 40°C and 80°C (Wolf *et al.*, 1998).

Studies by Wolf (1996), Warnock *et al.* (1997) and House *et al.* (1999) to confirm the existence of the HePRZ were broadly successful. In three different borehole settings the apatite helium ages were found to decrease rapidly at about the proper temperature, but problems arising from mineral inclusions, poorly known thermal histories, and other phenomena prevented a quantitative confirmation of the diffusivities extrapolated from laboratory measurement.

The previous studies (House *et al.*, 1999; Stockli *et al.*, 2000) provide compelling evidence that laboratory data adequately describe He diffusion characteristics for most apatites.

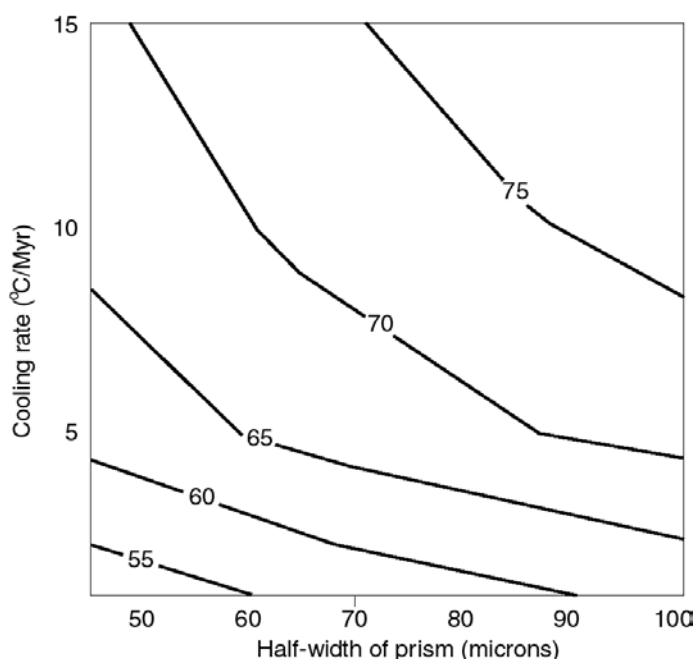


Fig. I.19 Helium closure temperature (T_c) as a function of grain size and cooling rate (modified from Farley, 2002). T_c was calculated assuming an activation energy of 33kcal/mol and $D=50\text{cm}^2/\text{sec}$ assuming spherical geometry and including the effects of α -ejection on He diffusion (more details in Farley, 2000).

I.5.3 The $^{40}\text{Ar}/^{39}\text{Ar}$ closure temperatures

Many studies have been carried out to investigate diffusion by domains and diffusion rates of Ar in different minerals (McDougall & Harrison, 1988; Baldwin et al., 1990; Foster et al., 1990; Harrison et al., 1991; Lovera, 1992; Hames & Bowring, 1994). In addition to theoretical calculations, estimates of closure temperature ranges have also been inferred from the pattern of age discordance in minerals from a single locality using different dating methods. Examples of natural experiments to obtain semi-quantitative values of closure temperatures are the calculation of the thermal effects on argon loss in a mineral due to heat conduction from an intrusion into the rocks of the contact aureole (Harrison & McDougall, 1980), and the interpolation of absolute age information with pressure-temperature information (by thermobarometry) of metamorphic mineral assemblages (Blanckenburg et al., 1989). The generally closure temperature ranges for the main K-bearing minerals are:

K-bearing mineral	Closure temperature	References
Hornblende	550 ± 50 °C	Harrison, 1981; Dahl, 1996a; Villa, 1996
White mica	400 ± 50 °C	Hames and Bowring, 1994
Biotite	325 ± 25 °C	Harrison et al., 1985; Dahl, 1996b
K-Feldspar	200 ± 50 °C	Onstott et al., 1989

I.5.4 Conclusions

The association of these different methods of dating will allow to constrain the thermal histories of the rocks in the Cycladic islands, Greece, between 550 ± 50 °C (closure temperature of the Ar/Ar system on amphibole) and ~ 40 °C (lower part of the partial retention zone of the helium for apatite).

The high closure temperatures (>300 °C) for the minerals used for $^{40}\text{Ar}/^{39}\text{Ar}$ dating experiments will be a good tool to place temporal constraints on the synkinematic granite emplacements in this area because their cooling is fast in footwalls of extensional faults. On the other hand, the FT method (which have a range of closure temperature between ~ 300 °C and ~ 60 °C) will be used for reconstruction of the exhumation stage in the upper crustal part of the Earth in relation with the extensional detachments observed on several Greek islands. In order to complete the results

obtained using the FT technique, the (U-Th)/He method will be used. This method will document the last stage of cooling at even lower temperatures than the apatite fission track dating (i.e. under $\sim 80^{\circ}\text{C}$) to understand tectonic processes that cause rock cooling as they pass through the upper 1-3 km of the crust.

Furthermore, the combination of the zircon FT, apatite FT and apatite (U-Th)/He methods will permit us to constrain the cooling history in the brittle part of the crust (Fig. I.20).

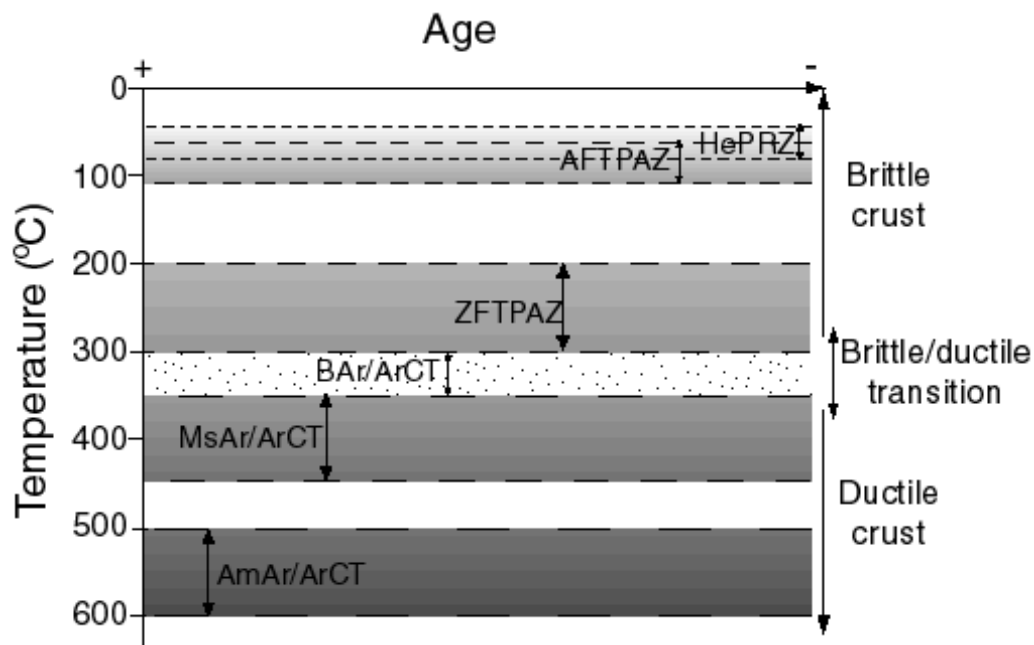


Fig. I.20 Closure temperatures of the different chronometers used in this study. The method association will allow to constrain the thermal histories of the rock from $\sim 500^{\circ}\text{C}$ to $\sim 40^{\circ}\text{C}$. AmAr/ArCT= closure temperature of the amphibole with the $^{40}\text{Ar}/^{39}\text{Ar}$ method ($550\pm 50^{\circ}\text{C}$); MsAr/ArCT= closure temperature of the muscovite with the $^{40}\text{Ar}/^{39}\text{Ar}$ method ($400\pm 50^{\circ}\text{C}$); BAr/ArCT= closure temperature of the biotite with the $^{40}\text{Ar}/^{39}\text{Ar}$ method ($300\pm 50^{\circ}\text{C}$); ZFTPAZ= zircon partial annealing zone of fission tracks ($\sim 300\text{-}200^{\circ}\text{C}$); AFTPAZ= apatite partial annealing zone of fission tracks ($\sim 110\text{-}60^{\circ}\text{C}$); HePRZ= partial retention zone of the helium in apatite ($\sim 80\text{-}40^{\circ}\text{C}$).

Chapter II

**Exhumation processes
and tectonic evolution of
the Aegean**

In this chapter aspects from published studies are summarized to provide a basis which allows integration of the results of the present study with the existing literature. It will introduce exhumation mechanisms and the tectonic setting of the Aegean region in its present-day configuration and during its history followed by the implications for this study.

II.1- Exhumation mechanisms

Exhumation occurs by three processes: ductile thinning, erosion and normal faulting (Ring et al., 1999a).

The main goal of this work is to constrain the cooling history of major extensional detachments in the Cyclades. Therefore we mainly focus on the normal faulting exhumation process.

However, erosion during normal faulting appears sometime to be an inescapable process of exhumation. Furthermore, penetrative deformation fabrics present in most exhumed mountain belts indicate that ductile flow is an important process.

II.1.1 Ductile flow

This process can either aid or hinder exhumation, depending upon whether ductile flow causes vertical thinning as associated with the formation of a sub-horizontal foliation, or vertical thickening as associated with the formation of a subvertical foliation.

The general observation of sub-horizontal foliations in the internal zones of many orogens shows that ductile thinning commonly aids exhumation (Wallis et al., 1993; Platt, 1993; Ring, 1995; Ring et al., 1999a). Ductile thinning by itself cannot fully exhume rocks and an additional exhumation process is required to bring rocks to the Earth's surface (Platt et al., 1998). Vanderhaeghe & Teyssier (1997) proposed a model for the formation of the Shuswap Metamorphic core complex, where late-orogenic gravitational collapse is accommodated by normal faulting of the brittle upper crust and ductile thinning of the mid- to lower crust. If exhumation occurs by a combination of processes, it is difficult to quantify the contribution of ductile thinning to exhumation. In such cases, the vertical rate at which a rock moved through its overburden and the rate of the remaining overburden at each step along the exhumation path have to be considered (Feehan & Brandon, 1999). To model the contribution of vertical ductile thinning on Ikaria (Greece), Kumerics et al. (2004) performed a complete study combining structural, metamorphic and geochronological data. Using a model calculation based on a ductile-strain-rate law, they estimated a ductile thinning contribution at 20% to the overall exhumation associated with extensional faulting on Ikaria.

II.1.2 Erosion

In earliest studies of alpine tectonics, erosion was recognized as an important process for unroofing the internal metamorphic zones of convergent mountain belts. Surficial erosion can locally be a very fast process, generally fast eroding region tend to be mountains, tectonically active and wet. Conversely, arid climates tend to have slow erosion rates regardless of the amount of topography (Ring et al., 1999a). However, erosion rates do not appear to be strongly influenced by climate as long as the climate is not arid (Pinet & Souriau, 1988).

Royden (1993a) have shown that at retreating subduction boundaries such as the Hellenic system, the tectonic expression includes topographically low mountains and little erosion. Jolivet et al. (2003) argue that the extension in the Aegean region is probably in association with erosion process but that erosion during the Miocene played a minor role in removing the overburden. Thomson et al. (1998) applied apatite fission track thermochronology on the Uppermost tectonic unit of Crete (Greece) to estimate an erosion rate of 0.65 km/Myr between 11 to 17 Ma. These previous studies indicate that the erosion is not a dominant process for rock exhumations in the Aegean region, with rates estimated at $\ll 1$ km/Myr.

II.1.3 Normal faulting

Low-angle normal faults are common to all Metamorphic Core Complexes (MCC; such as the Basin and Range province in the North American Cordillera or on Naxos island in the Greek Aegean sea) which developed during lithospheric extension. MCC's are recognized as fundamental extensional tectonic features in orogenic belt around the world and may be important for the exhumation of rocks from deep crustal levels along low-angle normal fault systems (Lister et al., 1984; Lister & Davis, 1989; Baldwin et al., 1993; Lister & Forster, 1996). There is abundant evidence that normal faulting aids the exhumation of metamorphic rocks, especially in the Aegean province (Lister et al., 1984; Thomson et al., 1999; Foster & Lister, 1999). The hallmark of normal faulting is the resetting of footwall rocks to a common isotopic age caused by rapid cooling as the hanging wall strips away. Low-angle normal faults can be evolved by various mechanism associated either with plate convergence or plate divergence (Wernicke, 1981).

The theoretical geometry of detachment zones has been discussed by several authors (Davis, 1983; Wernicke, 1985; Lister et al., 1986). The model geometry is based on the different rheological response of mantle and crustal sections of the lithosphere to extension (Fig. II.1a). The system evolution depends on extensional strain and conductive cooling of the mantle lithosphere, responding to extensional strain, followed by lithospheric stretching. The model shows that subsequent conductive cooling of the mantle lithosphere is sufficient to compensate the initial possible uplift of parts of the region (i.e. the hangingwall of a detachment). Under these conditions, footwall rocks might be subject to rapid upwelling, which will permit melting. Consequently, the footwalls of the detachment zones are often characterized by the occurrence of syn-tectonic intrusions.

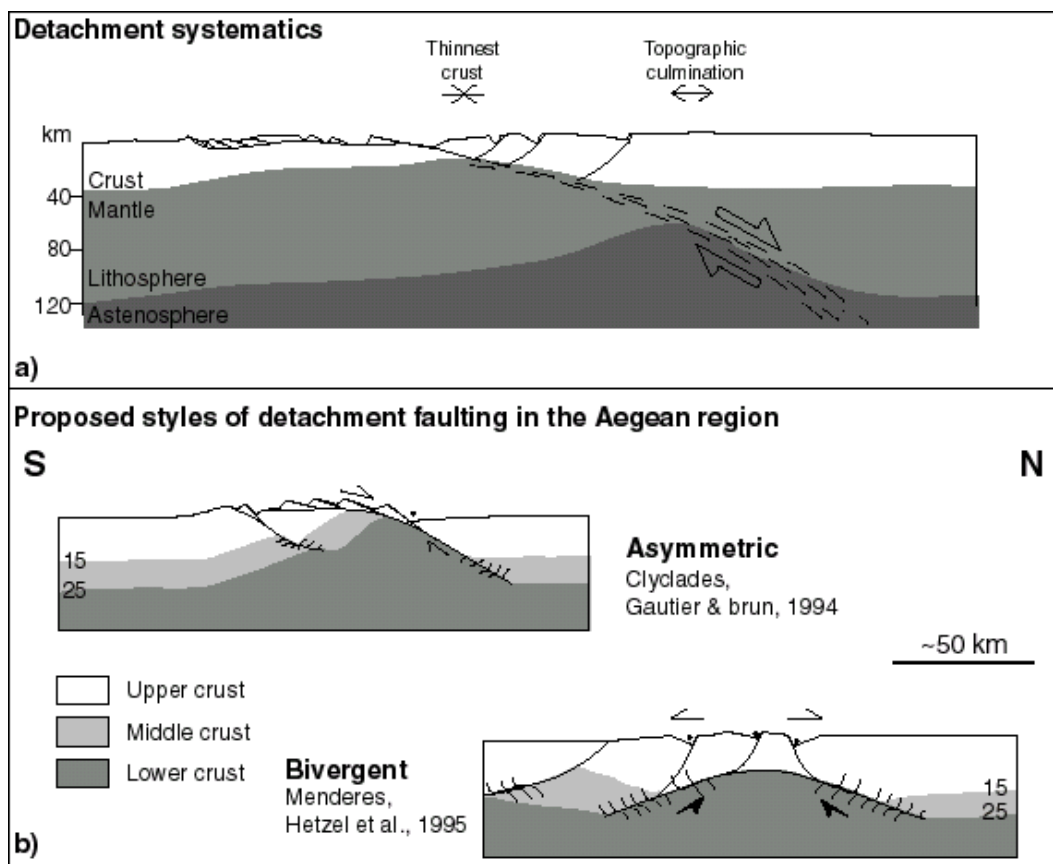


Fig. II.1 (a) Schematic geometry of a detachment zone which formed by simple shear of the entire lithosphere (from Wernicke, 1985). (b) Different styles of detachment faults that affect the upper and middle crust: Asymmetric extension accommodated by a single-sense detachment Fault (Gautier & Brun, 1994); Bivergent extension accommodated by two synchronously operating detachment zones with opposite shear senses (Hetzal et al., 1995).

In reality, detachment zones are more complex than described in theoretical models (see example of Ios, Chapter III.3). The detachment zones which have been observed in the Aegean demonstrate this complexity. Often, pre-existing zones of weakness are inherited and exploited by detachment zones (Emre & Sözbilir, 1997). The detachment zones in the Aegean may have been developed as single zones in an asymmetric extensional setting (Gautier & Brun, 1994), and double dipping zones in a bivergent extensional setting, which developed simultaneously (Hetzel et al., 1995), or which developed as a south dipping detachment overprinting a north dipping detachment which finally resulted in an overall bivergent extensional setting (Hetzel et al., 1995; Vanderberg & Lister, 1996) (Fig. II.1b).

II.1.4 Exhumation of metamorphic rocks in the Aegean

Large-scale extension in the Aegean was achieved by low angle normal faults, which caused exhumation of ductile basement rocks to surface levels and have been widely identified in the Aegean Region (Lister et al., 1984; Gautier & Brun, 1994; Hetzel et al. 1995; Jolivet et al., 1996; Vandenberg & Lister, 1996; Ring & Reischmann, 2002). Some authors have concluded that these detachment zones were the most important mechanism for exhumation of HP metamorphic assemblages (Gautier & Brun, 1994; Jolivet et al., 1994; Avigad et al., 1997). However, Ring et al. (2003) based on fission track ages and assuming a thermal field gradient of 40-30°C/km concluded that the Vari detachment on Syros and Tinos, which is characterized by fast slip and large offset, accomplished only the final ~6-9 km of the Cycladic blueschist exhumation from ~60km depth. Thomson et al. (1999) proposed that the exhumation of the external HP belt in the Early Miocene on Crete was almost fully accomplished in an extrusion wedge (Fig. II.2).

At around 36-32 Ma as the HP unit in the Cyclades was thrust onto the basal unit, normal faulting is reported from higher levels (Raouzaïos et al., 1996; see section II.2.1.1 for details about the HP formation rocks in the Aegean). Thrusting at depth, coupled with normal faulting suggest that an extrusion wedge formed in the Early Oligocene. This extrusion wedge aided the exhumation of the HP rocks (Ring and Layer, 2003).

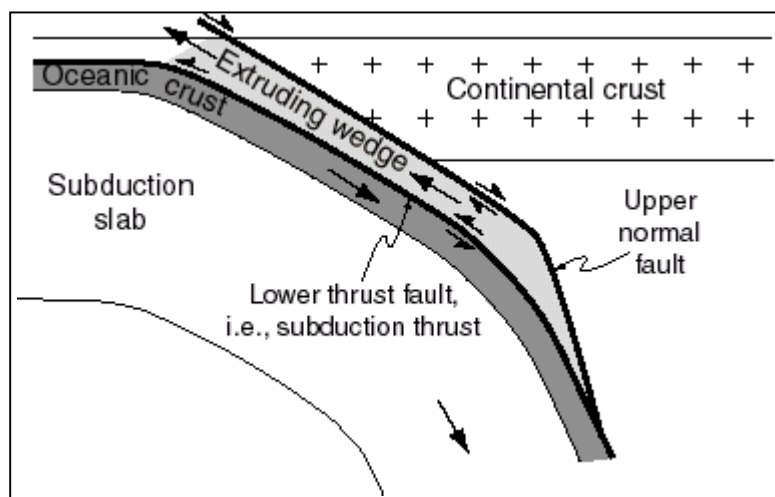


Fig. II.2 Schematic sketch of an extrusion wedge in a subduction setting (modified from Ring & Reischmann, 2002). The wedge is defined by the subduction thrust at the base and a normal fault at the top.

II.2- Geology of the Aegean

II.2.1 Configuration

The Aegean region is located in the eastern Mediterranean and forms part of the Apulian-Adriatic microplate between the overriding Eurasian plate and the subducting African plate. In the present-day configuration the western and southern boundaries of the Aegean region are formed by the

Hellenic subduction system (Fig. 2 in Introduction and Fig. II.3). The Hellenic orogen is composed, from south to north, of the following tectonic units:

- i) the pre-Apulian Zone;
- ii) the Ionian Zone;
- iii) the Pindos Zone, partially separated from the Ionian Zone by the platform carbonates of the Gavrovo-Tripolitza Zone;
- iv) the Cycladic Zone;
- v) the Pelagonian Zone;
- vi) the Vardar Zone;
- vii) the Serbo-Macedonian Massif;
- viii) the Rhodope Massif.

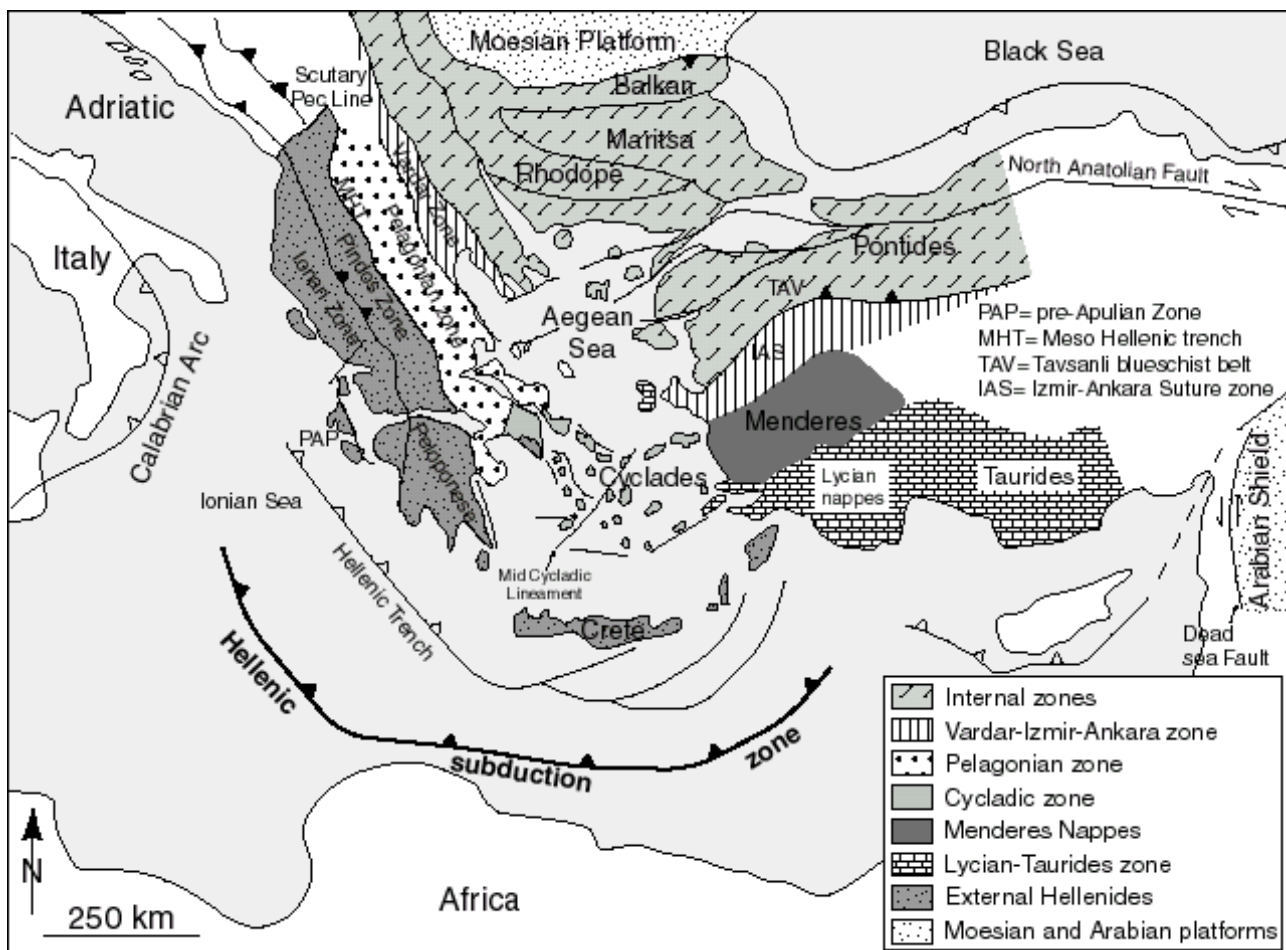


Fig. II.3 Aegean region and surrounding areas showing main tectonic domains, main basins and fault zones (modified from Lips 1998).

In general the first three units are referred to as the External Hellenides. They are characterized by Mesozoic to Tertiary platform carbonates and Eocene to Miocene flysch sequences. The other units are referred to as the Internal Hellenides.

The dominant tectonic unit of the Cycladic zone is the Cycladic blueschist unit, which comprises an ophiolitic mélange at the top and an underlying Carboniferous basement with a post Carboniferous cover sequence (Dürr et al., 1978). The Cycladic blueschist unit is overlain on some islands by the Upper unit (such as Tinos and Syros). In some windows in the Cycladic zone, the Basal unit, a part of the External Hellenides, crops out below the Cycladic blueschist unit (Avigad & Garfunkel, 1989).

The Pelagonian Zone is characterized by blueschist and greenschist facies metamorphosed, relic Hercynian basement units, which tectonically overly Mesozoic platform carbonates of the Cycladic zone and Tertiary flysch sequences (Schermer, 1993; Walcott, 1998). The Serbo-Macedonian belt and Rhodope Zone are composed by imbricated basement, which has been metamorphosed to eclogite, amphibolite, and/or greenschist facies condition and intruded by Tertiary granitoids (Burg et al., 1996). The Vardar Zone is characterized by ophiolite sequences, which have been related to the Neotethys and have been obducted in the Jurassic (Spray & Roddick, 1980).

Regional correlation of units between the Hellenides on mainland Greece and the Pontides and Taurides/Lycian nappes is obscured by the limited exposure of regionally correlatable units in the Cyclades and on Crete (Robertson & Dixon, 1984; Smith, 1996). Roughly, the Taurides appear to occur in an equivalent structural setting to the External Hellenides and are characterized by imbricated thrust sheets with a vergence towards the present-day active subduction zone (Lycian nappes, Collins & Robertson, 1997). The northern parts of the Pontides have been correlated to the Rhodope Massif (Okay et al., 1996).

The Moesian platform is situated north of the Rhodope zone (Fig. II.3) and is regarded to be part of stable Eurasia (Robertson and Dixon, 1984).

Ophiolites sequences are found at several locations, especially in the Pindos Zone, Vardar Zone, Izmir-Ankara Suture Zone and the Taurides (Fig. II.3). The widespread ophiolitic rocks has led to a discussion about the number and the locations of oceanic basins, that played a role in the tectonic development of the Aegean area. Most ophiolite sequences form part of allochthonous thrust sheets.

II.2.1.1 High pressure metamorphic sequences

Alpine shortening during the Late Mesozoic and Tertiary is due to the closure of the Neotethyan ocean and continent-continent collision of the Apulian-Adriatic microplate with Eurasia. The overall shortening during the Alpine convergence has been estimated from a minimum of ~135 km to a maximum of ~500 km (Zimmerman & Ross, 1976; Burchfield, 1980; Dewey et al., 1986).

In the Aegean, the occurrence of three high pressure metamorphic belts related to different stages of the Alpine tectonic history have been proposed (Papanikolaou, 1984; Gautier & Brun, 1994; Jolivet et al. 1996). The timing of metamorphic events of the tectonic units in the Aegean is summarized in the figure II.4.

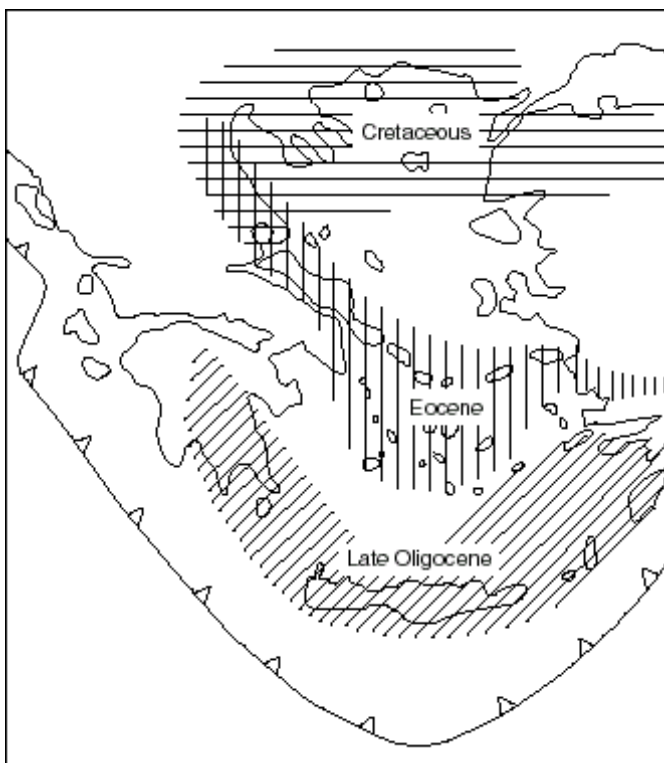


Fig. II.4 Spatial distribution of the three proposed HP metamorphic belts in the Aegean region, which are related to the Alpine Orogeny (following data and/or postulations from Bonneau & Kienast, 1982; Seidel et al., 1982; Papanikolaou, 1984; Gautier & Brun, 1994; Jolivet et al., 1996; Okay & Monie, 1997; Okay et al., 2002).

The proposed belts are exposed in the Rhodope Zone, Pontides, Pelagonian Zone, the Cyclades, Menderes Massif, the Peloponese Peninsula and Crete (Fig. II.4). The formation of HP metamorphic belts of varying ages has been related to different phases of regional shortening during the Alpine Orogeny (Fig. II.5) (Seidel et al., 1982; Jolivet et al., 1994; Avigad et al., 1997; Oberhänsli et al., 1998). Recently, Ring & Lister (2003) proposed that younging of high-pressure metamorphism in a southerly direction (Fig. II.4 and Fig. II.5) mimics the southward retreat of the Hellenic subduction zone. They suggested that the distinct stages of high-pressure metamorphism were controlled by underthrusting of mainly thinned continental crust fragments (such as Lycian nappes, Cycladic margin and External Hellenides) and that these punctuated events were superimposed on progressive slab retreat.

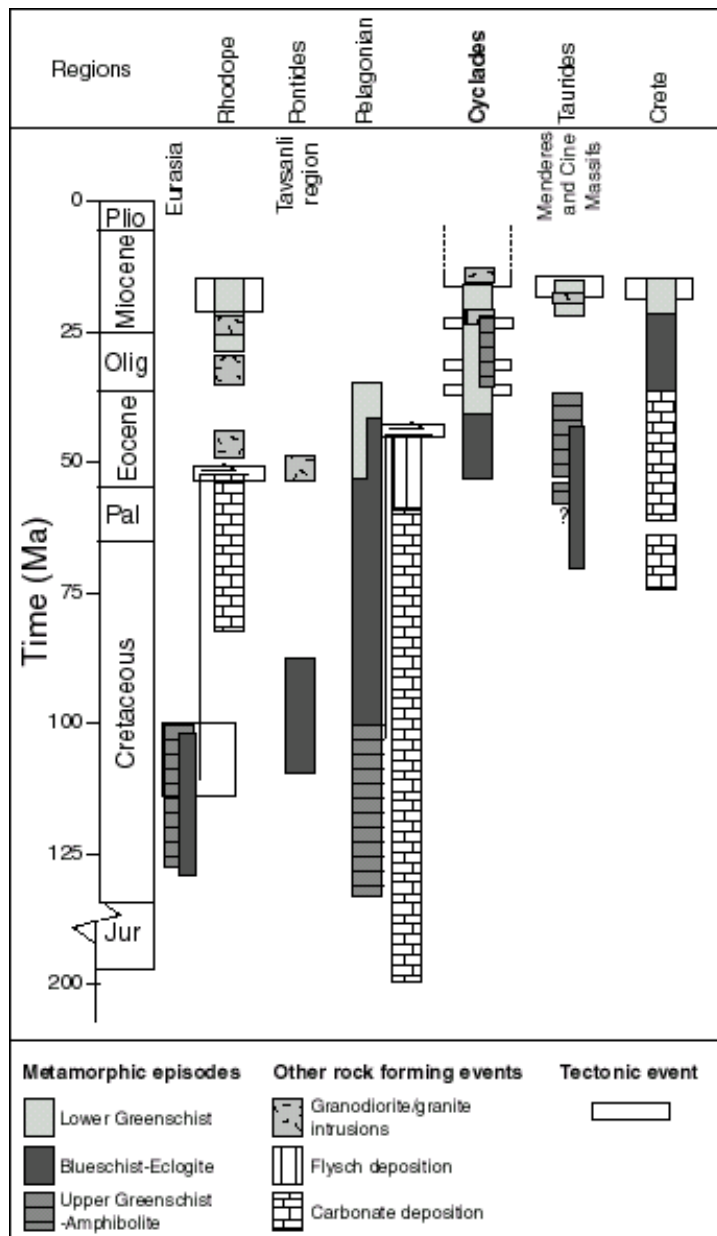


Fig. II.5 Timing of metamorphic and tectonic events recognized in the Aegean from North to South (modified from Lips, 1998; Data from Andriessen et al., 1979; Altherr et al., 1982; Wijbrans & McDougall, 1988; de Wet et al., 1989; Bröcker et al., 1993; Schermer, 1993; Baldwin & Lister, 1994; Harris et al., 1994; Okay et al., 1994; Dinter et al., 1995; Hetzel et al., 1995b; Hetzel & Reischmann, 1996; Jolivet et al., 1996; Okay et al., 1996; Wawrzenitz & Mposkos, 1997; Keay, 1998; Thomson et al., 1998).

II.2.1.2 The Cyclades

II.2.1.2.1 Geological setting

The Aegean region in the Eastern Mediterranean Sea has witnessed a prolonged history of convergence between African and Eurasian plates and the associated closure of the Tethys. The

convergence and collision of the Africa and Eurasia, and of continental fragments and microplates, between the two main continental plates, have shaped the Aegean area over the past ~200 Ma. In this belt, it is possible to distinguish major structural groups of units, separated by faults (Fig. II.6):

1. The basal unit, as part of the external Hellenides comprising metasedimentary and volcanic rocks of Permian to Tertiary age;
2. The Cycladic blueschist unit consisting of:
 - a Carboniferous basement nappe made up of Carboniferous orthogneiss overlain by
 - a post Carboniferous shelf series composed of metabasites and metasediments
 - an ophiolitic mélangé (ophiolitic rocks embedded in a serpentinitic and Metapelitic matrix).
 The Carboniferous basement and the post Carboniferous cover were intruded by middle Triassic granitoids.
- These units experienced at least 2 main episodes of metamorphism during the Alpidic orogeny, followed by a Miocene granitic plutonism:
 - ◆ a regional eclogite to blueschist metamorphism caused by the subduction of the Apulian-Adriatic microplate beneath Eurasia ($P = 15 \pm 3$ Kbar, $T = 450-500^{\circ}\text{C}$; Bröcker et al., 1993);
 - ◆ a subsequent greenschist to amphibolite facies overprint ($P = 5$ to 7 Kbar, $T = 400-500^{\circ}\text{C}$) (Altherr et al., 1982; Bröcker et al., 1993) which is thought to occur in response to extension of the Aegean crust;
3. The upper unit is rarely exposed and mainly consists of the unmetamorphosed composite Cycladic ophiolite nappe;
4. Sedimentary basins filled with Miocene and younger sediments.

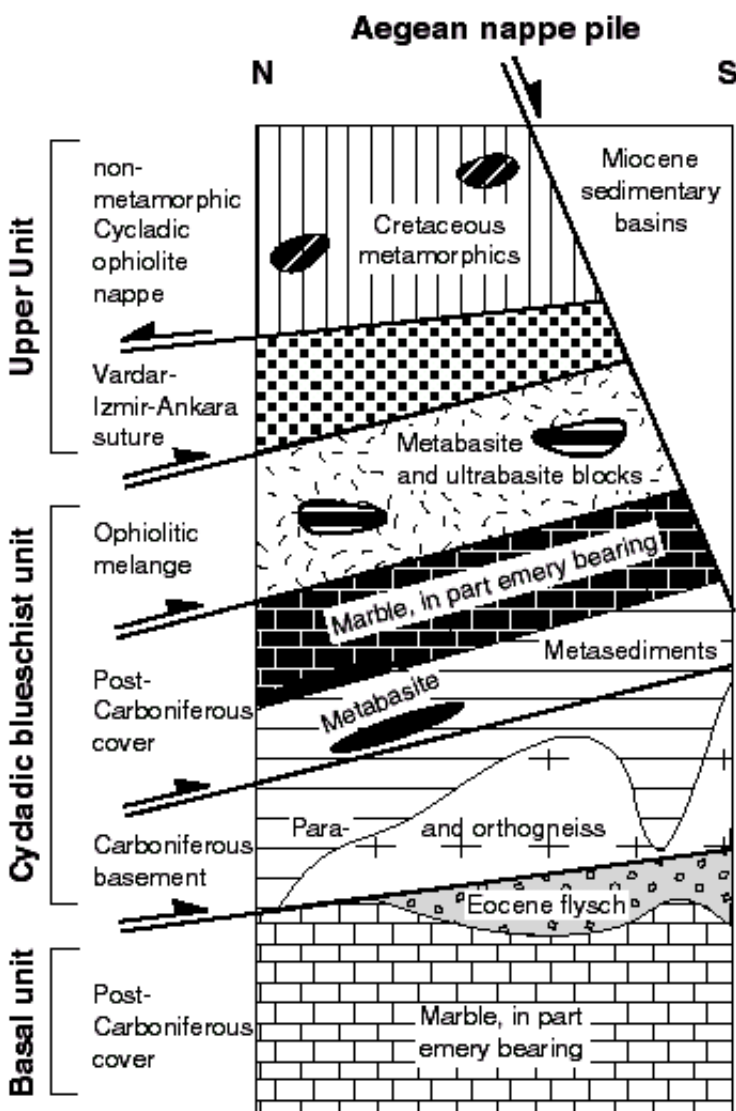


Fig. II.6 Idealized tectonostratigraphic columns of the nappe pile in the Aegean (modified from Ring et al., 1999b).

II.2.1.2.2 Timing of metamorphic events

The different units record very different metamorphic histories as shown by their petrologic and radiometric data. The Upper Unit has been metamorphosed under LP-HT conditions (M_0) at around 70 ± 10 Ma defined by K-Ar dating on hornblende, U/Pb on zircon by in-situ SHRIMP and conventional multi-grain dating (Altherr et al., 1994; Patzak et al., 1994; Keay, 1998; Brocker & Enders, 1999). The Cycladic Blueschist Unit (CBU) underwent a HP-LT metamorphism (M_1) dated between 55-40 Ma using K-Ar and $^{40}\text{Ar}/^{39}\text{Ar}$ on white micas (Andriessen et al., 1979; Altherr et al., 1982; Wijbrans & McDougall, 1988; Bröcker et al., 1993; Baldwin & Lister, 1994 and 1998). HP metamorphism was followed by greenschist to amphibolite (M_2) facies metamorphism dated from 25 to 16 Ma using the K-Ar and $^{40}\text{Ar}/^{39}\text{Ar}$ methods on hornblende, muscovite and biotite (Andriessen et al., 1979; Altherr et al., 1982; Wijbrans & McDougall, 1988; Bröcker et al., 1993).

On several islands, these two metamorphic units were intruded by granitic bodies. Using hornblende and/or biotite K-Ar and/or biotite Rb/Sr and/or SHRIMP U/Pb zircon methods the emplacement ages of the I-type granites have been defined between 23-9 Ma and between 18-11 Ma for the S-type granites (Altherr et al., 1982; Wijbrans and McDougall, 1988; Henjes-Kunst et al., 1988; Brocker et al., 1993; Keay, 1998).

II.2.2 The extensional regime

Investigation of the mechanisms that controlled the present-day extensional regime, which is interpreted to have operated since the Early- to Mid- Miocene (Jackson, 1994; Jolivet et al., 1994; Le Pichon et al., 1995; Meijer, 1995; Walcott, 1998), have concluded that the dominant mechanism which causes the extension of the overriding plate is the roll-back of the subducting slab.

The roll-back of the slab is caused by the rapid subduction of dense lithosphere relative to the overall convergence rate (Fig. II.7). This results in a seaward retreat of the subduction zone. The surface expression of the roll-back process shows the outward migration of the Hellenic arc.

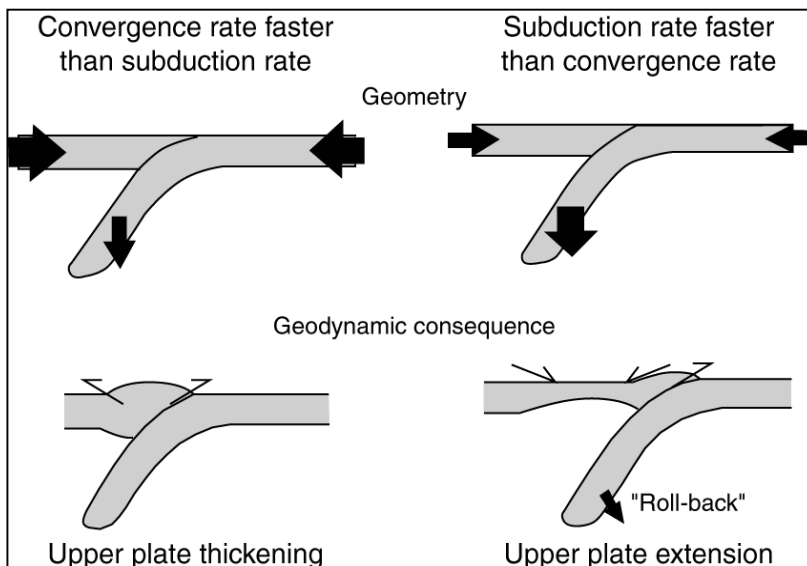


Fig. II.7 Relation between convergence and subduction rates in the distribution of contraction and extensional regimes in the overriding plate (modified from Royden, 1993a).

Local dynamics are mainly the gradual detachment of the subducting slab in the Hellenic subduction zone (Wortel & Spakman, 1992; Meijer, 1995) and the westward expulsion of Turkey in the latest Miocene-Pliocene. This expulsion of Turkey has been caused by the final collision of Arabia and Eurasia, and was accommodated by the development of the North and East Anatolian Fault Zone (McKenzie, 1978). The regional velocities show a westward movement of Turkey and a south-westward movement of the south-west Aegean at a rate of ~ 20 - 30 mm/yr and over 30 mm/yr respectively (Fig. II.8) (Le Pichon et al., 1995; Meijer & Wortel, 1997). However, a recent study on

the geodetic and finite strain pattern in the Aegean (Jolivet, 2001) shows that the pattern of extension is not significantly modified by the recent extrusion of the motion of Anatolia and Aegea. He concluded that the persistence over more than 25 Ma of the same pattern of extension suggests that the cause for extension resides within the Aegean lithosphere. According to Jolivet (2001), gravitational collapse allowed by slab retreat is the primary cause for post-orogenic extension in the Aegean.

The subducted portion of the African plate is expressed seismically by earthquake activity to depths of ~200 km (Makropoulos & Burton, 1984). Seismic tomography suggests the presence of a subducting slab to depths of ~600-800 km (Spakman et al., 1988), which has been interpreted to reflect at least ~60 Ma of subduction activity along the Hellenic system (Hatzfeld, 1994). A well defined subduction related volcanic arc, associated with the present-day subduction is found in the southern Cyclades. Older, Oligocene to Middle Miocene, calc-alkaline magmatism is observed further north and might reflect earlier stages of the developing Hellenic subduction zone (Piper & Piper, 1989), or might have been emplaced in an extensional regime related to the extensional collapse of the region and associated elevation of thermal gradients (Jones et al., 1992).

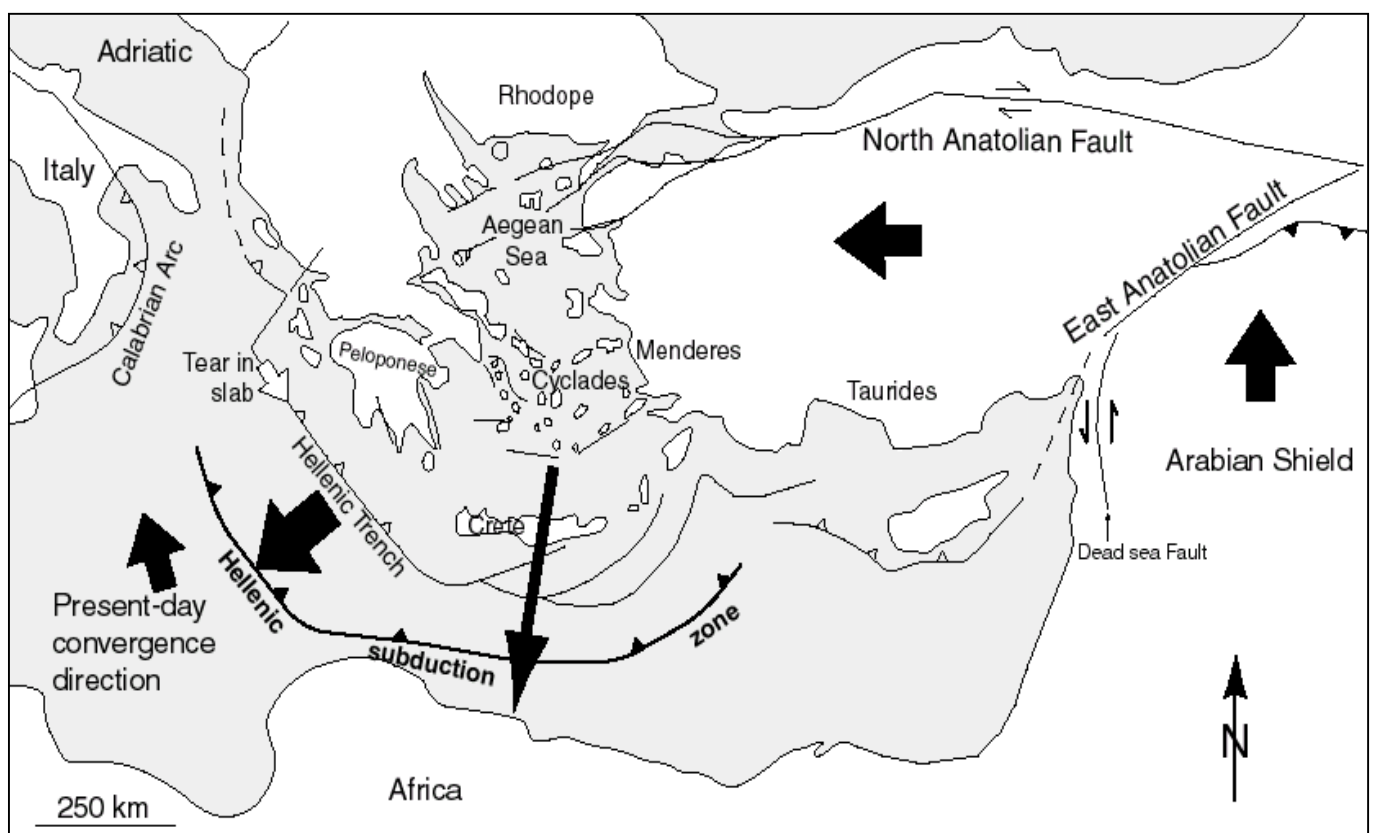


Fig. II.8 Current kinematics which control the present-day extension in the Aegean region (Jackson, 1994; Le Pichon et al., 1995). Black arrows indicate relative motions, white arrow indicates position and propagation direction of tear in subducted slab (Spakman et al., 1988; Meijer & Wortel, 1997).

The Aegean crust is characterized by large variations in thickness, which range from >45 km below the External Hellenides of mainland Greece and <20 km in the northern Cycladic region (Fig. II.9) (Tsokas & Hansen, 1997). These large differences in crustal thickness are most likely the result of crustal thinning as a response to initial reduction of the thickness of the lithospheric mantle, driven by excess potential energy in regions that originally had undercompensated crustal thickness (Platt & England, 1993).

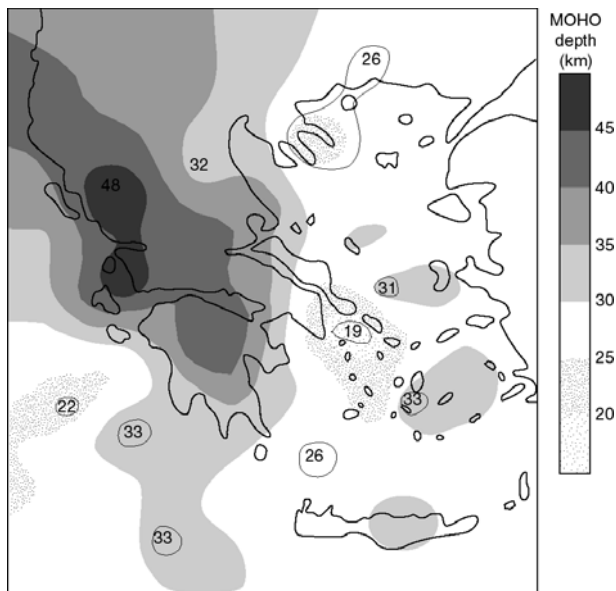


Fig. II.9 Schematic presentation on crustal thickness in the Aegean region, based on the Moho depth (Tsokas & Hansen, 1997).

II.3- Palaeogeographic evolution

The palaeogeographic development of the Eastern Mediterranean has been extensively studied (Dewey et al., 1973; Le Pichon & Angelier, 1979; Burchfield, 1980; Smith & Woodcock, 1982; Robertson & Dixon, 1984; Sengör et al., 1984; Dercourt et al., 1986; Ricou, 1994; Robertson, 1994). The geological history of the Aegean region starts after the Hercynian collision between Gondwana and Laurasia that resulted in the Pangea super continent (Ricou, 1994). The break-up of Pangea led to the development of Tethys Ocean (Fig. II.10: 240 Ma).

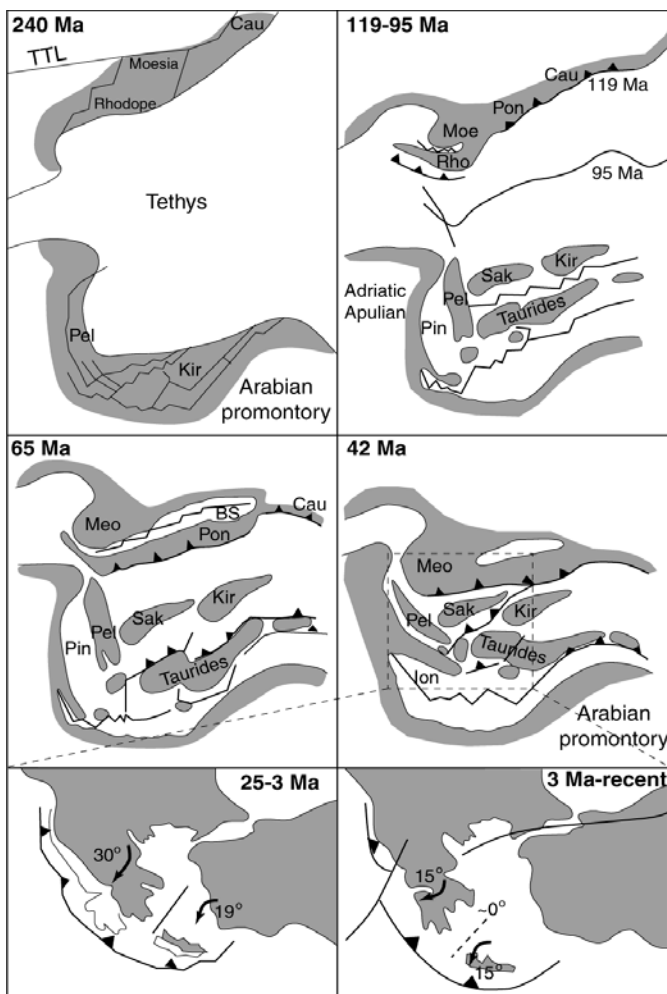


Fig. II.10 Palaeogeographic reconstruction (240-42 Ma from Robertson & Dixon, 1984; 25 to recent from Walcott, 1998, Kissel & Laj, 1988 and Duermeijer et al., 1998) showing reconstructed development of the eastern Mediterranean and the role of continental fragments and secondary basins of the Tethys seaway in the development of the southern Eurasia margin during the African-Eurasian convergence.

- 240 Ma: Proposed location of continental fragments in Triassic;

- 119-95 Ma: reconstruction shows the overall narrowing of Tethys due to N-S convergence of the African and Eurasian plates (position of southern margin of Europe relative to the Africa position has been drawn successively from 119 to 95 Ma);

- 65 Ma: Gradual closure of Tethys and accretion of continental fragments;

- 42 Ma: Collision of most fragments, closure of Pindos basin and formation of Ionian basin;

- 25-3 Ma: Development of the present-day Aegean configuration during extension of the overriding Eurasia plate above the subducting African plate. Clockwise rotation of mainland Greece and northern Cyclades, anticlockwise rotation of southern Cyclades. Development of Mid-Cycladic Lineament;

- 3 Ma to recent: Further outward migration of the overriding plate and associated rotation of individual blocks.

Abbreviations: TTL=Tornquist Teisseyre Line; Rho=Rhodope; Pel=Pelagonian; Kir=Kirsehir; Moe=Moesian; Pon=Pontides; Cau=Caucasus; Pin=Pindos basin; Sak=Sakarya; Ion=Ionian Sea.

Although there is a general consensus that the Tethys ocean consisted of a complex array of continental fragments and marginal basins, generally two major Tethyan oceans have been proposed (Dewey et al., 1973; Robertson & Dixon, 1984; Smith, 1996):

- a late Paleozoic to early Mesozoic Paleotethys in the north;
- a Late Triassic-Early Jurassic Neotethys in the south. These two oceans were separated by the Cimmerian continent (Sengör et al., 1984). Generally, it has been assumed that both Paleotethys and Neotethys were subducting towards the north, underneath Eurasia. Sedimentary basins of Neotethys, which formed following the rifting of the northern margin of the Gondwana, were progressively closed and incorporated into the evolving orogenic belt (Fig. II.10: 119 to 42 Ma). Orogenic activity accelerated in the late Cretaceous when relative motions between the African and Eurasian plates changed to roughly north-south convergence (Fig. II.10: 119 to 42 Ma; Fig. II.11). At the front of the advancing thrust sheets, thick flysch sequences accumulated in flexurally controlled foreland basins (Underhill, 1989). In the latest Cretaceous and Early Palaeocene 1800m of flysch were accumulated in the Vardar Zone. Also in the Pindos and Ionian Zones, substantial amounts of Eocene to Miocene flysch were deposited. Shortening started with the emplacement of oceanic lithosphere and continued with the formation of a tectonic imbricate after which thrusting subsequently migrated towards the more external parts, forming a typical fold-and thrust belt of the External Hellenides. During on-going convergence of the African and Eurasia plates, the Aegean region was affected by regional extension since the Miocene, which led to the present-day configuration (see section II.2.1.1 for a summary of chronologic events in the Aegean).

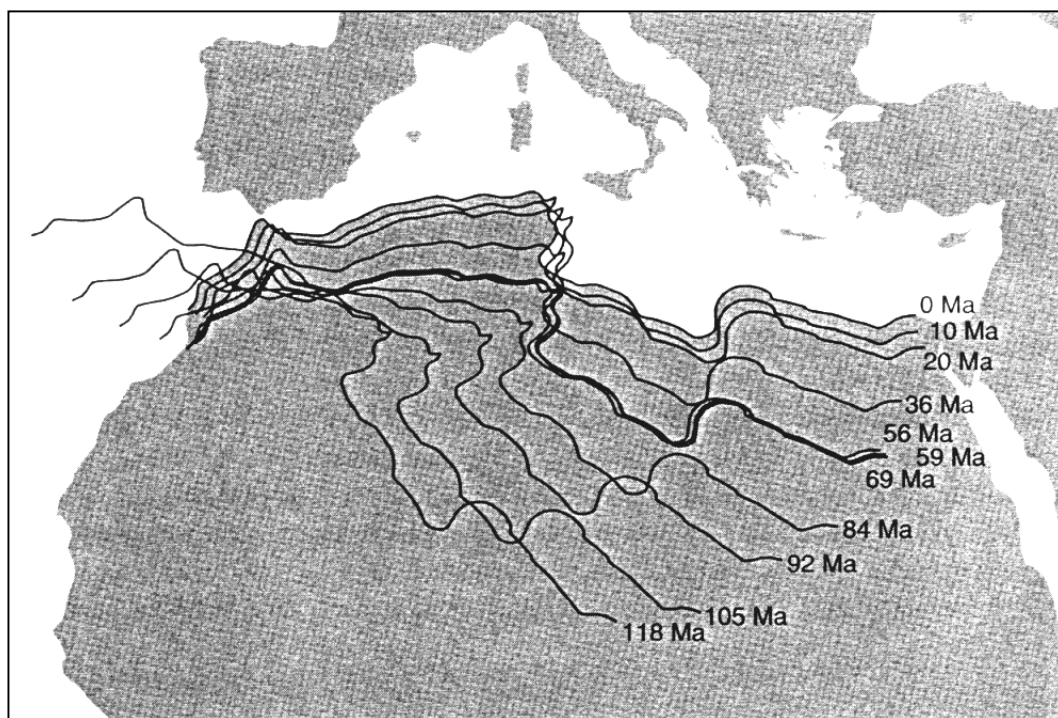


Fig. II.11 Reconstruction of the convergence between African and Eurasia plates, based on the movement and pole rotation of Africa-North America versus Eurasia- North America (from Müller & Roest, 1992). This drawing shows the change from oblique to dominant convergence of African and Eurasian plates since ~118 Ma and indicates the differences in overall rates since this time.

II.4 Implications for this study

The Cycladic islands in the central Aegean became part of the magmatic arc in the Late Miocene and are now in a back-arc position. The Cyclades are famous for their blueschists and spectacular extensional detachments. Most of these extensional detachments operated in an arc setting as indicated by the intrusion of arc-related granites into the detachment footwalls. These granodiorites

are, in general, part of the Late Miocene magmatic arc of the southward retreating Hellenic subduction zone. They intrude synkinematically into the footwall of the normal fault system (for example on Naxos, Mykonos, Ikaria, Tinos).

Systematic sampling parallel to the movement vector of the detachments was carried out, to constrain the cooling history in the footwalls of major extensional detachments in the Cycladic islands (Fig. II.12). The samples were collected from suitable lithologies (mainly granites) for apatite and zircon fission-track and apatite (U-Th)/He analysis to place constraints on the timing of detachment movement, help determine how many detachments exist in the Cyclades, measure long-term slip rates for each detachment and define the amount of displacement.

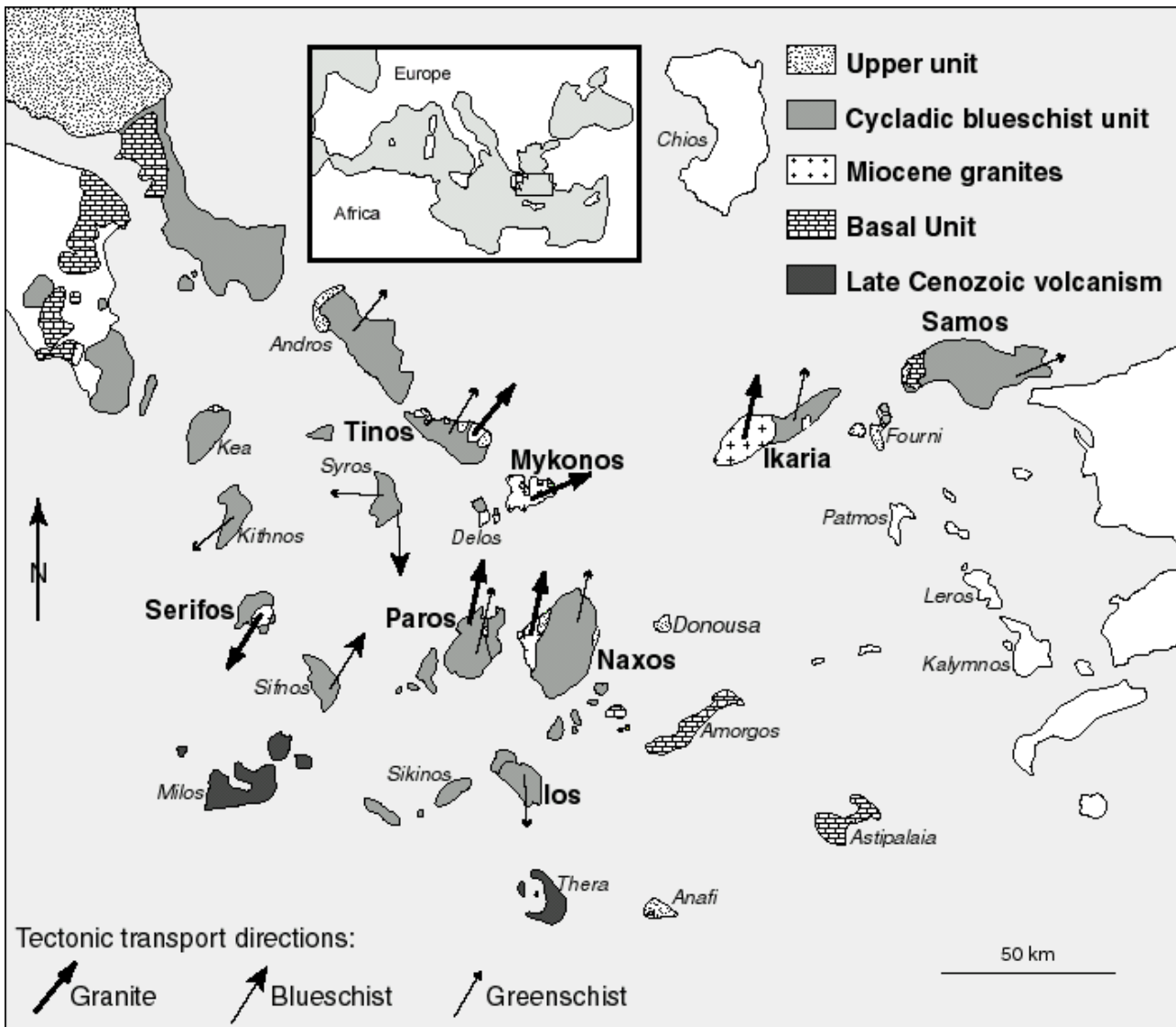


Fig. II.12 Simplified geologic map of the Cycladic zone with orientations of tectonic transport of different rock types: granite, greenschist facies and blueschist facies (map modified from Dürr et al., 1978; Altherr et al., 1982; Avigad & Garfunkel, 1991; Faure et al., 1991; Foster & Lister, 1999; Ring et al., 1999b).

Chapter III

Low-temperature geochronology:

Constraining the cooling history of
major extensional detachments in
the Cyclades, Greece.

In this chapter, the data obtained during this thesis are presented from north to south across the Cycladic zone (from Samos to Ios). In order to discuss the results, the geological setting and previous published geochronological data of each island are summarized (note: not all publications report errors on age data). Furthermore, in a last part of this chapter, we will discuss the problematic (U-Th)/He data recognized during this study.

The samples collected and dated during this thesis are listed in appendix 2. The detailed listing of the argon, fission track and (U-Th)/He results are provided in appendix 3, 4, 5. The formulae used for the calculation of slip and cooling rates and associated errors are given in appendix 6.

III.1 Samos

III.1.1 Geological setting

The geology of Samos Island comprises a series of nappes. At the structural top is the non-metamorphic Kallithea nappe (Upper unit) situated at the western tip of the island which contains numerous dikes of microdiorite, pyroxene leucodiorite, diorite, monzonite, granodiorite to granite, and pegmatite. This unit is underlain by the Cycladic blueschist unit composed of three different nappes: i) the ophiolitic Selçuk mélangé which contains blocks of metagabbro and garnet-mica schist in a matrix of serpentinite and garnet-mica schist; ii) the Ampelos nappe which consists of quartzite, metapelite and metabasite/metaacidite lenses overlain by metabauxite-bearing marble; and iii) the Agios Nikolaos (Carboniferous basement) nappe which contains garnet-mica schist intruded by Carboniferous granitoids (Ring & Layer, 2003). Below the Cycladic blueschist unit is the Kerketas nappe, which is part of the Basal unit and largely consists of a huge marble sequence and minor clastic deposits. Middle Miocene to Pliocene sediments occur in three grabens (Fig. III.1).

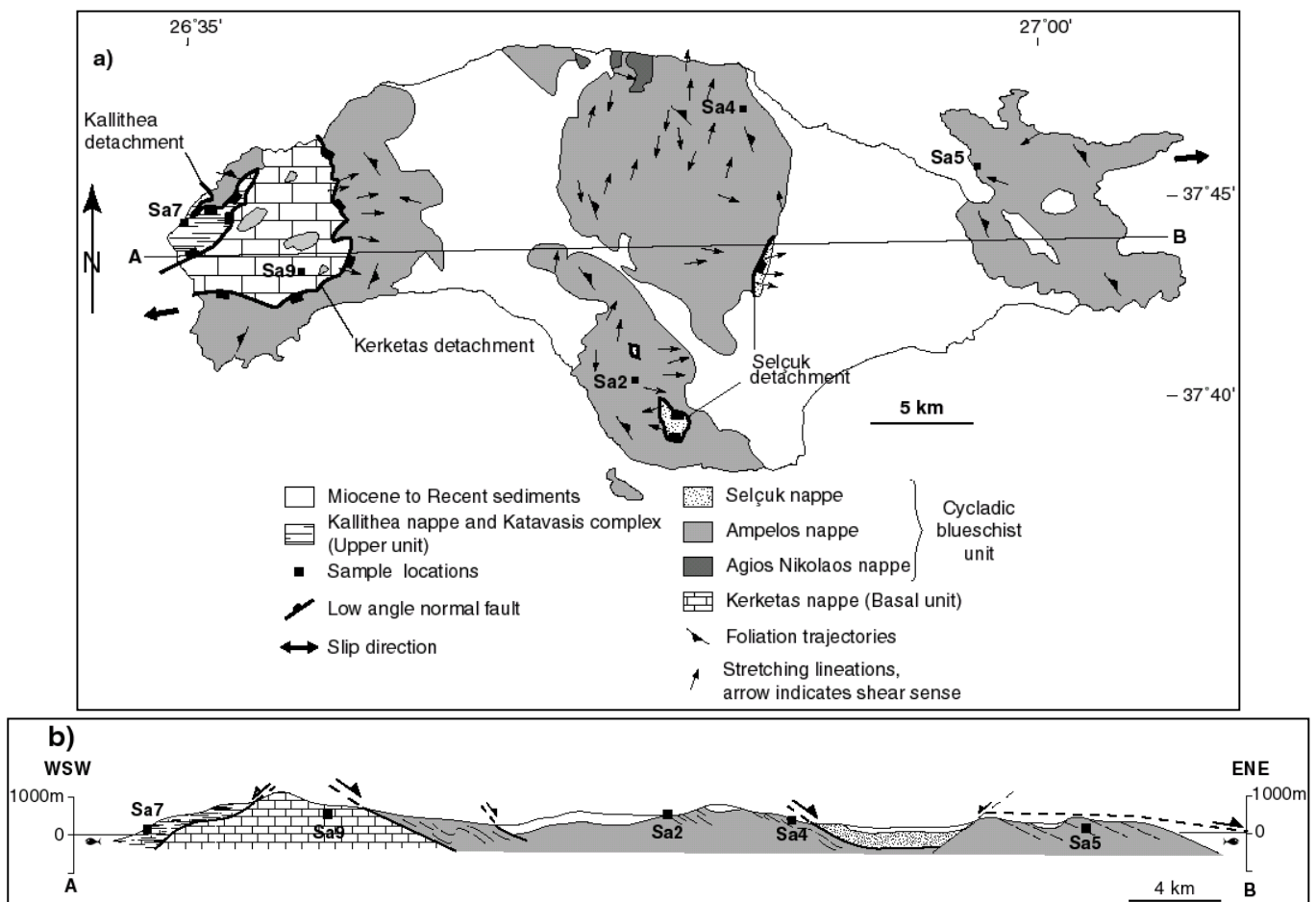


Fig. III.1 (a) Simplified geologic map of Samos Island and (b) WSW-ENE cross section (modified from Ring et al., 1999c); sample locations are indicated.

Ring et al. (1999c), on the basis of structural and metamorphic analysis show that deformation can be divided into four main stages: (1) Eocene and earliest Oligocene ~ESE-WNW oriented nappe stacking (D1 and D2) associated with blueschist- and transitional blueschist-greenschist metamorphism (M1 and M2). D2 caused emplacement of the blueschist unit onto the Kerketas nappe. (2) A subsequent history of Oligocene and Miocene horizontal crustal extension (D3) before and after greenschist metamorphism (M3). Ductile flow during D3 (Fig. III.1) generally caused displacement of upper units towards the ENE. (3) A short period of brittle E-W crustal contraction (D4) occurred around 9 Ma. (4) A phase of N-S directed normal faulting (D5, $\sim <9$ Ma to recent).

Three extensional fault systems mainly related to the D3 stage of deformation (Ring et al., 1999c) occur on Samos (Fig. III.1): (1) The top-to-the-N Kallithea detachment, which separates the Kallithea nappe from the Cycladic blueschist unit and the Kerketas nappe. (2) The top-to-the-ENE Kerketas detachment between the Kerketas nappe and the overlying Ampelos nappe. The Kerketas detachment is associated with the development of Middle Miocene graben (Weidmann et al. 1984; Ring et al. 1999c). (3) The top-to-the-ENE Selçuk extensional system between the Ampelos nappe and the Selçuk nappe (Fig. III.1).

III.1.2 Previous geochronological data

The Kallithea igneous complex is formed from numerous composite dikes. K-Ar dating on a hornblende concentrate from a monzodioritic sample yielded an age of 10.2 ± 0.2 Ma (Mezger et al., 1985) (Fig III.2). This age is interpreted as minimum age for the emplacement of the dikes.

Other dating has been carried out by Ring & Layer (2003) using the Ar/Ar method on rocks from the Cycladic blueschist unit (CBU) and the Basal unit (Fig III.2).

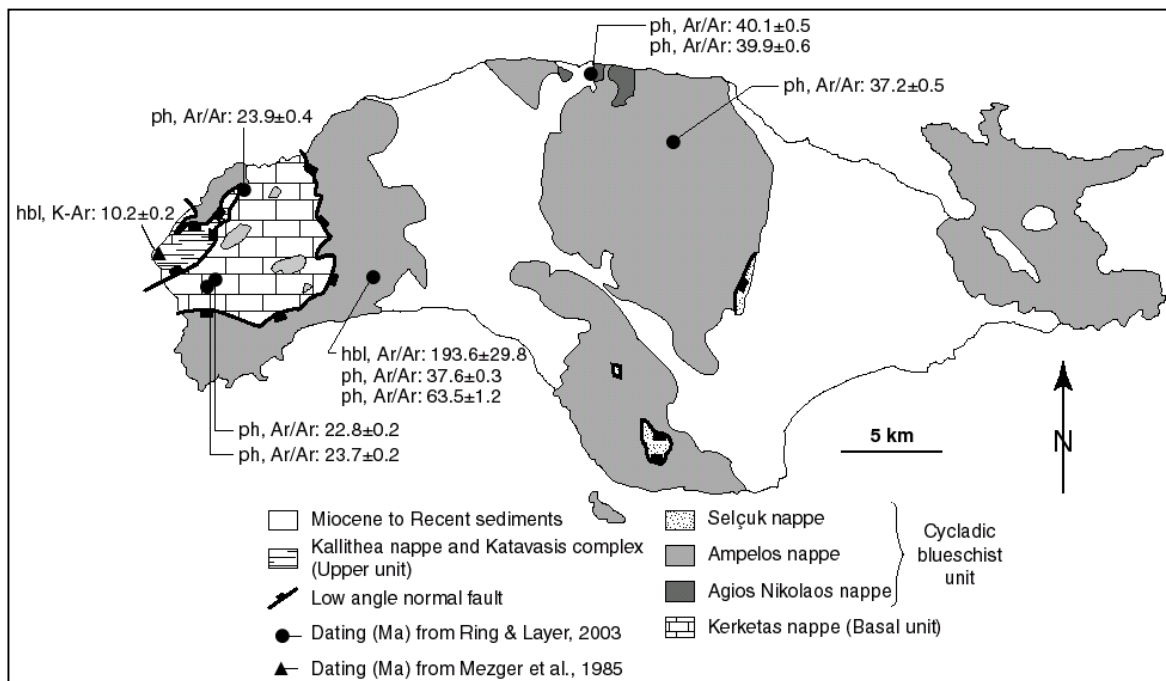


Fig.III.2 Simplified geological map of Samos (modified from Ring et al., 1999c) showing previous geochronological data from Ring & Layer (2003) and Mezger et al. (1985).

For the CBU, synkinematic phengite collected from a high-P shear zone defined a plateau age of 40.1 ± 0.5 Ma. This age is also seen in the first part of the release spectrum for a phengite from outside of the shear zone (39.9 ± 0.6 Ma). Two other samples from the same area define an age of 37.6 ± 0.3 Ma and 37.2 ± 0.5 Ma for white micas. Ring & Layer (2003) interpreted these ages of ~ 40 Ma to date shearing during high-pressure metamorphism. Hornblende from an augengneiss sample yielded a plateau age for the higher temperature of step heating at 193.6 ± 29.8 Ma fairly close to the

Triassic protolith age of the augengneiss (Ring et al., 1999c) and an isochron age of 56.8 ± 4.1 Ma. From the same sample, they defined an age plateau for biotite at 63.5 ± 1.2 Ma whereas the main age information from the white mica is 37.6 ± 0.3 Ma. The plateau defined on white mica show that progressively increasing ages in the final steps indicating an older event. Ring et al. (1999c) interpreted the ~ 55 -60 Ma age as the time of high-pressure metamorphism.

The Ar/Ar phengite ages of 24-21 Ma from the basal unit were interpreted by Ring et al. (2001b) to date phengite growth during high-pressure metamorphism in the Basal unit. This conclusion is corroborated by similar Rb/Sr phengite ages from the Basal unit on Tinos (see section III.3.2; Bröcker & Franz, 1998) and Evia (Ring & Reischmann, 2002).

III.1.3 Results

Given the geometry of extensional faulting on Samos, sampling was undertaken parallel to the main extensional transport direction \sim WSW-ENE (Fig. III.1) in order to monitor lateral passage of isotherms at the top of the footwall. Three samples were collected from the Ampelos nappe (Cycladic Blueschist Unit), one from the Kerketas nappe and one from the Kallithea nappe (Fig. III.1). Only zircon fission track (ZFT) was possible as apatite was missing (Table III.1). In the Ampelos nappe ZFT ages range from 20.3 ± 1.8 Ma to 18.1 ± 1.6 Ma whereas the sample from the Kerketas nappe is 14.1 ± 1.2 Ma and 7.3 ± 1 Ma for the Kallithea nappe. In the Ampelos nappe, ages increase westward in the direction of the footwall slip.

Table III.1. Samos fission-track data

Sample reference (rock type)	Lat. Long.	Elevation (m)	Distance in slip direction (km)	Mineral	Number of crystals	$P\chi^2$ (%)	FT age (Ma)
Sa2 (quartzite)	37°40'36" 26°48'16"	650	23.95 ± 2.4	zircon	12	72.2	20.3 ± 1.8
Sa4 (quartzite)	37°46'58" 26°51'19"	340	16.84 ± 1.7	zircon	16	98.5	19.3 ± 1.4
Sa5 (quartzite)	37°45'59" 26°57'35"	0	6.45 ± 0.7	zircon	12	99.5	18.1 ± 1.6
Sa7 (granite)	37°43'48" 26°34'06"	120		zircon	7	96.3	7.3 ± 1.0
Sa9 (quartzite)	37°42'52" 26°38'17"	570		zircon	12	99.6	14.1 ± 1.2

Zircon FT ages have been calculated using a zeta factors of 127.3 ± 4.4 and 332.9 ± 9.7 determined by multiple analyses of standards following the recommendations of Hurford (1990). Central ages are reported. All data are given for 2σ error level

III.1.4 Discussion

The age of 14.1 ± 1.2 Ma from the Basal unit indicates a minimum age for the Kerketas extensional system.

Ductile extension and exhumation of the Ampelos nappe below the Selçuk extensional system lasted until the Early Miocene as indicated by zircon fission track ages of 20-18 Ma, which consistently young eastward in the direction of hangingwall slip. The age variation yielded a minimum slip rate of 8.1 ± 1.7 km/Myr (Fig. III.3) for the brittle part of the Selçuk extensional fault

system. This high slip rate was not aided by melt lubrication. Based on this rate a minimum displacement of ~18 km can be calculated for the period from ~20-18 Ma.

The ZFT age of 7.3 ± 1 Ma from a granitic dike of the Kallithea unit indicates a cooling age in agreement with a published K-Ar hornblende age of 10.2 ± 0.4 Ma (at 2σ) (Mezger et al., 1985). If a closure temperature of $550 \pm 50^\circ\text{C}$ is assumed for the hornblende K-Ar system (Harrison, 1981; Dahl, 1996a; Villa, 1996) and, since cooling is rapid, a closure temperature of $250 \pm 50^\circ\text{C}$ for the zircon fission track system (Tagami et al., 1998) (see section I.5), it is possible to define a minimum cooling rate for this dike of the Kallithea nappe at $\sim 58^\circ\text{C}/\text{Myr}$. This dike is in the footwall of the Kallithea detachment and shows the same cooling characteristics as other footwall rocks in the Cyclades. Therefore, the fast cooling might be due to tectonically controlled exhumation related to the Kallithea detachment. This implies that the Kallithea detachment operated after 10.2 ± 0.4 Ma.

The timing constraints and the geographic pattern of ages indicate that the Kallithea, Selçuk and Kerketas extensional systems are unrelated to each other.

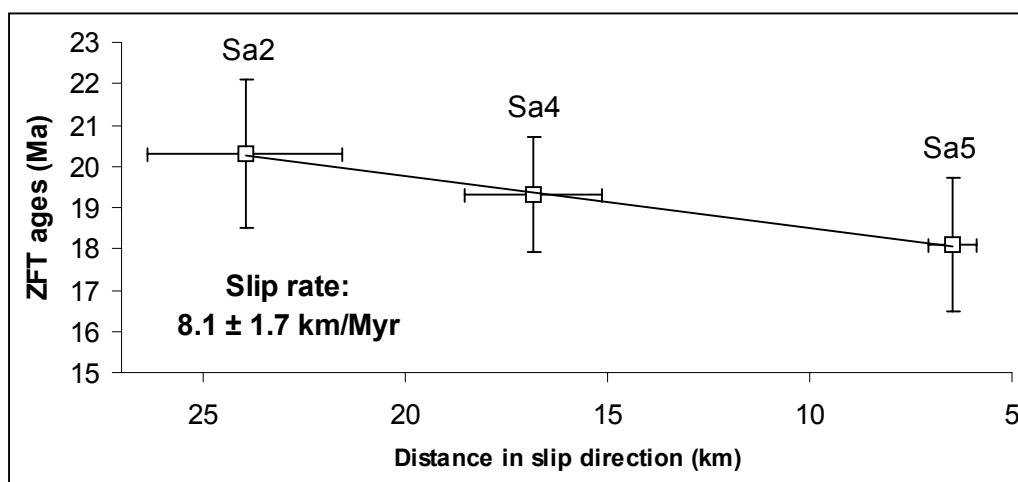


Fig. III.3 Plot of zircon fission-track (ZFT) ages (2σ) against distance in slip direction (2σ) for Selçuk detachment fault; estimated minimum slip rate is 8.1 ± 1.7 km/Myr (2σ).

III.2 Ikaria

III.2.1 Geological setting

The Island of Ikaria belongs to the Cycladic zone. Three tectonic units can be distinguished; they are from top to bottom: (a) The non-metamorphic Fanari nappe; (b) the Messaria nappe and (c) the Ikaria nappe (Fig. III.4). The general structure of Ikaria is dominated by a ~300-500 m thick ductile extensional shear zone, the Messaria shear zone, and two associated brittle detachment faults, the Messaria and Fanari detachments. The Messaria detachment is the upper crustal expression of the ductile Messaria shear zone. This extensional detachment/shear-zone system is referred as the Messaria extensional fault system (MEFS). The Fanari detachment is not associated with an underlying carapace shear zone. The Ikaria and Messaria nappes are separated from one another by the Messaria detachment. The Messaria shear zone developed in the upper parts of the Ikaria nappe. The Fanari detachment separates the Messaria nappe from Pliocene conglomerates of the Fanari nappe. The island has an asymmetric dome-shaped architecture (Fig. III.4; see Kumerics et al., 2004 for detailed cross section of the Ikaria island), the northwestern slopes of the island dip gently to the north and this dips mimics the shallow northern dip of the MEFS. The southern slopes of Ikaria Island dip more steeply to the south (Kumerics et al., 2004).

The Pliocene conglomerates of the Fanari nappe, which is part of the Upper unit, contain pebbles of metamorphic rocks, which are not exposed on Ikaria Island (Dürr et al. 1978). The Messaria nappe comprises metabauxite-bearing marble, graphite-rich calc-mica schist, chloritoid-kyanite-bearing phyllite, quartzite and greenschist (Altherr et al. 1982) and can be correlated with the

Ampelos nappe on nearby Samos Island (Ring et al. 1999b) (Fig. III.1). Both nappes are part of the passive-margin sequence of the Cycladic blueschist unit. The Ikaria nappe consists of a huge succession of metapelite as well as marble, calcisilicate rocks, amphibolite and quartzite. The lack of any high-pressure relics in the Ikaria nappe indicates that it does not belong to the Cycladic blueschist unit and is probably part of the Menderes nappes of westernmost Turkey (Kumerics et al., 2004). The Ikaria nappe was intruded by two synkinematic granites: a large I-type granite in the west and a small S-type granite in the southern part of the island (Altherr et al. 1982). The metapelite contains the amphibolite-facies mineral assemblage garnet-kyanite-staurolite-biotite-plagioclase (Altherr et al. 1982).

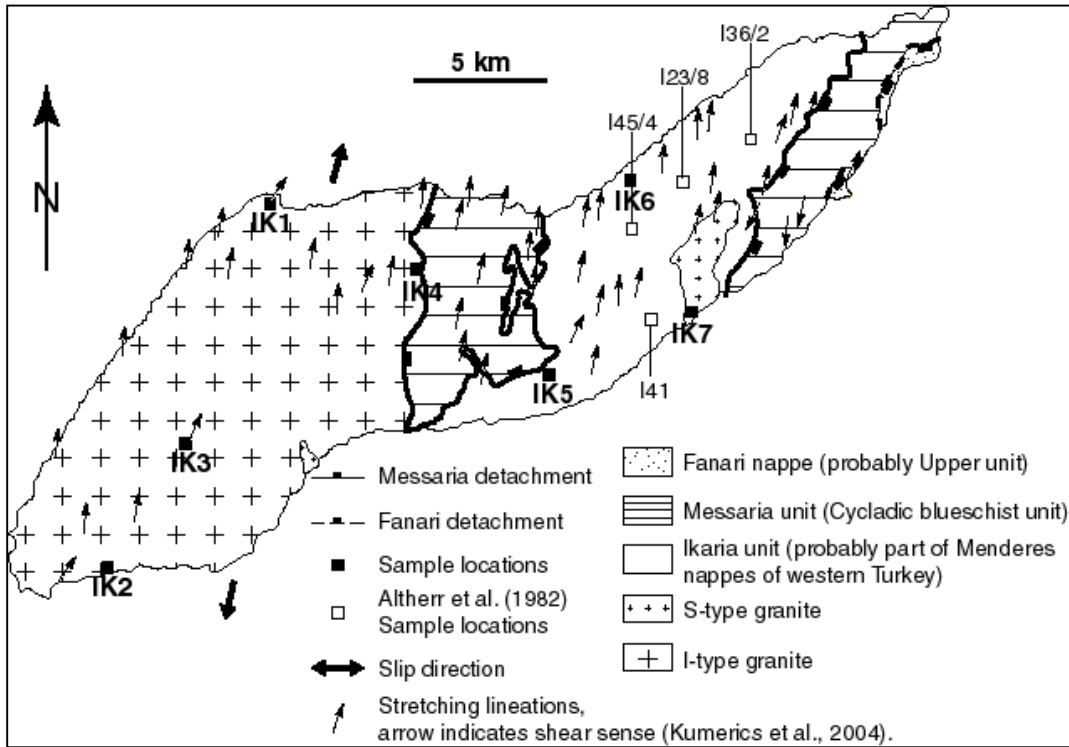


Fig. III.4 Simplified geologic map of Ikaria Island (modified from Altherr et al., 1982 and Kumerics et al., 2004). Shown are tectonic units, Messaria and Fanari extensional detachments and localities geochronological sample collected during this thesis and by Altherr et al. (1982).

III.2.2 Previous geochronological data

The uppermost tectonic unit (Fanari nappe) on the island of Ikaria is cut by dioritic dikes and contain pebbles of metamorphic rocks, which are not exposed on Ikaria island (Dürr et al., 1978) (Fig. III.4). K-Ar dating by Altherr et al., (1994), on hornblende from amphibolite clasts yielded an age of 84.4 ± 2.4 Ma whilst ages from dioritic dykes are 80.5 ± 1.4 Ma, 70.4 ± 1.1 Ma and 67.4 ± 1 Ma. The age of 70.4 ± 1.1 Ma is interpreted as a cooling age while the other ages are thought to be influenced by disturbance of the argon system owing to alteration products in the samples (argon loss and/or gain during hydrothermal overprint) (Altherr et al., 1994). These ages are in agreement with data published for the LP-HT metamorphism (M_0) of late Cretaceous from the Upper unit of other island such as Tinos and Syros (Patzak et al., 1994; Keay, 1998; Brocker & Enders, 1999).

For the other units of Ikaria, Altherr et al. (1982) published K-Ar ages. In the Messaria unit (Cycladic blueschist unit, see Fig. III.4) ages obtained on actinolite and a mixture of actinolite and biotite are 26.2 ± 0.3 Ma and 9.7 ± 0.1 Ma. Another sample from this unit gave a similar young age at 8.8 ± 0.2 Ma (biotite K-Ar). The older age is correlated with greenschist metamorphism (M_2).

In the Ikaria unit hornblende K-Ar ages range from 24.9 Ma to 16.6 Ma. Two concordant dates of 24.9 ± 0.7 Ma and 24.7 ± 0.7 Ma are interpreted as cooling ages and it is assumed that these ages are slightly younger than the culmination of greenschist metamorphism (M_2) while the other ages

are probably disrupted by the I-type granite intrusion which occurred after the culmination of metamorphism (Altherr et al., 1982). Ages obtained on biotite and muscovite by the K-Ar method range from ~22 Ma to ~9 Ma and are interpreted by Altherr et al. (1982) as cooling ages. The S-type granite intrusion of eastern Ikaria is dated at 18.1 ± 2.2 Ma (whole rock Rb/Sr dating) while the other results on biotite, muscovite using Rb/Sr and K-Ar methods range from 14.5-9.4 Ma are cooling ages (Altherr et al., 1982).

The minimum age for the intrusion of the I-type granite of western Ikaria is estimated by Altherr et al. (1982) at 22.7 ± 0.2 Ma (K-Ar on hornblende) which would have intruded only shortly after the culmination of the Barrovian metamorphism (M_2). However, the dated sample is from a large xenolith (probably a part of the Ikaria unit) within the I-type granite. This age could be interpreted as cooling age of the Ikaria unit unrelated to emplacement of the granodiorite. The other ages obtained on this granite range between 9 and 8.2 Ma on biotite (Rb/Sr and K-Ar methods) from the foliated part of the pluton and are interpreted as minimum ages for ductile deformation. Apatite fission track results define a cooling age of 7.1 Ma (Altherr et al., 1982).

III.2.3 Results

Sampling was undertaken parallel to the transport direction of the Messaria extensional fault system, i.e. ~NNE-SSW (Fig. III.4) (Kumerics et al., 2004). Four samples have been dated in the granodiorite (IK1 to IK4), one in the S-type granite of the eastern part (IK7) and two in the Ikaria unit (IK5 and IK6) (Fig. III.4). Most samples yielded both apatite and zircon.

The zircon fission track ages from the footwall of the MEFS range from 10.3 ± 0.6 Ma in the south to 6.3 ± 0.6 Ma in the north. The apatite fission track ages are between 8.4 ± 1.6 Ma (south) and 5.2 ± 1.8 Ma (north) and the apatite (U-Th)/He ages range from 6.0 ± 0.6 Ma (south) to 3.6 ± 0.4 Ma (north) (Table III.2a). All ages consistently young in a northward direction. The K-Ar ages obtained on biotite and muscovite by Altherr et al. (1982) are also younging from the south to the north (Fig. III.4 and Table III.2b).

Table III.2a. Ikaria fission-track and U-Th/He data

Sample reference (rock type)	Lat. Long.	Elevation (m)	Distance in slip direction (km)	Mineral	Number of crystals	$P\gamma_2$ (%)	FT age (Ma)	Mean track length (μm)	StD (μm)	Number of tracks measured	F_T	Helium age (Ma)
Ik1 (granodiorite)	37°38'02" 26°05'09"	20	4.15 ± 0.4	apatite	17	93.5	6.7 ± 1.8	14.14 ± 0.32	0.87	28	0.68	3.6 ± 0.4
				zircon	15	8.4	8.2 ± 0.8					
Ik2 (granodiorite)	37°31'11" 26°00'49"	50	18.50 ± 1.9	apatite	22	98.3	8.4 ± 1.6	14.18 ± 0.24	0.9	52	0.68	6 ± 0.6
				zircon	16	37.3	10.3 ± 0.6					
Ik3 (granodiorite)	37°33'21" 26°02'51"	760	14.05 ± 1.4	zircon	10	57.0	7.5 ± 0.8					
Ik4 (granodiorite)	37°36'49" 26°09'07"	60	5.30 ± 0.5	zircon	7	32.4	8.1 ± 0.8					
Ik5 (quartzite)	37°35'09" 26°12'13"	880	7.45 ± 0.7	apatite	24	96.7	6.8 ± 1.4	14.43 ± 0.42	1.02	23		
Ik6 (quartzite)	37°38'31" 26°14'26"	270	0.55 ± 0.6	apatite	19	95.5	6.2 ± 1.6	14.51 ± 0.38	1.12	35	0.689	5.6 ± 0.4
				zircon	3	95.1	8.6 ± 1.8					
Ik7 (S-type granite)	37°35'44" 26°15'22"	20	4.55 ± 0.5	apatite	16	93.8	5.2 ± 1.8	14.19 ± 0.36	0.93	26		
				zircon	12	100	6.3 ± 0.6					

Apatite and zircon FT ages have been calculated using a zeta factors of 127.3 ± 4.4 and 332.9 ± 9.7 determined by multiple analyses of standards following the recommendations of Hurford (1990). Central ages are reported. All data are given for 2σ error level.

Table III.2b. Muscovite K/Ar data (Altherr et al., 1982)

Sample reference (rock type)	Distance in slip direction 2σ (km)	K/Ar age (Ma)	Error 2σ
I35/12	1.10 ± 0.1	10.08	0.16
I23/8	2.55 ± 0.3	9.99	0.24
I45/4	4.25 ± 0.4	10.09	0.18
I41	7.30 ± 0.7	10.89	0.18

Sample from mylonites in the Messaria shear zone
(for localities, see Fig. III.4)

Temperature-time (T-t) paths have been calculated for the I-type granite (Fig. III.5a) and for the metasediments (Fig. III.5c) in the footwall of the MEFS have been calculated. The data for both rock units indicate rapid cooling from $\sim 300^\circ\text{C}$ to $\sim 80^\circ\text{C}$ within <5 Ma at minimum rates of $\sim 40^\circ\text{C}/\text{Myr}$ for the I-type granite and $\sim 25^\circ\text{C}/\text{Myr}$ for the metasediments of the Ikaria nappe. The mean track lengths in the apatite range from $14.18 \pm 0.32 \mu\text{m}$ to $14.14 \pm 0.24 \mu\text{m}$ for the I-type granite and $14.43 \pm 0.42 \mu\text{m}$ to $14.51 \pm 0.38 \mu\text{m}$ for the metasediments (Table III.2a) consistent with rapid cooling.

The cooling curves for samples from the I-type granite and the metasediments of the Ikaria nappe are different (Fig. III.5). We envisage that the T-t path for the Ikaria nappe reflects extension-related cooling during and after greenschist-facies metamorphism and that the relatively constant cooling rate is controlled by a constant rate of extensional slip. The I-type granite intruded synkinematically into the MEFS and its intrusion temperature was higher than temperatures for greenschist-facies metamorphism in the Ikaria nappe. Therefore, the I-type granite had more potential for initially fast cooling, which is reflected by the steep cooling curve between the zircon and apatite PAZ's (Fig. III.5a). After fast tectonically-controlled cooling from intrusion temperatures, the I-type granite had a similar cooling history as its country rocks.

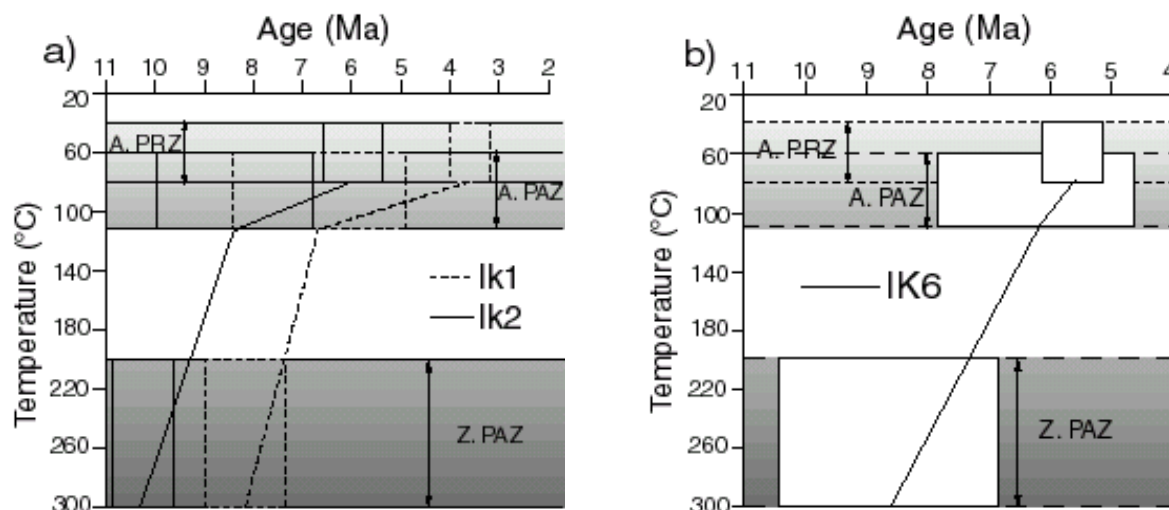


Fig. III.5 T-t diagrams showing cooling rates for the footwall of the Messaria extensional fault system. **(a)** T-t path for Ik1 and Ik2 from the I-type granite. **(b)** T-t path for Ik6 from metasediments of the Ikaria nappe. Boxes represent uncertainties on ages and temperatures (2σ); lines represent cooling path for each sample.

III.2.4 Discussion

In Figure III.6 samples IK1-IK4 from the I-type granite in the western part of the island are plotted along the slip direction and yielded slip rates of $6.0 \pm 0.2 \text{ km}/\text{Myr}$ (apatite (U-Th)/He), $8.4 \pm 0.9 \text{ km}/\text{Myr}$ (apatite fission track) and $8.5 \pm 0.9 \text{ km}/\text{Myr}$ (zircon fission track). The ages of the

samples IK5-IK7 (open symbols in Fig. III.6) are projected into the slip direction but were not used for the slip rate calculation because the projection over great distances may result in relatively great errors. However, it is noteworthy that, except for the (U-Th)/He age of IK6, the ages of samples IK5- IK7 plot reasonably close to the regression lines calculated for samples IK1-IK4 (Fig. III.6).

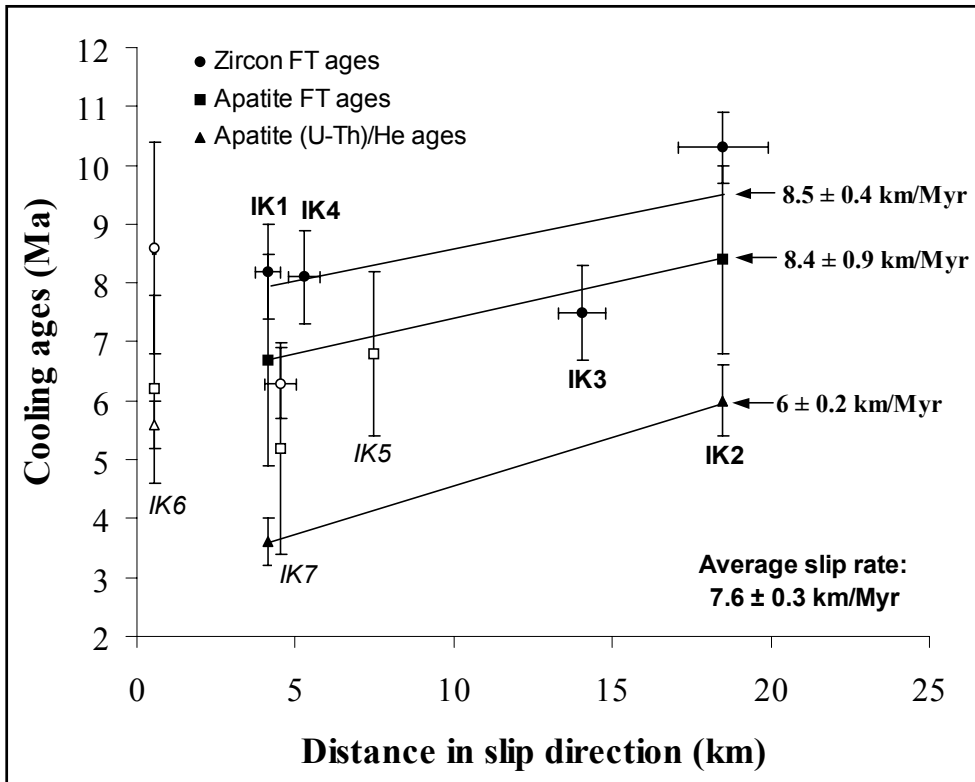


Fig. III.6 Plot of zircon fission-track (ZFT), apatite fission-track (AFT) and apatite (U-Th)/He ages (2σ) against distance in slip direction (2σ) for Messaria extensional fault system; estimated minimum slip rates are 8.5 ± 0.4 km/Myr (ZFT), 8.4 ± 0.9 km/Myr (AFT) and 6 ± 0.2 km/Myr (apatite (U-Th)/He) (2σ). Slip rates were calculated with samples from the I-type granite (Ik1 to Ik4). Samples Ik5 to Ik7 (open symbols) have been also projected following the slip direction; note that the ages from these samples plot along the regression lines calculated for the I-type granite.

We also calculated a slip rate from the K-Ar muscovite ages of Altherr et al. (1982) from the Messaria shear zone (Fig III.7). Kumerics et al. (2004) argue on the basis of detailed thin section work on samples from localities of the Altherr et al. (1982) sampling sites that mylonitization and recrystallization caused complete isotopic reequilibration. Therefore, the K-Ar ages are interpreted to date mylonitization related mineral growth. The fact that the K-Ar muscovite ages of Altherr et al. (1982) consistently young in a northerly direction and are consistently slightly older than the zircon fission track ages supports this interpretation, which implies that the muscovite ages of 11-10 Ma (Altherr et al. 1982) date ductile deformation in the Messaria shear zone. The muscovite ages yielded a slip rate of 8 ± 0.3 km/Myr, which is similar to the slip rates obtained from low-temperature thermochronology (Fig III.7).

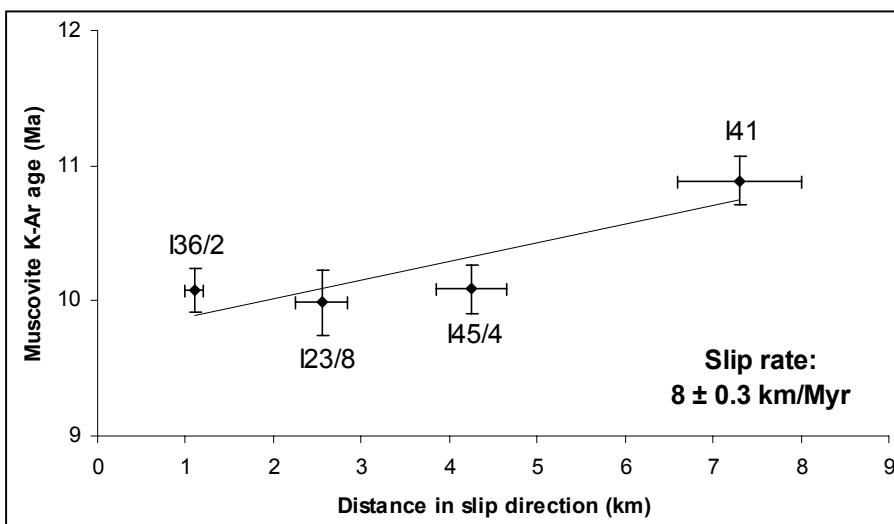


Fig. III.7 K-Ar muscovite ages (2σ) from Altherr et al. (1982) plotted along the slip direction; estimated minimum slip rate of 8 ± 0.3 km/Myr (2σ).

The progressive superposition of ductile, ductile-brittle and brittle structures in the footwall of the MEFS, brittle deformation in the hangingwall and the decrease of cooling ages parallel to the northward slip direction of the hangingwall reflects progressive southward migration of footwall exhumation and is typical for extensional fault systems above metamorphic core complexes. Initial movement in the ductile Messaria shear zone of the MEFS at ~11-10 Ma was accompanied and aided by the intrusion of two synkinematic granites and high thermal field gradient of 25-35 °C/Myr (Kumerics et al., 2004).

The MEFS operated from ~450-400°C to at least 80°C between ~11-3 Ma. T-t paths indicate rapid cooling as the footwall was dragged to the surface (Fig. III.5). The Messaria detachment probably rooted at brittle/ductile transition and its carapace Messaria shear zone in the directly underlying ductile crust. The fact that the cooling rates of both the I-type granite and the metapelite of the Ikaria nappe are fast is thought to be due to early intrusion of the granite during extensional shearing and that both rocks units were then exhumed and cooled together. This interpretation would imply intrusion ages of 11-10 Ma for the two synkinematic granites.

Minimum average slip rates at the MEFS were ~7-8 km/Myr. This rate would yield a minimum displacement of ~62 km for the period from ~11 to ~3 Ma.

III.3 Tinos

III.3.1 Geological setting

The tectonostratigraphic framework of Tinos comprises four subunits (Fig. III.8): the Akrotiri, the Upper, the Cycladic blueschist (also named Intermediate unit on Tinos) and the Basal units.

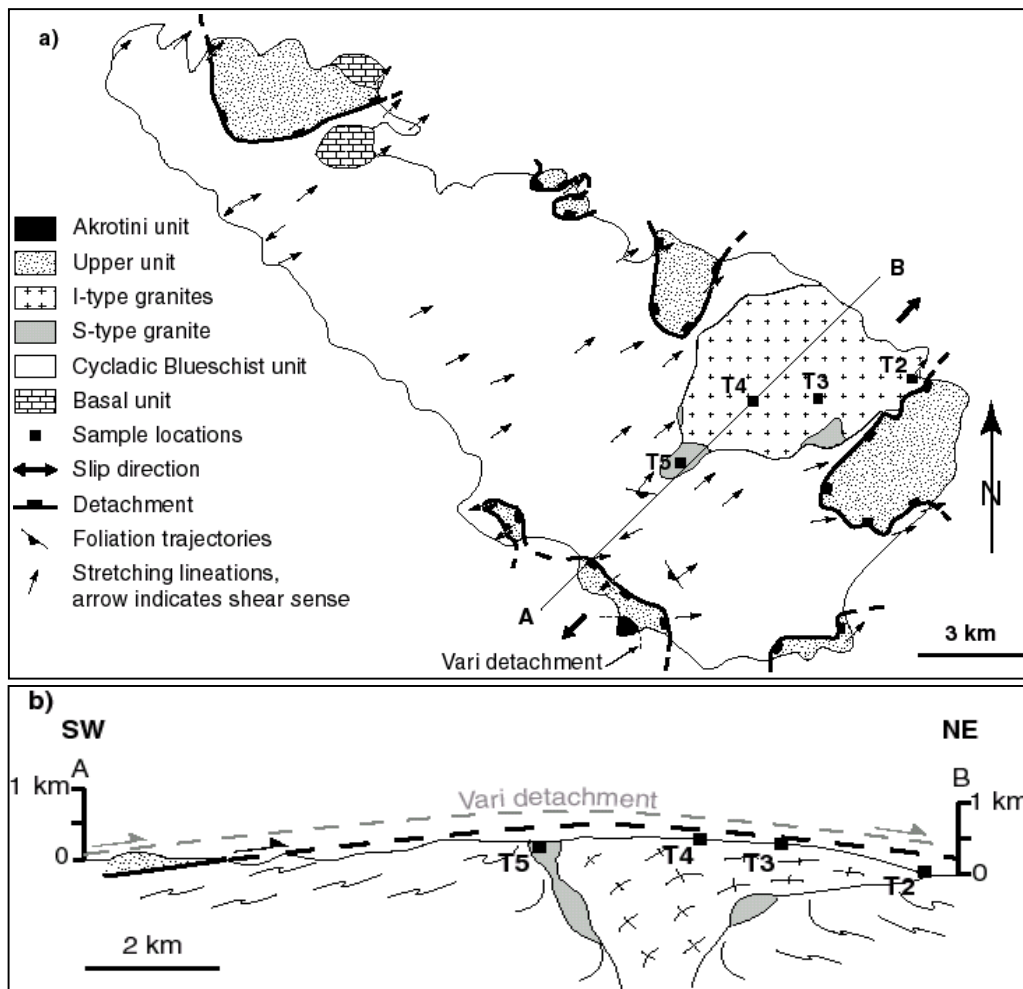


Fig. III.8 (a) Simplified geologic map of Tinos Island and (b) SW-NE cross section (modified from Gautier & Brun, 1994; Jolivet & Patriat, 1998 and Aubourg et al. 2000); sample locations are indicated.

The Akrotiri unit is only exposed in a single location in southern Tinos and consists mainly of amphiboles and paragneisses (Patzak et al., 1994). The Akrotiri unit and the Upper unit are separated by the Vari detachment (Maluski et al., 1987; Patzak et al., 1994).

The greenschist facies Upper unit comprises serpentinites, meta-gabbros, opicalcites and phyllitic rocks (Melidonis, 1980). Bröcker & Franz (2000) suggest that the Akrotiri unit could be a large block within the ophiolitic melange of the Upper unit.

The underlying Cycladic Blueschist unit (CBU or Intermediate Unit) and the Upper unit are separated by a shallow dipping contact, interpreted as an extensional ductile shear zone (Avigad and Garfunkel, 1989; Gautier and Brun, 1994; Patria and Jolivet, 1998; Jolivet and Patria, 1999) and consists of marbles, calcschists, siliciclastic metasediments as well as metavolcanic rocks (Melidonis, 1980). Most rocks have greenschist facies mineral assemblages, but relics of the earlier high pressure stage are preserved in many places (Bröcker et al., 1993).

The basal unit is only exposed in NW Tinos and mainly consists of various metamorphic carbonate rocks (Avigad and Garfunkel, 1989). An Early Miocene granodiorite intruded both the lower and the upper units, in the Eastern part of the island (Bröcker et al., 1993) and is responsible for contact metamorphism (Bröcker and Franz, 2000).

Most of the extensional ductile deformation is cut by the granodioritic pluton. The top-to-the-NE extension in the upper plate, around the pluton, continued during and after the intrusion and cooling stage (Jolivet and Patria, 1999).

III.3.2 Previous geochronological data

In figure III.9 and table III.3 a summary of previous geochronological data on Tinos island are shown.

Table III.3. Previous geochronological data from the Cycladic blueschist unit of Tinos

Rock Type	Metamorphic grade	Method	mineral dated	Age (Ma) $\pm 2\sigma$	Reference
Metabasic rock	Blueschist	Rb/Sr	Phengite + whole rock	36.9 \pm 0.4	Brocker & Franz, 1998
Metabasic rock	Blueschist	Rb/Sr	Phengite + epidote + whole rock	39 \pm 1.6	Brocker & Franz, 1998
Metabasic rock	Blueschist	Rb/Sr	Phengite + whole rock	37.4 \pm 0.4	Brocker & Franz, 1998
Quartz micaschist	Blueschist	Rb/Sr	Phengite + whole rock	32.5 \pm 0.6	Brocker & Franz, 1998
Quartz micaschist	Blueschist	Rb/Sr	Phengite + whole rock	39.5 \pm 0.4	Brocker & Franz, 1998
Glaucophanite	Blueschist	Ar/Ar	Phengite	43.8 \pm 0.2	Brocker et al., 1993
Glaucophanite	Blueschist	Ar/Ar	Phengite	42.3 \pm 0.2	Brocker et al., 1993
Quartz micaschist	Blueschist	Ar/Ar	Phengite + paragonite	44.5 \pm 0.3	Brocker et al., 1993
Glaucophane-chloritoid-micaschist	Blueschist	Ar/Ar	Phengite + paragonite	40.2 \pm 0.2	Brocker et al., 1993
Omphacite	Blueschist	Ar/Ar	Phengite	~ 43	Brocker et al., 1993
Meta-tuffite	Blueschist	Ar/Ar	Phengite	~ 41	Brocker et al., 1993
Omphacite	Blueschist	Ar/Ar	Phengite	~ 41.6	Brocker et al., 1993
Meta-acidite blue amphibole	Blueschist-greenschist transition	Ar/Ar	Phengite	29.2 \pm 0.3	Brocker et al., 1993
Metabasic greenschist	Blueschist-greenschist transition	Ar/Ar	Phengite	32.5 \pm 0.2	Brocker et al., 1993
Intermediate meta-volcanic rock	Blueschist-greenschist transition	Ar/Ar	Phengite	~ 31	Brocker et al., 1993
Meta-psammite	Blueschist-greenschist transition	Ar/Ar	Phengite + paragonite	~ 28	Brocker et al., 1993
Metabasic rock	Greenschist	Rb/Sr	Phengite + whole rock	28.9 \pm 0.3	Brocker & Franz, 1998
Calcareous micaschist	Greenschist	Rb/Sr	Phengite + whole rock	37.4 \pm 0.4	Brocker & Franz, 1998
Calcareous micaschist	Greenschist	Rb/Sr	Phengite + whole rock	39.9 \pm 0.7	Brocker & Franz, 1998
Calcschist	Greenschist	Rb/Sr	Phengite + whole rock	22.4 \pm 0.2	Brocker & Franz, 1998
Calcschist	Greenschist	Rb/Sr	Phengite + whole rock	23.5 \pm 0.2	Brocker & Franz, 1998
Meta-acidic rock	Greenschist	Rb/Sr	Phengite + epidote + whole rock	21 \pm 0.9	Brocker & Franz, 1998
Meta-acidic rock	Greenschist	Rb/Sr	Phengite + epidote + whole rock	20.9 \pm 0.8	Brocker & Franz, 1998
Meta-acidic rock	Greenschist	Rb/Sr	Phengite + epidote + whole rock	22.5 \pm 1.5	Brocker & Franz, 1998
Acidic meta-volcanic rock	Greenschist	Ar/Ar	Phengite	~ 21.7	Brocker et al., 1993
Meta-tuff	Greenschist	Ar/Ar	Phengite	~ 22.4	Brocker et al., 1993
Acidic meta-volcanic rock	Greenschist	Ar/Ar	Phengite	~ 22.1	Brocker et al., 1993
Acidic meta-volcanic rock	Greenschist	Ar/Ar	Phengite	~ 21.5	Brocker et al., 1993

Dating in the Akrotiri unit by Patzak et al. (1994) yielded ages ranging from 77 to 66 Ma (Hornblende K-Ar ages) that were interpreted as due to extraneous radiogenic argon. Therefore, they assumed that the older dates testify to an early, > 77 Ma old metamorphic event. The inherited argon was lost, to various degrees, during a second thermal event, little later than 66 Ma, i.e. at about the Cretaceous/Tertiary boundary (M_0). They interpreted K-Ar ages of 58.8 ± 0.6 Ma and 51.9 ± 0.6 Ma for muscovites derived from two Akrotiri gneisses as moderately rejuvenated, possibly during the Eocene HP/LT event. This would be indicated by formation of a second high-silica generation of muscovite.

Concerning the Upper unit, phyllitic rocks yielded inconsistent apparent ages between 92.4 ± 1.4 Ma and 20.8 ± 2.1 Ma, clearly indicating disturbance of the isotopic system (Bröcker & Franz, 1998). The authors assume that the younger ages are related to non-pervasive rejuvenation and resetting of the Rb/Sr system during tectonic juxtaposition of the Upper unit above the Cycladic blueschist unit. The youngest age at 20.8 ± 2.1 Ma obtained from a sample collected close to the tectonic contact is believed to approximate the timing of tectonic juxtaposition which probably occurred during a regional greenschist-facies episode producing a pervasive overprint in the structurally Cycladic blueschist unit. Moreover, a contact metamorphic phyllite from the outer aureole produced by the emplacement of the I-type granite provided an age of 16.6 ± 0.5 Ma (Fig. III.9a) (Bröcker & Franz, 1998).

In the Cycladic Blueschist Unit (CBU), K-Ar dating on blueschists (M_1) and greenschists (M_2) from Tinos are summarized in Kohlmann (1978) and published by Altherr et al. (1982). The 53.4-34.9 Ma age range of white mica separated from the blueschist facies rocks clearly documents mixed ages between the Eocene HP/LT event and the greenschist metamorphism overprinted. Phengites from the greenschist facies yielded K-Ar ages of 24.2-18.9 Ma, testifying to the Barrovian overprint and subsequent contact metamorphism (Altherr et al., 1982). The main results obtained on the CBU by Bröcker et al. (1993) and Bröcker & Franz (1998) are reported in the Table III.3. Bröcker et al. (1993) used $^{40}\text{Ar}/^{39}\text{Ar}$ dating (17 analyses) on white micas while Bröcker & Franz (1998) carried out Rb/Sr dating on whole rock, phengite paragonite and epidote (12 ages defined), to constrain the tertiary metamorphic evolution of the Cycladic blueschist tectonic unit. They obtained ages of 44-40 Ma, which are considered to represent dynamic recrystallization under peak or slightly post peak high-pressure metamorphism (M_1). The blueschist facies mineralogies were partially or totally replaced by retrograde greenschist facies assemblages during exhumation. This exhumation and overprint is documented by decreasing ages of 33-28 Ma in some greenschists and late-stage blueschist rocks and ages of 30-20 Ma in the lower temperature steps of the argon release pattern of blueschist micas (Bröcker et al., 1993). Some micas gave ages of 23-21 Ma which are assumed to represent incomplete resetting of systems caused by a renewed prograde phase of greenschist metamorphism. Subsequently, Bröcker & Enders (1999) provided zircon ages of 61 to 63 Ma for a jadeitite (Fig. III.9a). They proposed that the young $^{40}\text{Ar}/^{39}\text{Ar}$ and Rb/Sr ages previously obtained on white mica may indicate that these isotopic systems were continuously reset as a result of deformation-related recrystallisation which did not affect the zircon U-Pb systems. Although the morphologic criteria of the zircon are consistent with a magmatic origin, they favoured a syn-metamorphic, metasomatic origin. They argue that small amounts of unusual melts intruded into an accretionary complex during high pressure metamorphism. Therefore, they suppose that the high-pressure metamorphism in the Cyclades commenced significantly earlier than indicated by previous data.

A summary of all data provided in the CBU indicate that the HP/LT metamorphism (M_1) occurred from 63 to 40 Ma while the greenschist metamorphism (M_2) is dated from 24 to 19 Ma with a transitional period which partially reset the chronological system at 34 to 20 Ma.

The emplacement of the I-Type granite has been estimated at minimum ~16 Ma (hornblende K/Ar dating) by dating carried out on rocks from the granite itself (Altherr et al., 1982; Avigad et al., 1998) and the eastern aureole of contact metamorphism (Bröcker & Franz, 2000).

Younger ages from the western aureole (10-8 Ma) possibly date deformation that affected the marginal parts of the main intrusion (Fig. III.9b) (Bröcker & Franz, 2000).

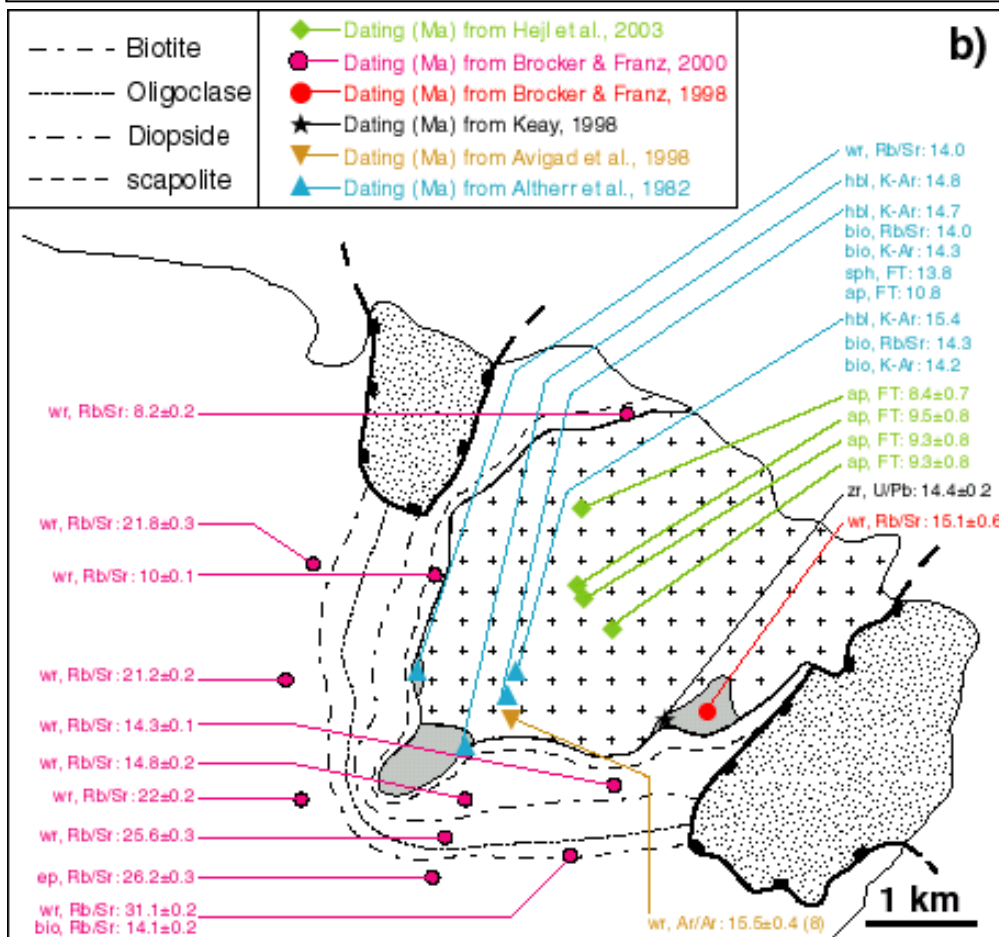
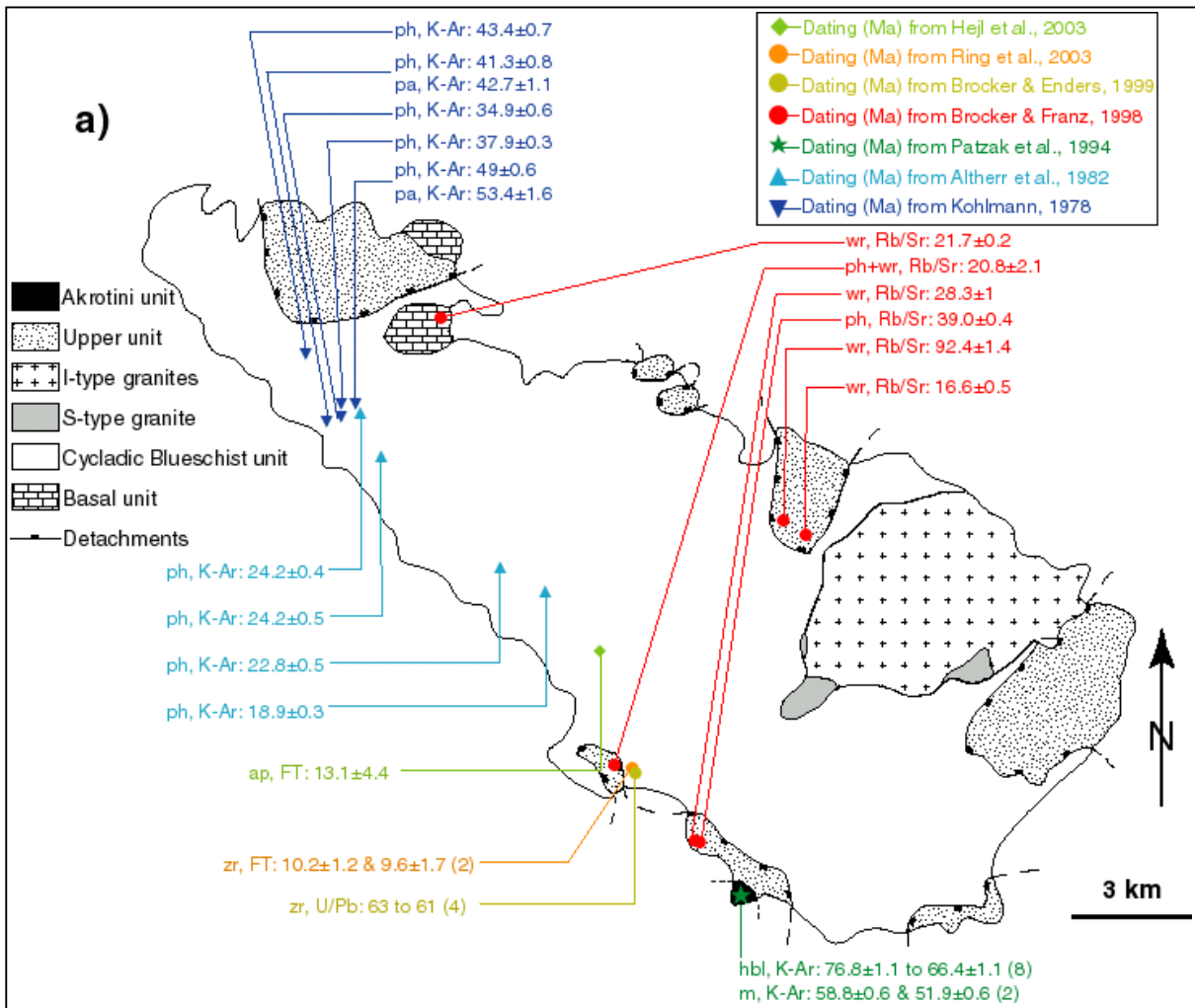


Fig. III.9 (a) Simplified geological map of Tinos (modified from Bröcker & Franz, 2000) showing a part of previous geochronological data. **(b)** Mineral zone pattern in the contact aureole of the I-type granite of Tinos (modified from Bröcker & Franz, 2000). Abbreviations: FT = Fission Track; hbl = hornblende; m = muscovite; bio = biotite; ph = phengite; pa = paragonite; wr = whole rock; ap = apatite; zr = zircon. All ages are in millions of years and given for 1σ error level excepted dating from Bröcker & Franz, 1998 and Bröcker & Franz, 2000 given for 2σ.

The other ages from the contact aureole provide ages consistent with greenschist metamorphism because the intensity of contact metamorphism related to the main granite intrusion is not sufficient to reset the Rb/Sr system. S-type granite intrusives were also dated between 15-14 Ma (Altherr et al., 1982; Bröcker & Franz, 1998; Keay, 1998). Moreover, K-Ar analyses of 6 dacitic dikes from the Cycladic blueschist and Upper units yielded an mean age of 11.4 ± 0.4 Ma (Avigad et al., 1998).

Apatite Fission track dating from the main granite body yielded ages of 8.4 to 10.8 Ma (Altherr et al., 1982; Hejl et al., 2002) while in the CBU one age of 13.1 ± 4.4 Ma (Fig. III.9) was obtained (Hejl et al., 2002). Zircon fission track ages range around 10 Ma in the CBU (Ring et al., 2003). Ring et al. (2003) used these results to estimate a cooling rate for the Tinos footwall of at least ~ 60 °C/Myr in agreement with an estimate of Hejl et al. (2002).

III.3.3 Results

Apatite and zircon fission track, apatite (U-Th)/He and hornblende $^{40}\text{Ar}/^{39}\text{Ar}$ ages are listed in Table III.4. Three samples have been collected in the I-type granite (T2 to T4) and one (T5) in the S-type granite located in southwestern part of the main pluton (Fig. III.8). Samples have been collected following the slip direction NE-SW (Patriat & Jolivet, 1998; Aubourg et al., 2000) (Fig. III.8).

Table III.4. Tinos fission-track and U-Th/He data

Sample reference (rock type)	Lat. Long	Elevation (m)	Distance in slip direction (km)	Mineral	Number of crystals	P χ^2 (%)	FT age (Ma)	Mean track length (μm)	StD (μm)	Number of tracks measured	F $_T$	Helium age (Ma)	% of argon released	$^{40}\text{Ar}/^{39}\text{Ar}$ age (Ma)	
T2 (granodiorite)	37°36'39" 25°14'08"	0	0.76 \pm 0.08	apatite	30	97.1	11.9 \pm 2.0	14.75 \pm 0.32	1.19	58	0.69	10.0 \pm 0.6			
				zircon	11	83.3	12.2 \pm 1.0								
T3 (granodiorite)	37°36'19" 25°12'17"	340	2.98 \pm 0.3	apatite	21	98.4	12.6 \pm 2.6	14.21 \pm 0.38	1.14	37	0.66	10.4 \pm 0.8			
				zircon	13	96.8	13.3 \pm 0.8								
				amphibole										77.9	13.7 \pm 0.7
T4 (granodiorite)	37°35'46" 25°11'45"	465	4.22 \pm 0.4	apatite	23	63.8	12.8 \pm 2.4				0.68	11.9 \pm 1.0			
				zircon	15	96.2	13.8 \pm 1.0								
				amphibole										48.5	14.4 \pm 0.8
T5 (S-type granite)	37°34'35" 25°09'39"	300	6.60 \pm 0.7	zircon	12	100	14.4 \pm 1.2								

Apatite and zircon FT ages have been calculated using a zeta factors of 127.3 ± 4.4 and 332.9 ± 9.7 determined by multiple analyses of standards following the recommendations of Hurford (1990). Central ages are reported. All data are given for 2σ error level.

ZFT ages range between 14.4 ± 1.2 Ma and 12.2 ± 1 Ma and AFT ages from 12.8 ± 2.4 Ma to 11.9 ± 2 Ma. Apatite (U-Th)/He ages range from 11.9 ± 1 Ma to 10.0 ± 0.6 Ma. Apatite mean track lengths are 14.75 ± 0.32 μm and 14.21 ± 0.38 μm for T2 and T3. The ages obtained from each of the three methods gave internally consistent results that generally decrease in the direction of top-to-the NE hangingwall transport on Tinos.

$^{40}\text{Ar}/^{39}\text{Ar}$ method has been applied on the sample T3 and T4 from the I-type granite. For each sample, one amphibole grain was analysed using laser probe step-heating (see chapter I). Hornblende T3 exhibits a flat age spectrum for a large percentage of the argon released (~ 78 %), with a corresponding plateau age of 13.7 ± 0.7 Ma (Fig. III.10a). The second sample T4 gives a plateau age of 14.4 ± 0.8 Ma for ~ 49 % of the argon released (Fig. III.10b). The first heating increments of both samples have older ages correlated with low Ca/K ratios, indicating contribution probably of some tiny mica inclusions that could have trapped excess argon (Fig. III.10). The isochron correlation plots do not give more precise information than the age spectra due to a relative scattering of the data points (see appendix 3).

The hornblende $^{40}\text{Ar}/^{39}\text{Ar}$ and ZFT ages relate the rapid cooling of the I-type granite from ~ 550 °C to ~ 300 °C within < 1 Ma. The ZFT and AFT ages from the three samples in the I-type

granite, overlap within error and together with the long apatite track-length data ($> 14\mu\text{m}$) support very rapid cooling from $\sim 300^\circ\text{C}$ to $\sim 120^\circ\text{C}$ within ≤ 1 Ma (Fig. III.11). The (U-Th)/He ages from the granodiorite are between 11.9 ± 1 Ma to 10 ± 0.6 Ma. The difference in age between the AFT data and apatite (U-Th)/He ages relates to a fall in cooling rate between the base of the AFT PAZ ($\sim 110^\circ\text{C}$) and the base of the He PRZ ($\sim 80^\circ\text{C}$) (Fig. III.11). Overall, the data indicate rapid cooling of the I-type granite of Tinos at minimum $\sim 109^\circ\text{C}/\text{Myr}$ between ~ 15 - 10 Ma (from $\sim 550^\circ\text{C}$ to $\sim 80^\circ\text{C}$) while this minimum cooling rate is $\sim 57^\circ\text{C}/\text{Myr}$ between ~ 14 - 10 Ma (from $\sim 300^\circ\text{C}$ to 80°C) (Fig. III.11).

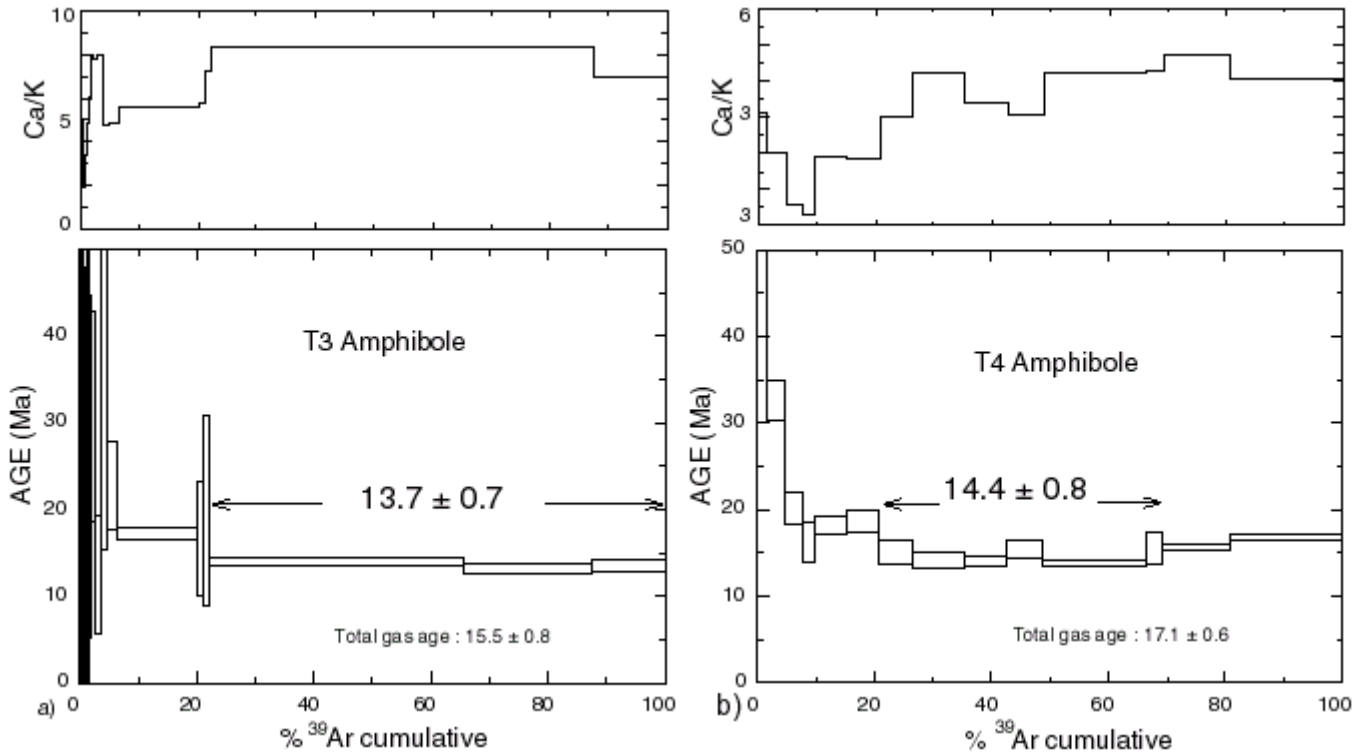


Fig. III.10 $^{40}\text{Ar}/^{39}\text{Ar}$ ages spectra and Ca/K ratio evolution of amphiboles from the I-type granite of Tinos. (a) T3 Plateau age of 13.7 ± 0.7 Ma. (b) T4 plateau age of 14.4 ± 0.8 Ma. Ages are given at 2σ error level.

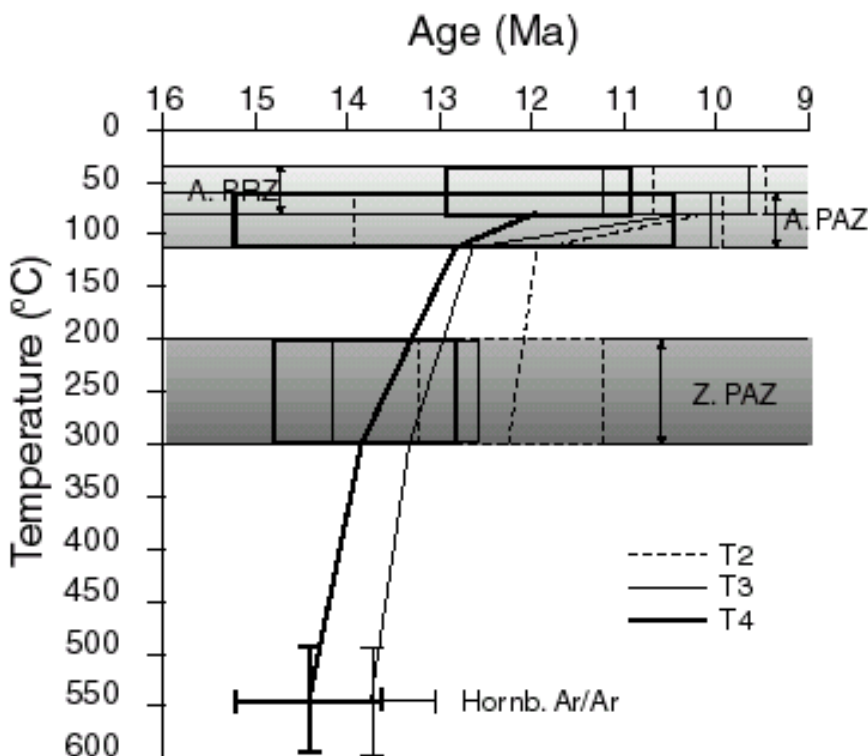


Fig. III.11 Temperature/time evolution for samples (T2, T3 and T4) from the Tinos granodiorite, from the hornblende $^{40}\text{Ar}/^{39}\text{Ar}$ closure temperature (Hornb. Ar/Ar), across zircon and apatite fission-track partial annealing zones (Z. PAZ and A. PAZ) and apatite partial retention zone for (U-Th)/He system (A. PRZ); boxes represent uncertainties on ages and temperatures (2σ); lines represents cooling path for each samples.

III.3.4 Discussion

The decrease of cooling ages parallel to the northeastward slip direction of the hangingwall allows minimum slip rates to be calculated for the Tinos detachment. The results give slip rates of 2.5 ± 0.2 km/Myr (ZFT), 3.7 ± 1.5 km/Myr (AFT) and 2.3 ± 0.2 km/Myr (apatite (U-Th)/He) (Fig. III.12). The slip rate for the Tinos detachment remained fairly constant at ~ 3 km/Myr between $\sim 300^\circ\text{C}$ to 80°C (see section I.5). A minimum displacement calculation for the brittle part of Tinos extensional fault resulted in ~ 12 km offset between ~ 14 -10 Ma.

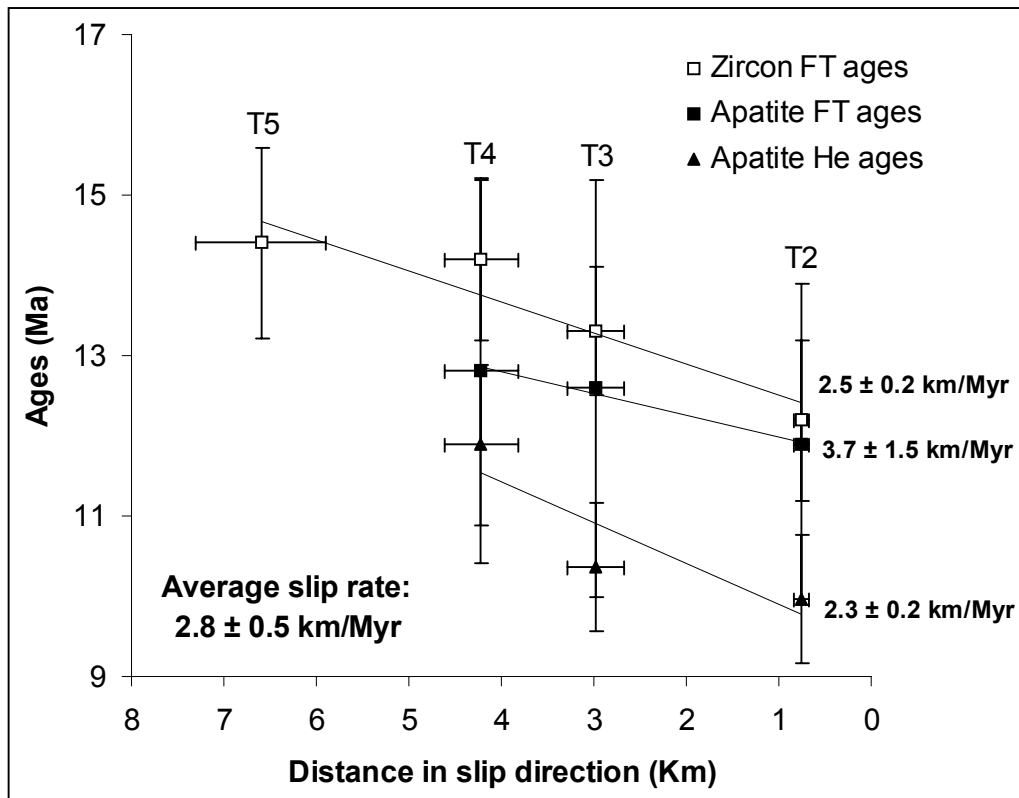


Fig. III.12 Plot of zircon fission-track (ZFT), apatite fission-track (AFT) and apatite (U-Th)/He ages (2σ) against distance in slip direction (2σ) for the Tinos extensional system; estimated minimum slip rates are 2.5 ± 0.2 km/Myr (ZFT), 3.7 ± 1.5 km/Myr (AFT) and 2.3 ± 0.2 km/Myr (apatite (U-Th)/He). The minimum average slip rate for this detachment is 2.8 ± 0.5 km/Myr (2σ).

The estimation of the slip rate and consequently the offset of the Tinos detachment are smaller than the previous estimation of ~ 6.5 km/Myr for the slip rate and ~ 20 km for the offset between ~ 12 -9 Ma proposed by Ring et al. (2003) for the Vari detachment. It was assumed that the detachment expose on Tinos is the same as on Syros and therefore, they used data from the both islands. This implies a large distance for the estimation of the slip rate and consequently increases the error on the calculation. Nevertheless, this new data indicate that the Vari detachment operated when the Tinos detachment was still active and that the slip rate seems to be faster on the Vari detachment than on the Tinos detachment.

The $^{40}\text{Ar}/^{39}\text{Ar}$ ages define a minimum age of ~ 15 Ma for emplacement of the I-type granite of Tinos in agreement with the previous dating carried out on this pluton (see section III.3.2; Altherr et al., 1982; Avigad et al., 1998; Bröcker & Franz, 2000). Moreover, the age of the T4 sample is significantly older than the age of the T3 sample. These ages increase in the direction of footwall slip indicating that the Tinos extensional system was active at ~ 15 Ma. Therefore, the Tinos extensional system promoted granite exhumation (syntectonic granite) and causing fast tectonically-controlled cooling. The estimation of the minimum slip rate from these ages is 1.8 ± 0.4 km/Myr. This is probably slightly underestimated owing to the high closure temperature of the hornblende

$^{40}\text{Ar}/^{39}\text{Ar}$ system and poorly constrained trend based on only two dating (Fig. III.13) (Ketcham, 1996; see Introduction).

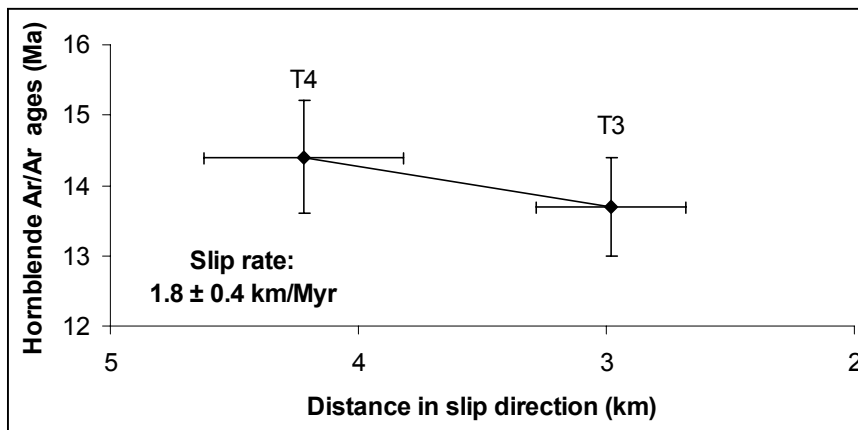


Fig. III.13 Plot of hornblende $^{40}\text{Ar}/^{39}\text{Ar}$ ages (2σ) against distance in slip direction (2σ) for Tinos extensional system; estimated minimum slip rate is 1.8 ± 0.4 km/Myr (2σ).

III.4 Mykonos

III.4.1 Geological setting

Mykonos is dominated by an I-type monzogranite intruded into marble, metapelite and metabasite of Cycladic blueschist unit. A low-angle normal fault dipping about 30° NE cuts the top of the monzogranite in the northern part of the island (Fig. III.14) (Avigad and Garfunkel, 1991; Faure et al., 1991; Lee and Lister, 1992). The hanging wall comprises rare blocks of Permo-Triassic limestones and relics of the Upper unit (tectono-sedimentary unit), essentially composed of conglomerates and sandstone (Sánchez-Gómez et al., 2002). The footwall granite exhibits a thick zone of mylonitization with top-to-the-ENE sense of shear, which is overprinted by brecciation and cataclasis close to the contact (Lee & Lister, 1992).

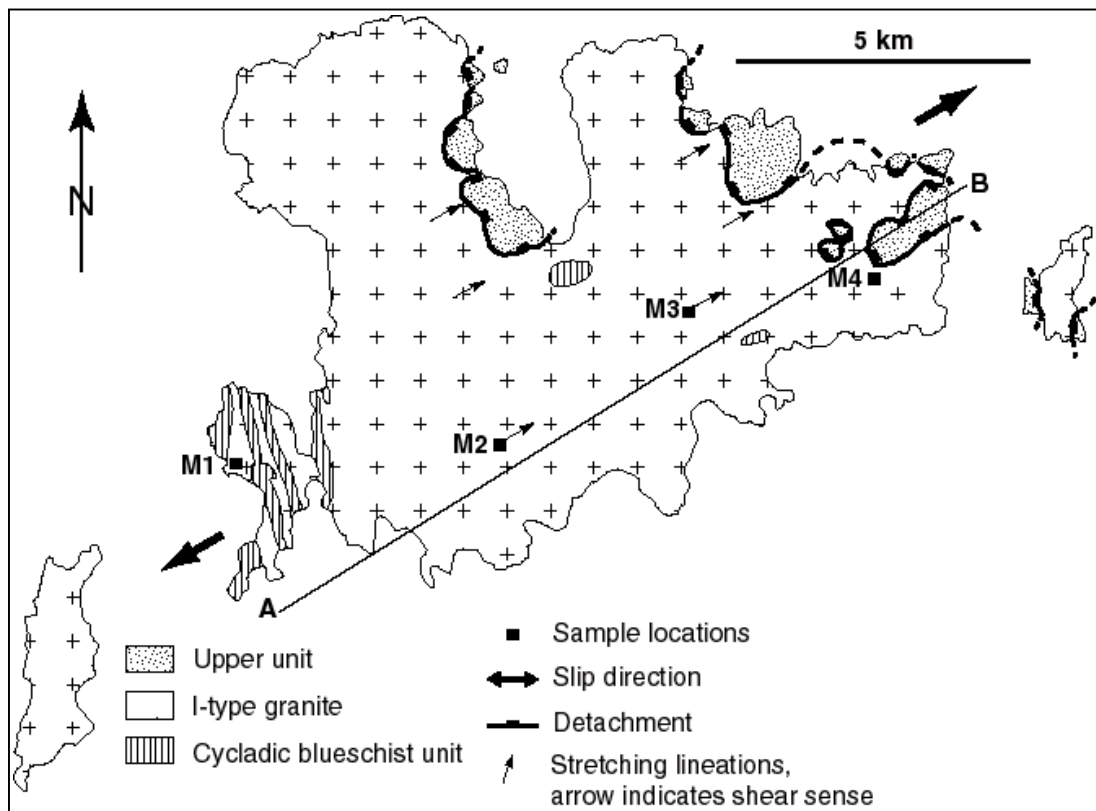


Fig. III.14 (a) Simplified geologic map of Mykonos Island (modified from Altherr et al., 1982 and Sánchez-Gómez et al., 2002) with sample locations.

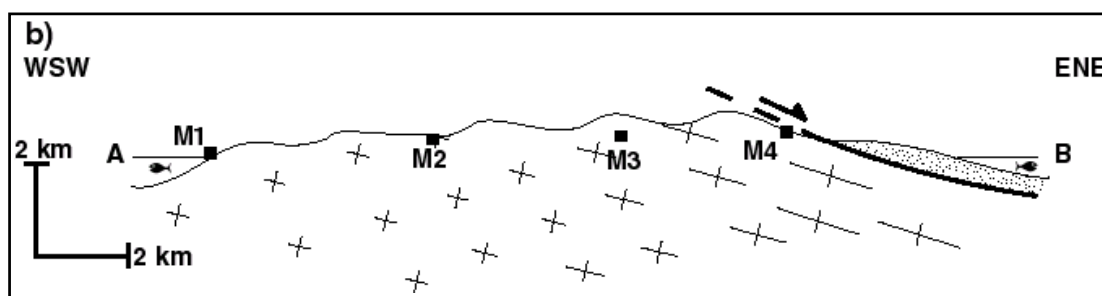


Fig. III.14 (b) WSW-ENE cross section (modified from Faure et al., 1991); sample locations are indicated.

III.4.2 Previous geochronological data

Two samples from the granite have been dated by Altherr et al. (1982) using the K-Ar method on hornblende and gave ages of 12 ± 0.3 Ma and 10.7 Ma without any specific pattern of the ages relative to the slip direction. The second age is defined on a sample where the hornblende was not pure (biotite inclusions) which can explain the younger cooling age. Consequently Altherr et al. supposed that the minimum age for the emplacement of this granite is ~ 12 Ma. Biotite ages using K-Ar and Rb/Sr methods from the granite range from 10.5 Ma to 10.1 Ma and are interpreted as cooling ages. Hornblende from amphibolite gave ages of 14.2 ± 0.3 Ma, 13.7 ± 0.4 Ma and 10.9 ± 0.3 Ma. The last age has been defined on a strongly deformed sample. The deformation could cause partial outgassing of the hornblende. For this reason, Altherr et al. (1982) considered that the cooling age for this amphibolite is around 14 Ma.

Sánchez-Gómez et al. (2002) focused on K-Ar and $^{40}\text{Ar}/^{39}\text{Ar}$ geochronology of minerals in boulders from hangingwall conglomerates (Fig. III.14). Abundant mica from metamorphic clasts yielded cooling ages between 99 ± 1 Ma and 84.7 ± 3 Ma. For Sánchez-Gómez et al. (2002) these clasts probably belong to a vast Pelagonian-type rock mass that covered the internal Hellenides from the Olympos to the central Cyclades (Sánchez-Gómez et al., 2002). One metamorphic clast gave an age of 67.8 ± 1.4 Ma in agreement with the previous ages obtained on other islands for LP-HT metamorphism (M_0) which is recognized in the Upper unit on Ikaria or Tinos for instance (see section III.2.2 and III.3.2) (Patzak et al., 1994; Keay, 1998; Bröcker & Enders, 1999). Biotites from granitic clasts yielded cooling ages from 14.4 ± 0.3 Ma to 10.3 ± 0.3 Ma. These granitic clasts appear at the top of the Upper unit. On Mykonos and Paros, sheared and mylonitic granites appear first followed by undeformed granites in the tectono-sedimentary pile. This sequence of occurrence indicates progressive exhumation of the footwall of a ductile-brittle mid-Miocene detachment. However, Sánchez-Gómez et al. (2002) did not find clasts of I-type granite similar of the type constituting the footwalls of Mykonos. They concluded that the lithology of the granite clasts better fits the S-type granite from Paros or from the core of the metamorphic dome of Naxos (see section III.5 and III.6).

Apatite fission track dating from Altherr et al. (1982) and Hejl et al. (2002) provided ages of 10 to 7.6 Ma for the granite using the grain population method. Associated with track lengths, these ages indicate very rapid cooling exceeding 100 °C/Myr (Hejl et al., 2002).

III.4.3 Results

Four samples have been collected in the monzogranite along a ENE-WSW profile parallel to the tectonic transport direction (Fig. III.14) (Lee & Lister, 1992).

ZFT and AFT ages range respectively from 13 ± 0.8 to 10.7 ± 0.8 Ma and 12.5 ± 2.2 to 10.5 ± 1.8 Ma while apatite (U-Th)/He ages are between 11.1 ± 1 Ma and 8.9 ± 0.8 Ma (Table III.5). Apatite mean track lengths are between 14-15 μm .

Table III.5. Mykonos fission-track and U-Th/He data

Sample reference (rock type)	Lat. Long.	Elevation (m)	Distance in slip direction (km)	Mineral	Number of crystals	P χ^2 (%)	FT age (Ma)	Mean track length (μm)	StD (μm)	Number of tracks measured	F _T	Helium age (Ma)
M1 (granodiorite)	37°25'35" 25°18'04"	10	13.90 ± 1.3	apatite	28	95.3	12.5 ± 2.2				0.67	11.1 ± 1
				zircon	15	94.9	13.0 ± 0.8					
M2 (granodiorite)	37°25'47" 25°21'43"	145	9.80 ± 1.0	apatite	24	89.0	10.6 ± 1.2	14.66 ± 0.18	0.67	62	0.689	9.3 ± 0.8
				zircon	11	90.0	11.6 ± 0.8					
M3 (granodiorite)	37°26'47" 25°23'45"	95	6.20 ± 0.6	apatite	25	97.7	10.5 ± 1.8				0.67	10.5 ± 0.8
				zircon	10	97.4	10.9 ± 1.0					
M4 (granodiorite)	37°27'29" 25°25'46"	140	3.02 ± 0.3	apatite	21	98.9	10.5 ± 1.8	14.28 ± 0.28	1.06	56	0.63	8.9 ± 0.8
				zircon	13	88.2	10.7 ± 0.8					

Apatite and zircon FT ages have been calculated using a zeta factors of 127.3 ± 4.4 and 332.9 ± 9.7 determined by multiple analyses of standards following the recommendations of Hurford (1990). Central ages are reported. All data are given for 2σ error level.

The ages obtained from each of the three methods gave internally consistent results that generally decrease in the direction of hangingwall slip, i.e. ENE (Fig.III.14). The results yielded minimum slip rates of 4.8 ± 0.3 km/Myr (ZFT), 8.6 ± 1.9 km/Myr (AFT) and 7.4 ± 0.6 km/Myr (apatite (U-Th)/He) (Fig. III.15).

ZFT and AFT ages overlap within error and together with the long apatite track-length data ($>14 \mu\text{m}$) support very rapid cooling from $\sim 300^\circ\text{C}$ to $\sim 110^\circ\text{C}$ within ≤ 1 Ma (Fig. III.16). (U-Th)/He ages from the granodiorite range from 8.9 ± 0.8 to 11.1 ± 1 Ma. The difference in age between the AFT data and apatite (U-Th)/He ages relates to a fall in cooling rate between the base of the AFT PAZ ($\sim 110^\circ\text{C}$) and the base of the He PRZ ($\sim 80^\circ\text{C}$) (Fig. III.16). Overall, the data indicate rapid tectonically-controlled cooling of the I-type granite of Mykonos at minimum in average $\sim 75^\circ\text{C}/\text{Myr}$ between ~ 13 -9 Ma (Fig. III.16).

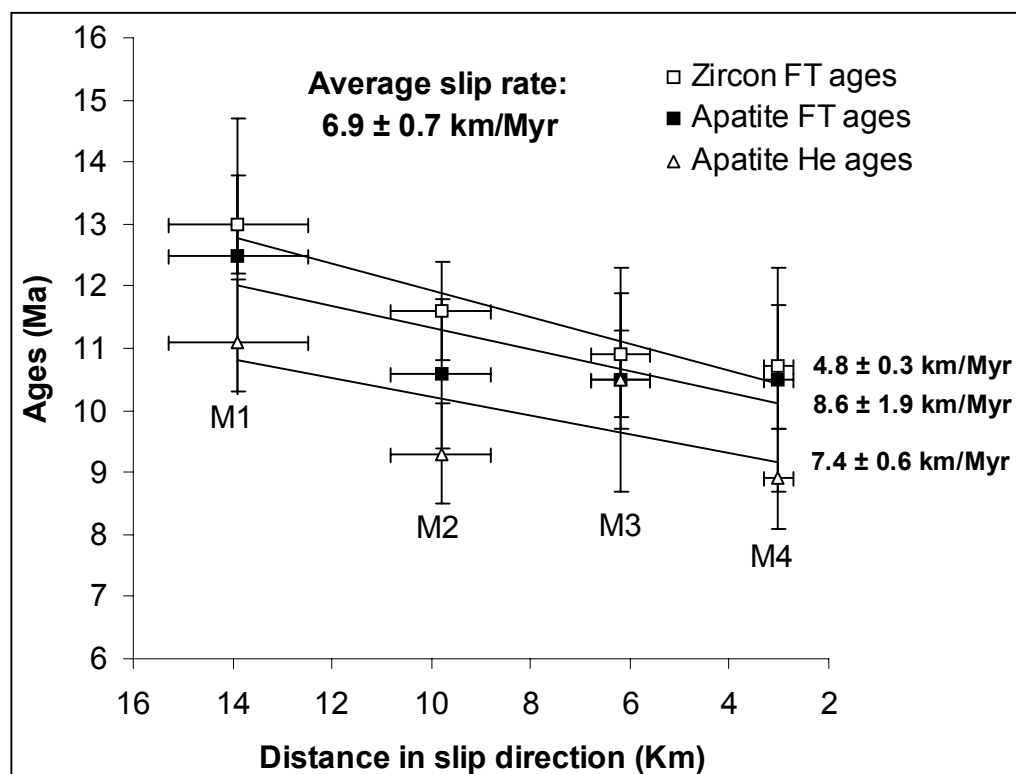


Fig. III.15 Plot of zircon fission-track (ZFT), apatite fission-track (AFT) and apatite (U-Th)/He ages (2σ) against distance in slip direction (2σ) for detachment fault of Mykonos; estimated minimum slip rates are 4.8 ± 0.3 km/Myr (ZFT), 8.6 ± 1.9 km/Myr (AFT) and 7.4 ± 0.6 km/Myr (apatite (U-Th)/He). The minimum average slip rate estimated for this detachment is 6.9 ± 0.7 km/Myr (2σ).

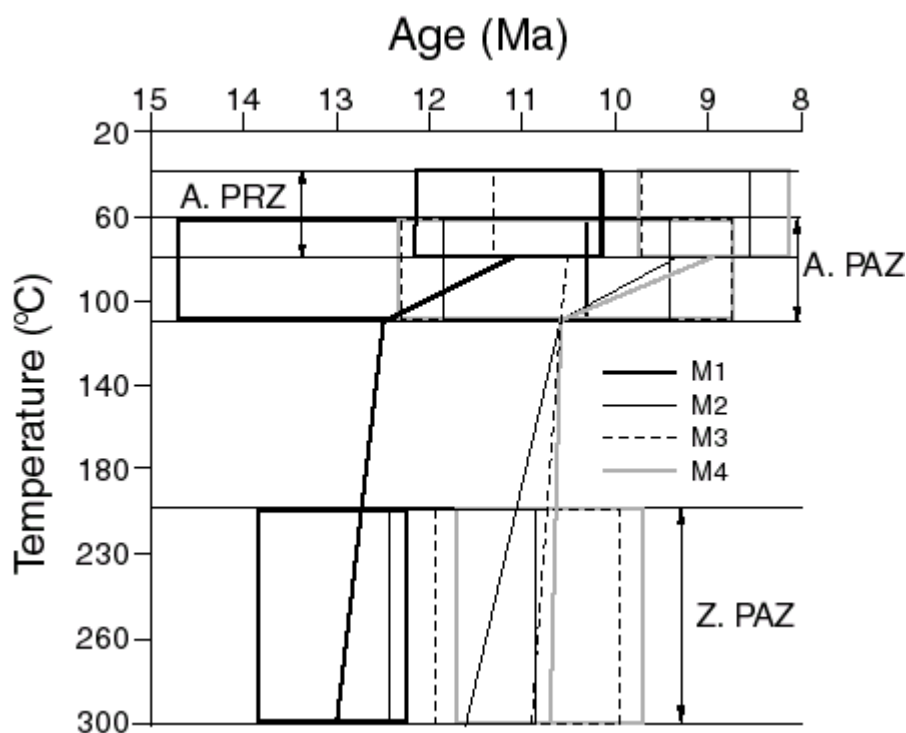


Fig. III.16 Temperature/time evolution for samples (M1, M2, M3 and M4) from the Mykonos monzogranite across zircon and apatite fission-track partial annealing zones (Z. PAZ and A. PAZ) and apatite partial retention zone for (U-Th)/He system (A. PRZ); boxes represent uncertainties on ages and temperatures (2σ); line represents cooling path of each samples.

III.4.4 Discussion

Results show that the average slip rate for the brittle Mykonos extensional fault system is 6.9 ± 0.7 km/Myr between $\sim 300^\circ\text{C}$ to $\sim 80^\circ\text{C}$. A minimum displacement calculation resulted in ~ 28 km of offset on the Mykonos detachment between ~ 13 -9 Ma. This displacement and the dip angle of $\sim 30^\circ$ for the detachment of Mykonos (Avigad and Garfunkel, 1991; Faure et al., 1991; Lee and Lister, 1992) provides a minimum amount of exhumation of 14 km for the footwall of this detachment.

The exhumation in the brittle crust must be due to erosion and normal faulting. To constrain the erosion rate is difficult. Topography above a retreating subduction zone is generally considered to be low (Royden, 1993) and therefore erosion rates were probably small (see section II.1.1). Assumed an erosion rate of maximum 0.65 km/Myr (as estimated by Thomson et al. (1998) for Crete) show that ~ 2.6 km were eroded between ~ 13 -9 Ma. This would suggest that the Mykonos detachment accounted for ~ 11 km of exhumation which is in agreement with the previous estimation made by Ring et al. (2003) for the Vari detachment of Tinos and Kumerics et al. (2004) for the Messaria extensional fault system of Ikaria.

III.5 Naxos

III.5.1 Geological setting

The geology of Naxos Island can be divided into three main units: (1) the Upper non-metamorphic unit; (2) the Cycladic blueschist unit; and (3) a granodiorite massif (Fig. III.17).

The Cycladic blueschist unit (CBU) is intruded by the granodiorite, which produced a contact metamorphic aureole of about 500m from the contact. The very thin and non-metamorphosed Cycladic ophiolite nappe of Permian to Miocene age (Upper unit) overlie the CBU in tectonic contact (Jansen, 1973).

The CBU of Naxos is a metamorphic complex which contains many chemically distinct lithologies (Jansen & Schuiling, 1976). Calcitic and dolomitic marble units predominate, but metapelites are found throughout the sequence, and amphiboles occur in central Naxos. Ultramafic

rocks in lenses are present throughout the metamorphic complex. At low M_2 grade these rocks contain talc, magnesite and actinolite, whereas at high M_2 grade well preserved peridotites are sometimes rimmed by amphibole and mica. The rocks in the migmatite core are separated from the metasedimentary sequence by a semi-continuous horizon of ultramafic rocks. A second horizon of ultramafic rocks is located somewhat higher in the metasedimentary sequence. The marble units within the metasediments contain metamorphosed bauxite lenses, with diaspore in zone I, and corundum in higher grade rocks (Fig. III.18a) (Feenstra, 1985).

The granodiorite adjacent to west coast is coarse grained, with biotite as the dominant mafic mineral, and minor hornblende and pale green pyroxene.

The early glaucophane schist metamorphism, M_1 , in south-east Naxos, reached metamorphic temperatures of 400-480°C and pressures of about 9 kbar (Feenstra, 1985). M_1 mineral assemblages in the mica schists include phengite, glaucophane, paragonite, chlorite, garnet, chloritoid and albite.

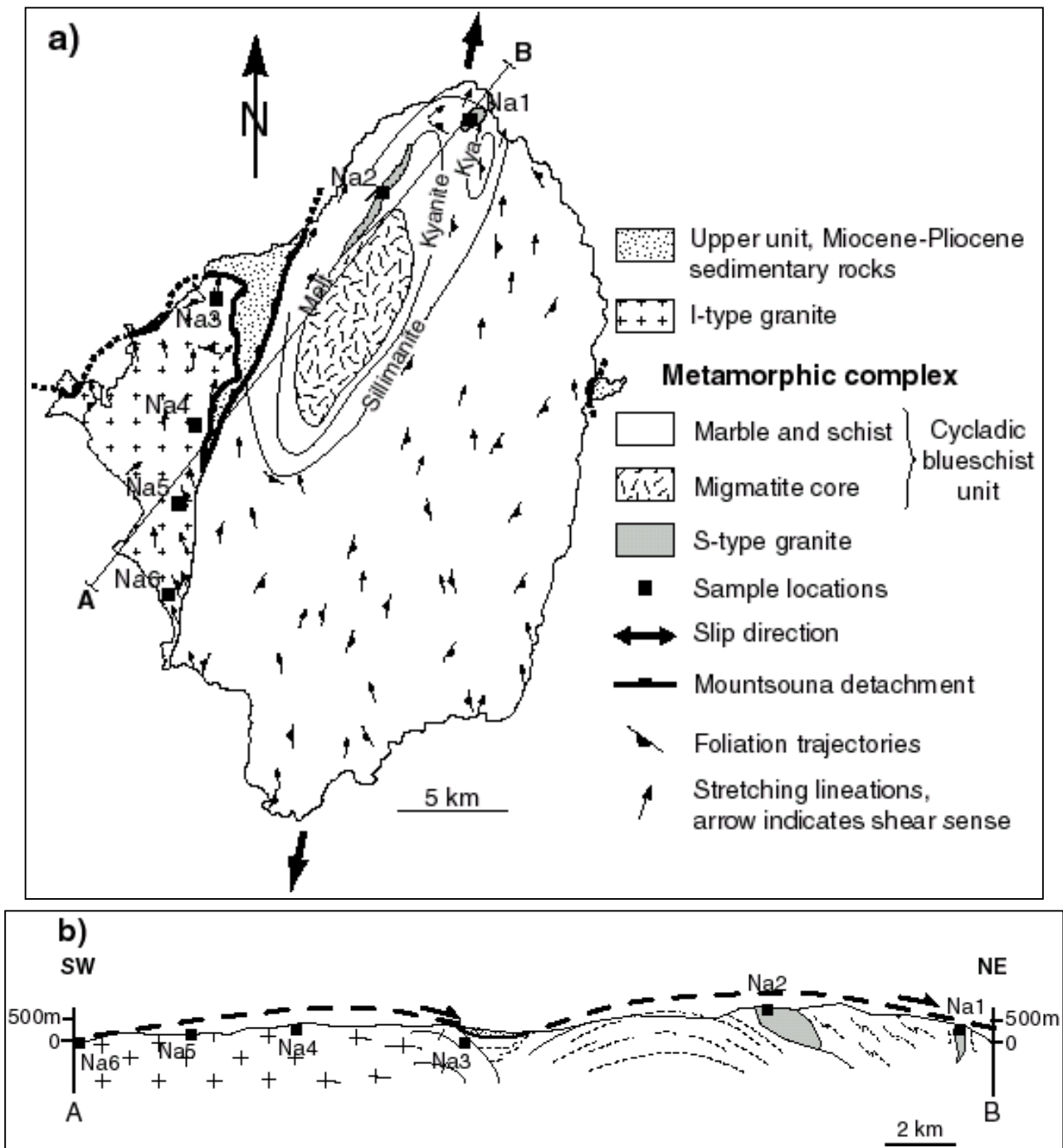


Fig. III.17 (a) Simplified geologic map of Naxos Island and (b) NNE-SSW cross section (modified from Jansen and Schuiling, 1976; Wijbrans and MacDougall, 1988; Buick, 1991; Gautier et al., 1993); sample locations are indicated.

In contrast to most other Cycladic islands, the Miocene Barrovian-type metamorphism reached anatectic conditions on Naxos ($670\pm 50^\circ\text{C}$ and 5-7 kbar) (Jansen and Schuiling, 1976; Buick and Holland, 1989) and created an onion-shaped migmatite dome in the central part of the island. Barrovian-type metamorphism occurred in a fore-arc position (Ring and Layer, 2003). During the waning stages of migmatization a number of S-type granites intruded the northern part of the island between 15 and 11 Ma (Keay et al., 2001). High-temperature metamorphism and intrusion of the S-type granites was synchronous with ductile extensional deformation in the >1 km thick, shallowly dipping Mountsouna shear zone (Lister and Forster, 1996), which is the ductile expression of the Mountsouna extensional fault system. Buick and Holland (1989) argued that high-temperature metamorphism developed during ductile shearing. Hence, extensional shearing started at or before the peak of high temperature metamorphism dated at 20-16 Ma (Wijbrans and McDougall, 1988) when the crust on Naxos was weak. The broad ductile shear zone grades tectonically upward into the narrow (~ 20 -30 m thick) brittle Mountsouna detachment, the latter of which is interpreted as the upper crustal expression of the Mountsouna extensional fault system (Buick, 1991; John and Howard, 1995). At ~ 14 -12 Ma, a huge granodiorite body intruded the western part of Naxos island (Andriessen et al., 1979). This granodiorite is part of the Late Miocene magmatic arc of the southward retreating Hellenic subduction zone and intruded synkinematically into the footwall of the brittle Mountsouna extensional fault system (Buick, 1991). Numerous pseudotachilytes associated with the brittle Mountsouna extensional fault system formed in the granodiorite (Lister and Forster, 1996) and one sample yielded a K/Ar age of 9.9 ± 0.4 Ma (Andriessen et al., 1979). Pronounced hydrothermal activity of overpressured fluids at the brittle Mountsouna extensional fault system is indicated by metasomatic fronts, cinder cones, drusy quartz fillings on pervasive crack systems, opaline quartz as well as iron and sulphur staining (Lister and Forster, 1996). Due to late-stage folding about N-S axes, the Mountsouna extensional fault system has an arched architecture and crops out only at the western and eastern limits of Naxos Island. Kinematic indicators show a consistent top-NNE sense of shear for the Mountsouna extensional fault system (Buick, 1991; Gautier et al., 1993). NNE-SSW extension caused the elongation of the migmatite dome.

III.5.2 Previous geochronological data

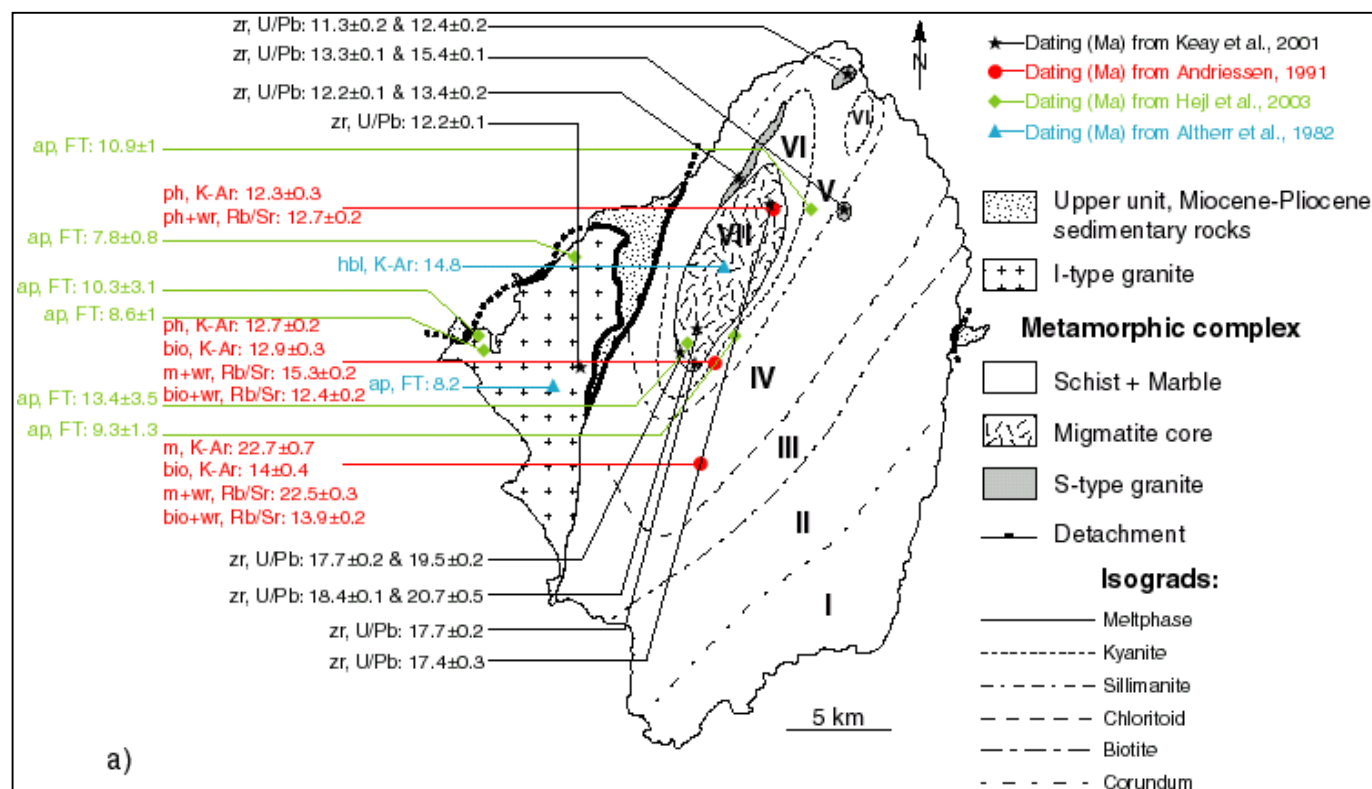
A lot of dating has been carried out on the Naxos Island (Fig. III.18). Particularly, Andriessen et al. (1979) and Wijbrans & McDougall (1988) provide a geochronological framework for the Alpine events of metamorphism and granitic magmatism on Naxos. They constrain the oldest phase of high-pressure/medium-temperature metamorphism (M_1) preserved in some relics in the SE part of the island (zone I, Fig. III.18) at 45 ± 5 Ma (Middle Eocene). In central Naxos, M_1 phase has been erased by a younger metamorphism (M_2) which is associated with development of a thermal dome. Most data from the lower grade (M_{2a}) part range around 25 ± 5 Ma (zones II and III, Fig. III.18) while for the high grade (M_{2b}) the ages are 15 ± 5 Ma (zones IV to VII, fig. III.18) (Altherr et al., 1982; Andriessen et al., 1979; Wijbrans & McDougall, 1988; Andriessen, 1991; Keay et al., 2001).

Using the K/Ar and $^{40}\text{Ar}/^{39}\text{Ar}$ ages on biotite, white mica and hornblende from sample collected mainly in the metamorphic complex (Fig. 17 and Fig. 18a), by Andriessen et al. (1979), Wijbrans and McDougall (1986, 1988) and Andriessen (1991), John and Howard (1995) showed that the ages systematically increase southwards in the direction of footwall transport of the MEFS. Therefore, John and Howard (1995) estimated slip rates of 5.1 ± 0.6 km/Myr (K/Ar on biotite), 7.6 ± 2.8 km/Myr (K/Ar on white mica) and 4.7 ± 2.5 km/ Myr ($^{40}\text{Ar}/^{39}\text{Ar}$ on hornblende). They only used ages <16 Ma for their calculations since they argued that only ages <16 Ma can be safely related to movement on the Mountsouna extensional fault system. Importantly, their data only constrain the slip rate of the ductile shear zone of the Mountsouna extensional fault system.

The main period of magmatic activity (granodiorite intrusive on the west coast of Naxos) is dated between 14-12 Ma (Wijbrans & McDougall, 1988; Keay et al., 2001). Rb/Sr whole rock isochron age of 11.1 ± 0.7 Ma reported by Andriessen et al. (1979) is a minimum age estimate,

because the slope of this isochron is controlled by analyses of late pegmatites and aplites. S-type granite intrusives were dated by Keay et al. (2001) using SHRIMP U/Pb zircon method and range in age from 15.4 ± 0.1 Ma to 11.3 ± 0.2 Ma.

Some apatite fission track dating was performed by the grain population technique (Wagner, 1968; Gleadow, 1981; Wagner & Van Der Haute, 1992) and provide ages from 10.3 Ma to 8.2 Ma for the granodiorite (Altherr et al., 1982; Hejl et al., 2003) and from 13.4 ± 3.5 Ma to 9.3 ± 1.3 Ma for the high grade metamorphic rocks (Hejl et al., 2003). Hejl et al. deduced from these data and track lengths investigation rapid cooling in the Middle/Late Miocene at maximum rates of $130^\circ\text{C}/\text{Myr}$.



Zone	Method	Andriessen et al., 1979	Method	Wijbrans & McDougall, 1988
I	K-Ar	wm: 32.2±0.9 to 48.3±1.5 (12)	K-Ar	wm: 38.5±0.4 to 48.6±0.5 (8)
II	K-Ar K-Ar	m: 32.5±1 to 46.7±1.5 (6)	K-Ar K-Ar	wm: 24.3±0.4 to 38.6±0.4 (7) bio: 10.9±0.1 (1)
III	K-Ar K-Ar K-Ar	hbl: 21.3±0.6 (1) m: 19.1±0.6 & 29.3±0.6 (2)	K-Ar K-Ar K-Ar	hbl: 50.7±0.6 & 31.6±0.4 (2) wm: 20.7±0.2 to 27.8±0.3 (5) bio: 12.5±0.1 (1)
IV	K-Ar K-Ar K-Ar K-Ar	hbl: ~15.4 (3) m: 10.2±0.2 to 15.2±0.5 (7) bio: 10.8±0.3 to 12.7±0.4 (6) trm: 13.6±0.3 to 17.9±1.8 (4)	K-Ar K-Ar K-Ar K-Ar	hbl: 15.9±0.8 to 17.5±0.3 (3) wm: 12.8±0.1 to 19.4±0.3 (4) bio: 10.1±0.1 to 10.6±0.1 (3)
V	K-Ar K-Ar K-Ar	hbl: 9.4±1 to 15.9±0.6 (5) bio: 9.7±0.3 to 12.2±0.4 (4)	K-Ar K-Ar K-Ar	hbl: 12.7±0.1 to 15.5±0.2 (5) m: 13.1±0.1 (1) bio: 10.7±0.1 (1)
VI	K-Ar K-Ar K-Ar	hbl: 54±1.6 (1) m: 11.6±0.4 & 12.7±0.4 (2) bio: 11.3±0.3 (1)		
VII	K-Ar K-Ar K-Ar	hbl: 18.8±0.6 (1) m: 11.4±0.3 & 12.1±0.4 (2) bio: 5.7±0.2 to 11.9±0.4 (4)	K-Ar K-Ar K-Ar	hbl: 16±0.2 (1) m: 11.3±0.1 to 12.2±0.1 (3) bio: 11.1±0.1 & 11.0±0.1 (2)
Granodiorite	Rb/Sr	wr: 11.1±0.7	K-Ar K-Ar	hbl: 12.1±0.2 to 13.6±0.2 (4) bio: 11.2±0.1 & 11.4±0.1 (2)

Fig. III.18 (a) Simplified geological map of Naxos showing isograds (modified from Jansen & Schuiling, 1976) and previous geochronological results. Roman numbers indicate metamorphic zones: I = diaspore; II = chlorite-sericite; III = biotite-chloritoid; IV = kyanite; V = kyanite-sillimanite transition; VI = sillimanite; VII = migmatite. **(b)** Table summarizing dating obtained in the different metamorphic zones (Andriessen et al., 1979; Wijbrans & McDougall, 1988). Numbers in brackets=Numbers of dating done.

Abbreviations: FT = Fission Track; hbl = hornblende; wm = white micas; m = muscovite; bio = biotite; ph = phengite; wr = whole rock; ap = apatite; zr = zircon. All ages are in millions of years and given for 1σ error level.

III.5.3 Results

To obtain slip rates for the brittle Mountsouna extensional fault system, six samples were collected from granitic rocks in the footwall of the Mountsouna extensional fault system along a NNE-SSW profile parallel to the tectonic transport direction of the Mountsouna extensional fault system (Fig. III.17).

Apatite and zircon fission track and apatite (U-Th)/He ages are quoted to the 2σ level (Table III.6). ZFT ages range between 11.8 ± 0.8 Ma and 9.7 ± 0.8 Ma and AFT ages from 11.2 ± 1.6 Ma to 8.2 ± 1.2 Ma. Apatite mean track lengths are between 14-15 μm . Apatite (U-Th)/He ages range from 10.7 ± 1 Ma to 8.9 ± 0.6 Ma.

Table III.6. Naxos fission-track and U-Th/He data

Sample reference (rock type)	Lat. Long.	Elevation (m)	Distance in slip direction (km)	Mineral	Number of crystals	$P\chi^2$ (%)	FT age (Ma)	Mean track length (μm)	StD (μm)	Number of tracks measured	F_T	Helium age (Ma)
Na 1 (S-type granite)	37°11'19" 25°32'25"	30	1.40 ± 0.1	apatite	20	38.1	8.2 ± 1.2					
Na 2 (S-type granite)	37°09'54" 25°29'44"	175	5.33 ± 0.5	apatite	11	90.1	8.7 ± 2.6	14.53 ± 0.42	1.21	32		
Na 3 (I-type granite)	37°07'12" 25°24'46"	70	11.44 ± 1.1	apatite	17	94.0	9.3 ± 2.6	14.71 ± 0.46	1.13	25	0.667	8.9 ± 0.6
				zircon	14	63.6	9.7 ± 0.8					
Na 4 (I-type granite)	37°04'23" 25°24'34"	102	17.33 ± 1.7	apatite	20	96.9	9.8 ± 1.8				0.689	9.1 ± 0.8
				zircon	16	99.4	10.6 ± 0.8					
Na 5 (I-type granite)	37°02'18" 25°23'47"	130	20.77 ± 2.1	apatite	17	67.7	10.7 ± 2.2	14.49 ± 0.38	1.13	36	0.696	9.2 ± 0.8
				zircon	17	99.8	11.1 ± 0.8					
Na 6 (I-type granite)	37°00'24" 25°23'19"	2	25 ± 2.5	apatite	24	73.4	11.2 ± 1.6				0.708	10.7 ± 1.0
				zircon	14	54.2	11.8 ± 0.8					

Apatite and zircon FT ages have been calculated using a zeta factors of 127.3 ± 4.4 and 332.9 ± 9.7 determined by multiple analyses of standards following the recommendations of Hurford (1990). Central ages are reported. All data are given for 2σ error level.

The ages obtained from each of the three methods gave internally consistent results that systematically decrease northwards in the direction of hangingwall slip. The results yielded minimum slip rates for the brittle Mountsouna extensional fault system of 6.5 ± 0.4 km/Myr (ZFT), 8.2 ± 0.5 km/Myr (AFT) and 10.4 ± 0.8 km/Myr (apatite (U-Th)/He) (Fig. III.19).

The ZFT and AFT ages from the four samples collected in the granodiorite overlap within error and together with the long apatite track-length data ($> 14\mu\text{m}$) support very rapid cooling from $\sim 300^\circ\text{C}$ to $\sim 110^\circ\text{C}$ within < 1 Ma (Fig. III.20). The (U-Th)/He ages from the granodiorite range from 8.9 ± 0.6 Ma to 10.7 ± 1 Ma. The difference in age between the AFT data and apatite (U-Th)/He ages relates to a fall in cooling rate between the base of the AFT PAZ ($\sim 110^\circ\text{C}$) and the base of the He PRZ ($\sim 80^\circ\text{C}$) (Fig. III.20). Thus it is likely that the He ages broadly record the time at which rapid major fault movement ended. Overall, the data indicate very rapid tectonically-controlled cooling of the granodiorite at minimum $\sim 108^\circ\text{C}/\text{Myr}$ between ~ 12 -9 Ma (Fig. III.20).

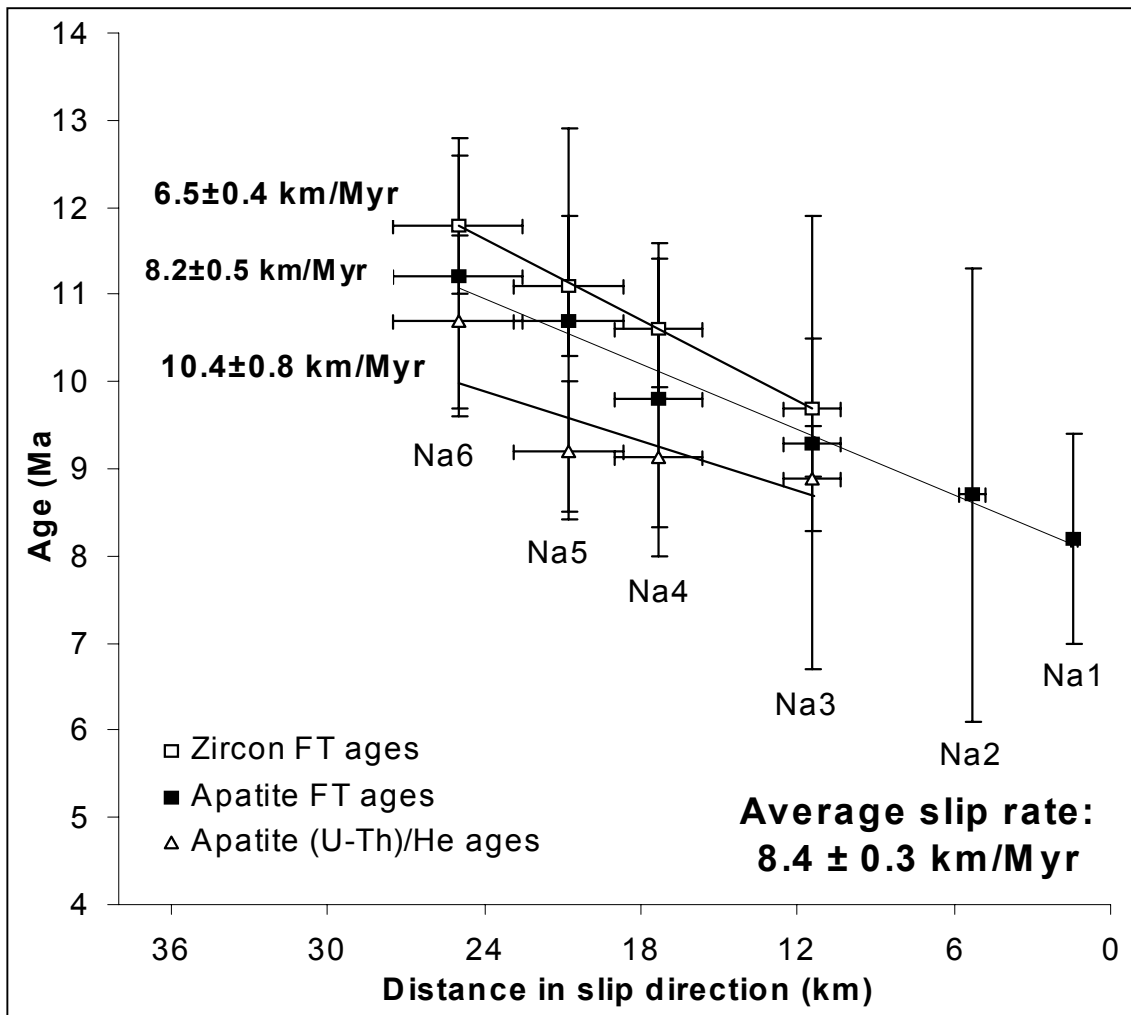


Fig. III.19 Plot of zircon fission-track (ZFT), apatite fission-track (AFT) and apatite (U-Th)/He ages (2σ) against distance in slip direction (2σ) for Mountsoua extensional system; estimated minimum slip rates are 6.5 ± 0.4 km/Myr (ZFT), 8.2 ± 0.5 km/Myr (AFT) and 10.4 ± 0.8 km/Myr (apatite (U-Th)/He). The minimum average slip rate for this detachment is estimated at 8.4 ± 0.3 km/Myr (2σ).

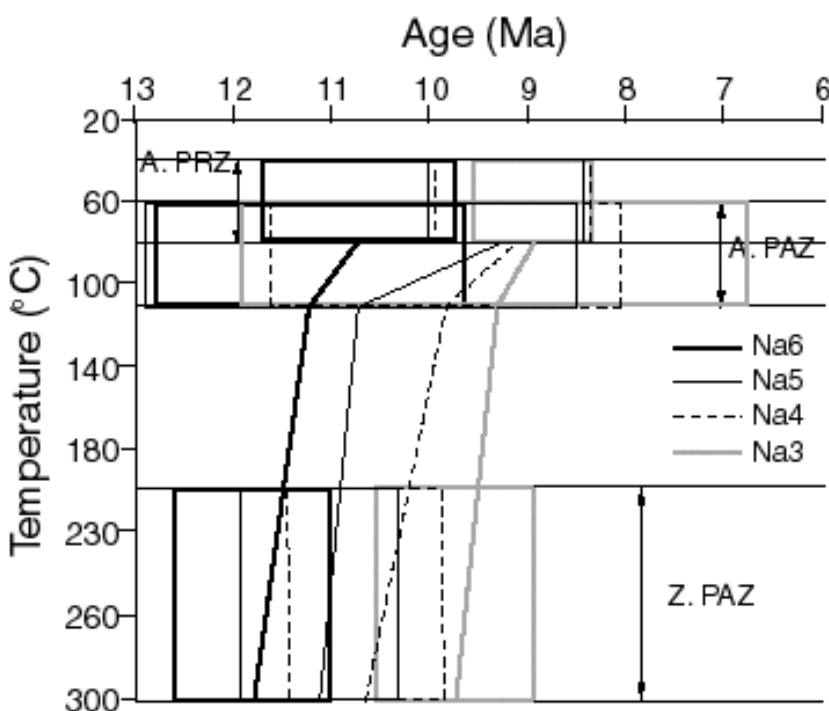


Fig. III.20 Temperature/time evolution for samples (Na3, Na4, Na5 and Na6) from the Naxos granodiorite across zircon and apatite fission-track partial annealing zones and apatite partial retention zone for (U-Th)/He system; boxes represent uncertainties on ages and temperatures (2σ); line represents cooling path of each sample.

III.5.4 Discussion

Our data show that the slip rate for the brittle Mountsouna extensional fault system is around ~9-8 km/Myr from ~300°C to ~40°C. The slip rate estimated by John and Howard (1995) for the ductile Mountsouna extensional fault system is on average 5.8 ± 1 km/Myr and seems to be slightly smaller than the rates recorded for the brittle Mountsouna extensional fault system. However, slip-rate calculations assume that isotherms are unaffected by faulting. What is the significance of the different slip rates reported by John and Howard (1995) for the ductile Mountsouna extensional fault system and those reported by us for the brittle Mountsouna extensional fault system? Two explanations are considered: (1) The average slip rate of ~6 km/Myr calculated using the results reported by John and Howard (1995) significantly underestimates the true slip rate because of pronounced advection of isotherms. If, for simplicity, it is assumed that this rate is underestimated by the maximum amount of 40% given by Ketcham (1996), then the true slip rate would be ~9-8 km/Myr. The problem with this interpretation is that we do not exactly know when ductile shearing commenced. Buick and Holland (1989) and Buick (1991) argued that shearing probably commenced before the peak of high-temperature metamorphism at 20-16 Ma. If so, the isotherms might have already achieved steady-state conditions at ~16 Ma in which case the average slip rate estimated from the data reported by John and Howard (1995) do not seriously underestimate the true slip rate. If the average slip rate is underestimated, it is similar to the average slip rate for the brittle Mountsouna extensional fault system estimated in this study using low-temperature thermochronology. In this case, the slip rate along the Mountsouna extensional fault system on Naxos is constant across the brittle/ductile transition.

(2) The second explanation proposes that there is a slight increase in slip rates across the brittle/ductile transition, although the thickness of the fault zone narrowed considerably. The narrowing of the deforming zone indicates localization of deformation during decreasing temperatures as the Mountsouna extensional fault system was exhumed. I argue that the intrusion of the huge arc-related granodiorite close to the Mountsouna extensional fault system, widespread subsequent formation of frictional melts along the fault surface as evidenced by the numerous pseudotachylites and fluid circulation along the fault surface were the most important factors for increasing the slip rate in the brittle crust. I suggest that the crust on Naxos was weak at the start of extensional faulting and that the intrusion of granodiorite close to the brittle fault zone increased the weakness considerably and accelerated the slip rate as the footwall of the Mountsouna extensional fault system was exhumed and cooled. The succeeding formation of pseudotachylite by frictional melting during seismogenic faulting enhanced slip weakening. The large amount of pseudotachylite beneath the brittle Mountsouna extensional fault system suggests that a molten layer formed along the fault plane with increasing displacement and probably caused a considerable drop in fault strength. Hollister and Crawford (1986) demonstrated the important role of melt lubrication during deformation and argued that weakening of the crust in the presence of melt leads to a drastic increase in deformation rates due to a pronounced drop in strength across zone occupied by melt. Furthermore, the fluids circulating along the fault surface were overpressurized and contributed to fault-zone weakening in the brittle crust.

The data of John and Howard (1995) suggest a minimum average slip rate of ~6 km/Myr in the ductile Mountsouna extensional fault system and my new data imply a minimum average slip rate of ~9-8 km/Myr for the brittle Mountsouna extensional fault system. A minimum displacement calculation for the southern segment of the Mountsouna extensional fault system on Naxos, which yielded the oldest ages, resulted in ~24 km of offset between ~16-12 Ma and ~25 km offset between ~12-9 Ma, giving a minimum total displacement of ~49 km on the Mountsouna extensional fault system. The data suggest, if offset on the Ios detachment is also considered (Fig. II.12 and Fig. III.25), that the thin and non-metamorphosed Cycladic ophiolite nappe in the hangingwall of the Mountsouna extensional fault system is a far-traveled, dismembered extensional nappe that may have been derived from the Island of Crete. The long-lived activity and the high slip rate lends support to the hypothesis that much of the ~250 km of post Oligocene extension in the Aegean Sea was resolved on a few major normal fault systems.

III.6 Paros

III.6.1 Geological setting

On Paros (Fig. III.21), the lowest footwall unit is thought to belong to the Cycladic Blueschist Unit. It comprises gneisses at the bottom, and amphibolite, amphibole schists and thick marbles at the top, all intensively folded and sheared (Gautier and Brun, 1994). S-type granite and pegmatitic dikes intrude the whole Cycladic blueschist unit sequence (Altherr et al., 1982). An upper metamorphic was defined along the southern and western coast (Papanikolaou, 1980) and consists of low-grade metamorphosed diabases, Permian marbles, and phyllites. A low-angle, ductile-to-brittle normal fault is exposed at the top of the Cycladic blueschist unit in the northern part of the island and is usually correlated with the Mountsouna extensional fault system of Naxos (Lee & Lister, 1992; Gautier and Brun, 1994). Kinematic indicators at the fault plane indicate top-to-the NE sense of movement (Lee & Lister, 1990; Gautier and Brun, 1994). The hanging wall (Upper unit) is built up by tectono-sedimentary unit and Pliocene-Recent sediments, as well as an ophiolitic slice covered by Cretaceous limestones (Sánchez-Gómez et al., 2002).

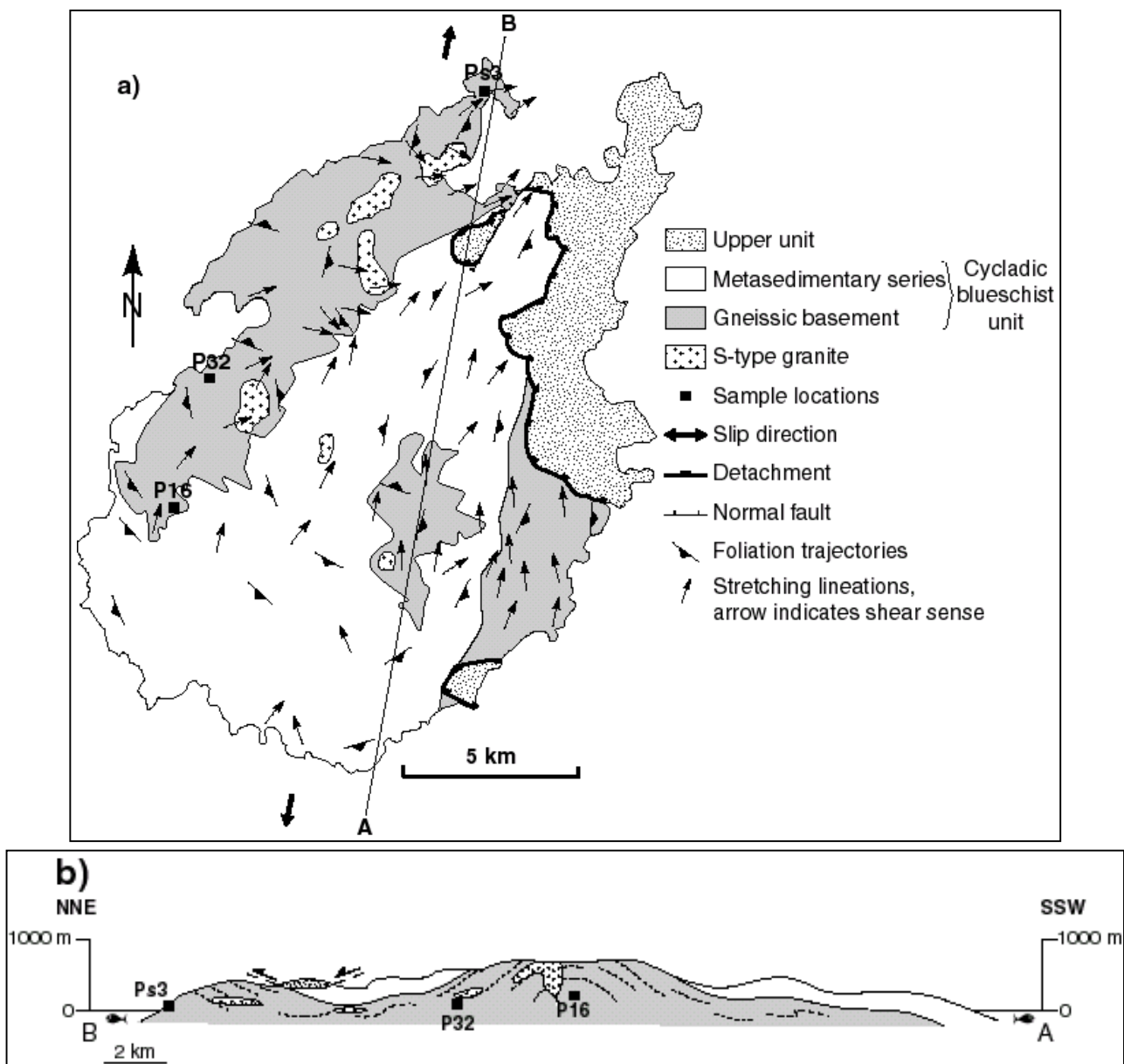


Fig. III.21 (a) Simplified geologic map of Paros Island and (b) NNE-SSW cross section (modified from Jansen, 1973; Papanikolaou, 1980; Gautier et al., 1993); sample locations are indicated.

III.6.2 Previous geochronological data

On Paros, the different events are poorly constrained by geochronology. The main results are provided by Altherr et al. (1982). They obtained cooling ages of 12.4 Ma and 11.5 Ma by K-Ar dating on muscovite and biotite for one of S-type granite intrusions (Fig. III.21). The same authors defined cooling ages around 11 Ma for samples from the paragneiss of the lower unit using the same method. In the metasedimentary series, the ages obtained using the K-Ar on hornblende range around 13 Ma. Baldwin & Lister (1994) provided the same range of cooling ages for the S-type granite (12-10 Ma).

Sánchez-Gómez et al. (2002) carried out the same type of study on Paros than on Mykonos on boulders from hangingwall conglomerates (see section III.4.2). They obtained the same range of ages on mica concentrates from clasts between 99.9 ± 2 Ma to 80.9 ± 1.6 Ma and for biotite concentrate from granite clasts from 11.3 ± 0.3 Ma to 10.9 ± 0.4 Ma. The ages for biotite from S-Type granitic clasts are in agreement with the ages previously defined by Altherr et al. (1982) and Baldwin & Lister (1994). In addition, on Paros, Sánchez-Gómez et al. (2002) have dated, using the whole-rock K/Ar methods, volcanic clasts at ~ 10 Ma. Moreover, a group of mica concentrates from metamorphic clasts yielded ages from 15.7 ± 1 Ma to 13.5 ± 0.3 Ma. For Sánchez-Gómez et al. (2002), these metamorphic clasts possibly represent exhumation of mid-crustal levels. One whole rock K-Ar age at 40.3 ± 0.8 Ma from a metapelite clast is correlated to the HP-LT metamorphism event (M_1) recognized everywhere in the Aegean area.

Two samples from metasedimentary rocks of the lower unit have been dated using the apatite fission track population method (Hejl et al., 2003). The ages are 9.9 ± 1.1 Ma and 9.3 ± 0.6 Ma. Together with track lengths distribution and K-Ar biotite age from Altherr et al. (1982) they estimated a rapid cooling at a rate of 70 °C/Myr between 10 and 8 Ma.

III.6.3 Results

Three samples have been collected in the gneissic basement of the Cycladic blueschist unit following the NE-SW slip direction (Fig. III.21). Only fission track dating have been carried out because of the numerous fluid and zircon inclusions in the apatite which made the handpicking selection difficult for the (U-Th)/He dating (Table III.7).

Table III.7. Paros fission-track data

Sample references (rock type)	Lat. Long.	Elevation (m)	Distance in slip direction (km)	Mineral	Number of crystals	$P\chi^2$ (%)	FT age (Ma)	Mean track length (μm)	StD (μm)	Number of tracks measured
Ps3 (gneiss)	37°08'53" 25°13'20"	10	0.80 \pm 0.08	apatite	17	83.6	10.5 \pm 2.0	14.39 \pm 0.30	0.83	29
				zircon	11	99.7	11.1 \pm 1.0			
P16 (gneiss)	37°03'01" 25°07'50"	15	14.10 \pm 1.4	apatite	17	100	12.7 \pm 2.8	14.73 \pm 0.24	1.03	68
				zircon	7	100	13.1 \pm 1.4			
P32 (gneiss)	37°04'55" 25°08'40"	8	10.18 \pm 1	apatite	19	97.9	12.1 \pm 1.8	14.97 \pm 0.34	1	33
				zircon	8	95.3	12.4 \pm 1.4			

Apatite and zircon FT ages have been calculated using a zeta factors of 127.3 ± 4.4 and 332.9 ± 9.7 determined by multiple analyses of standards following the recommendations of Hurford (1990). Central ages are reported. All data are given for 2σ error level.

Samples from Paros yield ZFT ages from 13.1 ± 1.4 Ma to 11.1 ± 1 Ma while AFT are between 12.7 ± 2.8 Ma and 10.5 ± 2 Ma. Apatite mean track lengths range from 14.39 ± 0.30 μm to 14.97 ± 0.34 μm . The ages obtained from each methods gave internally consistent results that generally decrease in the direction of hangingwall slip (NNE). The results yielded minimum slip rates of 6.8 ± 0.7 km/Myr (ZFT) and 6.0 ± 0.9 km/Myr (AFT) (Fig. III.22). The ZFT and AFT ages overlap within error and together with the long apatite track-length data (>14 μm) support very rapid cooling from $\sim 300^\circ\text{C}$ to $\sim 110^\circ\text{C}$ within <1 Ma. The data indicate very rapid cooling of the gneissic basement between ~ 13 - 10 Ma.

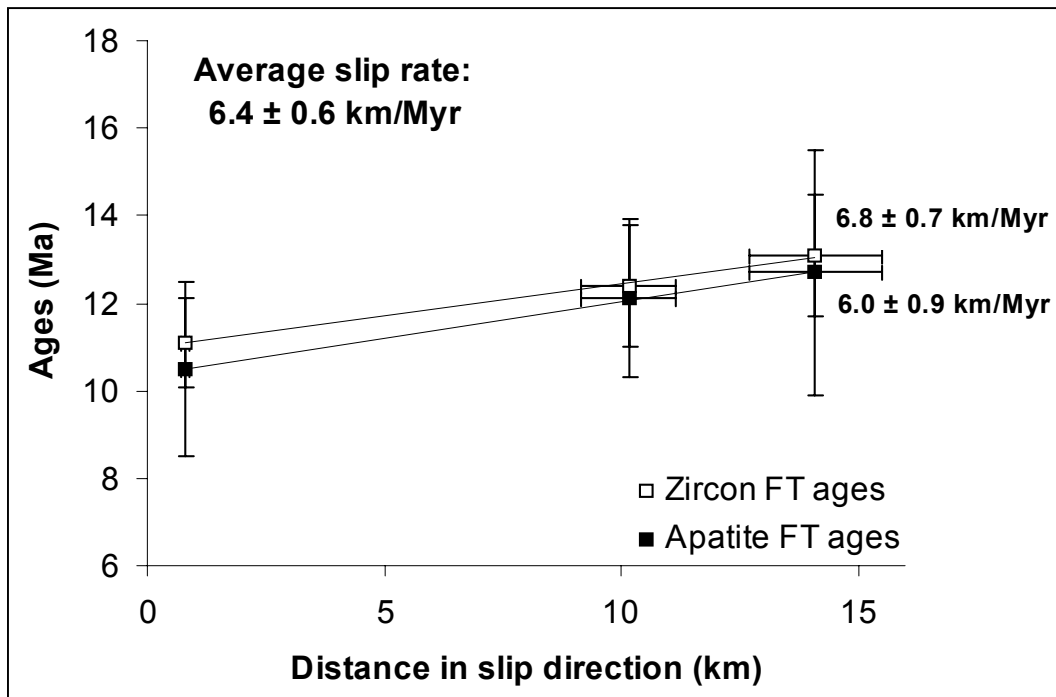


Fig. III.22 Plot of zircon fission-track (ZFT) and apatite fission-track (AFT) ages (2σ) against distance in slip direction (2σ) for the detachment fault of Paros; estimated minimum slip rates are 6.8 ± 0.7 km/Myr (ZFT), 6.0 ± 0.9 km/Myr (AFT). The minimum average slip rate for this detachment is estimated at 6.4 ± 0.6 km/Myr (2σ).

III.6.4 Discussion

The results show that the slip rates estimated for the detachment exposed on Paros remained fairly constant at 6.4 ± 0.6 km/Myr between $\sim 300^\circ\text{C}$ to $\sim 110^\circ\text{C}$ on the period of 13-10 Ma. A minimum displacement calculation for this detachment, resulted in ~ 17 km of offset between ~ 13 - 10 Ma.

Albeit the Paros detachment is usually correlated to the Mountsouna extensional fault system of Naxos (Gautier et al., 1990; Gautier and Brun, 1994), the minimum average slip rate estimated for the Paros detachment is slower than the minimum average slip rate obtained (~ 9 - 8 km/Myr; see section III.5.3 and III.5.4) on the brittle part of the Mountsouna extensional fault system on Naxos. I interpret that the slip rate difference was due to the huge granodiorite intrusion which occurred on Naxos around 14-12 Ma while on Paros only small S-type granites intruded the footwall of the detachment. I suggest that the large scale Naxos/Paros extensional fault system recorded locally faster slip rate owing to huge granodiorite intrusion on Naxos. Furthermore, the data of John and Howard (1995) suggest a minimum average slip rate of ~ 6 km/Myr in the ductile Mountsouna extensional fault system similar to the slip rate estimated for the brittle part of the Naxos/Paros extensional fault system exposed on Paros. Therefore, I argue that on Paros because no huge granite intrusion occurred the slip rate is probably constant across the brittle/ductile transition while on Naxos the intrusion of granodiorite closeness to the brittle fault zone increased the weakness considerably and accelerated the slip rate as the footwall of the Mountsouna extensional fault system was exhumed and cooled.

III.7 Serifos

III.7.1 Geological setting

The I-type granite of Serifos (Fig. III.23) intruded into a series of calc-silicate marbles and calc-mica schist. Blueschist metamorphism of the country rocks is proven by glaucophane relics in the metasediments of the northern-most part of the island (Altherr et al., 1982) and therefore the country rocks of the granite belong to the Cycladic blueschist unit. The southern part of this granitic pluton is foliated and deformed to an ultramylonite while the northern part below the detachment is intrusive to the country rock (Grasemann et al., 2002). To the north, the granodiorite intrusion has created a broad contact metamorphic aureole with skarn formation. Salemink (1980) has mapped four metamorphic isograds from the pluton border outwards: a garnet, scapolite, hornblende and actinolite zone (Fig. III.23). The granodiorite and the country rocks are cut by numerous dykes of dacitic to rhyolitic composition (Altherr et al., 1982).

Kinematic criteria indicate top-to-the S sense of movement for the extensional fault system exposed mainly at the rim of the island (Grasemann et al., 2002). For Grasemann et al. (2002) Serifos represents the footwall of a metamorphic core complex.

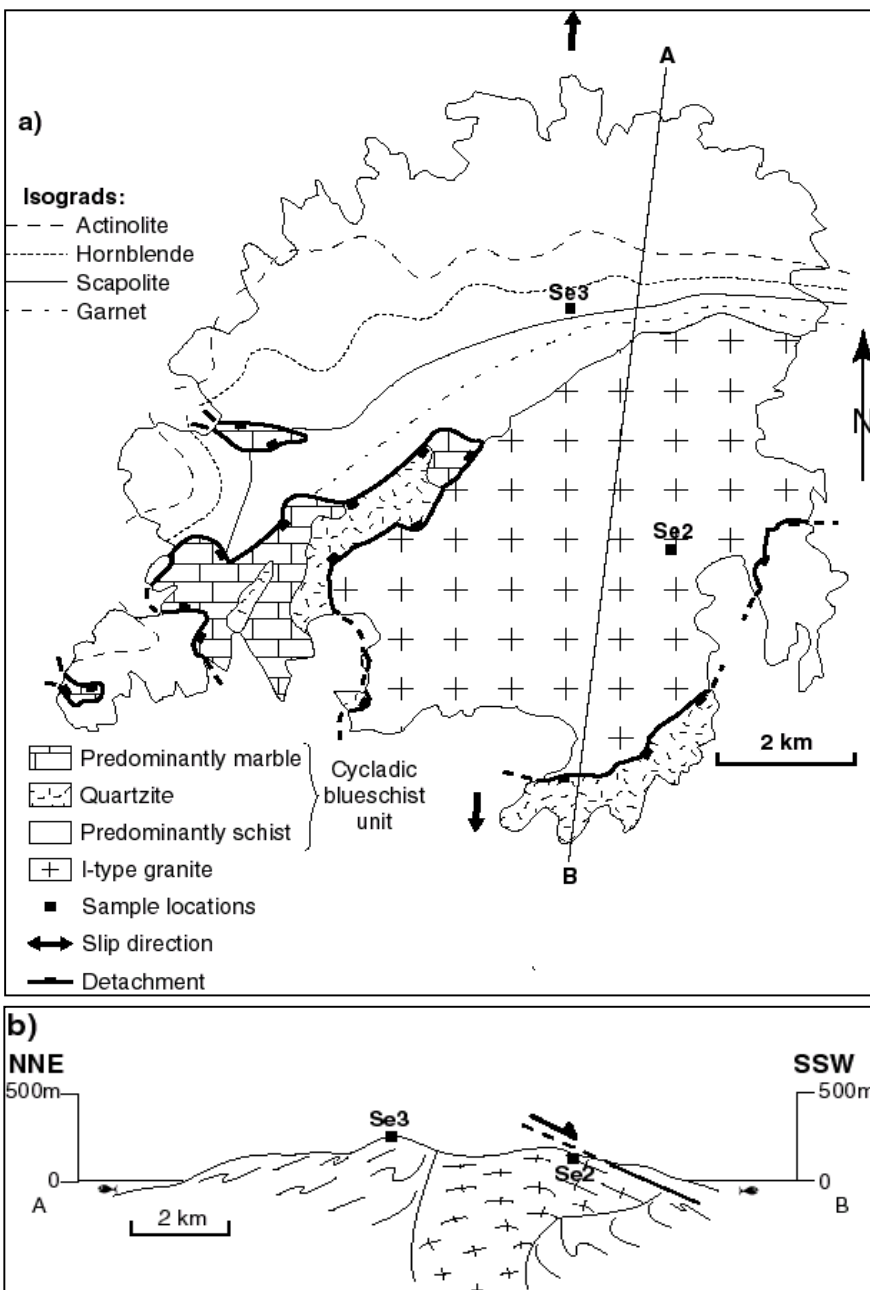


Fig. III.23 (a) Simplified geologic map of Serifos Island and (b) NNE-SSW cross section (modified from Altherr et al., 1982); sample locations are indicated.

III.7.2 Previous geochronological data

On Serifos the main results obtained by Altherr et al. (1982), from the granodiorite, yielded a K-Ar hornblende age of 9.5 ± 0.3 Ma while biotite shows identical K-Ar and Rb/Sr dates of respectively 8.6 ± 0.1 Ma and 8.6 ± 0.2 Ma respectively. One fission track date on apatite provided an age of 8 Ma. Additionally, hornblende and biotite from one rhyodacitic dyke within the metamorphic aureole have been dated. The K-Ar date on hornblende is 8.5 ± 0.2 Ma while biotite gave similar ages at 8.7 ± 0.2 Ma (K-Ar method) and 8.2 ± 0.2 Ma (Rb/Sr method). All these data were interpreted as cooling ages indicating a minimum age of 9.5 Ma for the emplacement of the granodiorite.

K-Ar dates of 29.9 ± 0.5 Ma on phengite and of about 32 Ma on different mixtures of phengite and chlorite have been obtained by Altherr et al. (1982). They interpreted these ages as mixed ages between a supposed Eocene metamorphic event (M_1) and Miocene metamorphic event (M_2) and/or reheating connected with the intrusion of the granodiorite.

Subsequently, Hejl et al. (2003) analysed 4 samples using the apatite fission track method. They obtained ages ranging from 6.7 ± 0.8 Ma to 5.3 ± 0.6 Ma. Associated with track length measurements they estimated a maximum cooling rates of >50 °C/Myr.

III.7.3 Results

Two samples have been dated (Se2 and Se3). Se2 comes from the granodiorite while Se3 is a rhyodacite dyke from the Cycladic blueschist unit in the footwall of the Serifos detachment (Fig. III.23). Zircon fission track analysis has been carried out on the two samples but apatite fission track and (U-Th)/He dating have carried out only on the sample Se2 (Table III.8) due to a lack of apatite.

Table III.8. Serifos fission-track and U-Th/He data

Sample reference (rock type)	Lat. Long.	Elevation (m)	Mineral	Number of crystals	$P\chi^2$ (%)	FT age (Ma)	Mean track length (μm)	StD (μm)	Number of tracks measured	F_T	Helium age (Ma)
Se2 (granite)	37°09'10" 24°30'25"	140	apatite	19	97.7	10.3 ± 2.6	14.95 ± 0.42	1	23	0.7	7.5 ± 0.5
			zircon	9	96.5	11.4 ± 1.0					
Se3 (schist)	37°10'50" 24°29'38"	380	zircon	7	99.2	8.6 ± 1.6					

Apatite and zircon FT ages have been calculated using a zeta factors of 127.3 ± 4.4 and 332.9 ± 9.7 determined by multiple analyses of standards following the recommendations of Hurford (1990). Central ages are reported. All data are given for 2σ error level.

The samples yielded ZFT ages of 11.4 ± 1 Ma (Se2) and 8.6 ± 1.6 Ma (Se3), and an AFT age of 10.3 ± 2.6 Ma with mean track length at 14.95 ± 0.42 μm for Se2. Apatite (U-Th)/He dating yielded an age of 7.5 ± 0.5 Ma. The ages obtained from each methods on the sample Se2 gave internally consistent results. The ZFT (11.4 ± 1 Ma) and AFT (10.3 ± 2.6 Ma) ages overlap within error and together with the long apatite track-length data (~ 15 μm) support very rapid cooling from $\sim 300^\circ\text{C}$ to $\sim 110^\circ\text{C}$ (Fig. III.24). The difference in age between the AFT age (10.3 ± 2.6 Ma) and apatite (U-Th)/He age (7.5 ± 0.5 Ma) relates to a fall in cooling rate between the base of the AFT PAZ ($\sim 110^\circ\text{C}$) and the base of the He PRZ ($\sim 80^\circ\text{C}$) (Fig. III.24). The data indicate rapid cooling of the granodiorite at minimum $\sim 39^\circ\text{C/Myr}$ between ~ 11 -7 Ma (Fig. III.24).

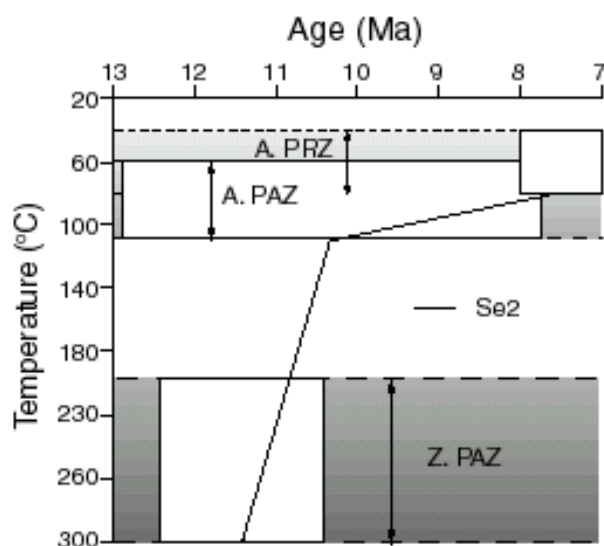


Fig. III.24 Temperature/time evolution for Se2 from the Serifos granodiorite across zircon and apatite fission-track partial annealing zones and apatite partial retention zone for (U-Th)/He system; white boxes represent uncertainties on ages and temperatures (2σ); black line represents cooling path.

III.7.4 Discussion

The ZFT age (8.6 ± 1.6 Ma) obtained on the Se3 sample from rhyodacitic dyke within the metamorphic aureole is interpreted as cooling age. The rapid magmatic cooling calculated for the granodiorite of Serifos at minimum $\sim 39^\circ\text{C}/\text{Myr}$ could not have been controlled by erosion only but cooling is thought to be tectonically controlled. Therefore, this result supports a model of extensional thinning of the crust due to ductile shearing and low-angle normal faulting as the predominant process of plutonic unroofing. Consequently, it is envisaged that the T-t path of the granite reflects a synkinematic intrusion into the extensional fault system of Serifos and its intrusion temperature was higher than temperatures for country rocks. Therefore, the I-type granite had more potential for initially fast cooling, which is reflected by the steep cooling curve between the zircon and apatite PAZ's (Fig. III.24). After fast tectonically-controlled cooling from intrusion temperatures, the I-type granite had a slower cooling history. Furthermore, the ZFT age of 11.4 ± 1 Ma from the I-type granite indicates the minimum age for the detachment faulting of Serifos.

III.8 Ios

III.8.1 Geological setting

The lower plate of the Ios metamorphic core complex consists of strongly deformed granitic gneisses structurally overlain by amphibolite facies garnet-mica schists that together form the pre-Alpine basement of the Cycladic blueschist unit. This basement is tectonically overlain by a marble-schist series comprising metamorphosed Mesozoic carbonate, pelitic, ophiolitic and volcanic rocks which form the upper plate and are correlated with the upper parts of the Cycladic blueschist unit (Fig. III.25 and Fig. II.6) (Jansen and Schuiling, 1976; Dürr et al., 1978; Van Der Maar and Jansen, 1983).

Evidence for a M_0 pre-Alpine (~ 300 Ma) amphibolite facies metamorphism and/or magmatic phase within the Ios basement has been recognized from isotopic data (Henjes-Kunst & Kreuzer, 1982; Baldwin & Lister, 1998). Subsequent Alpine events have almost completely erased other evidence for this M_0 event. The later Alpine metamorphic events are: M_1 , HP-LT metamorphism which resulted in the formation of jadeite, chloritoid and glaucophane (Van Der Maar & Jansen, 1983) and an overprinting M_2 Miocene greenschist facies metamorphism characterised by the growth of chlorite, albite, biotite and garnet (Van Der Maar & Jansen, 1983). Pressure estimates for M_1 are 9-11 kbar, with temperatures ranging from 350 - 400°C (Van Der Maar & Jansen, 1983). M_2 is estimated to have occurred at 5-7 kbar, with temperatures ranging from 380 - 420°C (Van Der

Maar & Jansen, 1983). More recent estimation yield P-T condition at 12.6 ± 0.6 kbar and $475 \pm 25^\circ\text{C}$ for M_1 and ~ 4 kbar and $>400^\circ\text{C}$ for M_2 (Grütter, 1993).

The upper levels of the basement complex on Ios have been intensively deformed (during a D_4 stage of deformation) by a Late Miocene crustal-scale, top-to-the south shear zone, termed the South Cycladic Shear Zone (SCSZ) (Lister et al., 1984; Vandenberg & Lister, 1996). The lower structural levels of the SCSZ are cut by localized top-to-the north shear zones (Lister & Keay, 1996), which appear to form a different generation of shear zones from those that were previously recognized. Also, detailed structural mapping reveals non-coaxial ductile deformation with a top-to-the north sense of shear in the northern part of the island, and a top-to-the south sense of shear in the south (Fig. III.25) (Gautier & Brun, 1994b). However, the dominant sense of shear is top-to-the south (Gautier & Brun, 1994b).

The upper levels of the SCSZ are truncated by a system of low-angle faults (the Ios detachment fault system). These faults accomplish the final juxtaposition of the basement and overlying blueschist sequence (Forster & Lister, 1999). On the basis of ramp geometries and ductile structures in the footwall, Forster & Lister (1999) argued for a top-to-the south sense of movement along this detachment. Moreover, multiple low-angle normal faults, such as the Coastal and André faults occur both in the series and the basement above and below the Ios detachment (Forster & Lister, 1999).

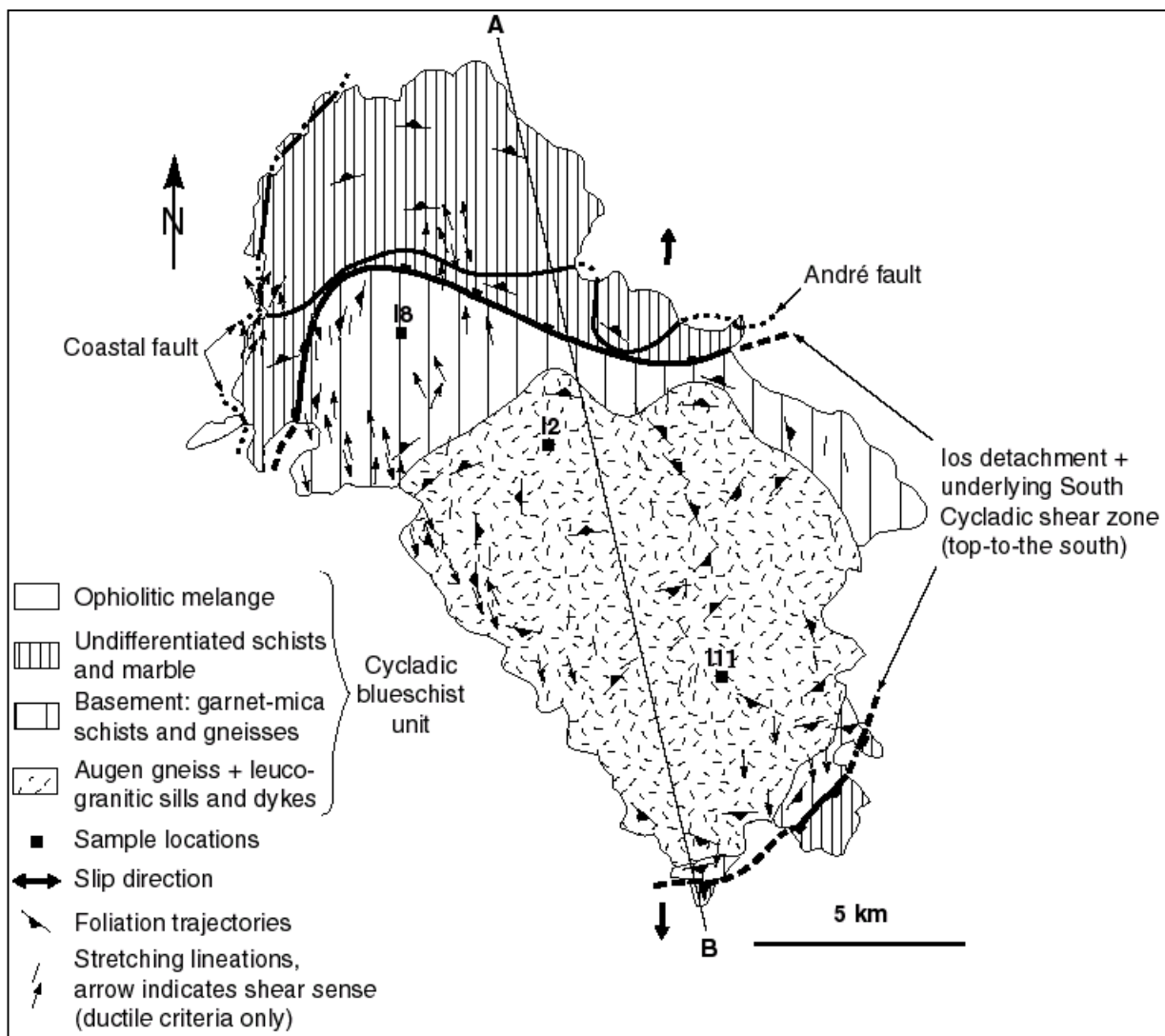


Fig. III.25 Simplified geologic map of Ios Island (modified from Gautier & Brun, 1994 and Vandenberg and Lister, 1996); sample locations are indicated.

III.8.2 Previous geochronological data

An estimate for the timing of M_1 on Ios comes from the $^{40}\text{Ar}/^{39}\text{Ar}$ spectra of a fresh blueschist sample which contains evidence for closure at ~ 39 Ma thought to reflect peak or post-peak M_1 followed by partial resetting at ~ 29 Ma in response to rehydration during decompression (Grütter, 1993). Nevertheless, Andriessen (1978) estimated the peak of M_1 around 43 Ma on the basis of K-Ar dating on white micas. Several generations of white micas have been identified on Ios (Henjes-Kunst & Kreuzer, 1982; Baldwin & Lister, 1998). The firsts thought to preserve ages associated with Variscan amphibole metamorphism affecting the basement of Ios ~ 500 -300 Ma. Second generation micas yield K-Ar ages of 39-34 Ma that were related to M_1 by Henjes-Kunst & Kreuzer (1982) while Baldwin & Lister (1998) report older $^{40}\text{Ar}/^{39}\text{Ar}$ apparent ages ranging from 58-42 Ma with a plateau at 54 Ma thought to approximate the timing of M_1 . Thus the timing of M_1 is estimated from 55-40 Ma. A third generation of sericitic micas seem to be associated with M_2 greenschist facies metamorphism yields a K-Ar age of 25.7 Ma (Henjes-Kunst & Kreuzer, 1982), while $^{40}\text{Ar}/^{39}\text{Ar}$ apparent ages of ~ 32 -31 Ma and also ~ 21 Ma are interpreted to reflect recrystallization under greenschist conditions (Baldwin & Lister, 1998). Thus the timing of M_2 is estimated around 26 ± 5 Ma.

$^{40}\text{Ar}/^{39}\text{Ar}$ thermochronology on some M_1 K-feldspar from the Ios basement reveals argon loss during a ~ 14 Ma event thought to be associated with magmatic activity (Baldwin & Lister, 1998) recognized in several islands (Tinos, Mykonos, Naxos, and Paros) and also supported by a whole rock-phengite Rb/Sr age of ~ 13 Ma from a meta-aplite dyke deformed probably in D_4 shear zones which intrude basement rocks (Henjes-Kunst & Kreuzer, 1982; Vandenberg & Lister, 1996). Vandenberg & Lister (1996) propose that this age may date one of the D_4 shear zones.

Subsequently, Hejl et al. (2003) analysed 3 samples using the apatite fission track method yielding ages that range from 13.3 ± 1.1 Ma to 8.3 ± 1.1 Ma. Associated with track length measurements they estimated a maximum cooling rate of over 50 °C/Myr occurred about 11 Ma.

III.8.3 Results

Apatite and zircon fission track, apatite (U-Th)/He ages are listed in Table III.9.

Table III.9. Ios fission-track and U-Th/He data

Sample reference (rock type)	Lat. Long.	Elevation (m)	Distance in slip direction (km)	Mineral	Number of crystals	P χ^2 (%)	FT age (Ma)	Mean track length (μm)	StD (μm)	Number of tracks measured	F_T	Helium age (Ma)
I2 (gneiss)	36°43'24" 25°19'08"	270	3.37 \pm 0.3	apatite	24	100.0	12.2 \pm 1.4	14.73 \pm 0.22	0.76	52	0.73	10.8 \pm 1.0
				zircon	8	98.5	14.0 \pm 1.6					
I8 (gneiss)	36°40'32" 25°21'23"	70	0.95 \pm 0.1	apatite	23	99.6	11.0 \pm 1.4	14.39 \pm 0.28	0.92	43	0.76	9.5 \pm 0.8
				zircon	12	97.1	13.2 \pm 1.4					
I11 (gneiss)	36°44'33" 25°17'27"	200	8.93 \pm 0.9	zircon	10	99.9	14.5 \pm 1.6					

Apatite and zircon FT ages have been calculated using a zeta factors of 127.3 ± 4.4 and 332.9 ± 9.7 determined by multiple analyses of standards following the recommendations of Hurford (1990). Central ages are reported. All data are given for 2σ error level.

Three samples from the footwall of the South Cycladic Shear Zone of Ios have been dated. One sample (I8) have been collected in the amphibolite facies garnet-mica schists and two (I2 and I11) in the granitic gneisses, along a N-S profile parallel to the tectonic transport direction (Fig. III.25) (Gautier & Brun, 1994b; Vandenberg & Lister, 1996). Apatite and zircon fission track and apatite

(U-Th)/He dating have been carried out on the samples I8 and I2 while only zircon fission track have been carried out on I11 owing to the apatite lack in this sample (Table III.9; see appendix 2).

The zircon fission track ages range from 14.5 ± 1.6 Ma in the south to 13.2 ± 1.4 Ma in the north. The apatite fission track ages are 12.2 ± 1.4 Ma for I2 (south) and 11.0 ± 1.4 Ma for I8 (north) and the apatite (U-Th)/He ages for the same samples are 10.8 ± 1 Ma (south) and 9.5 ± 0.8 Ma (north) (Table III.8). All ages consistently young in northward direction.

Temperature-time (T-t) paths for two samples from the basement (Fig. III.26) in the footwall of the Ios detachment have been calculated. The data indicate rapid cooling from $\sim 300^\circ\text{C}$ to $\sim 80^\circ\text{C}$ within <4 Ma at minimum average rates of $\sim 36^\circ\text{C}/\text{Myr}$. The mean track lengths in the apatite range from $14.73 \pm 0.22 \mu\text{m}$ to $14.39 \pm 0.28 \mu\text{m}$ (Table III.8) and support rapid cooling.

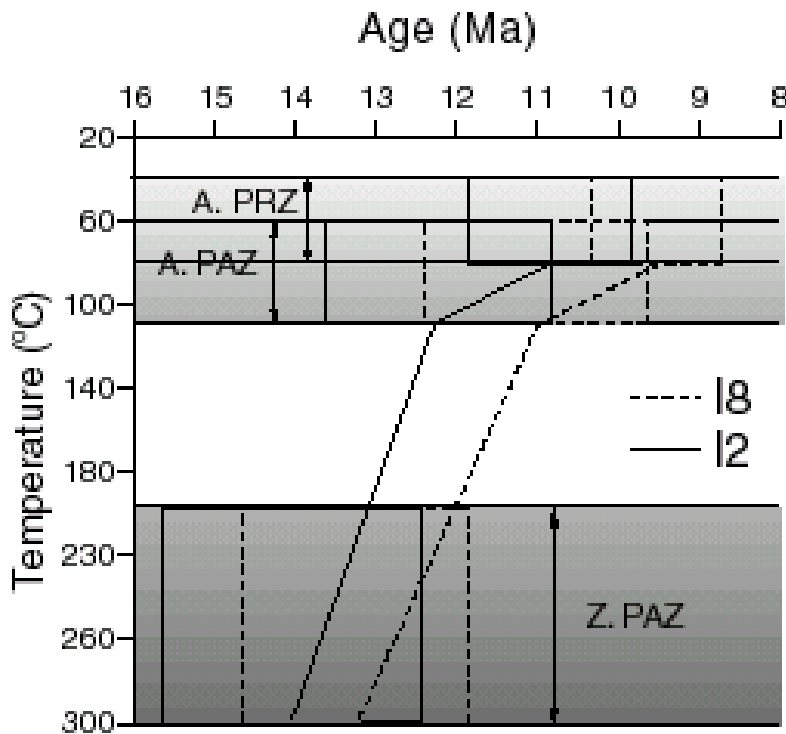


Fig. III.26 Temperature/time evolution for two samples from the basement of Ios across zircon and apatite fission-track partial annealing zones and apatite partial retention zone for (U-Th)/He system; boxes represent uncertainties on ages and temperatures (2σ); black line and dotted line represents cooling path of I2 and I8.

III.8.4 Discussion

The results decrease from south to north indicating a top-to-the north sense of movement. Ages derived from thermochronometers constrain the cooling history of the rocks since $\sim 300^\circ\text{C}$ to $\sim 80^\circ\text{C}$. The data constrain the brittle part of an extensional fault system (see introduction, Sibson, 1977). Moreover, the results yielded minimum slip rates of 6.3 ± 1.5 km/Myr (ZFT), 2.0 ± 0.4 km/Myr (AFT) and 1.9 ± 0.2 km/Myr (apatite (U-Th)/He) (Fig. III.27). The slip rate estimated using the zircon fission track ages of three samples is higher than the slip rates defined by the other methods with only two samples. Therefore, the slip rates estimated are poorly constraint and more dating will be necessary to know exactly if there is a real variation of the slip rate from 300°C to 110°C . Nevertheless, the average slip rate estimated for the detachment responsible of the age variations is 3.4 ± 0.5 km/Myr between $\sim 300^\circ\text{C}$ to $\sim 80^\circ\text{C}$. A minimum displacement calculation for this detachment, resulted in ~ 17 km of offset between ~ 15 - 9 Ma.

This data show that the detachment which have exhumed the rock from $\sim 300^\circ\text{C}$ up to $\sim 80^\circ\text{C}$ have a top-to-the north sense of movement. The data indicate that detachment faulting commenced at a minimum of 14.5 ± 1.6 Ma. Vandenberg & Lister (1996) proposed an age of ~ 13 Ma for the main shearing. Because this age is provided from a meta-apatite dyke deformed by ductile top-south shearing, it is only a minimum age for the shearing on Ios which probably started earlier. This

result does not contradict the fact that detachment faulting probably occurred after shearing on Ios because the results and the age from the meta-aplite dyke are only a minimum estimate for the start of the brittle detachment faulting and ductile shearing.

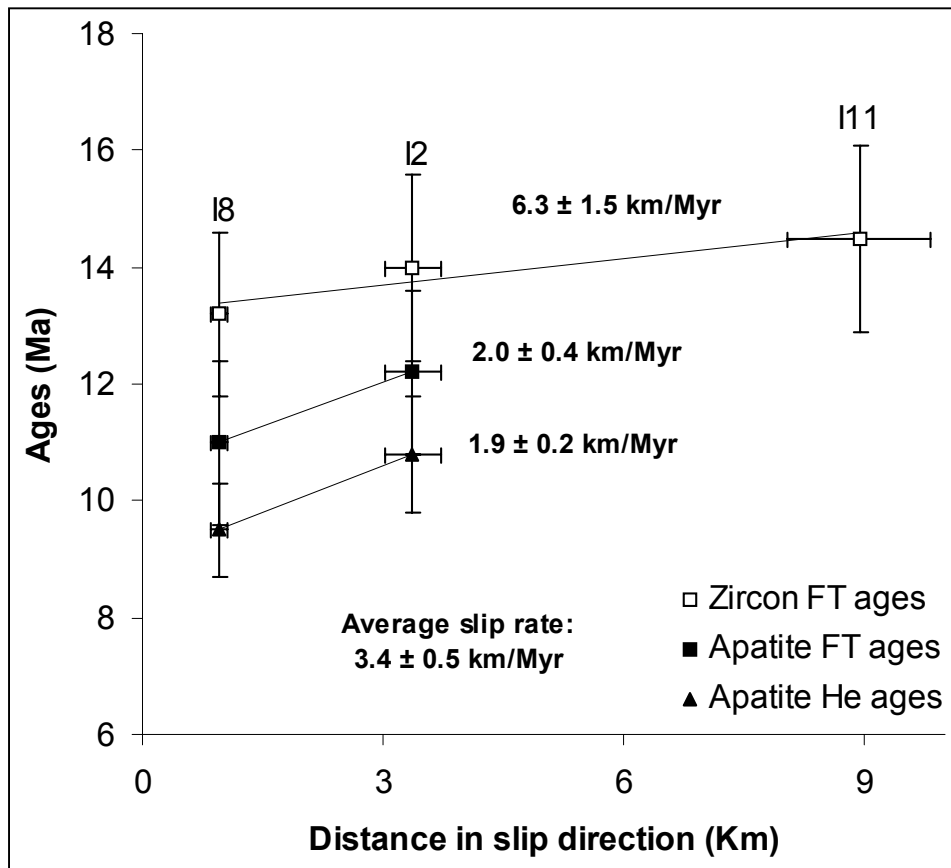


Fig. III.27 Plot of zircon fission-track (ZFT), apatite fission-track (AFT) and (U-Th)/He ages (2σ) against distance in slip direction (2σ) for a detachment fault of Ios; estimated minimum slip rates are 6.3 ± 1.5 km/Myr (ZFT), 2.0 ± 0.4 km/Myr (AFT) and 1.9 ± 0.2 km/Myr (apatite (U-Th)/He). The minimum average slip rate for this detachment is estimated as 3.4 ± 0.5 km/Myr (2σ).

On Ios, the main sense of shear is top-to-the south (Lister et al., 1984; Gautier & Brun, 1994b; Vandenberg & Lister, 1996) while the sense of movement along the Ios detachment is more problematic owing to the lack of brittle kinematic criteria. Forster & Lister (1999) argued for a top-to-the south sense of movement for this detachment fault. However, there is no kinematic criteria which allow rejection of a top-to-the north sense of movement for the Ios detachment faulting. Moreover, multiple low-angle normal faults (such as the André fault or the Coastal fault: Forster & Lister, 1999) occur on Ios island but their senses of movement are poorly constrained. These new data suggest a top-to-the north detachment fault which would occur after movement on the South Cycladic Shear Zone broadly in the same zone and/or a detachment located more on the north of the island as the André or Coastal fault (Fig. III.28).

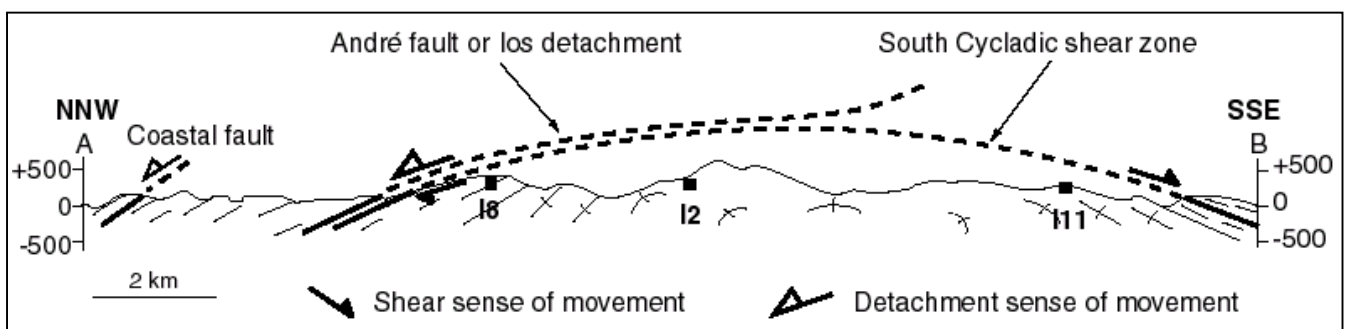


Fig. III.28 Cross section interpretation of our data modified from Vandenberg & Lister (1996) and Forster & Lister (1999). Shown the top-to-the south South Cycladic Shear Zone and top-to-the north detachments fault. The main detachment fault can be the André fault described by Forster & Lister (1999) or the Ios detachment which has a sense of movement not clearly defined (Forster & Lister, 1999).

III.9 Problematic (U-Th)/He data

During this study I discovered some problems with (U-Th)/He dating. This comparatively new method is ideally suited to monitor processes acting near the Earth surface. However, occasionally this isotopic system provides inconsistent data compared to the fission track results. In this part, I attempt to explain inconsistent data using apatite cathodoluminescence pictures, thin section observations and chemistry of the apatites.

III.9.1 Sample Ik6 from Ikaria

Sample Ik6 is from metasediments of the Ikaria nappe is a deformed quartzite. Three aliquots of four apatites have been dated using (U-Th)/He method (Table III.10).

Table III.10. (U/Th)/He data for Ik6 sample

Sample name	Raw age (Ma)	Corr. age (Ma)	U ppm	Th ppm	He nmol/g	Ft	mean r μm	mean l μm	RE	AFT age (Ma)	ZFT age (Ma)
IK6-A	3.582	5.098	11.308	1.004	0.225	0.703	43.569	184.277	0	6.2 \pm 0.8	8.6 \pm 0.9
IK6-B	8.3	11.376	10.784	1.528	0.503	0.729	50.712	179.991	0		
IK6-C	4.162	6.127	12.861	1.644	0.3	0.679	40.712	175.706	1		

All data are given for 1 σ error level. Raw age = age before Ft correction; Corr. age = Ft corrected age; mean r = mean width; mean l = mean length; RE = re-extract; AFT = Apatite Fission track; ZFT = Zircon Fission Track.

For calculation of the (U-Th)/He age, aliquot IK6-B was excluded as it yields an abnormally old age compared to the apatite and zircon fission track ages.

Cathodoluminescence (CL) was used to study the distribution of U and Th in the apatite crystals selected for analysis (Fig. III.29). The CL images show no specific zonation and/or inclusions that might explain the anomalous old Ik6-B age.

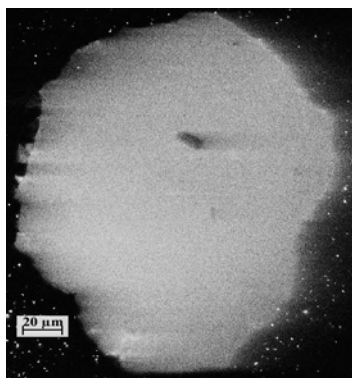


Fig. III.29 Cathodoluminescence picture of apatite from Ik6 sample without zoning. The black spot in middle of the grain is an inclusion of feldspar.

Comparisons were made with the (U-Th)/He results from the other samples (Ik 1 & 2) collected on this island. Sample Ik6 yields a higher U/Th ratio than Ik1 & 2 (Fig. III.30; see appendix 5 for analyses details) whilst aliquot Ik6-B contains slightly more He than the other aliquots from the same sample (Ik6-A and Ik6-C; Fig. III.30). This explains the anomalous older age for sample Ik6.

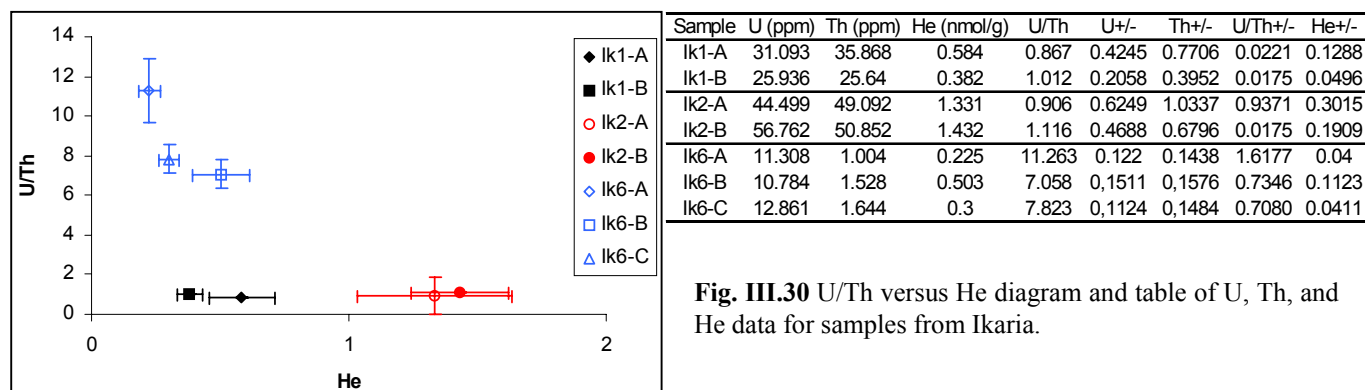


Fig. III.30 U/Th versus He diagram and table of U, Th, and He data for samples from Ikaria.

Farley (2003) recognise the existence of problematic samples which contain seemingly good apatites that yield irreproducible and anomalously old He ages. These observations apply specifically to rocks which have LREE depletion, compared with LREE enrichment in most non-problematic apatites. Sample Ik6 shows this pattern of LREE depletion compared to the non-problematic sample Ik2 (Fig. III.31).

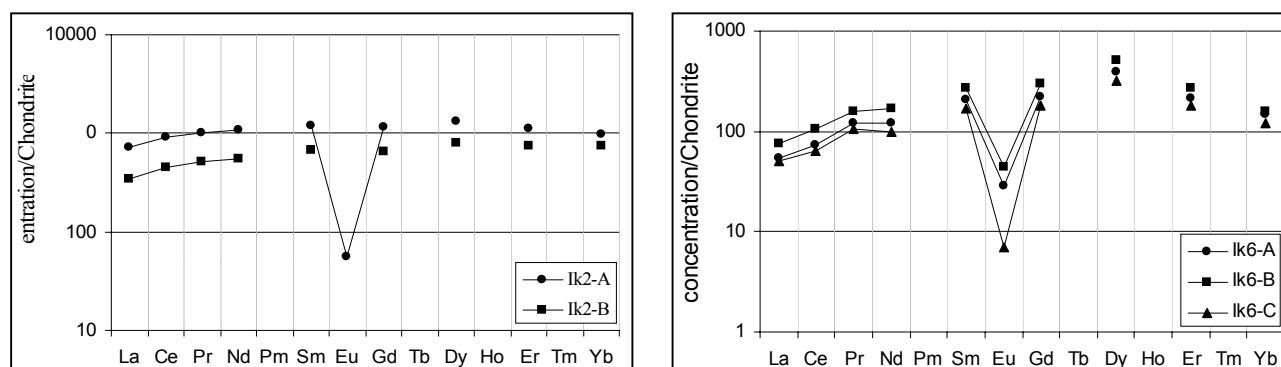


Fig. III.31 REE diagrams of apatites from the Ik2 and Ik6 samples.

Farley (2003) argues that inclusions and/or U and Th zonation cannot explain the aberrant ages and proposes a possible role for He implantation from U-Th rich neighbouring minerals (such as monazite, zircons, titanite). Study of a thin section of sample Ik6, does not reveal a particularly high concentration of U-Th rich minerals. However, thin section observations may not be completely representative of the rock sample and the possibility that some localised He implantation has taken place cannot be ruled out.

If implantation is the main cause of anomalous ages, the only way to test for such an effect is to map directly helium and U-Th profiles on apatite grains, ideally within the rock section where the relationship to adjacent grains will be known. This is technically difficult and beyond the scope of this project.

III.9.2 Sample T2 from Tinos

Sample T2 is from a granodiorite belonging to the main granitic body of Tinos island. Four aliquots each comprising four apatite grains were analysed by the (U-Th)/He method (Table III.11).

Table III.11. (U/Th)/He data for T2 sample

Sample name	Raw age (Ma)	Corr. age (Ma)	U ppm	Th ppm	He nmol/g	U/Th ratio	He Error	U/Th Error	Ft	mean r μm	mean l μm	RE	AFT age (Ma)	ZFT age (Ma)
T2-A	5.302	8.088	11.904	22.278	0.494	0.53434	0.0583	0.0094	0,655	39.998	152.135	0	11.9 \pm 1	12.2 \pm 0.5
T2-B	11.233	16.067	10.034	18.616	0.88	0.539	0.1949	0.0153	0,699	44.284	239.988	0		
T2-C	8.242	11.212	11.363	21.982	0.741	0.51692	0.2065	0.0173	0,735	52.854	205.704	0		
T2-D	7.228	10.61	16.566	27.666	0.907	0.59879	0.1531	0.0128	0,681	41.426	205.704	0		

All data are given for 1 σ error level. Raw age = age before Ft correction; Corr. age = Ft corrected age; mean r = mean width; mean l = mean length; RE = re-extract; AFT = Apatite Fission track; ZFT = Zircon Fission Track

For calculation of the (U-Th)/He age, aliquot T2-B was excluded as it yields an abnormally old age compared to the apatite and zircon fission track ages.

If the data are plotted as U/Th versus He it can be seen that aliquot T2-B has a significantly higher He content (0.88 nmol/g) than the other aliquots which have a similar U/Th ratio. This explains why the T2-B aliquot gave a significantly older helium age (Fig. III.32).

Cathodoluminescence (CL) investigation on apatites from the sample T2 do not reveal any specific zonation and/or inclusions that might explain the old T2-B age. However, CL investigation have not been done directly on the grains from the T2-B aliquot.

Thin section investigations show several large titanite crystals (> 500 μm) in the T2 sample (Fig. III.33). Titanite typically has U/Th levels close to zircon and therefore produces large amounts of helium relative to apatite. In Fig. III.33, thin section photomicrographs show apatite crystals

included (Fig. III.33a) or in the vicinity of titanite (Fig. III.33b) which can explain why some apatites from this sample give anomalous ages. Apatite grains enclosed in a U/Th bearing mineral will have some helium implanted in them from ejection of alpha particles (^4He nuclei) and in addition the higher helium production rate of titanite would be expected to lead to some diffusion of helium into the enclosed apatite grains which would have a lower helium concentration.

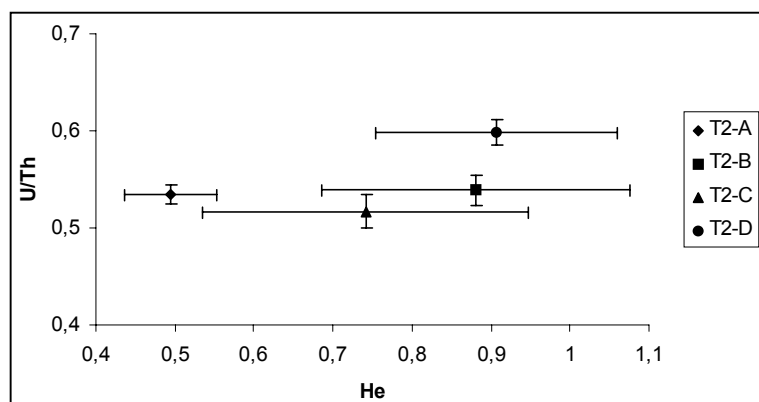


Fig. III.32 U/Th versus He diagram of the four aliquots analyzed for (U-Th)/He dating.

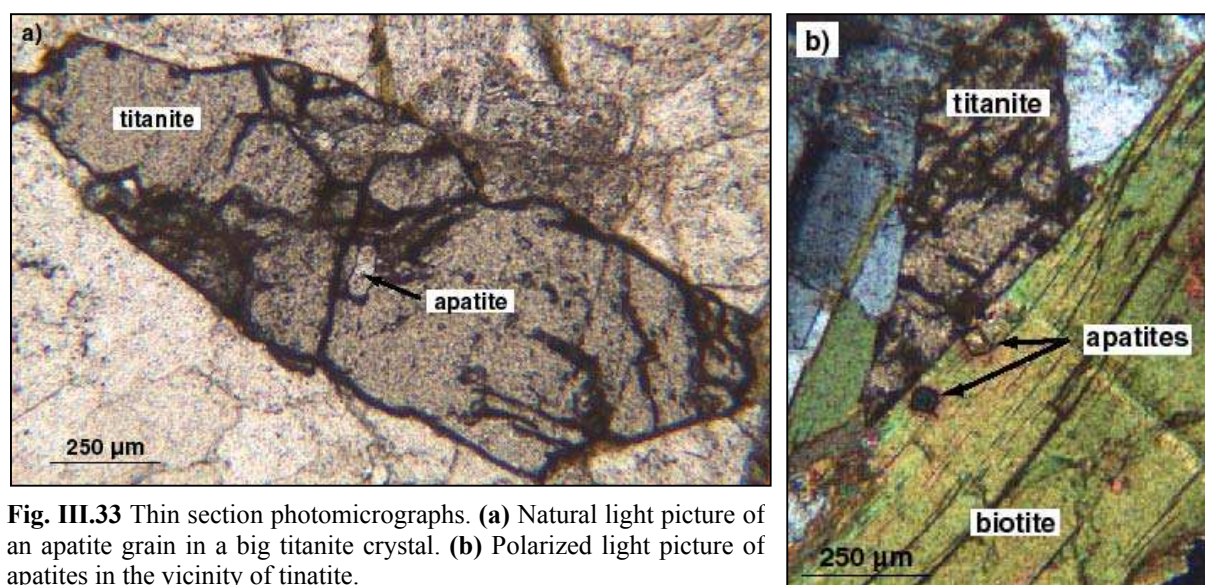


Fig. III.33 Thin section photomicrographs. (a) Natural light picture of an apatite grain in a big titanite crystal. (b) Polarized light picture of apatites in the vicinity of titanite.

III.9.3 Sample M3 from Mykonos

Sample M3 is a granodiorite. Four aliquots of four apatites have been dated (Table III.12). Aliquots M3-B and M3-C which yield abnormally old ages compared to the apatite and zircon fission track ages were excluded from calculation of the (U-Th)/He age.

Table III.12. (U/Th)/He data for M3 sample

Sample name	Raw age (Ma)	Corr. age (Ma)	U ppm	Th ppm	He nmol/g	U/Th ratio	He Error	U/Th Error	Ft	mean r μm	mean l μm	RE	AFT age (Ma)	ZFT age (Ma)
M3-A	7.029	10.145	32.514	28.908	1.502	1.125	0.0243	0.2632	0.693	42.855	197.133	0	10.5 \pm 0.9	10.9 \pm 0.5
M3-B	13.969	21.225	23.216	14.71	2.027	1.578	0.0309	0.2366	0.658	38.569	162.849	0		
M3-C	10.995	16.138	37.363	24.89	2.584	1.501	0.0333	0.447	0.681	39.998	224.989	0		
M3-D	7.04	10.794	35.834	16.291	1.518	2.2	0.0408	0.1710	0.652	37.141	169.277	0		

All data are given for 1σ error level. Raw age = age before Ft correction; Corr. age = Ft corrected age; mean r = mean width; mean l = mean length; RE = re-extract; AFT = Apatite Fission track; ZFT = Zircon Fission Track

These two aliquots yield higher He contents (ranging from 2 to 2.5 nmol/g) than aliquots M3-A and M3-D which have a constant He content (~ 1.5 nmol/g) (Fig. III.34).

Apatite CL images do not reveal any zonation but show zircon inclusions and some inclusions of quartz and feldspar (Fig. III.35) which unlike zircon will not contain U and Th. In most cases inclusions in apatite are detected during the grain selection process but occasionally inclusions are missed because the inclusions are oriented parallel to the c-axis (see chapter I.3.1) and are extinct at the same time as the apatite host under crossed-polarised light. Inclusion free samples are verified by reproducible ages whilst samples with inclusion lead to significant He above the blank during re-extracts (see Chapter I.4.1). Significant He was measured during the re-extracts for M3-B and M3-C indicating the presence of inclusions such as zircon.

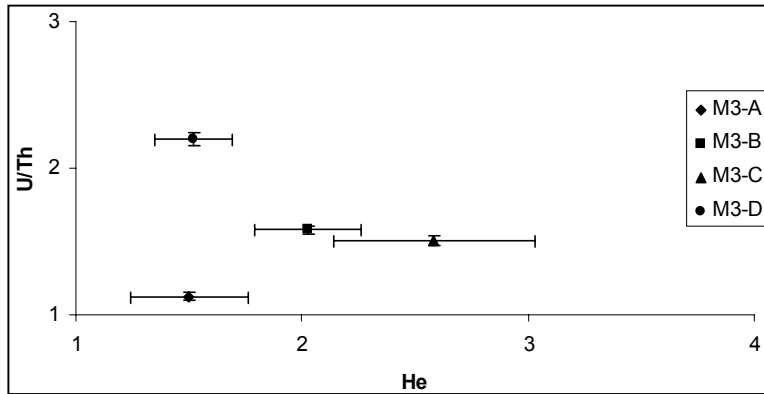


Fig. III.34 U/Th versus He diagram of the four aliquots analyzed for (U-Th)/He dating.

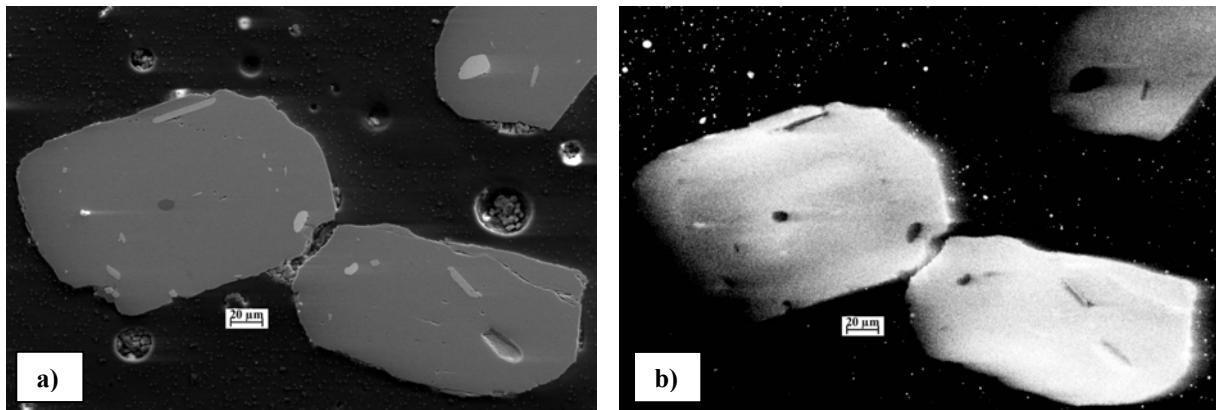


Fig. III.35 Pictures from M3 sample. (a) Surface picture of apatite grains showing zircon (light grey) and feldspar (dark grey) inclusions. (b) Apatite CL picture does not reveal zonation.

Thin section examination of this sample has identified high U/Th content minerals such as titanite (Fig. III.36a), monazite (Fig. III.36b) and zircon (Fig. III.36c) and apatite grains full of fluid inclusions (Fig. III.36d). These observations provide some indication of possible causes of spurious results through He implantation. The presence of fluid inclusions might also provide an explanation for poor data however they have not been systematically studied and it is not known how they might degrade an analysis other than by possibly contributing non-parental helium during rock crystallisation.

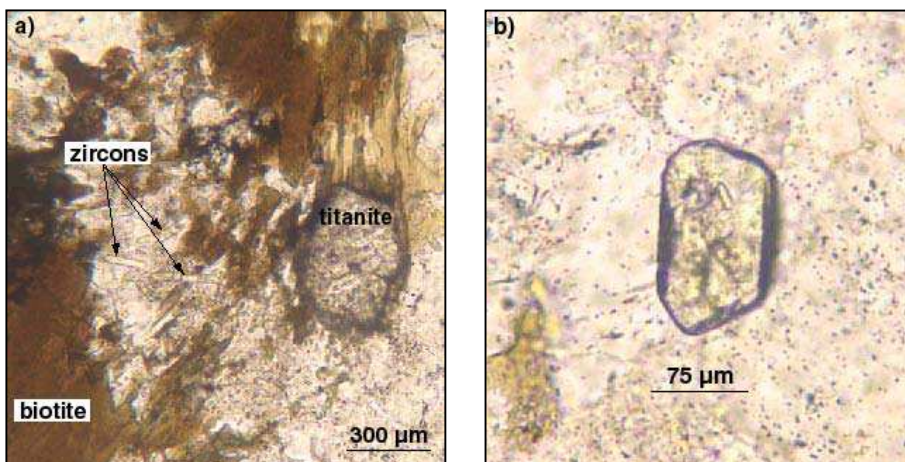


Fig. III.36 Thin section photomicrographs under natural light showing: (a) titanite, biotite and zircons; (b) monazite grain;

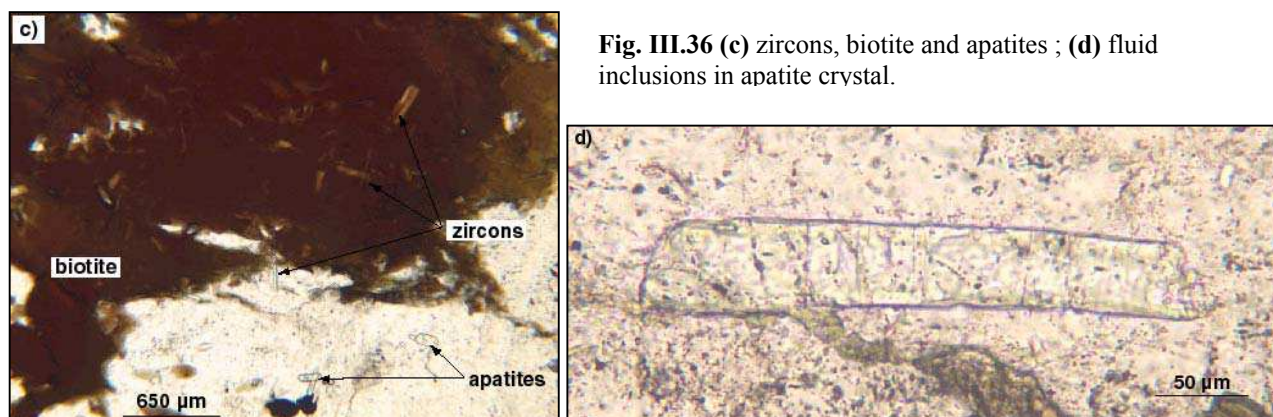


Fig. III.36 (c) zircons, biotite and apatites ; **(d)** fluid inclusions in apatite crystal.

There are a number of possibilities that might explain the irreproducibility of ages but more investigation could be necessary to constrain the exact cause of these age disturbances.

III.9.4 Samples Na1 and Na2 from Naxos

Samples Na1 and Na2 are from S-type granites located at the northern end of Naxos island (Fig. III.17). Four aliquots each comprising four apatite grains were analysed (Table III.13). The analyses gave irreproducible and anomalously old He ages compared to the apatite fission track ages and other dating evidence which show a consistent trend of increasing age to the south of the island (see Fig. III.17 and section III.5.3). Therefore, (U-Th)/He ages from these two samples were not used for slip rate estimation on Naxos (see section III.5.3).

Table III.13. (U/Th)/He data for Na1 and Na2 samples

Sample name	Raw age (Ma)	Corr. age (Ma)	U ppm	Th ppm	He nmol/g	Ft	mean r μm	mean l μm	RE	AFT age (Ma)
Na1-A	10.249	14.812	30.974	2.673	1.761	0.692	40.95	211.418	0	8.2±0.6
Na1-B	7.307	11.26	45.419	7.108	1.871	0.649	36.189	168.563	0	
Na1-C	10.9	14.58	30.858	5.776	1.91	0.747	52.14	231.417	0	
Na1-D	9.129	12.866	41.131	16.008	2.228	0.709	44.284	231.417	0	
Na2-A	7.615	11.823	8.212	1.991	0.359	0.644	35.713	171.42	0	8.7±1.3
Na2-B	9.344	16.201	11.17	3.651	0.611	0.576	28.57	167.135	0	
Na2-C	7.781	11.091	10.19	2.552	0.456	0.701	44.284	186.419	0	
Na2-D	12.536	19.059	10.35	2.134	0.74	0.657	37.855	160.706	0	

All data are given for 1σ error level. Raw age = age before Ft correction;

Corr. age = Ft corrected age; mean r = mean width; mean l = mean length; RE = re-extract;

AFT = Apatite Fission track; ZFT = Zircon Fission Track

The results of all samples from the Naxos island (Na 1-6) were plotted as U/Th vs He (Fig. III.37) to try and understand the causes of poor reproducibility.

Sample	U (ppm)	Th (ppm)	He (nmol/g)	U/Th	U+/-	Th+/-	U/Th+/-	He+/-
Na1-A	30.974	2.673	1.761	11.588	0.2522	0.1561	0.6833	0.2289
Na1-B	45.419	7.108	1.871	6.390	0.2282	0.1741	0.1598	0.1500
Na1-C	30.858	5.776	1.91	5.342	0.5902	0.2745	0.2737	0.5851
Na1-D	41.131	16.008	2.228	2.569	0.5598	0.4152	0.0753	0.4867
Na2-A	8.212	1.991	0.359	4.125	0.0543	0.1449	0.3014	0.0378
Na2-B	11.17	3.651	0.611	3.059	0.0463	0.1474	0.9616	0.0402
Na2-C	10.19	2.552	0.456	3.993	0.1129	0.1665	0.2642	0.0804
Na2-D	10.35	2.134	0.74	4.850	0.0725	0.1491	0.34057	0.0822
Na3-B	29.967	38.502	1.236	0.778	0.2588	0.564	0.0132	0.1709
Na3-C	24.074	28.527	1.032	0.844	0.2697	0.5472	0.0187	0.1844
Na3-D	28.301	38.297	1.171	0.739	0.194	0.4722	0.0104	0.1276
Na4-A	39.365	73.202	1.971	0.538	0.4721	1.2792	0.0114	0.3795
Na4-B	57.98	113.118	2.831	0.513	0.6068	1.6818	0.0093	0.4767
Na5-A	36.265	50.561	1.634	0.717	0.3981	0.8559	0.0145	0.2883
Na5-B	38.457	58.35	1.866	0.659	0.4925	1.1084	0.0151	0.3842
Na6-A	42.055	56.805	2.225	0.740	0.5674	1.1341	0.0178	0.4828
Na6-B	32.796	44.735	1.745	0.733	0.3015	0.6672	0.0128	0.2574

Fig. III.37 (a) Table of U, Th, and He data for samples from Naxos.

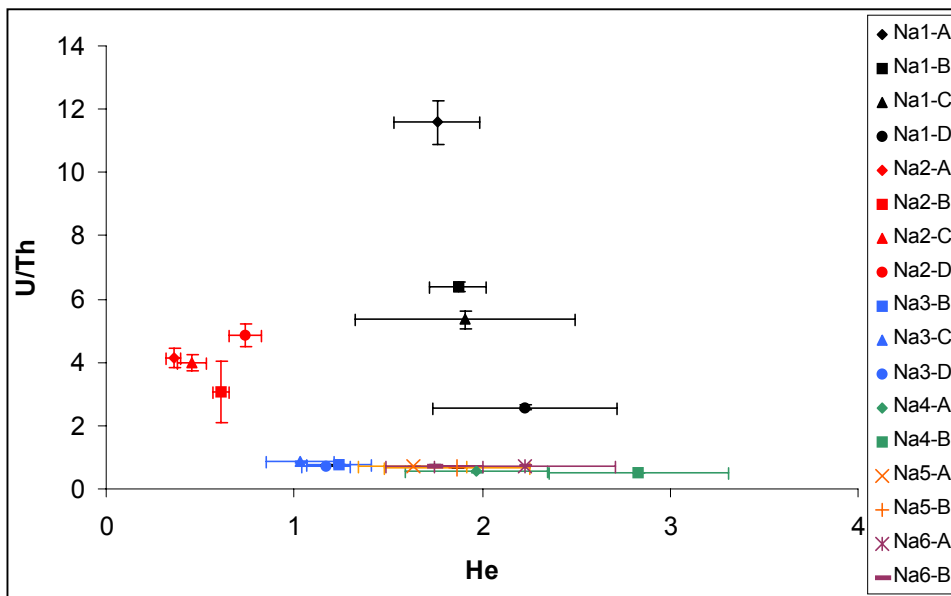


Fig. III.37 (b) U/Th versus He diagram and table of U, Th, and He data for samples from Naxos.

The plots reveal a fairly constant low U/Th ratio (< 1) for samples from the main granitic body of Naxos (Na3 to Na6) while the two samples (Na1 and Na2) from S-type granites yield a variable higher U/Th ratio. This observation can be correlated with a high U/Th ratio for Na1-A to -D and Na2-A to -D aliquots related to a low Th content (Fig. III.37). This spuriously low value is at odds with the rest of the data and might be an analytical problem. Thorium is notoriously difficult to keep in solution and may have precipitated out during analysis.

CL images of the apatites show some zircon inclusions in the Na2 sample but no specific zoning is apparent in either of the two samples.

The thin section observations of Na1 sample show tourmaline associated with undeformed muscovite (Fig. III.38).

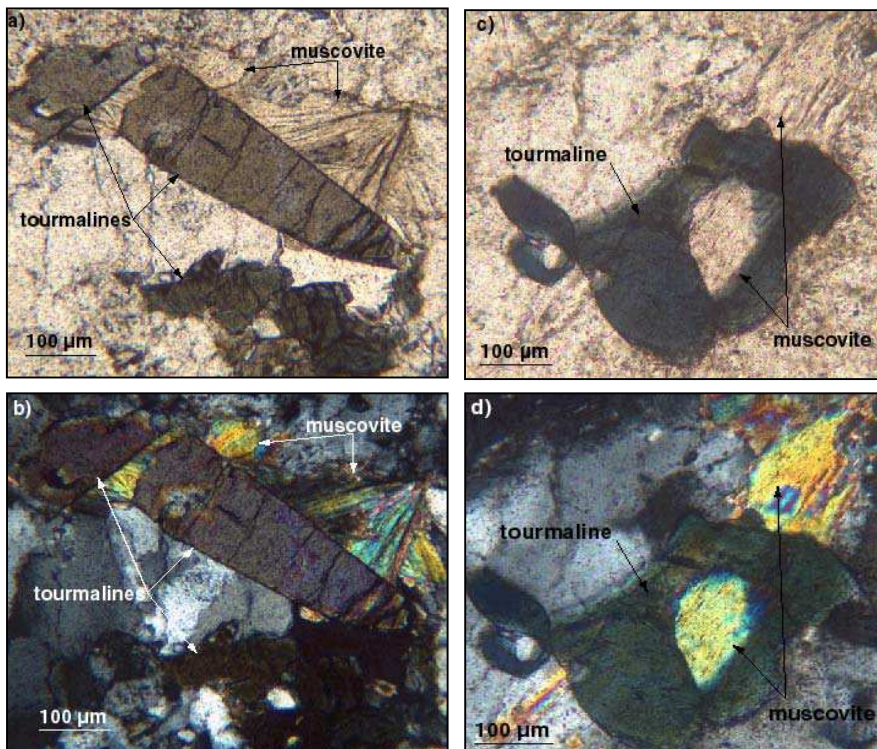


Fig. III.38 Thin section photomicrographs under natural light (a, c) and polarized light (b, d) showing tourmaline associated with undeformed muscovite.

Muscovites appear deformed in other mineral associations such as garnet (Fig. III.39). Tourmaline formation is usually related to fluid percolation in rocks. The undeformed muscovite indicates that any fluid flow post-dates deformation.

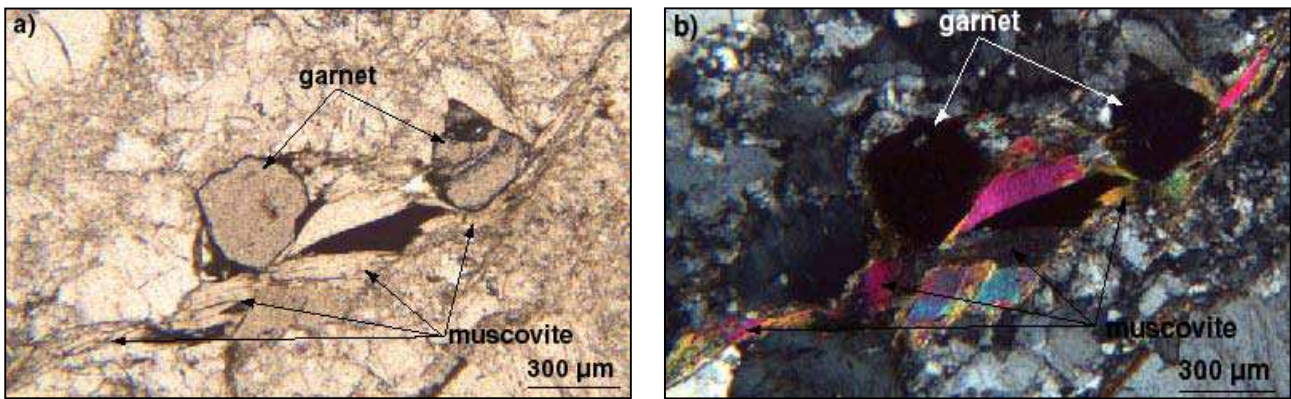


Fig. III.39 Thin section photomicrographs under natural light (a) and polarized light (b) showing muscovite deformed associated with garnet.

The thin sections from Na2 also indicate fluid flow because the biotite has been chloritized (Fig. III.40a) and apatite grains contain lots of fluid inclusions (Fig. III.40b).

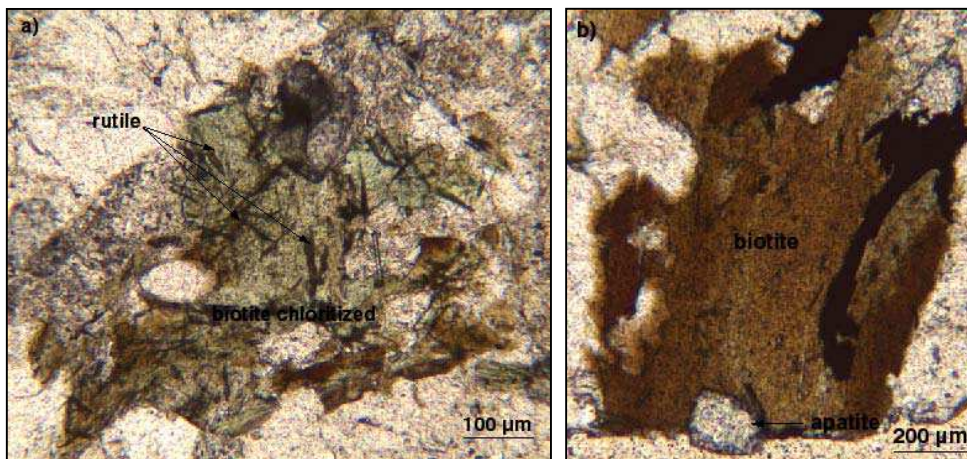


Fig. III.40 Thin section photomicrographs under natural light showing: (a) biotite chloritized within rutile crystals and (b) apatite crystal within fluid inclusions.

The evidence from plots of U/Th vs He and thin section observations suggest that the (U-Th)/He ages from samples Na1 and Na2 have been disturbed by fluids supporting the case for excluding the results from slip rate estimation.

III.9.5 Se2 sample from Serifos

Sample Se2 is from an I-type granite. Four aliquots each comprising four apatite grains were analysed (Table III.14). Aliquot Se2-C which yields an abnormally old age compared to the apatite and zircon fission track ages has been excluded from the calculation of the (U-Th)/He age.

Table III.14. (U/Th)/He data for Se2 sample

Sample name	Raw age (Ma)	Corr. age (Ma)	U ppm	Th ppm	He nmol/g	U/Th ratio	He Error	U/Th Error	Ft	mean r µm	mean l µm	RE	AFT age (Ma)	ZFT age (Ma)
Se2-A	5.86	8.136	10.011	29.587	0.541	0.338	0.1724	0.0068	0.72	45.712	308.556	0	10.3±1.3	11.4±0.5
Se2-B	5.161	7.734	13.544	33.994	0.604	0.398	0.0921	0.0076	0.667	39.998	201.419	1		
Se2-C	10.18	14.137	12.653	32.798	1.127	0.386	0.3180	0.0125	0.72	47.855	257.13	0		
Se2-D	4.741	6.635	9.648	26.404	0.409	0.365	0.0901	0.0098	0.714	47.14	197.133	0		

All data are given for 1σ error level. Raw age = age before Ft correction; Corr. age = Ft corrected age; mean r = mean width; mean l = mean length; RE = re-extract; AFT = Apatite Fission track; ZFT = Zircon Fission Track

The plot of U/Th vs He show similar U/Th ratios for all four aliquots is fairly (between ~0.4 to ~0.34) whilst the He content for Se2-C (> 1 nmol/g) is significantly higher than the three other aliquots (Se2-A, Se2-B and Se2-D) which have a He content ranging from ~0.4 to ~0.6 nmol/g (Fig.

III.41). This suggests non parental helium has been introduced into the grain either through implantation, inward diffusion or from inclusions.

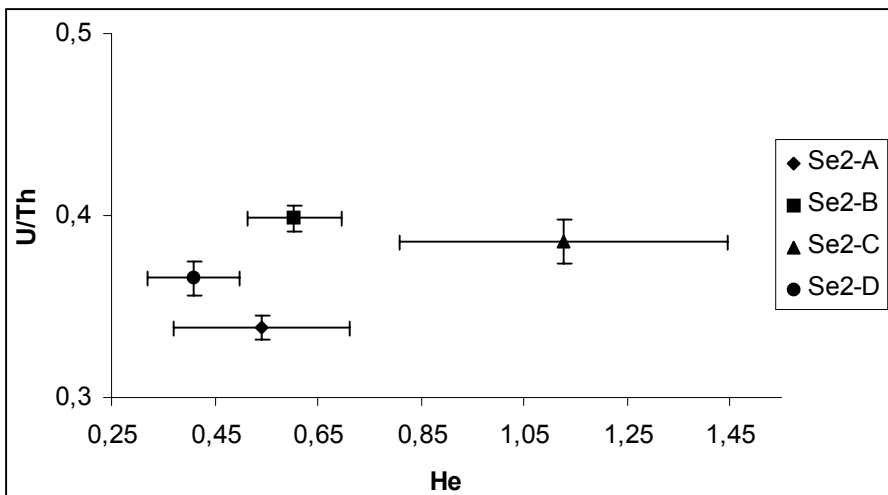


Fig. III.41 U/Th versus He diagram of the four aliquots analyzed for (U-Th)/He dating.

Apatite CL images show the presence of some zircon inclusions but no evidence of zoning.

Study of thin sections show the sample is strongly altered (Fig. III.42), with partial biotite alteration into chlorite and numerous fluid inclusions in apatite grains consistent with alteration by fluids. Fluid flow in rocks is generally not homogenous, and some areas may be relatively unaffected while other areas are highly altered. Fluid flow may also remove uranium (especially the U^{+6} highly movable) however, examination of the apatite FT grain mounts and mica uranium maps do not show any evidence that this has taken place.

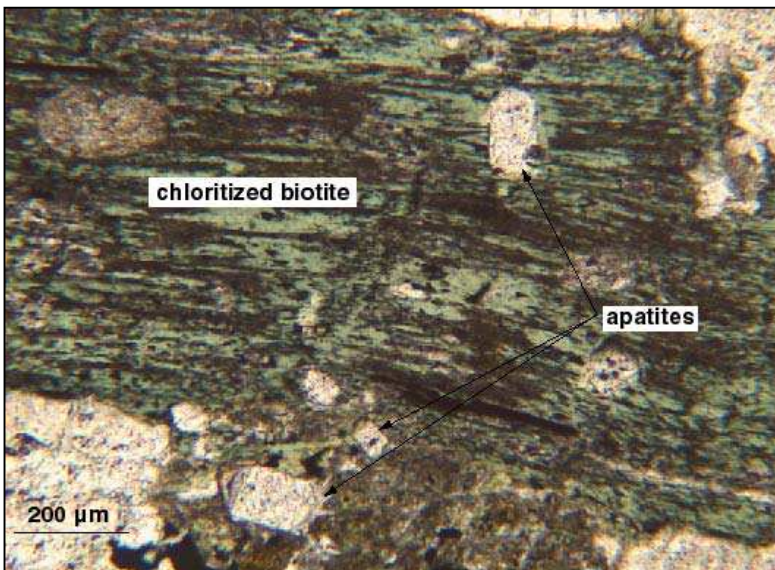


Fig. III.42 Thin section photomicrograph under natural light showing biotite partially chloritized and apatite crystals within fluid inclusions.

At this stage it is difficult to establish a clear link between fluid alteration of a rock sample and its possible influence on the integrity of the apatite helium system. Future more detailed work is required in this important area.

Chapter IV

Tectonic
implications

In the previous chapter, I have presented and discussed the results obtained for each Cycladic island sampled during this thesis. In this chapter, I summarize the major findings (Table IV.1) and tentatively interpret the data in a regional context by comparing the islands from a tectono-lithostratigraphic angle (Fig. IV.1). This will allow to distinguish the differences and similarities related to the nappe piles and extensional fault systems in the Aegean and to estimate the role of Miocene normal faulting for blueschist exhumation.

IV.1 Summary of results and major findings

IV.1.1 Dating carried out

During this thesis forty five samples, from eight different islands, have been collected. Only thirty four samples were useful for dating (see appendix 2). Of these samples, thirty one have been dated by the zircon fission track method, twenty four by the apatite fission track technique, nineteen by the (U-Th)/He method and two using the $^{40}\text{Ar}/^{39}\text{Ar}$ technique on hornblende. Therefore, seventy six ages were obtained (Table IV.2). However, two (U-Th)/He ages from S-type granites of Naxos (Na1 and Na2) were not used. In chapter III (section III.9), I have shown that problematic (U-Th)/He data can be related to accessory mineral inclusions (such as zircon or monazite) and/or implantation phenomenon and/or analytical problems. In the specific case of the Naxos S-type granite samples, indications of fluid circulation have been recognized (tourmaline in the samples) which could imply disturbance of the (U-Th)/He system. Moreover, the low thorium content might be an analytical problem related to the difficulty to keep thorium in solution which may have precipitated during analysis. Consequently, I have ruled out these data.

IV.1.2 Timing, slip rate, cooling story and offset of the extensional fault system

IV.1.2.1 Samos

Three extensional fault systems are exposed on Samos: (1) The top-to-the-N Kallithea detachment, which separates the Kallithea nappe from the Cycladic blueschist unit and the Kerketas nappe; (2) The top-to-the-ENE Kerketas detachment between the Kerketas nappe and the overlying Ampelos nappe; (3) The top-to-the-ENE Selçuk extensional system between the Ampelos nappe and the Selçuk nappe (Fig. IV.1).

A zircon fission track age from the Basal unit indicate that the Kerketas detachment operated at 14.1 ± 0.8 Ma while the age obtained from the Kallithea unit allow to estimate that the Kallithea detachment operated at 7.3 ± 0.5 Ma. Furthermore, three samples from the Ampelos nappe allow to estimate a minimum slip rate along the Selçuk detachment at 8.1 ± 1.7 km/Myr and an age of ~ 20 -18 Ma for this detachment (Table IV.1) which imply a minimum offset of 18 km for the period from ~ 20 -18 Ma. This high slip rate was not aided by melt lubrication. The timing constraints and the geographic pattern of ages indicate that the Kallithea, Selçuk and Kerketas extensional systems are unrelated to each other.

IV.1.2.2 Ikaria

For the Messaria detachment the data obtained using low-temperature thermochronometers have permitted to estimate a minimum slip rate of 7.6 ± 0.3 km/Myr between ~ 10 -3 Ma. Using the previous muscovite K/Ar ages obtained by Altherr et al. (1982) from the Ikaria nappe, I have estimated a slip rate of 8 ± 0.3 km/Myr for the ductile part of the Messaria extensional fault system which operated at ~ 11 -10 Ma. The combination of these results allow to deduce a minimum average slip rate for the Messaria extensional fault system of ~ 8 km/Myr. This rate would yield a minimum displacement of ~ 60 km for the period from ~ 11 to ~ 3 Ma.

Table IV.1. Data compilation for the extensional fault systems studied

Island	Normal faulting name	Displacing direction (top-to-the-...)		Minimum Slip rate (km/Myr) on extensional		Minimum age of granite intrusion (Ma)		Minimum average cooling rate (°C/Myr) granite country rocks	Duration (Ma)		Minimum age for the onset of		Minimum Offset (km)	Exhumation (km) related to
		Detachment	Shear	Detachment	Shear	S-type	I-type		Detachment	shear	Detachment	Shear		
Samos	Kalitheia	N				10.2 ± 0.4 (Hom. K/Ar on granitic dyke)		~58	~10-7		after 10.2 ± 0.4 (Hom. K/Ar)			
	Selcuk	ENE	ENE	8.1 ± 1.7					20-18		20.3 ± 1.8 (ZFT)		~18	
	Kerkiras	ENE	ENE								14.1 ± 1.6 (ZFT)			
Ikaria	Fanari	NNE				~11-10 (Musc. K/Ar)		~40	10-3	~11-10	10.3 ± 0.6 (ZFT)		~53	~7
	Messaria	NNE	NNE	7.6 ± 0.3 ¹								10.9 ± 0.2 (Musc. K/Ar)	~8	
Tinos	Vari	NE		~6.5		~1.5-1.4 (wr. Rb/Sr)		~60	12-9	~21-14	11.9 ± 1.2 (ZFT)		~20	~6-9
	Tinos	NE	NE	2.8 ± 0.5				~57	14-10		14.4 ± 1.2 (ZFT)		~12	
Mykonos	Mykonos	NE	NE	6.9 ± 0.7		~13 (Hom. K/Ar)		~75	13-9		13 ± 0.8 (ZFT)		~28	~11
Naxos	Mountsouna	NNE	NNE	8.4 ± 0.3	5.8 ± 1.3 ²	~1.5-1.1 (wr. U/Pb)	~1.4-1.2 (Hom. K/Ar)	~108	12-9	~20/16-12	11.8 ± 0.8 (ZFT)		~25	
	Mountsouna	NNE	NNE	6.4 ± 0.6		~13 (Musc. K/Ar)			13-10		13.1 ± 1.4 (ZFT)		~17	
Serifos		S	S				11.4 ± 1.0 (ZFT)	~39	11-9		11.4 ± 1.0 (ZFT)			
	Ios	SCSZ	S						15-9		14.5 ± 1.6 (ZFT)		~17	
	Ios, André or Coastal fault??	N		3.4 ± 0.5		~14 (Feld. Ar/Ar)		~36						

The detachment is the brittle part of an extensional fault system while the shear is the ductile part of an extensional fault system. The ages are given at 2σ error level. Data in italics are published results. The minimum age for the shearing and granite intrusion are from Altherr et al. (1982), Henjes-Kunst & Kreuzer (1982), Wijbrans & McDougall (1988), Mezger et al. (1995), Vandenberg & Lister (1996), Baldwin & Lister (1998), Bröcker & Franz (2000), Keay et al. (2001) and Ring et al. (2003). ZFT=zircon fission track dating; Hom. K/Ar=Homoblende K/Ar dating; Musc. K/Ar=Muscovite K/Ar dating; wr. Rb/Sr=whole rock Rb/Sr dating; wr + ph. Rb/Sr=whole rock and phenogite Rb/Sr dating; zr. U/Pb=zircon U/Pb dating; Feld. Ar/Ar=K-feldspar Ar/Ar dating.

¹ Slip rate estimated using the muscovite K/Ar ages obtained by Altherr et al. (1982) for rock from the Ikaria unit. ² Slip rate estimated by Jolin & Howard (1995). ³ The occurrence of allochthonous Pliocene sediments in the hangingwall of the Fanari detachment indicates that movement on it continued until or commenced after ~5 Ma (Kumrictis et al., 2004).

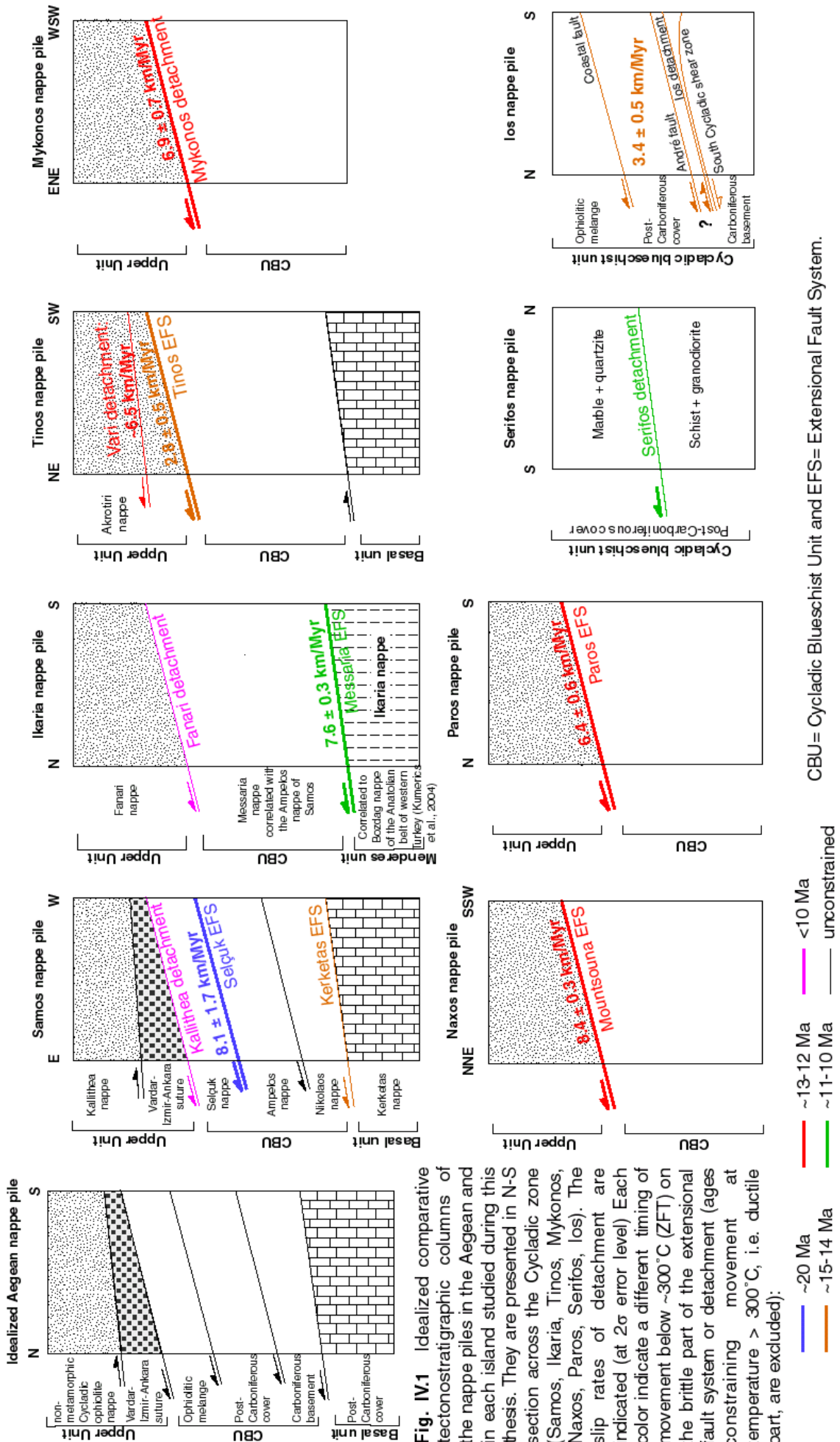


Table IV.2. Listing of ages obtained in the Cycladic islands.

Island and Sample Name	ZFT ages (Ma \pm 2 σ)	AFT ages (Ma \pm 2 σ)	Apatite (U-Th)/He ages (Ma \pm 2 σ)	Amp. Ar/Ar ages (Ma \pm 2 σ)	Number of samples collected	Number of samples dated
SAMOS						
Sa2	20.3 \pm 1.8	x	x	x		
Sa4	19.3 \pm 1.4	x	x	x		
Sa5	18.1 \pm 1.6	x	x	x	9	5
Sa7	7.3 \pm 1.0	x	x	x		
Sa9	14.1 \pm 1.2	x	x	x		
IKARIA						
Ik1	8.2 \pm 0.8	6.7 \pm 1.8	3.6 \pm 0.4	x		
Ik2	10.3 \pm 0.8	8.4 \pm 1.6	6.0 \pm 0.6	x		
Ik3	7.5 \pm 0.8	x	x	x		
Ik4	8.1 \pm 0.8	x	x	x	7	7
Ik5	x	6.8 \pm 1.4	x	x		
Ik6	8.6 \pm 1.8	6.2 \pm 1.6	5.6 \pm 0.4	x		
Ik7	6.3 \pm 0.6	5.2 \pm 1.8	x	x		
TINOS						
T2	12.2 \pm 1.0	11.9 \pm 2.0	10.0 \pm 0.6	x		
T3	13.3 \pm 0.8	12.6 \pm 2.6	10.4 \pm 0.8	13.7 \pm 0.7	7	4
T4	13.8 \pm 1.0	12.8 \pm 2.4	11.9 \pm 1.0	14.4 \pm 0.8		
T5	14.4 \pm 1.2	x	x	x		
MYKONOS						
M1	13.0 \pm 0.8	12.5 \pm 2.2	11.1 \pm 1.0	x		
M2	11.6 \pm 0.8	10.6 \pm 1.2	9.3 \pm 0.8	x	4	4
M3	10.9 \pm 1.0	10.5 \pm 1.8	10.5 \pm 0.8	x		
M4	10.7 \pm 0.8	10.5 \pm 1.8	8.9 \pm 0.8	x		
NAXOS						
Na1	x	8.2 \pm 1.2	13.4 \pm 0.8*	x		
Na2	x	8.7 \pm 2.6	14.5 \pm 0.8*	x		
Na3	9.7 \pm 0.8	9.3 \pm 2.6	8.9 \pm 0.6	x	6	6
Na4	10.6 \pm 0.8	9.8 \pm 1.8	9.1 \pm 0.8	x		
Na5	11.1 \pm 0.8	10.7 \pm 2.2	9.2 \pm 0.8	x		
Na6	11.8 \pm 0.8	11.2 \pm 1.6	10.7 \pm 1.0	x		
PAROS						
Ps3	11.1 \pm 1.0	10.5 \pm 2.0	x	x		
P16	13.1 \pm 1.4	12.7 \pm 2.8	x	x	3	3
P32	12.4 \pm 1.4	12.1 \pm 1.8	x	x		
SERIFOS						
Se2	11.4 \pm 1.0	10.3 \pm 2.6	7.5 \pm 0.5	x	4	2
Se3	8.6 \pm 1.6	x	x	x		
IOS						
I2	14 \pm 1.6	12.2 \pm 1.4	10.8 \pm 1.0	x		
I8	13.2 \pm 1.4	11 \pm 1.4	9.5 \pm 0.8	x	5	3
I11	14.5 \pm 1.6	x	x	x		
Total:	31	24	19	2	45	34
Total of dating carried out: 76						* Ages unused

Furthermore, the calculations of the cooling rate for the granodiorite and the metapelite of the Ikaria nappe yield results at respectively ~ 40 and $\sim 25^\circ\text{C}/\text{Myr}$. The fast cooling rate of the granite is thought to be due to early intrusion of the granite during extensional shearing in the colder Ikaria nappe. Therefore, the I-type granite had more potential for initially fast cooling, which is reflected by the steep cooling curve between the zircon and apatite PAZ's. After fast tectonically-controlled cooling from intrusion temperatures, the I-type granite had a similar cooling history as its country rocks. This interpretation would imply intrusion ages of 11-10 Ma for the two synkinematic granites.

IV.1.2.3 Tinos

Two detachments are exposed on Tinos: the Vari detachment and the Tinos detachment (Fig. IV.1). My data have constrained the slip rate and timing of Tinos extensional fault system. I have estimated a minimum slip rate for the brittle part of this extensional fault system of 2.8 ± 0.5 km/Myr. Two hornblende ages increase in the direction of footwall slip indicating that the Tinos extensional system was active at ~ 15 Ma. These ages allowed to calculate a slip rate of 1.8 ± 0.4 km/Myr for the Tinos detachment which is probably slightly underestimated owing to the high closure temperature of hornblende $^{40}\text{Ar}/^{39}\text{Ar}$ system (Ketcham, 1996) and poorly constrained with only two dating. Therefore, a minimum average slip rate of ~ 3 -2 km/Myr for the Tinos detachment can be approximated between 15-10 Ma which implies a displacement of ~ 15 -10 km. Furthermore, the data indicate rapid cooling of the I-type granite of Tinos between ~ 15 -10 Ma (from $\sim 550^\circ\text{C}$ to $\sim 80^\circ\text{C}$). These data demonstrated that the cooling history between $\sim 550^\circ\text{C}$ and $\sim 80^\circ\text{C}$ of the granodiorite was tectonically controlled by the Tinos extensional fault system (i.e. syntectonic granite).

IV.1.2.4 Mykonos

On Mykonos, the cooling rate of the monzogranite have been estimated at minimum $\sim 75^\circ\text{C}/\text{Myr}$ between 13-9 Ma. This rapid cooling is related to the Mykonos detachment which controlled granite exhumation. Therefore, a minimum slip rate have been constrain at 6.9 ± 0.7 km/Myr which implies a minimum displacement of 28 km from ~ 13 Ma to ~ 9 Ma. This displacement and the published dip angle of $\sim 30^\circ$ for the detachment (Avigad and Garfunkel, 1991; Faure et al., 1991; Lee and Lister, 1992) of Mykonos provides a minimum amount of exhumation of 14 km for the footwall of this detachment.

IV.1.2.5 Naxos/Paros

The Paros detachment is usually correlated to the Mountsouna extensional fault system of Naxos (Gautier et al., 1990; Gautier and Brun, 1994). The minimum average slip rate at 6.4 ± 0.6 km/Myr estimated for the Paros detachment is slower than the minimum average slip rate of 8.4 ± 0.3 km/Myr obtained on the brittle part of the Mountsouna extensional fault system on Naxos. I interpret that the slip rate difference was due to the huge granodiorite intrusion which occurred on Naxos around 14-12 Ma while on Paros only small S-type granites intruded the footwall of the detachment. Therefore, the data yield a rapid minimum slip rate at ~ 9 -8 km/Myr between 12-9 Ma implying a minimum displacement of ~ 25 km for the Naxos detachment while the minimum average slip rate at 7-6 km/Myr related to the Paros detachment yield a minimum displacement of ~ 17 km. I have also estimated that the tectonically controlled cooling rate of the huge Naxos granodiorite intrusion was very fast at a minimum of $\sim 108^\circ\text{C}/\text{Myr}$ from 300°C to 80°C (Table IV.1).

IV.1.2.6 Serifos

A rapid minimum cooling rate of $\sim 39^\circ\text{C}/\text{Myr}$ for the granodiorite of Serifos has been calculated (Table. IV.1). This fast cooling is thought to be tectonically controlled. Therefore, this result

supports a model of extensional thinning of the crust due to ductile shearing and low-angle normal faulting as the predominant process of pluton unroofing (Graseman et al., 2002). Consequently, I envisage that the cooling history of the granite reflects a synkinematical intrusion into the extensional fault system of Serifos which operated within passive margin sequence of the Cycladic Blueschist Unit (Fig. IV.1). Furthermore, the zircon fission track age from the I-type granite indicates that the Serifos detachment started to operate at minimum 11.4 ± 0.5 Ma (Table IV.1).

IV.1.2.7 Ios

On Ios, previous field work revealed a top-to-the south shear sense on the ductile South Cycladic Shear Zone. Owing to the lack of brittle indicators, any tectonic transport direction for the detachment part of this extensional fault system are necessarily speculative. I have demonstrated the usefulness of applying low-temperature thermochronometers to constrain the tectonic transport direction for detachments. The ages obtained on Ios get younger to the north indicating a top-to-the north sense of movement for the detachment responsible for exhumation from 300°C to 80°C . The data allow to calculate a fast minimum cooling rate for the rocks of the footwall of $\sim 36^\circ\text{C}/\text{Myr}$ and a minimum slip rate of 3.4 ± 0.5 km/Myr between ~ 15 -9 Ma implying a minimum displacement of 17 km (Table IV.1). Field work investigations would be necessary to identify the detachment which caused the age variation. I can only speculate that this detachment could be the Ios detachment related to the South Cycladic Shear Zone or the André fault located in the northern part close to the Ios extensional system or the Coastal fault exposed along the north coast of Ios (Fig. IV.1).

IV.2 Comparisons of the Miocene extensional fault systems in the Aegean

IV.2.1 Extensional fault system connections

The extensional fault system of Paros correlates with the Mountsouna extensional fault system of Naxos (Lee & Lister, 1992; Gautier and Brun, 1994). This interpretation has been corroborated by the similar estimated timing and slip direction of the detachment exposed on the two islands (Table IV.1, see sections IV.1.2.5).

On Ikaria, the Messaria extensional fault system (MEFS) is exposed at the top of the Ikaria nappe while the Fanari detachment occurred at the top of the Messaria nappe (Fig. IV.1). Kumerics et al. (2004), interpreted the Fanari detachment (top-to-the-NNE) as a brittle fault in the hangingwall of the Messaria extensional fault system ultimately related to the latter (Table IV.1). Kumerics et al. (2004) tentatively correlate the Fanari and Kallithea detachments on Ikaria and Samos because both have the same shear sense and have non-metamorphic units in their hangingwall, which contain Pliocene sediments. If it was accepted that the Fanari detachment is related to the MEFS, then the Kallithea detachment would also be part of the MEFS (Fig. IV.2a). Furthermore, our zircon fission track ages obtained on Samos indicate that the Kallithea, Selçuk and Kerketas extensional systems are unrelated to each other (Table IV.1, see section IV.1.2.1). Therefore, the Selçuk and Kerketas extensional systems are unrelated to the Messaria extensional fault of Ikaria (Fig. IV.2b).

The previous published data on the Vari detachment on Tinos, indicate a slip rate of ~ 6.5 km/Myr and a displacement of ~ 20 km between 12-9 Ma (Ring et al., 2003). These results are significantly higher than the slip rate and offset obtained during this thesis on the Tinos detachment (Table IV.1, see section IV.1.2.3). Therefore, the Vari and Tinos detachment seem to be unrelated. Thus, the ductile extensional shear zone on Tinos is not obviously related to the brittle Vari detachment on this island but with the Tinos detachment (Fig. IV.2a).

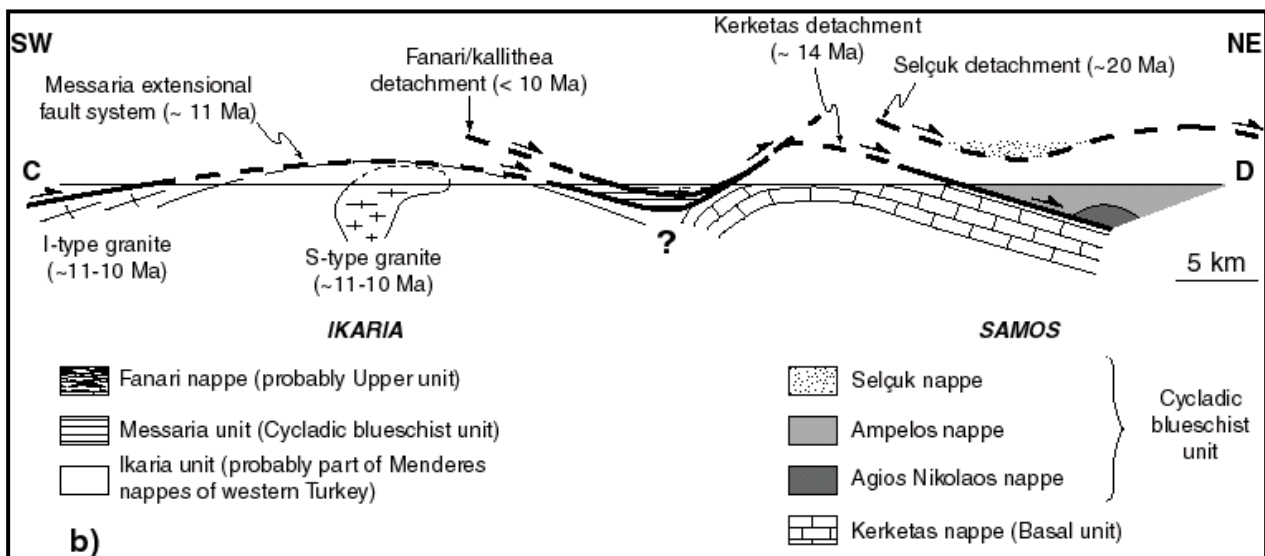
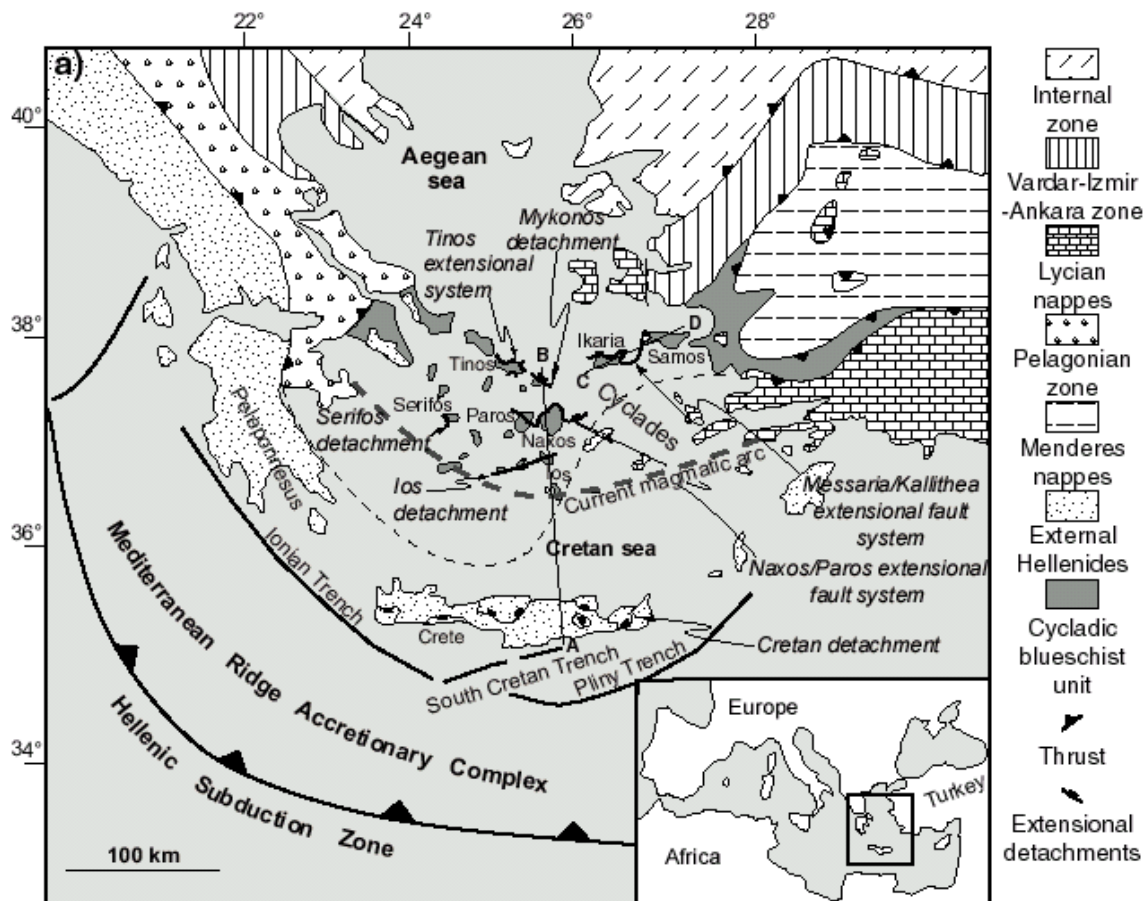


Fig. IV.2 (a) Generalized tectonic map of the Hellenides (modified after Ring et al., 2003) showing the Cycladic Blueschist unit and the main extensional fault system correlation (Naxos/Paros and Ikaria/Samos).

(b) Schematic NNE-SSW cross section across Ikaria and Samos showing fault connections between the Messaria, Fanari and Kallithea detachment.

IV.2.2 Timing

The fission track and (U-Th)/He data constrain the timing of the brittle part of the extensional fault systems (= detachments) exposed in the Cycladic islands. The zircon fission track method is a useful tool to estimate when the extensional fault systems reached the brittle part upper crust and detachment faulting commenced (see introduction section 2). Therefore the ZFT data yield a minimum age for the extensional fault system (shear zone + detachment). However, previously

published age data provide information about granite intrusions and the ductile part of the extensional fault system (= shear zone) which allow in conjunction with the new dating provided in this thesis to reconstitute the history of these extensional fault systems.

The oldest zircon fission track age obtained for the brittle part of the Selçuk extensional fault system indicate an age of 20.3 ± 0.9 Ma. This time constrain demonstrate that ductile shear associated with the Selçuk extensional fault system was the first system which started to operate (before ~ 21 -20 Ma) in the Cycladic islands studied during this thesis (Table IV.1, Fig. IV.1).

On Tinos, the ductile extensional shear zone is dated at 20.8 ± 2.1 Ma (Bröcker & Franz, 1998) while the fission track and (U-Th)/He dating demonstrated that the brittle Tinos extensional detachment operated between ~ 14 -10 Ma. The Tinos extensional fault system was active from ~ 21 Ma to ~ 10 Ma. On this island, a granodiorite intruded into the footwall of the Tinos extensional fault system at minimum ~ 16 Ma (Altherr et al., 1982; Avigad et al., 1998; Bröcker & Franz, 2000) followed by minor S-type granitic intrusions at ~ 15 -14 Ma (Altherr et al., 1982; Bröcker & Franz, 1998; Keay, 1998). A second detachment fault occurred between 12-9 Ma (see section IV.2.2.1; Ring et al., 2003).

According to Buick (1991), extensional shearing at the Naxos/Paros extensional fault system commenced before anatexis at or before ~ 20 -16 Ma (Buick 1991). Our data indicate that the Naxos/Paros detachment (brittle part of the extensional fault system) operated from 300°C to 80°C between 13-9 Ma. Therefore, the Naxos/Paros extensional fault system operated between ~ 20 -9 Ma. After the onset of extensional shearing small S-type granite bodies intruded at ~ 15 -14 Ma into the footwall of this extensional fault system followed by the intrusion of a huge granodiorite at ~ 14 -12 Ma on Naxos.

Vandenberg & Lister (1996) proposed a poorly constrained minimum age at ~ 13 Ma for shearing in the South Cycladic Shear Zone on Ios (see chapter III, section III.8.2 and III.8.4). However, the zircon fission track data obtained during this study constrain a minimum age of 14.5 ± 0.8 Ma for the detachment which exhumed the rock from 300°C to 80°C . Assuming that the detachment occurred at the same time or after ductile shearing, I propose that ductile shearing is probably slightly older than the previous estimation of ~ 13 Ma and occurred before 14.5 ± 0.8 Ma. My data indicate that the detachment operated between 15-9 Ma.

For the Kerketas, Mykonos, and Serifos extensional fault system constrains for detachment faulting (brittle part of the extensional fault systems) are provided by this study. The Kerketas detachment (Samos) started to operate at 14.1 ± 0.8 Ma while on Mykonos the detachment operated between ~ 13 -10 Ma and on Serifos the detachment started at 11.4 ± 0.5 Ma. On these two islands the granite intrusions are dated respectively at minimum ~ 13 Ma and ~ 12 Ma.

On Ikaria, initial movement in the ductile Messaria shear zone of the Messaria extensional fault system is estimated at ~ 11 -10 Ma (using the Muscovite K/Ar dating of Altherr et al., 1982) and was accompanied and aided by the intrusion of two synkinematic granites. The Messaria extensional fault system operated between ~ 11 -3 Ma.

The last detachments operating in the studied islands are probably the Kallithea and Fanari detachments exposed on Samos and Ikaria. The timing constraints indicate that the Kallithea detachment operated between ~ 10 -7 Ma while the Fanari detachment continued to move until or commenced to move after ~ 5 Ma (Kumerics et al., 2004).

The main conclusions concerning the timing of the events in the islands studied during this thesis are (Fig. IV.3):

- The Selçuk shear zone of Samos started to operate probably before 21 Ma followed by the Tinos and Naxos/Paros extensional shear zone at ~ 21 -20 Ma, the Ios extensional shear zone (or South Cycladic shear zone) at ~ 15 -14 Ma and the Messaria shear zone at ~ 11 Ma;
- On Naxos the granite intrusions occurred after the onset of shearing while on Ikaria the Messaria ductile shearing and the magmatism seem to be synchronous. On Tinos, the granite intrusion occurred slightly after or synchronously to the onset of ductile shearing of the Tinos extensional fault system;

- On Mykonos and Serifos, no timing constrain are provided about a possible ductile extensional shearing related to the detachment exposed on these islands;
- On Tinos and Ios several detachments seem to operate at the same time;
- A main period of detachment faulting activity is related to major granitic intrusions between 15-10 Ma;
- The Tinos granodiorite intruded at or before ~16 Ma;
- The Selçuk detachment related to the Selçuk shear zone is the older one while the Kallithea and Fanari detachments are the younger which operated between 10-7 Ma on Samos and ~5 Ma on Ikaria;
- No specific patterns of the timing events are related to the spatial locations of the islands.

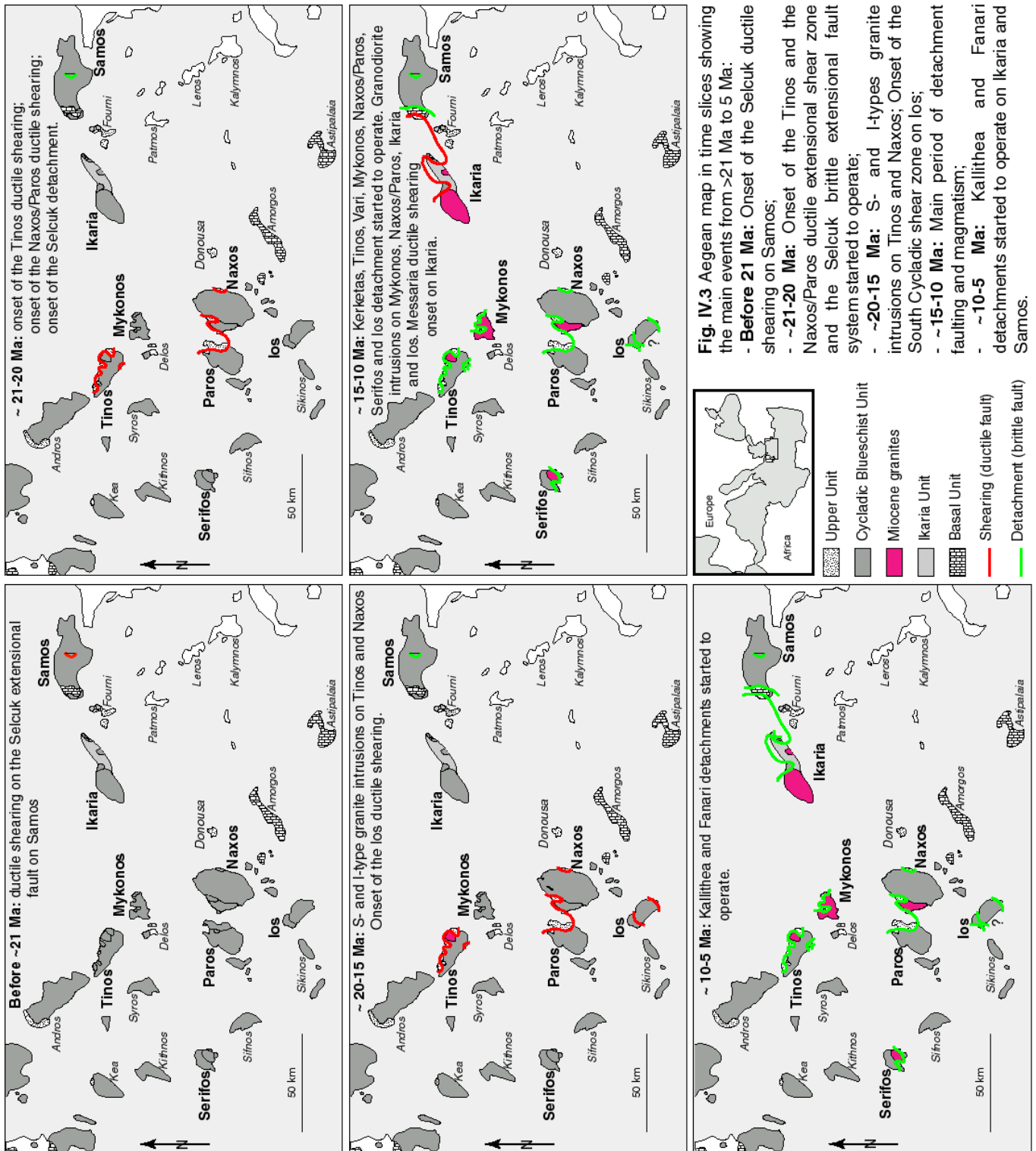


Fig. IV.3 Aegean map in time slices showing the main events from >21 Ma to 5 Ma:

- **Before 21 Ma:** Onset of the Selçuk ductile shearing on Samos;
- **~21-20 Ma:** Onset of the Tinos and the Naxos/Paros ductile extensional shear zone and the Selçuk brittle extensional fault system started to operate;
- **~20-15 Ma:** S- and I-types granite intrusions on Tinos and Naxos; Onset of the South Cycladic shear zone on Ios;
- **~15-10 Ma:** Main period of detachment faulting and magmatism;
- **~10-5 Ma:** Kallithea and Fanari detachments started to operate on Ikaria and Samos.

IV.2.3 Differences and similarities

The progressive evolution of ductile deformation in mylonitic shear zones towards brittle detachment fault systems has been documented on Ikaria, Tinos, Naxos/Paros and Ios islands (Buick 1991; Vandenberg & Lister 1996). On other islands (e.g. Mykonos, Serifos) ductile extensional shearing and/or brittle detachment faulting has also been reported (Avigad & Garfunkel 1989; Urai et al. 1990; Lee & Lister 1992; Gautier & Brun 1994; Lister & Raouzaïos 1996; Lister & Forster 1996; Ring et al. 2003) but the intimate association of ductile and brittle deformation is less clear.

The kinematic indicators in the Messaria shear zone and the brittle Messaria and Fanari detachments together with the spatial trend of footwall cooling ages indicate a general top-to-the-NNE sense of movement. However, in the southeast of Ikaria, late-stage top-to-the-SSW shear-sense indicators occur at the Messaria detachment (Kumerics et al., 2004). Kumerics et al. (2004) envisage that these late-stage minor antithetic extensional structures were related to updoming of Ikaria. Albeit, the South Cyclades shear zone (SCSZ) on Ios was top-to-the-S displacing and operated at minimum ~15-14 Ma (Vandenberg & Lister, 1996), the structural evolution of the shear zone is similar to that on Ikaria. Detailed structural mapping of Ios reveals non-coaxial ductile deformation with locally a top-to-the north sense of shear (see section III.8, Fig. III.25) (Gautier & Brun, 1994b; Vandenberg and Lister, 1996). Furthermore, as on Ikaria, the SCSZ was associated with the intrusion of granites. However, an important difference between Ios and Ikaria is that the SCSZ was top-to-the S displacing while the new data provided in this thesis suggest a top-to-the N sense of movement for the detachment faulting (Fig. IV.4). This antithetic displacement of shear zone and detachment faulting have been only demonstrated on Ios (Table IV.1 and Fig. IV.4).

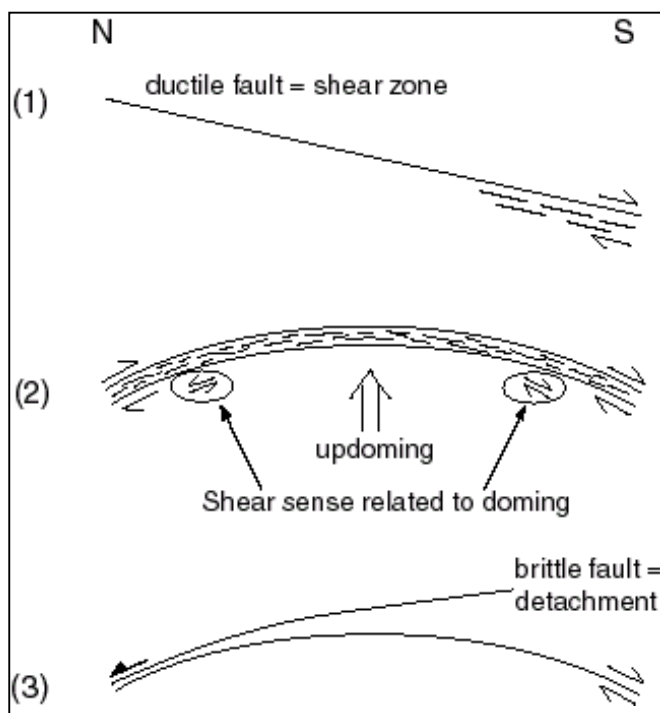


Fig. IV.4 Three stages of the evolution of the extensional deformation on Ios. (1) Inception of the South Cycladic shear zone. (2) Updoming of the footwall with minor antithetic top-to-the north sense of shear. (3) Inception at ~ 15-14 Ma of the detachment related top-to-the north.

Moreover, the slip rate estimated on Ios is significantly slower than on the other islands but similar to the one obtained on Tinos. The particularity of Ios and Tinos is that several detachments operated at the same time (Coastal fault, André fault and Ios detachment on Ios and Vari and Tinos detachment on Tinos). This could explain the slower slip rates because the extension could be distributed on several detachments. Moreover, on Ios there is no huge granitic intrusion as on the other islands which could help the movement along the detachment.

The minimum slip rates on the Selçuk, Messaria, Vari and Mykonos detachments range between 8-7 km/Myr while on Naxos the minimum slip rate estimated is slightly higher at ~9-8 km/Myr.

Buick & Holland (1989) suggested that extensional shearing commenced at P-T conditions of $\sim 400\text{--}700^\circ\text{C}$ and 5-7 kbar indicating that the extensional shear zone rooted in the lower crust (Fig. IV.5) and that the temperatures rose during extensional faulting. On the other islands the extensional shear zones rooted probably at the brittle/ductile transition (Kumerics et al., 2004). An other particularity of the Naxos extensional fault system is that the slip rate seems to increase from ~ 6 km/Myr (minimum average slip rate calculated using data provided by John & Howard, 1995) to $\sim 8\text{--}9$ km/Myr across the brittle/ductile transition while on Ikaria, the data indicate that the slip rate is constant ~ 8 km/Myr across this transition. I correlate the increase in the slip rate across the brittle/ductile transition on Naxos with the intrusion of the huge granodiorite at the detachment onset while on Ikaria the granodiorite intrusion is synchronous to the shearing onset (see section III.2 and III.5). Moreover, Figure IV.5 show that the footwall of the Mountsouna extensional fault system was significantly hotter than on other islands which can induce faster slip rate. Therefore, the specific context of extensional fault system occurrence on Naxos (high P-T conditions, post-onset shearing for the granodiorite intrusion) militate for slightly higher slip rate on the detachment related to the ductile extensional shearing.

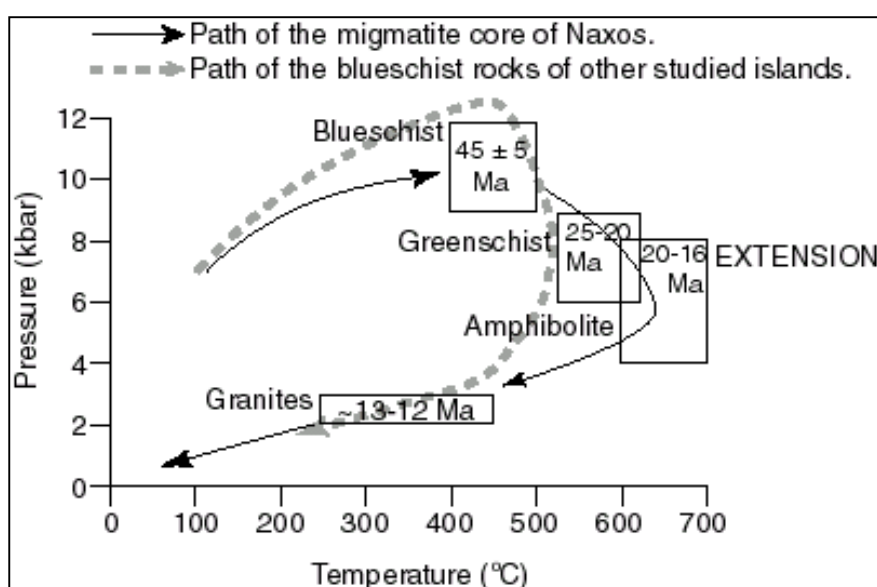


Fig. IV.5 Pressure-temperature-time history of the Naxos migmatite core (modified after Buick & Holland, 1989) compared to P-T history path (grey dotted line) of other islands studied. Boxes = metamorphic conditions according to Buick & Holland (1989).

Usually, the detachment exposed on Paros is correlated to the Mountsouna extensional fault system of Naxos (Gautier et al., 1990; Gautier and Brun, 1994). However, the minimum average slip rate of 6.4 ± 0.6 km/Myr estimated for the Paros detachment is slower than the minimum average slip rate of 8.4 ± 0.3 km/Myr obtained for the brittle part of the Mountsouna extensional fault system on Naxos but is similar to the minimum average slip rate of $\sim 5.8 \pm 1$ km/Myr estimated using the data provided by John and Howard (1995) for the ductile Mountsouna extensional fault system. Therefore, it can be argued that on Paros because no huge granite intrusion occurred, the slip rate is probably constant across the brittle/ductile transition while on Naxos the intrusion of granodiorite close to the brittle fault zone increased the weakness considerably and accelerated the slip rate as the footwall of the Mountsouna extensional fault system was exhumed and cooled. Consequently, the large scale Naxos/Paros extensional fault system could record locally faster slip rate (owing to huge granodiorite intrusion on Naxos).

To conclude, the differences and similarities related to the islands, are:

- An antithetic displacement of shear zone (top-to-the south) and detachment faulting (top-to-the north) have been only demonstrated on Ios (Fig. IV.6);
- The slow slip rate of ~ 3 km/Myr calculated for Tinos and Ios are related to the occurrence of several detachments at the same time;

- The Selçuk, Messaria, Vari and Mykonos detachments have similar slip rates at $\sim 8\text{-}7$ km/Myr;
- On Ikaria, the slip rate of the Messaria extensional fault system is constant across the brittle/ductile transition because the Ikaria granodiorite intruded synchronously to the shearing onset;
- The Naxos extensional fault system is unique in the Aegean owing to: **i)** the faster slip rate of $\sim 9\text{-}8$ km/Myr on the Naxos detachment which is related to the specific context of formation of the Naxos extensional fault system; **ii)** the increase in slip rates on Naxos across the brittle/ductile transition from ~ 6 km/Myr to $\sim 9\text{-}8$ km/Myr which is probably due to the intrusion of a huge granodiorite at the detachment onset and is related to specific P-T condition constrained on this island; **iii)** the extensional shear zones which rooted in the lower crust while on most islands (such as Ikaria, Tinos and Ios) they rooted probably at the brittle/ductile transition; **iv)** the large scale Naxos/Paros extensional fault system could record locally faster slip rate owing to huge granodiorite intrusion on Naxos.
- The main period of detachment faulting and magmatism activities have been defined at $\sim 15\text{-}10$ Ma. Therefore, the rapid cooling of the footwall and fast slip rate is tentatively interpreted to be due to the development of the detachments (especially the Messaria/Kallithea, Mykonos, Serifos, and Ios detachments) in relatively hot and thus weakened rocks of the magmatic arc;
- No specific patterns of the slip rates are related to the spatial locations of the islands.

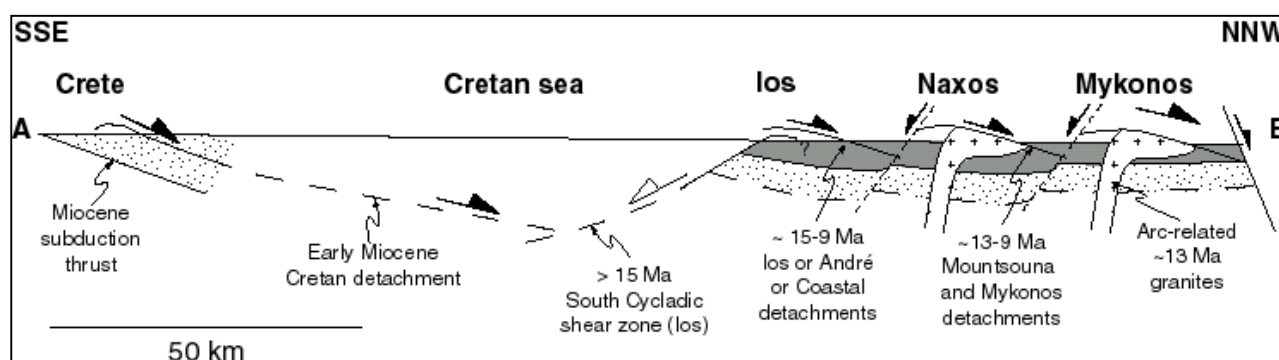


Fig. IV.6 Interpretative schematic NNE-SSW cross section showing nappe pile and time constraints (my data) for major Miocene detachments in southern Aegean (modified after Ring et al., 2003); Moutsouna and Mykonos detachments are related top-to-the NNE (Altherr et al., 1982; Buick, 1991; Gautier et al., 1993; Sánchez-Gómez et al., 2002) while the Ios detachment is related top-to-the NNE (my data) and the South Cycladic shear zone is top-to-the SSW (Vandenberg & Lister, 1996).

IV.3 Miocene normal faulting and exhumation

In the Cycladic islands, the tiny sedimentary outcrops which are preserved in some areas were tectonically juxtaposed above the metamorphic rocks and granites by low-angle normal faulting (Lister et al., 1984). A recent geochronological study of clasts from sedimentary sequences of Mykonos and Paros (Sánchez-Gómez et al., 2002) demonstrate that a part of the clastic material stored in the sedimentary sequences derived from rocks similar to those currently exposed in the footwall below the detachments. However, on these two islands, Sánchez-Gómez et al. (2002) do not find clasts corresponding to Cycladic blueschist unit (such as blueschist or even marble) or I-type granite exposed on Mykonos. This implies that the Cycladic blueschist unit and I-type granite were not exposed at the onset of extensional faulting at the Oligo-Miocene time (Gautier & Brun, 1994; Avigad et al., 1997; Sánchez-Gómez et al., 2002). The study of Sánchez-Gómez et al. (2002) does not allow to constrain where the footwall units related to extensional fault systems were situated in the crustal levels during the Miocene. However, Avigad et al. (1997) deduced from P-T-t paths of the Cycladic blueschists (Fig. IV.7) that at the onset of extensional fault systems (Oligo-

Miocene), blueschists were already situated at shallow crustal levels of no more than 20 km. This implies that intra/back-arc extension did not contribute significantly to the exhumation of the Cycladic blueschists from depths of ~60 km.

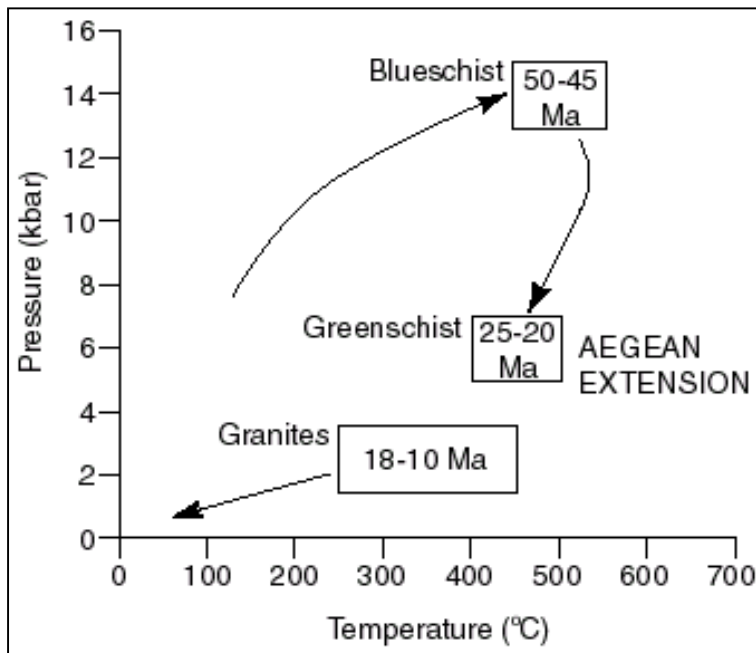


Fig. IV.7 Simplified pressure-temperature-time (P-T-t) path of blueschist facies rocks of the Cycladic blueschist belt exposed in the studied islands (modified from Avigad et al., 1997) except for the migmatite core of Naxos (see fig. IV.4). Data sources are: Andriessen et al., 1979; Altherr et al., 1982; Wijbrans & McDougall, 1988; Buick & Holland, 1989; Okrusch & Bröcker, 1990; Avigad et al., 1992; Bröcker et al., 1993.

The retrograd path is dominated by isothermal decompression. A major greenschist facies metamorphic overprint affected the blueschists in the Oligo-Miocene when they reached relatively shallow crustal levels corresponding to pressures of ~7-5 kbar. The Oligo-Miocene overprint was coeval with the onset of Aegean back arc extension.

Furthermore, Ring et al. (2003) estimated that the Vari detachment exposed on Tinos and Syros accomplished the final ~6-9 km of exhumation of the Cycladic blueschist unit during the Middle/Late Miocene (Table IV.1).

On the basis of strain and rotation data, Kumerics et al. (2004) showed that extensional faulting on Ikaria in the Messaria extensional fault system was accompanied by vertical thinning which caused ~20% or 3 km of exhumation of the Ikaria nappe during extensional shearing from ~15 km depth (deduced from metamorphic data). The remaining 80% of exhumation must be due to erosion and normal faulting. An assumed erosion rate of maximum 0.65 km/Myr (as estimated by Thomson et al. (1998) for Crete) between ~11-3 Ma (timing constrain for the duration of the Messaria extensional fault system of Ikaria) yields a total erosion of ~5 km. Thus, ~7 km of exhumation of the Ikaria nappe must have been due to normal faulting (Table IV.1). It has been estimated that the Mykonos detachment can accomplish rock exhumation from the last ~11 km of depth (Table IV.1, see section IV.1.2.4).

Therefore, Miocene normal faulting in the Cycladic islands seems to be only responsible for the final 15-10 % of total exhumation of rocks and particularly of the Cycladic blueschists. The Cycladic blueschists evidently achieved most of their exhumation before the onset of intra-arc normal faulting, i.e. in a fore-arc position (see section II.1.4). Furthermore, the compilation of the offsets calculated for Samos, Ikaria, Tinos, Mykonos, Naxos/Paros and Ios on detachments allow to estimate a total offset of >160 km, suggesting that detachment faulting is the primary agent achieving extension since Miocene time. This result is in agreement with the previous estimation of ~250 km proposed by McKenzie (1978).

Conclusions

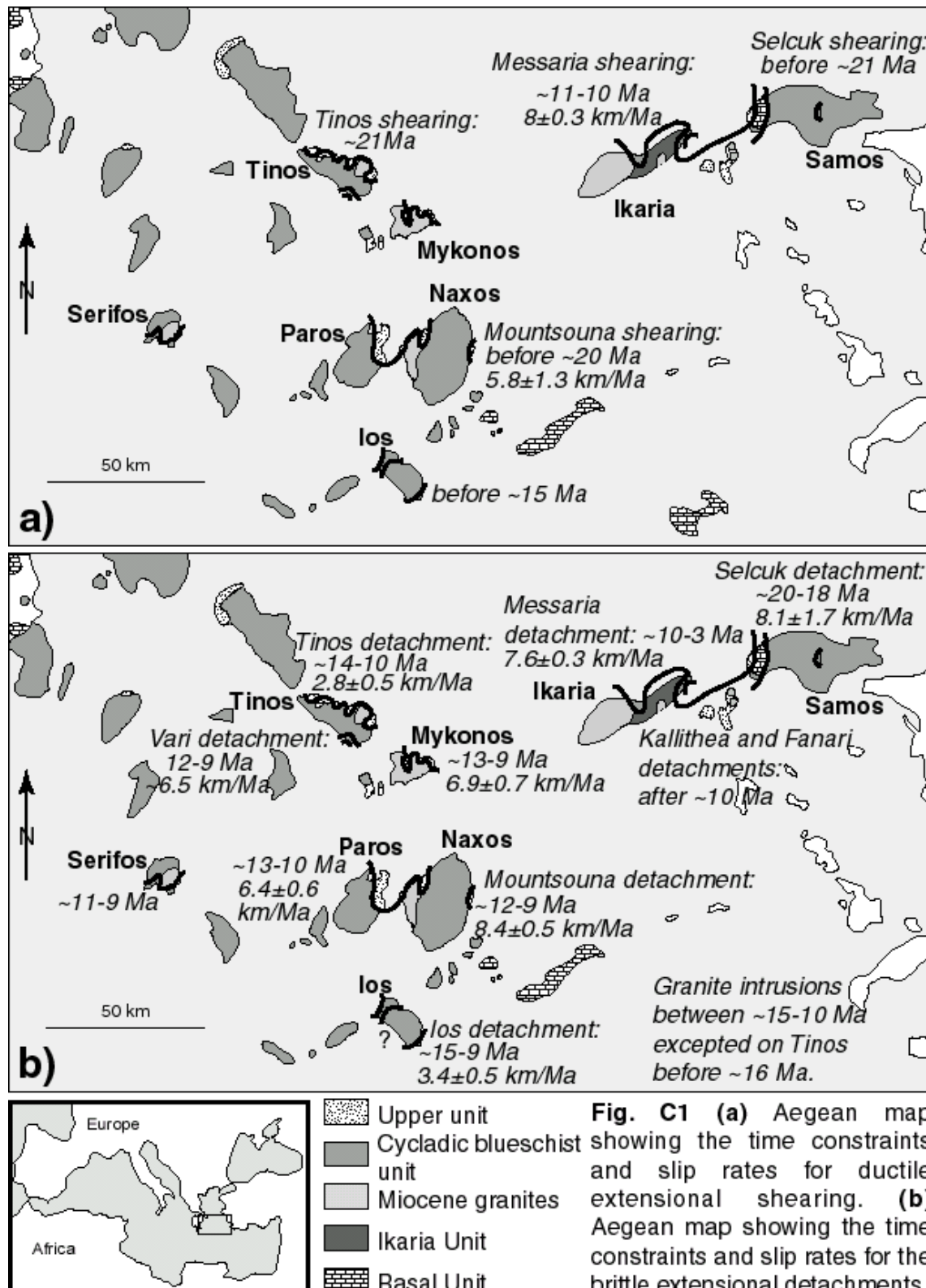
1. Conclusions of this thesis

During this thesis I have constrained, using thermochronology, the timing and slip rates of the Miocene extensional fault systems in the Cycladic islands of the Aegean Sea. From the results I have been able to make the following conclusions:

- Tectonic implications:

1. The time constraints on shear zones (ductile part of the extensional fault systems) indicate that the Selçuk shearing on Samos started to operate first >21 Ma followed by the Tinos and Naxos/Paros shear zones at ~21-20 Ma, the Ios shearing at ~15-14 Ma and the Messaria shearing of Ikaria at ~11 Ma (Fig. C1a). On the other hand, the timing constraints on detachments (brittle part of the extensional fault systems) demonstrate that the Selçuk detachment is the oldest detachment which started to operate at ~20 Ma while the Messaria/Kallithea/Fanari detachments are younger and operated between 10-3 Ma (Fig. C1b).
2. The timing of the events in the islands studied indicate that at about 15-10 Ma, when the granites intruded, a number of detachments started to operate (Kerketas, Messaria/Kallithea, Mykonos, Serifos and Ios) or continued to remain active (Tinos and Naxos/Paros extensional fault system). This intimate relationship between arc-related magmatism and extensional detachment (especially for the Messaria/Kallithea, Mykonos, Ios, and Serifos detachments) was aided by relatively high thermal gradients and extensional stresses caused by an extensional boundary condition related to the subduction-zone retreat. This induced rapid cooling of the footwalls at ~75-25°C/Myr and fast slip rates at ~8-7 km/Myr (Fig. C1).
3. The Naxos extensional fault system is unique in the Aegean because: **i)** the Naxos detachment exhibit a slightly faster slip rate at ~8-9 km/Myr related to the specific context of formation of the Naxos extensional fault system; **ii)** the slip rate slightly increased across the brittle/ductile transition from ~6 km/Myr to ~8-9 km/Myr owing to the intrusion of a huge granodiorite at the detachment onset and the specific P-T condition constrained on this island. On Ikaria, the slip rate on the Messaria extensional fault system is constant at ~8 km/Myr across the brittle/ductile transition because the Ikaria granodiorite intruded synchronously to the shearing onset; **iii)** the extensional shear zones were rooted in the lower crust while on most islands (such as Ikaria, Tinos and Ios) they were probably rooted at the brittle/ductile transition (Fig. C1); **iv)** the large scale Naxos/Paros extensional fault system could record locally faster slip rate owing to huge granodiorite intrusion on Naxos.
4. The synchronous occurrence of several detachments on a single island have been demonstrated on Tinos and Ios and may explain their slower slip rate at ~3 km/Myr (Fig. C1).
5. On Ikaria and Ios minor antithetic extensional structures have been recognized and related to updoming. However, an important difference between Ios and Ikaria is that the shear zone of Ios involved top-to-the south displacement while the new thermochronological data determined for this thesis indicate a top-to-the-N sense of movement for the detachment faulting. This antithetic displacement of a shear zone and a detachment has been only demonstrated on Ios.
6. No specific pattern of the extension timing and slip rate have been recognized in the Aegean.

7. Miocene normal faulting in the Cyclades is only responsible for the last 15-10% of the total exhumation required for the Cycladic blueschist unit (demonstrated on Ikaria and Mykonos), but fast-slipping normal faults were the primary agent for the opening of the Aegean Sea.



- Related to the methodology:

1. This study highlights the usefulness of applying different thermochronometers for constraining the long-term evolution of extensional fault systems. I have shown by the

combination of low-temperatures thermochronometers (300-80°C) that in some cases it is possible to constrain the brittle history of extensional fault systems. Therefore, the theoretical model of the rocks exhumation seems to be a good approximation which allow to define a minimum slip rate for the different detachments studied (Fig. C2).

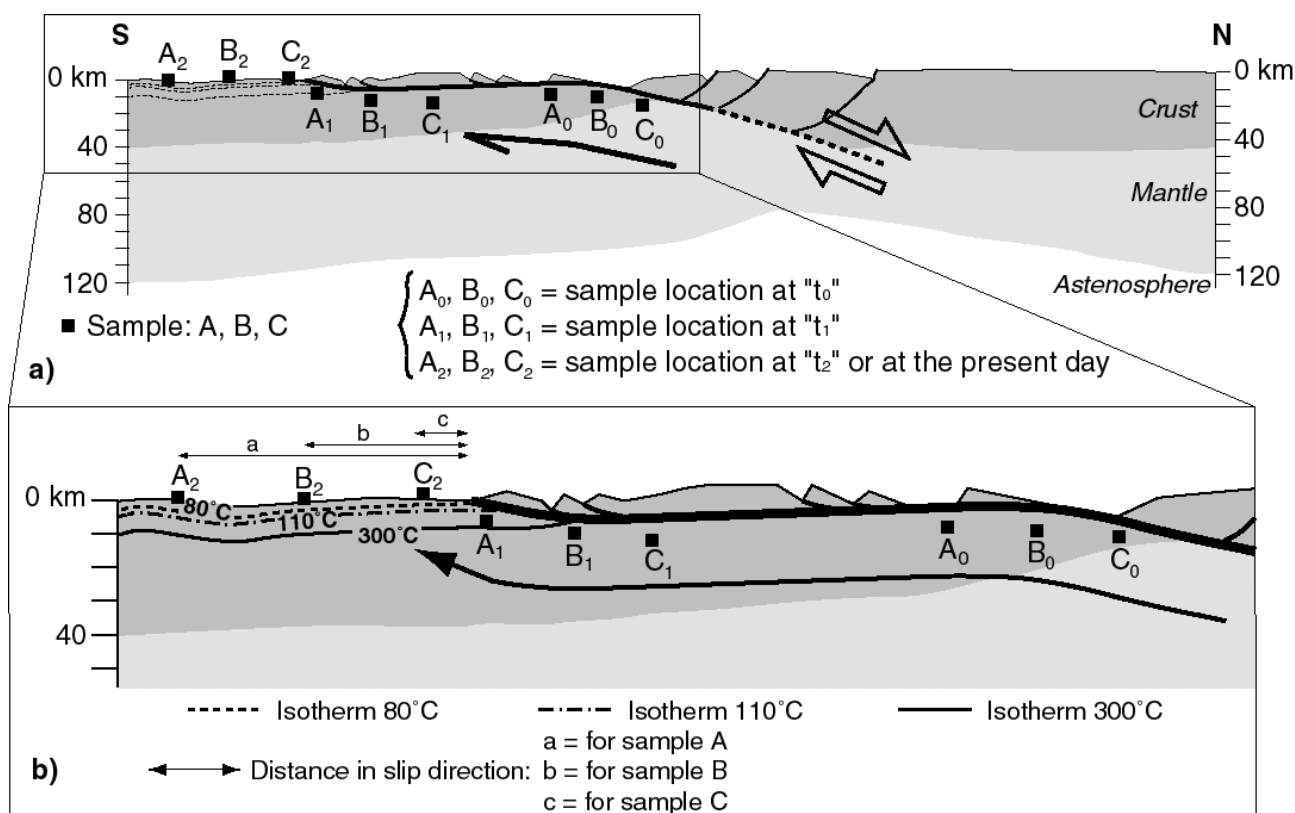


Fig. C2 Theoretical model of exhumation of the rocks to the Earth's surface during episodes of faulting. **(a)** Example of the geometry of fault showing rock locations in the time. **(b)** Enlargement of the circled zone showing the isotherms in the crust related to the methods of dating used during this study and the distance in the slip direction related to the actual samples locations on the field (A_2, B_2, C_2).

2. In some samples (such as S-type granite), (U-Th)/He dating can be problematic, giving poor reproducibility and/or anomalous ages. This is considered to be related to accessory mineral inclusions (such as zircon or monazite) and/or fluid infiltration and/or He implantation.

2. Future work and recommendations

To complete this study more age data would be necessary, especially on Ios, to better constrain the top-to-the-north detachment faulting recognized in this thesis and on Serifos to define the slip rate of the extensional fault system.

Furthermore, I discovered some problems with (U-Th)/He dating. This comparatively new method is ideally suited to monitor processes acting near the Earth surface. However, occasionally this isotopic system provides inconsistent data (compared to the fission track method) related to perturbation of the He system by fluid infiltration and/or He implantation. The last two aspects are technically very difficult to monitor thus it is hard to establish a definitive link between fluid alteration of a rock sample and its possible influence on the integrity of the apatite helium system. If implantation is the main cause of anomalous ages, the only way to test for such an effect is to map directly helium and U-Th profiles in apatite grains, ideally within the rock section where the relationship to adjacent grains are known. This is technically difficult and beyond the scope of this project but it is something that needs further detailed investigation in the near future.

Bibliography

- Altherr, R. & Siebel, E., 1977. Speculations on the geodynamic evolution of the Attic-Cycladic crystalline complex during alpidic times. In: *Geology of the Aegean Region*, (Eds. Kallergis, G.), Proceedings, VI Colloquium, Athens, pp. 347-351. Institute of Geology and Mineralogy Exploration.
- Altherr, R., Kreuzer, H., Wendt, I., Lenz, H., Wagner, G.H., Keller, J., Harre, W. & Höhndorf, A. 1982. A late Oligocene/early Miocene high temperature belt in the Attic-Cycladic crystalline complex (SE Pelagonian, Greece). *Geologisches Jahrbuch* **E23**, 97-164.
- Altherr, R., Kreuzer, H., Lenz, h., Wendt, I., Harre, W. & Dürr, S., 1994. Further Evidence for a late cretaceous Low-pressure/high-temperature Terrane in the Cyclades, Greece. *Chemie der Erde geochemistry* **54**, 319-328.
- Altherr, R. & Siebel, W., 2002. I-type plutonism in a continental back-arc setting: Miocene granitoids and monzonites from the central Aegean Sea, Greece. *Contributions to Mineralogy and Petrology* **143**, 397-415.
- Andriessen, P.A.M. 1978. Isotopic age relation within the polymetamorphic complex of the island of Naxos (Cyclades, Greece). PhD thesis, ZWO-Laboratorium voor Isotopen-Geologie, Utrecht University; *Geologica Ultraiectina* **3**.
- Andriessen, P.A.M., Boelrijk, N.A.I.M., Hebeda, E.H., Priem, E.H., Verdurmen, T., & Verschure, R.H. 1979. Dating the events of metamorphism and granitic magmatism in the Alpine Orogen of Naxos (Cyclades, Greece). *Contributions to Mineralogy and Petrology* **69**, 215-225.
- Andriessen, P.A.M. 1991. K-Ar and Rb-Sr age determinations on micas of impure marbles of Naxos, Greece: The influence of metamorphic fluids and lithology on the blocking temperature. *Schweizer Mineralogisch Petrographische Mitteilungen* **71**, 89-99.
- Armstrong, P.A., Ehlers, T.A., Chapman, D.S., Farley, K.A. & Kamp, P.J.J., 2002. Exhumation of the central Wasatch Mountains, Utah: 1. Patterns and Timing of Exhumation Deduced from Low-Temperature Thermochronology Data. *Journal of Geophysical Research*, in press.
- Aubourg, C., Hebert, R., Jolivet, L. & Cartayrade, G., 2000. The magnetic fabric of metasediments in a detachment shear zone: the example of Tinos island (Greece). *Tectonophysics* **321**, 219-236.
- Avigad, D. & Garfunkel, T. 1989. Low-angle faults above and below a blueschist belt—Tinos Island, Cyclades, Greece. *Terra Nova* **1**, 182-87.
- Avigad, D. & Garfunkel, Z., 1991. Uplift and exhumation of high-pressure metamorphic terrains: the example of the Cycladic blueschist belt (Aegean Sea). *Tectonophysics* **188**, 357-372.
- Avigad, D., Matthews, A., Evans, B.W. & Garfunkel, Z., 1992. cooling during the exhumation of a blueschist terrane: Sifnos (Cyclades), Greece. *European journal of Mineralogy* **4**, 619-634.
- Avigad, D., Garfunkel, Z., Jolivet, L. & Azañón, J.M., 1997. Back arc extension and denudation of Mediterranean eclogites. *Tectonics* **16**, 924-941.
- Avigad, D., 1998. High-pressure metamorphism and cooling on SE Naxos (Cyclades, Greece). *European Journal of Mineralogy* **10**, 1309-1319.
- Avigad, D., Baer, G. & Heimann, A., 1998. Block rotations and continental extension in the central Aegean Sea: palaeomagnetic and structural evidence from Tinos and Mykonos (Cyclades, Greece). *Earth and Planetary Science Letters* **157**, 1998.
- Bahr, R., Lippolt, H.J. & Wernicke, R.S., 1994. Temperature-induced ⁴He degassing of specularite and botryoidal hematite: A ⁴He retentivity study. *Journal of Geophysical Research* **99**, 17,695-17,707.
- Baker, J., Bickle, M.J., Buick, I.S., Holland, T.J.B. & Matthews, A., 1989. Isotopic and petrological evidence for the infiltration of water-rich fluids during the Miocene M2 metamorphism on Naxos, Greece. *Geochimica et Cosmochimica Acta* **53**, 2037-2050.
- Baker, J. & Matthews, A., 1995. The stable isotopic evolution of a metamorphic complex, Naxos, Greece. *Contributions to Mineralogy and Petrology* **120**, 391-403.
- Baldwin, S.L. & Harrison, T.M., 1989. Geochronology of blueschists from West-Central Baja California and the timing of uplift in subduction complexes. *Journal of Geology* **97**, 149-163.
- Baldwin, S.L., Harrison, T.M. & Fitzgerald, J.D., 1990. Diffusion of ⁴⁰Ar in metamorphic hornblende. *Contributions to Mineralogy and Petrology* **105**, 691-703.
- Baldwin, S.L., Lister, G.S., Hill, E.J., Foster, D.A. & McDougall, I., 1993. Thermochronologic constraints on the tectonic evolution of active metamorphic core complexes, d'entrecasteaux islands, Papua New Guinea. *Tectonics* **12**, 611-628.
- Baldwin, S.L. & Lister, G.S., 1994. P-T-t paths of Aegean metamorphic core complexes: Ios, Paros and Syros. *US Geological Survey Circular*, 19.
- Baldwin, S.L. & Lister, G.S., 1998. Thermochronology of the South Cyclades Shear Zone, Ios, Greece: Effects of ductile shear in the argon partial retention zone. *Journal of Geophysical Research* **103**, 7315-7336.
- Barbarand, J., Carter, A., Wood, I. & Hurford, T., 2003. Compositional and structural control of fission-track annealing in apatite. *Chemical Geology* **198**, 107-137.
- Bhandari, N., Bhat, S.G., Lal, D., Rajagopalan, G., Tamhane, A.S. & Venkatavaradan, V.S., 1971. Fission fragments in apatite: recordable track lengths. *Earth and Planetary Science letters* **13**, 191-199.
- Bigazzi, G., 1981. The problem of the decay constant λ_f of ²³⁸U. *Nuclear Tracks and Radiation Measurements* **5**, 35-44.
- Biliris, H., Paradissis, D., Veis, G., England, P., Featherstone, W., Parsons, B., Cross, P., Rands, P., Rayson, M., Sellers, P., Ashkenazi, V., Davison, M., Jackson, J. & Ambraseys, N., 1991. Geodetic determination of tectonic deformation in central Greece from 1900 to 1988. *Nature* **350**, 124-129.

- Bohnhoff, M., Makris, J., Papanikolaou, D. & Stavrakakis, G., 2001. Crustal investigation of the Hellenic subduction zone using wide aperture seismic data. *Tectonophysics* **343**, 239-262.
- Bonneau, M., Blake, M.C., Geyssant, J., Kienast, J.R., Lepvrier, C., Maluski, H. & Papanikolaou, D., 1980. Tectonique sur la signification des séries métamorphiques (schistes bleus) des Cyclades (Hellénides, Grèce). L'exemple de l'île de Syros. *Compte Rendu Académie des Sciences* **290**, 1463-1466.
- Bonneau, M. & Kienast, J.R., 1982. Subduction, collision et schistes bleus : l'exemple de l'Égée (Grèce). *Bulletin de la Société Géologique de France* **XXIV**, 785-791.
- Bonneau, M., 1982. Évolution géodynamique de l'arc égéen depuis le Jurassique supérieur jusqu'au Miocène. *Bulletin de la Société Géologique de France* **XXIV**, 229-242.
- Bonneau, M., 1984. Correlation of the Hellenide nappes in the south-east Aegean and their tectonic reconstruction. In: *The geology evolution of the eastern Mediterranean* (Eds Dixon, J.E. & Robertson, A.H.F.). Geological Society Special Publication **17**, 517-527.
- Boronkay, K. & Doutsos, T., 1994. Transpression and transtension within different structural levels in the central Aegean region. *Journal of Structural Geology* **16**, 1555-1573.
- Brady, R.J., 2002. Very high slip rates on continental extensional faults; new evidence from (U-Th)/He thermochronometry of the Buckskin Mountains, Arizona. *Earth and Planetary Science Letters* **197**, 95-104.
- Brandon, M.T., 1992. Decomposition of fission-track grain-age distributions. *American Journal of Science* **292**, 535-564.
- Brandon, M.T., Roden-Tice, M.K. & Garver, J.I. 1998. Late Cenozoic exhumation of the Cascadia accretionary wedge in the Olympic Mountains, NW Washington State. *Geological Society of America Bulletin* **110**, 985-1009.
- Brix, M.R., Stöckhert, B., Seidel, E., Theye, T., Thomson, S.N. & Küster, M., 2002. Thermobarometric data from a fossil zircon partial annealing zone in high pressure-low temperature rocks of eastern and central Crete, Greece. *Tectonophysics* **349**, 309-326.
- Bröcker, M., 1990. Blueschist-to-greenschist transition in metabasites from Tinos Island, Cyclades, Greece: Compositional control or fluid infiltration? *Lithos* **25**, 25-39.
- Bröcker, M., Kreuzer, H., Matthews, A. & Okrusch, M., 1993. ⁴⁰Ar/³⁹Ar and oxygen isotope studies of polymetamorphism from Tinos Island, Cycladic blueschist belt, Greece. *Journal of Metamorphic Geology* **11**, 223-240.
- Bröcker, M. & Franz, L., 1994. The Contact Aureole on Tinos (Cyclades, Greece). Field relationships, Petrography and P-T Conditions. *Chemie der Erde* **54**, 262-280.
- Bröcker, M. & Franz, L., 1998. Rb-Sr isotope studies on Tinos Island (Cyclades, Greece): additional time constraints for metamorphism, extent of infiltration-controlled overprinting and deformational activity. *Geological Magazine* **135**, 369-382.
- Bröcker, M. & Enders, M., 1999. U-Pb zircon geochronology of unusual eclogite-facies rocks from Syros and Tinos (Cyclade, Greece). *Geological Magazine* **136**, 111-118.
- Bröcker, M. & Franz, L., 2000. The contact aureole on Tinos (Cyclades, Greece): tourmaline-biotite geothermometry and Rb-Sr geochronology. *Mineralogy and Petrology* **70**, 257-283.
- Bröcker, M. & Enders, M., 2001. Unusual bulk-rock compositions in eclogite-facies rocks from Syros and Tinos (Cyclades, Greece): implications for U-Pb zircon geochronology. *Chemical Geology* **175**, 581-603.
- Brown, R., 1991. Backstacking apatite fission-track "stratigraphy": A method for resolving the erosional and isostatic rebound components of tectonic uplift histories. *Geology* **19**, 74-77.
- Buick, I.S. & Holland, T.J.B., 1989. The P-T-t path associated with crustal extension, Naxos, Cyclades, Greece. In: *Evolution of Metamorphic Belts* (eds Daly, J.S. et al.). Geological Society Special Publication **43**, 365-369.
- Buick, I.S. & Holland, T.J.B., 1991. The nature and distribution of fluids during amphibolite facies metamorphism, Naxos (Greece). *Journal of metamorphic Geology* **9**, 301-314.
- Buick, I.S., 1991a. Mylonite fabric development on Naxos, Greece. *Journal of Structural Geology* **13**, 643-655.
- Buick, I.S., 1991b. The late Alpine evolution of an extensional shear zone, Naxos, Greece. *Journal of the Geological Society of London* **148**, 93-103.
- Burbank, D., Leland, J., Fielding, E., Anderson, R., Brozovic, N., Reid, M. & Duncan, C., 1996. Bed rock incision, rock uplift and threshold hillslopes in the northwestern Himalayas. *Nature* **379**, 505-510.
- Burchfield, B.C., 1980. Eastern European Alpine system and Carpathian orocline as example of collision tectonics. *Tectonophysics* **63**, 31-61.
- Candan, O., Özcan Dora, O., Oberhänsli, R., Oelsner, F. & Dürr, S., 1997. Blueschist relics in the Mesozoic cover series of the Menderes Massif and correlations with Samos Island, Cyclades. *Schweizer Mineralogisch Petrographische Mitteilungen* **77**, 95-99.
- Carlson, W.D., Donelick, R.A. & Ketcham, R.A., 1999. Variability of apatite fission-track annealing Kinetics: I. Experimental results. *American Mineralogist* **84**, 1213-1223.
- Carpéna, V. & Mailhé, D., 1993. Fission-track dating: its importance in geology In: *Nuclear Methods of Dating* (eds Roth, E. & Poty, B.). Kluwer Academic Publishers, 189-233.
- Corrigan, J., 1991. Inversion of apatite fission track data for thermal history information. *Journal of geophysical research* **96**, 10,347-10,360.
- Dahl, P.S., 1996a. The crystal-chemical basis for argon retention in micas: Inferences from interlayer partitioning and implications for geochronology. *Contributions to Mineralogy and Petrology* **123**, 22-39.

- Dahl, P.S., 1996b. The effects of composition on retentivity of argon and oxygen in hornblende and related amphiboles: A field-tested empirical model. *Geochimica and Cosmochimica Acta* **60**, 3687-3700.
- Dalrymple, G.B. & Lanphere, M.A., 1971. $^{40}\text{Ar}/^{39}\text{Ar}$ technique of K-Ar dating: A comparison with the conventional technique. *Earth Planetary sciences letters* **12**, 300-308.
- Davis, D., Suppe, J. & Dahlen, F.A., 1983. Mechanics of Fold-and-Thrust Belts and Accretionary Wedges. *Journal of Geophysical Research* **88**, 1153-1172.
- Davis, G.H. & Coney, P.J., 1979. Geologic development of the Cordilleran metamorphic core complexes. *Geology* **7**, 120-124.
- Davis, G.H., 1983. Shear-zone model for the origin of metamorphic core complexes. *Geology* **11**, 342-347.
- De Wet, A.P., Miller, J.A., Bickle, M.J. & Chapman, J., 1989. Geology and geochronology of the Arnea, Sithonia and Ouranopolis intrusions, Chalkidiki Peninsula, northern Greece. *Tectonophysics* **161**, 65-79.
- Dercourt, J., Zonenshain, L.P., Ricou, L.-E., Kazmin, V.G., Le Pichon, X., Knipper, A.L., Grandjacquet, C., Sbertshikov, I.M., Geyssant, J., Lévrier, D.H., Pechersky, D.H., Boulin, J., Sibuet, J.-C., Savostin, L.A., Sorokhtin, O., Westphal, M., Bazhenov, M.L., Lauer, J.P. & Biju-Duval, B., 1986. Geological evolution of the Tethys belt from the Atlantic to the Pamirs since the Lias. *Tectonophysics* **123**, 241-315.
- Dewey, J.F., Pitman III, W.C., Ryan, W.B.F. & Bonnin, J., 1973. Plate tectonics and evolution of the Alpine system. *Geological Society of America Bulletin* **84**, 3137-3180.
- Dewey, J.F., Hempton, M.R., Kidd, W.S.F., Saroglu, F. & Sengör, A.M.C., 1986. Shortening of continental lithosphere: the neotectonics of Eastern Anatolia—a young collision zone. In: Coward, M.P. & Ries, A.C., *Collision tectonics*. Blackwell, 3-36.
- Dinter, D.A., Macfarlane, A., Hames, W., Isachsen, C., Bowring, S. & Royden, L., 1995. U-Pb and $^{40}\text{Ar}/^{39}\text{Ar}$ geochronology of the Symvolon granodiorite: Implications for the thermal and structural evolution of the Rhodope metamorphic core complex, northeastern Greece. *Tectonics* **14**, 886-908.
- Dixon, J.E., Feenstra, A., Jansen, J.B.H., Kreulen, R., Ridley, J., Salemink, J. & Schuiling, R.D., 1985. Chemical transport in metasomatic processes, excursion guide to fieldtrip, Seriphos, Syros, Naxos. In: *Nato Advanced Study Institute*, 1-51.
- Dodson, M.H., 1973. Closure temperature in cooling geochronological and petrological systems. *Contributions to Mineralogy and Petrology* **40**, 259-274.
- Dokka, R.K., Mahaffie, M.J. & Snoko, A.W., 1986. Thermochronologic evidence of major tectonic denudation associated with detachment faulting, northern Ruby Mountains-east Humboldt range, Nevada. *Tectonics* **5**, 995-1006.
- Dokka, R.K., 1993. Original dip and subsequent modification of a Cordilleran detachment fault, Mojave extensional belt, California. *Geology* **21**, 711-714.
- Donelick, R.A. & Miller, D.S., 1991. Enhanced TINT fission track densities in low spontaneous track density apatites using ^{252}Cf -derived fission fragment tracks: a model and experimental observation. *Nuclear Tracks and Radiation Measurements* **18**, 301-307.
- Donelick, R.A., 1991. Crystallographic orientation dependence of mean etchable fission track length in apatite: An empirical model and experimental observations. *American Mineralogist* **76**, 83-91.
- Draper, G. & Bone, R., 1981. Denudation rates, thermal evolution, and preservation of blueschist terrains. *Journal of Geology* **89**, 601-613.
- Duddy, I.R., Green, P.F. & Laslett, G.M., 1988. Thermal annealing of fission tracks in apatites; 3, Variable temperature behaviour. *Chemical Geology* **73**, 25-38.
- Duermeijer, C.E., Krijgsman, W., Langereis, C.G. & Ten Veen, J.H., 1998. Post early Messinian counter-clockwise rotations on Crete: implications for late Miocene to Recent kinematics of the southern Hellenic Arc. *Tectonophysics* **298**, 177-189.
- Dürr, S., Altherr, R., Keller, J., Okrusch, M. & Seidel, E., 1978. The median Aegean crystalline belt: Stratigraphy, structure, metamorphism, magmatism. In: *Alps, Appennines, Hellenides* (eds. Closs, H., et al.), pp. 537-564. Stuttgart: Schweizerbart.
- Ehlers, T.A., Armstrong, P.A. & Chapman, D.S., 2001. Normal fault thermal regimes and the interpretation of low-temperature thermochronometers. *Physics of the Earth and Planetary Interiors* **126**, 179-194.
- Ehlers, T.A. & Farley, K.A., 2003. Apatite (U-Th)/He thermochronometry: methods and applications to problems in tectonic and surface processes. *Earth and Planetary Science Letters* **206**, 1-14.
- Emre, T. & Sözbilir, H., 1997. Field evidence for metamorphic core complex, detachment faulting and accommodation faults in the Gediz and Büyük Menderes Grabens, Western Anatolia. *IESCA 1995 proceedings* **1**, 73-94.
- Ernst, W.G., 1975. Systematics of large-scale tectonics and age progressions in alpine and circum-pacific blueschist belts. *Tectonophysics* **26**, 229-246.
- Farley, K.A., Wolf, R.A., & Silver, L.T., 1996. The effects of long alpha-stopping distances on (U-Th)/He ages. *Geochimica et Cosmochimica Acta* **60**, 4223-4229.
- Farley, K.A., 2000. Helium diffusion from apatite: general behaviour as illustrated by Durango fluorapatite. *Journal of Geophysical Research* **105**, 2903-2914.
- Farley, K.A., 2002. (U-Th)/He dating: Technique, Calibrations, and applications. In: *Noble gas geochemistry* (Eds. Porcelli, P.D., Ballentine, C.J., Wieler, R.), *Review of Mineralogy and Geochemistry* **47**, 819-843.

- Farley, K.A. 2003. Problematic samples for apatite (U-Th)/He dating: Some possible causes and solutions. *Abstract AGU 2003 fall meeting*.
- Fassoulas, C., Kiliyas, A. & Mountrakis, D., 1994. Postnappe stacking extension and exhumation of high-pressure/low-temperature rocks in the island of Crete, Greece. *Tectonics* **13**, 127-138.
- Faure, G., 1986. Principles of geology. 2nd ed. Wiley, New York. 590p.
- Faure, M., Bonneau, M. & Pons, J., 1991. Ductile deformation and syntectonic granite emplacement during the late Miocene extension of the Aegea (Greece). *Bulletin de la Société Géologique de France* **162**, 3-11.
- Fayon, A.K., Peacock, S.M., Stump, E. & Reynolds, S.J. 2000. Fission track analysis of the footwall of the Catalina detachment fault, Arizona: Tectonic denudation, magmatism, and erosion. *Journal of Geophysical Research* **105**, 11.047-11.062.
- Fechtig, H. & Kalbitzer, S. 1966. The diffusion of argon in potassium bearing solids. In: *Potassium-Argon Dating* (eds. Schaeffer, O.A. and Zahringer, J.), Heidelberg, Springer, 68-106.
- Feehan, J.G. & Brandon, M.T. 1999. Contribution of ductile flow to exhumation of low-temperature, high-pressure metamorphic rocks: San Juan-Cascade nappes, NW Washington State. *Journal of Geophysical Research-Solid Earth* **104**, 10883-10902.
- Feenstra, A., 1985. Metamorphism of bauxites on Naxos, Greece. *Geologica Ultraiectina* **39**.
- Fitzgerald, P.G., Sorkhabi, R.B., Redfield, T.F. & Stump, E., 1995. Uplift and denudation of the central Alaska Range: A case study in the use of apatite fission track thermochronology to determine absolute uplift parameters. *Journal of Geophysical research* **100**, 20,175-20,191.
- Fleischer, R.L., Price, P.B. & Walker, R.M., 1975. *Nuclear Tracks in solids*. Berkeley: University of California Press, 605p.
- Foster, D.A., Marrison, T.M., Copland, P. & Heizler, M.T., 1990. Effect of excess argon within large diffusion domains on K-feldspar age spectra. *Geochimica and Cosmochimica Acta* **54**, 1699-1708.
- Foster, D.A., Miller, D.S. & Miller, C.S., 1991. Tertiary extension in the old woman mountains area, California: evidence from apatite fission track analysis. *Tectonics* **10**, 875-886.
- Foster, D.A., Gleadow, A.J.W., Reynolds, S.J. & Fitzgerald, P.G., 1993. Denudation of Metamorphic Core Complexes and the Reconstruction of the Transition Zone, West Central Arizona: Constraints From Apatite Fission Track Thermochronology. *Journal of Geophysical Research* **98**, 2167-2185.
- Foster, D.A. & John, B.E. 1999. Quantifying tectonic exhumation in an extensional orogen with thermochronology: examples from the southern Basin and Range province. In: *Exhumation processes: Normal faulting, ductile flow and erosion* (Eds. Ring, U., et al.), pp. 343-64. Geological Society of London, Special Publications no. 154.
- Forster, M.A. & Lister, G.S., 1999. Detachment faults in the Aegean core complex of Ios, Cyclades, Greece. In: *Exhumation Processes: Normal Faulting, Ductile Flow and Erosion* (eds Ring, U., et al.). Geological society, London, Special Publication **154**, 305-323.
- Forster, M.A. & Lister, G.S., 1999. Separate episodes of eclogite and blueschist facies metamorphism in the Aegean metamorphic core complex of Ios, Cyclades, Greece. In: *Continental Tectonics* (eds Mac Niocall, C. & Ryan, P.D.). Geological society of London Special publications **164**, 157-177.
- Fytikas, M., Innocenti, F., Manetti, P., Mazzuoli, R., Peccerillo, A. & Villari, L. 1984. Tertiary to Quaternary evolution of volcanism in the Aegean region. In: *The Geological evolution of the eastern Mediterranean* (Eds. Robertson, A.H.F. & Dixon, J.E), pp. 687-699. Geological Society of London, Special Publications no. 17.
- Galbraith, R.F. & Laslett, G.M., 1988. Some calculations relevant to thermal annealing of fission tracks in apatite. *Proceeding of the Royal Society of London* **419**, 305-321.
- Galbraith, R.F., Laslett, G.M., Green, P.F. & Duddy, I.R, 1990. Apatite fission track analysis; geological thermal history analysis based on a three dimensional random process of linear radiation damage. *Proceeding of the Royal Society of London* **332**, 419-438.
- Galbraith, R.F. 1992. Statistical models for mixed ages. 7th International Workshop on Fission Track Thermochronology, Abstracts with Programs, Philadelphia, July 1992.
- Galbraith, R.F. & Laslett, G.M., 1993. Stastistical models for mixed fission track age. *Nuclear Tracks and Radiation Measurements* **21**, 459-470.
- Gallagher, K., 1995. Evolving temperature histories from apatite fission-track data. *Earth and Planetary Science Letters* **136**, 421-435.
- Gallagher, K., Brown, R. & Johnson, c., 1998. Fission track analysis and its applications to geological problems. *Annual Revue Earth and Planetary Sciences* **26**, 519-572.
- Ganor, J., Matthews, A. & Paldor, N., 1991. Diffusional Isotopic Exchange Across an Interlayered Marble-Schist Sequence With an Application to Tinos, Cyclades, Greece. *Journal of Geophysical Research* **96**, 18073-18080.
- Gans, P.B., Miller, E.L., McCarthy, J. & Ouldcott, M.L., 1985. Tertiary extensional faulting and evolving ductile-brittle transition zones in the northern Snake Range and vicinity: New insights from seismic data. *Geology* **13**, 189-193.
- Gans, P.B. 1987. An open-system, two-layer crustal stretching model for the eastern Great Basin. *Tectonics* **6**, 1-12.
- Ganzawa, Y., 1983. Geometry factor in fission track dating. *Journal of the Faculty of Science* **20**, 195-202.
- Garfunkel, Z., Anderson, C.A. & Schubert, G., 1986. Mantle circulation and the lateral migration of subducted slabs. *Journal of Geophysical Research* **91**, 7205-7223.

- Garver, J.I., Brandon, M.T., Roden-Tice, M. & Kamp, P.J.J., 1999. Exhumation history of orogenic highlands determined by detrital fission-track thermochronology. In: *Exhumation processes: Normal faulting, ductile flow and erosion* (Eds. Ring, U., et al.). Geological Society of London, Special Publications no. **154**, 283-304.
- Gautier, P., Ballèvre, M., Brun, J-P. & Jolivet, L., 1990. Extension ductile et bassins sédimentaires mio-pliocènes dans les Cyclades (îles de Naxos et Paros). *Compte rendu Académie des Sciences* **310**, 147-153.
- Gautier, P., Brun, J-P. & Jolivet, L., 1993. Structure and Kinematics of upper Cenozoic extensional detachment on Naxos and Paros (Cyclades Islands, Greece). *Tectonics* **12**, 1180-1194.
- Gautier, P. & Brun, J.P., 1994. Crustal-scale geometry and kinematics of late-orogenic extension in the central Aegean (Cyclades and Evvia). *Tectonophysics* **238**, 399-424.
- Gautier, P. & Brun, J.P., 1994b. Ductile crust exhumation and extensional detachments in the central Aegean (Cyclades and Evvia island). *Geodinamica Acta* **712**, 57-85.
- Gautier, P., 1995. Géométrie crustale et cinématique de l'extension tardi-orogénique dans le domaine centre-égéen, îles des Cyclades et d'Eubée (Grèce). *PhD thesis, Géosciences Rennes, Université Rennes I*, 420p.
- Gleadow, A.J.W. & Lovering, J.F., 1977. Geometry factor for external detectors in fission track dating. *Nuclear Track Detection* **1**, 99-106.
- Gleadow, A.J.W. & Duddy, I.R., 1981. A natural long-term track annealing experiment on apatite. *Nuclear Tracks and Radiation Measurements* **5**, 169-74.
- Gleadow, A.J.W., 1981. Fission track dating methods: What are the real alternatives? *Nuclear Tracks and Radiation Measurements* **5**, 3-14.
- Gleadow, A.J.W., Duddy, I.R., Green, P.F. & Hegarty, K.A., 1986. Fission track lengths in the apatite annealing zone and the interpretation of mixed ages. *Earth and Planetary Science Letters* **78**, 245-254.
- Gleadow, A.J.W., Duddy, I.R., Green, P.F. & Lovering, J.F., 1986. Confined track lengths in apatite: a diagnostic tool for thermal history analysis. *Contributions to Mineralogy and Petrology* **94**, 405-415.
- Glodny, J., Bingen, B., Austrheim, H., Molina, J.F., & Rusin, A. 2002. Precise eclogitization ages deduced from Rb/Sr mineral systematics; the Maksyutov Complex, Southern Urals, Russia. *Geochimica et Cosmochimica Acta* **66**, 1221-1235.
- Grasemann, B., Zamolyi, A., Petrakakis, K., Rambousek, C. & Igelseder, C., 2002. Ein neuer Metamorphic Core Complex in den West-Kykladen (Serifos, Greichenland). *Erlanger Geologische Abhandlungen* **3**, 36-37.
- Green, P.F., 1981. A new look at statistics in fission-track dating. *Nuclear Tracks and Radiation Measurements* **5**, 77-86.
- Green, P.F. & Hurford, A.J., 1984. Thermal neutron dosimetry for fission track dating. *Nuclear Tracks and Radiation Measurements* **9**, 231-241.
- Green, P.F., 1985. Comparison of zeta calibration baselines for fission-track dating of apatite, zircon and sphene. *Chemical Geology* **58**, 1-22.
- Green, P.F., Duddy, I.R., Gleadow, A.J.W., Tinegate, P.R. & Laslett, G.M., 1986. Thermal annealing of fission tracks in apatite; 1, A qualitative description. *Chemical Geology* **59**, 237-253.
- Green, P.F., 1988. The relationship between track shortening and fission track age reduction in apatite: combined influences of inherent instability, annealing anisotropy, length bias and system calibration. *Earth and Planetary Science Letters* **89**, 335-352.
- Green, P.F., Duddy, I.R., Laslett, G.M., Hegarty, K.A., Gleadow, A.J.W. & Lovering, J.F., 1989a. Thermal annealing of fission tracks in apatite, 4, Quantitative modelling techniques and extension to geological timescale. *Journal of Petroleum Geology* **12**, 111-114.
- Green, P.F. & Duddy, I.R., 1989b. Some comments on Paleotemperature estimation from apatite fission track analysis. *Chemical Geology* **79**, 155-182.
- Grütter, H.S., 1993. Structural and metamorphic studies on Ios, Cyclades, Greece. *PhD Thesis, Cambridge*, 227p.
- Hall, R., Audley-Charles, M.G. & Carter, D.J., 1984. The significance of Crete for the evolution of the Eastern Mediterranean In: *The geological evolution of the eastern Mediterranean* (Eds Dixon, J.E. & Robertson, A.H.F.). Geological society Special publications **17**, 499-517.
- Hames, W.E. & Bownig, S.A., 1994. An empirical evaluation of the argon diffusion geometry in muscovite. *Earth and Planetary sciences letter* **124**, 161-167.
- Hansen, K. & Brooks, C.K., 2002. The evolution of the East Greenland margin as revealed from fission-track studies. *Tectonophysics* **349**, 93-111
- Harris, N.B.W., Kelley, S. & Okay, A.I., 1994. Post-collision magmatism and tectonics in northwest Anatolia. *Contributions to Mineralogy and Petrology* **117**, 241-252.
- Harrison, T.M., 1981. Diffusion of ⁴⁰Ar in hornblende. *Contributions to Mineralogy and Petrology* **78**, 324-331.
- Harrison, T.M., Duncan, I. & MacDougall, I., 1985. Diffusion of ⁴⁰Ar in biotite: Temperature, pressure and compositional effects. *Geochimica and Cosmochimica Acta* **49**, 2461-2468.
- Harrison, T.M., Lovera, O.M. & Heizler, M.T., 1991. ⁴⁰Ar/³⁹Ar results for alkali feldspar containing diffusion domains with differing activation energy. *Geochimica and Cosmochimica Acta* **55**, 1435-1448.
- Hatzfeld, D., Pedotti, G., Hatzidimitriou, P. & Makropoulos, K., 1990. The strain pattern in the western Hellenic arc deduced from a microearthquake survey. *Geophysical Journal International* **101**, 181-202.

- Hatzfeld, D., 1994. On the shape of the subducting slab beneath the Peloponnese, Greece. *Geophysical Research letter* **21**, 173-176.
- Hejl, E., 1995. Evidence for unetchable gaps in apatite fission tracks. *Chemical Geology* **122**, 259-269.
- Hejl, E., Riedl, H., Soulakellis, N., Van Den Haute, P. & Weingartner, H., 2000. Young Neogene tectonics and relief development on the Aegean islands of Naxos, Paros and Ios (Cyclades, Greece). *Mitteilungen der Österreichischen Geologischen Gesellschaft* **93**, 105-127.
- Hejl, E., Riedl, H. & Weingartner, H., 2002. Post-plutonic unroofing and morphogenesis of the Attic-Cycladic complex (Aegea, Greece). *Tectonophysics* **349**, 37-56.
- Henjes-Kunst, F. & Kreuzer, H., 1982. Isotopic dating of pre-Alpidic rocks from the island of Ios (Cyclades, Greece). *Contributions to Mineralogy and Petrology* **80**, 245-253.
- Hetzl, R., Ring, U., Akal, C. & Troesch, M., 1995. Miocene NNE-directed extensional unroofing in the Menderes Massif, southwestern Turkey. *Journal of the Geological Society of London* **152**, 639-654.
- Hetzl, R., Passchier, C.W., Ring, U. & Dora, O.O., 1995. Bivergent extension in orogenic belts : The Menderes Massif (southwestern Turkey). *Geology* **23**, 455-458.
- Hetzl, R. & Reischmann, T., 1996. Intrusion age of Pan-African augen gneisses in the southern Menderes Massif and the age of cooling after Alpine ductile extensional deformation. *Geological Magazine* **133**, 565-572.
- Hollister, L.S. and Crawford, M.L., 1986. Melt-enhanced deformation: A major tectonic process. *Geology* **14**, 558-561.
- House, M.A., Wernicke, B.P., Farley, K.A. & Dumitru, T.A., 1997. Cenozoic thermal evolution of the central Sierra Nevada, California, from (U-Th)/He thermochronometry. *Earth and Planetary Science Letters* **151**, 167-179.
- House, M.A., Wernicke, B.P. & Farley, K.A., 1998. Dating topography of the Sierra Nevada, California, using apatite (U-Th)/He ages. *Nature* **396**, 66-69.
- House, M.A., Farley, K.A. & Kohn, B., 1999. An empirical test of helium diffusion in apatite: borehole data from the Otway basin, Australia. *Earth and Planetary Science Letters* **170**, 463-474.
- House, M.A., Farley, K.A. & Stockli, D., 2000. Helium chronometry of apatite and titanite using Nd-YAG laser heating. *Earth and Planetary Science Letters* **183**, 365-368.
- Howard, K.A. and Foster, D.A., 1996. Thermal and unroofing history of a thick, tilted Basin-and-Range crustal section in the Tortilla Mountains, Arizona. *Journal of Geophysical Research* **101**, 511-522.
- Hughes, J.M., Cameron, M. & Crowley, K.D., 1989. Structural variations in natural F, OH and Cl apatites. *American Mineralogist* **74**, 870-876.
- Hurford, A.J. & Green, P.F., 1982. A users' guide to fission track dating calibration. *Earth and Planetary Science Letters* **59**, 343-354.
- Hurford, A.J. & Green, P.F., 1983. The zeta age calibration of fission-track dating. *Chemical Geology* **1**, 285-317.
- Hurford, A.J. & Hammerschmidt, K., 1985. $^{40}\text{Ar}/^{39}\text{Ar}$ and K/Ar dating of the bishop and fish canyon tuffs: calibration ages for fission-track dating standards. *Chemical Geology* **58**, 23-32.
- Hurford, A.J. & Watkins, R.T., 1987. Fission-track age of the tuffs of the buluk member, bakate formation, northern Kenya: a suitable fission-track age standard. *Chemical Geology* **66**, 209-216.
- Hurford, A.J. 1990b. Standardisation of fission-track dating calibration: Recommendation by the Fission Track Working Group of the I.U.G.S. Subcommittee on Geochronology. *Chemical Geology* **80**, 171-78.
- Hurford, A.J. & Carter, A., 1991. The role of fission track dating. In: *Discrimination of provenance in Developments in Sedimentary Provenance Studies* (eds Morton, A.C., Todd, S.P., Haughton, P.D.W.). Geological society of London, special publication **57**, 67-78.
- Jackson, J., 1994. Active tectonics of the Aegean region. *Annual Review Earth and Planetary Sciences* **22**, 239-271.
- Jansen, J.B.H. 1973. The geology of Greece, Island of Naxos. *Institute for Geology and Mineral Exploration* (Athens).
- Jansen, J.B.H. & Schuiling, R.D. 1976. Metamorphism on Naxos; petrology and geothermal gradients. *American Journal of Science* **276**, no. 10, 1225-1253.
- Jezequel, P., 1990. Méthodes actuelles de séparation de phases minérales en laboratoire. *Manuels & methods, éditions du BRGM*, 137p.
- John, B.E. & Howard, K.A. 1995. Rapid extension recorded by cooling-age patterns and brittle deformation, Naxos, Greece. *Journal of Geophysical Research* **100**, no. B7, 9969-9979.
- Jolivet, L., Brun, J-P., Lallemand, S. & Patriat, M., 1994b. 3D-kinematics of extension in the Aegean region from the early Miocene to the Present, insights from the ductile crust. *Bulletin de la Société Géologique de France* **165**, 185-209.
- Jolivet, L., Daniel, J.M., Truffert, C. & Goffé, B., 1994. Exhumation of deep crustal metamorphic rocks and crustal extension in arc and back-arc regions. *Lithos* **33**, 3-30.
- Jolivet, L., Goffé, B., Monié, P., Truffet-Luxey, C., Patriat, M. & Bonneau, M., 1996. Miocene detachment in Crete and exhumation P-T-t paths of high-pressure metamorphic rocks. *Tectonics* **15**, 1129-1153.
- Jolivet, L. & Patriat, M., 1999. Ductile extension and the formation of the Aegean Sea. In: *The Mediterranean Basins; Tertiary Extension within Alpine Orogen* (eds Durand, B., Jolivet, L., Horvath, F. & Seranne, M.). Geological society of London, special publication **156**, 427-456.
- Jolivet, L. & Goffé, B., 2000. Les dômes métamorphiques extensifs dans les chaînes de montagnes. Extension syn-orogénique et post-orogénique. *Compte Rendu Académie des Sciences* **330**, 739-751.
- Jolivet, L., 2001. A comparison of geodetic and finite strain pattern in the Aegean, geodynamic implications. *Earth and Planetary Science Letters* **187**, 95-104.

- Jolivet, M., 2001. Cinématique des déformations au nord Tibet, Thermochronologie traces de fission, modélisation analogique et étude de terrain. *PhD thesis, ISTEEM, Université Montpellier II*, 483p.
- Jonckheere, R., Mars, M., Van Den haute, P., Rebetez, M. & Chambaudet, A., 1993. L'apatite de Durango (Mexique) : Analyse d'un minéral standard pour la datation par traces de fission. *Chemical Geology* **103**, 141-154.
- Jones, C.E., Tarney, J., Baker, J.H. & Gerouki, F., 1992. Tertiary granitoids of Rhodope, northern Greece: magmatism related to extensional collapse of the Hellenic Orogen? *Tectonophysics* **210**, 295-314.
- Katzir, Y., Matthews, A., Garfunkel, Z., Schliestedt, M. & Avigad, D., 1996. The tectono-metamorphic evolution of a dismembered ophiolite (Tinos, Cyclades, Greece). *Geology Magazine* **133**, 237-254.
- Katzir, Y., Avigad, D., Matthews, A., Garfunkel, Z. & Evans, B.W., 1999. Origin and metamorphism of ultrabasic rocks associated with a subducted continental margin, Naxos (Cyclades, Greece). *Journal of Metamorphic Geology* **17**, 301-318.
- Keay, S. 1998. The geological evolution of the Cyclades, Greece: constraints from SHRIMP U-Pb geochronology. *Unpublished Ph.D. thesis, Australian National University Canberra*, 341p.
- Keay, S., Lister, G., Buick, I. 2001. The timing of partial melting, Barrovian metamorphism and granite intrusion in the Naxos metamorphic core complex, Cyclades, Aegean Sea, Greece. *Tectonophysics* **342**, 275-312.
- Ketcham, R. A. 1996. Thermal models of core-complex evolution in Arizona and New Guinea: Implications for ancient cooling paths and present-day heat flow. *Tectonics* **15**, 933-51.
- Kissel, C. & Laj, C., 1988. The tertiary geodynamical evolution of the Aegean arc: a paleomagnetic reconstruction. *Tectonophysics* **146**, 183-201.
- Kohlmann, A., 1978. Die Überprägung hochdruckmetamorpher Serien auf der Insel Tinos, Kykladen (Griechenland). *Diploma Thesis, Technische Universität Braunschweig*, 106p.
- Kohn, B.P. & Green, P.F., 2002. Low-temperature thermochronology: from tectonics to landscape evolution. *Tectonophysics* **349**, preface.
- Koukouvelas, I.K. & Kokkalas, S., 2003. Emplacement of the Miocene west Naxos pluton (Aegean Sea, Greece): a structural study. *Geology Magazine* **140**, 45-61.
- Kreulen, R., 1989. Fluid/rock ratios during metamorphism at Naxos: reply. *Contributions to Mineralogy and Petrology* **103**, 127-129.
- Kumerics, C., Ring, U., Brichau, S., Régnier, J.L & Glodny, J.. The extensional Ikaria shear zone and associated brittle detachment faults, Aegean Sea, Greece. *Geological Society of London*, **Submitted**.
- Kyung, J.B., Chwae, U., Im, C.B. & Lee, H. 2002. Palaeoseismological approach along Yangsan Fault in the southeastern part of the Korean Peninsula. *Geological Society of America*, Annual meeting.
- Laslett, G.M., Kendall, W.S., Gleadows, A.J.W. & Duddy, I.R., 1982. Bias in measurement of fission track lengths distributions. *Nuclear Tracks and Radiation Measurements* **6**, 79-85.
- Laslett, G.M., Gleadow, A.J.W. & Duddy, I.R., 1984. The relationship between fission-track length and track density in apatite. *Nuclear Tracks and Radiation Measurements* **9**, 29-38.
- Laslett, G.M., 1987. Thermal annealing of fission tracks in apatite. *Chemical Geology* **65**, 1-13.
- Laslett, G.M. & Galbraith, R.F., 1996. Statistical modelling of thermal annealing of fission tracks in apatite. *Geochimica et Cosmochimica Acta* **60**, 5117-5131.
- Le Pichon, X. & Angelier, J., 1979. The Hellenic arc and trench system: a key to the neotectonic evolution of the eastern Mediterranean area. *Tectonophysics* **60**, 1-42.
- Le Pichon, X., 1981. Subduction and tectonic pattern in the eastern Mediterranean area. *Terra Abstract* **1**, 105-108.
- Le Pichon, X., Chamot-Rooke, N., Huchon, P. & Luxey, P., 1993. Implications des nouvelles mesures de géodésie spatiale en Grèce et en Turquie sur l'extrusion latérale de l'Anatolie et de l'Égée. *Compte Rendu Académie des Sciences* **316**, 983-990.
- Le Pichon, X., Chamot-Rooke, N., Noomen, R. & Veis, G., 1994. Cinématique de l'Anatolie-Égée par rapport à l'Europe stable à partir d'une combinaison des mesures de triangulation géodésique sur 80 ans aux mesures de type Satellite Laser Ranging (SLR) récentes. *Compte Rendu Académie des Sciences* **318**, 1387-1393.
- Le Pichon, X., Chamot-Rooke, N., Lallemand, S., Noomen, R. & Veis, G., 1995. Geodetic determination of the kinematics of central Greece with respect to Europe: Implications for eastern Mediterranean tectonics. *Journal of Geophysical Research* **100**, 12,675-12,690.
- Lee, J. & Lister, G.S. 1990. Miocene extension in the Cycladic blueschist belt, Greece. *Eos* **71**, 1634.
- Lee, J. & Lister, G.S. 1992. Late Miocene ductile extension and detachment faulting, Mykonos, Greece. *Geology* **20**, 121-24.
- Lippolt, H.J., Leitz, M., Wernicke, R.S. & Hagedorn, B., 1994. (U-Th)/He dating of apatite: experience with samples from different geochemical environments. *Chemical Geology* **112**, 179-191.
- Lips, A.L.W., 1999. Temporal constraints on the kinematics of the destabilization of an orogen; syn- to post-orogenic extensional collapse of the Northern Aegean region. PhD thesis, Utrecht University; *Geologica Ultraiectina* **166**, 221p.
- Lister, G.S., Banga, G. & Feenstra, A. 1984. Metamorphic core complexes of Cordilleran type in the Cyclades, Aegean Sea, Greece. *Geology* **12**, 21-25.
- Lister, G.S., Etheridge, M.A. & Symonds, P.A., 1986. Detachment faulting and evolution of passive continental margins. *Geology* **14**, 246-250.

- Lister, G.S. & Davis, G.A., 1989. The origin of metamorphic core complexes and detachment faults formed during Tertiary continental extension in the northern Colorado River region, U.S.A.. *Journal of Structural Geology* **11**, 65-94.
- Lister, G.S. & Forster, M. 1996. Inside the Aegean metamorphic core complexes. *Technical Publications of the Australian Crustal Research Centre* **45**, 110p.
- Lister, G.S. & Keay, S.M. 1996. The lower plate of Ios Core Complex. In: *Inside the Aegean Metamorphic Core Complexes. Field Guide to the island of Thera, Ios, Naxos and Paros* (Eds. Lister, G.S. & Forster, M.A.). Australian Crustal Research Center, Technical Publications no. **45**.
- Lister, G.S. & Raouzaïos, A., 1996. The tectonic significance of a porphyroblastic blueschist facies overprint during Alpine orogenesis: Sifnos, Aegean sea, Greece. *Journal of Structural Geology* **18**, 1417-1435.
- Lovera, O.M., 1992. Computer programs to model $^{40}\text{Ar}/^{39}\text{Ar}$ diffusion data from multidomain samples. *Computers and Geosciences* **18**, 789-813.
- Lutz, T.M. & Omar, G., 1991. An inverse method of modelling thermal histories from apatite fission-track data. *Earth and Planetary Science Letters* **104**, 181-195.
- Makris, J. & Stobbe, C., 1984. Physical properties and state of the crust and upper mantle of the eastern Mediterranean Sea deduced from geophysical data. *Marine Geology* **55**, 347-363.
- Makropoulos, K.C. & Burton, P.W., 1984. Greek tectonics and seismicity. *Tectonophysics* **106**, 275-304.
- Maluski, H., Bonneau, M. & Kienast, J.R., 1987. Dating the metamorphic events in the Cycladic area: $^{39}\text{Ar}/^{40}\text{Ar}$ data from metamorphic rocks of the island of Syros (Greece). *Bulletin de la Société Géologique de France* **3**, 833-842.
- Maluski, H., Monié, P., Kienast, J.R. & Rahmani, A., 1990. Location of extraneous argon in granulitic-facies minerals: A paired microprobe-laser probe $^{40}\text{Ar}/^{39}\text{Ar}$ analysis. *Chemical Geology* **80**, 193-217.
- Martin, L. & Mascle, J., 1989. Structure et évolution récente de la mer Égée : III, La mer de Crète. *Compte Rendu Académie des Sciences* **309**, 2061-2067.
- Martin, L. & Mascle, J., 1989. Structure et évolution récente de la mer Égée : le domaine nord-égéen. *Compte Rendu Académie des Sciences* **309**, 1039-1045.
- Mastrakas, N. & Seymour, K.S., 2000. Geochemistry of Tinos granite: A window to the Miocene microplate tectonics of the Aegean region. *Neues Jahrbuch fuer Mineralogie* **175**, 295-315.
- McDougall, I. & Harrison, T.M., 1988. Geochronology and Thermochronology by the $^{40}\text{Ar}/^{39}\text{Ar}$ method. *Oxford University Press, New York* 212p.
- McInnes, B.I.A., Farley, K.A., Sillitoe, R.H. & Kohn, B.P., 1999. Application of apatite (U-Th)/He thermochronometry to the determination of the sense and amount of vertical fault displacement at the Chuquicamata Porphyry Copper Deposit, Chile. *Economic Geology* **94**, 937-948.
- McKenzie, D., 1978. Active tectonics of the Alpine-Himalayan belt: The Aegean Sea and surrounding regions. *Royal Astronomical Society Geophysical Journal* **55**, 217-254.
- Meghraoui, M., Gomez, F., Sbeinati, R., Van Der Woerd, J., Mouty, M., Darkal, A.N., Radwan, Y., Layyous, I., Al Najjar, H., Darawcheh, R., Hijazi, F., AL-Ghazzi, R. & Barazangi, M. 2003. Evidence for 830 years of seismic quiescence from palaeoseismology, archaeoseismology and historical seismicity along the Dead Sea Fault in Syria. *Earth and Planetary Science Letters* **210**, 35-52.
- Meijer, P.T., 1995. Dynamics of active continental margins: the Andes and the Aegean region. PhD thesis, Utrecht University; *Geologica Ultraiectina* **130**, 220p.
- Meijer, P.T. & Wortel, M.J.R., 1997. Present-day dynamics of the Aegean region: a model analysis of the horizontal pattern of stress and deformation. *Tectonics* **16**, 879-895.
- Melidonis, N.G., 1980. The geological structure and mineral deposits of Tinos island (Cyclades, Greece). *The geology of Greece* **13**, 1-80.
- Mercier, J.L., Sorel, D. & Simeakis, K., 1987. Changes in the state of stress in the overriding plate of a subduction zone: the Aegean Arc from the Pliocene to the Present. *Annales Tectonicæ* **1**, 20-39.
- Merrihue, C. & Turner, G., 1966. Potassium-argon dating by activation with fast neutrons. *Journal of Geophysical Research* **71**, 2852-2857.
- Mezger, K., Altherr, R., Okrusch, M., Henjes-Kunst, F. & Kreuzer, H., 1985. Genesis of acid/basic rock associations: a case study The Kallithea intrusive complex, Samos, Greece. *Contributions to Mineralogy and Petrology* **90**, 353-366.
- Mitchell, J.G., 1968a. The $^{40}\text{Ar}/^{39}\text{Ar}$ method for potassium-argon age determination. *Geochimica Cosmochimica Acta* **32**, 781-790.
- Mposkos, E. & Perdikatsis, V., 1984. Petrology of Glaucofane Metagabbros and Related Rocks from Samos, Aegean Island (Greece). *Neues Jahrbuch fuer Mineralogie* **149**, 43-63.
- Müller, R.D. & Roest, W.K., 1992. Fracture zones from combined Geosat and Seasat data. *Journal of Geophysical Research* **97**, 3337-3350.
- Nakanishi, T., Takemura, K., Okada, A., Morino, M., & Havashida, A. 2002. Identification of multiple faulting of the Median Tectonic line active fault system in the Tokushima Plain based on High-resolution sedimentological analysis. *Journal of Geography* **111**, 60-80.
- Nier, A.O., 1950. A redetermination of the relative abundances of the isotopes of carbon, nitrogen, oxygen, argon and potassium. *Physical Research* **77**, 789-793.

- O'Sullivan, P.B. & Parrish, R.R., 1995. The importance of apatite composition and single-grain ages when interpreting fission track data from plutonic rocks: a case study from the Coast Ranges, British Columbia. *Earth and Planetary Science Letters* **132**, 213-224.
- Oberhänsli, R., Monié, P., Candan, O., Warkus, F.C., Partzch, J.H. & Özcan Dora, O., 1998. The age of blueschist metamorphism in the Mesozoic cover series of the Menderes Massif. *Schweizer Mineralogisch Petrographische Mitteilungen* **78**, 309-316.
- Okay, A.I. & Kelley, S.P., 1994. Tectonic setting, petrology and geochronology of jadeite+glaucophane and chloritoid+glaucophane schists from north-west Turkey. *Journal of Metamorphic Geology* **12**, 455-466.
- Okay, A.I., Satir, M., Maluski, H., Siyako, M., Monié, P., Metzger, R. & Akyüz, S., 1996. Paleo- and Neo-Tethyan events in northwestern Turkey: geologic constraints. In Yin, A. & Harrison, T.M., *The tectonic evolution of Asia*. Cambridge University Press, 420-441.
- Okay, A.L. & Monié, P., 1997. Early Mesozoic subduction in the Eastern Mediterranean: Evidence from Triassic eclogite in northwest Turkey. *Geology* **25**, 595-598.
- Okay, A.L., Monod, O. & Monié, P., 2002. Triassic blueschists and eclogites from northwest Turkey: vestiges of the Paleo-Tethyan subduction. *Lithos* **64**, 155-178.
- Okrusch, M., Richter, P. & Katsikatsos, 1984. High-pressure rocks of Samos, Greece. *Geological Society Special publication* **17**, 529-536.
- Okrusch, M. & Bröcker, M., 1990. Eclogites associated with high-grade blueschists in the Cyclades archipelago, Greece: A review. *European Journal of Mineralogy* **2**, 451-478.
- Papanikolaou, D., 1979. Unités tectoniques et phases de déformation dans l'île de Samos, Mer Egée, Grèce. *Bulletin Société géologique de France* **XXI** **6**, 745-752.
- Papanikolaou, D.J., 1984. The three metamorphic belts of the Hellenides: a review and a kinematic interpretation. In: Robertson, A.H.F. & Dixon, J.E., *the geological evolution of the eastern Mediterranean*. *Geological Society Special Publication* **17**, 551-561.
- Parra, T., Vidal, O. & Jolivet, L., 2002. Relation between the intensity of deformation and retrogression in blueschist metapelites of Tinos Island (Greece) evidenced by chlorite-mica local equilibria. *Lithos* **63**, 41-66.
- Passchier, C.W., 1987. Stable positions of rigid objects in non-coaxial flow—a study in vorticity analysis. *Journal of Structural Geology* **9**, 679-690.
- Patria, M. & Jolivet, L., 1998. Post-orogenic extension and shallow-dipping shear zones; study of a brecciated decollement horizon in Tinos (Cyclades, Greece). *Compte Rendu Académie des Sciences* **326**, 355-362.
- Patzak, M., Okrusch, M. & Kreuzer, H., 1994. The Akrotiri Unit on the island of Tinos, Cyclades, Greece: Witness to a lost terrane of Late Cretaceous age. *Neues Jahrbuch fuer Geologie und Palaeontologie* **194**, 211-252.
- Pe-Piper, G. & Piper, D.J.W., 1989. Spatial and temporal variation in late Cenozoic back-arc volcanic rocks, Aegean Sea region. *Tectonophysics* **169**, 113-134.
- Pe-Piper, G. & Kotopouli, C.N., 1991. Geochemical characteristics of the Triassic igneous rocks of the island of Samos, Greece. *Neues Jahrbuch fuer Mineralogie* **162** **2**, 135-150.
- Pe-Piper, G., 2000. Origin of S-type granites coeval with I-type granites in the Hellenic subduction system, Miocene of Naxos, Greece. *European Journal of Mineralogy* **12**, 859-875.
- Pinet, P. & Souriau, M., 1988. Continental erosion and large-scale relief. *Tectonics* **7**, 563-582.
- Platt, J.P., 1986. Dynamics of orogenic wedges and the uplift of high-pressure metamorphic rocks. *Geological Society America Bulletin* **97**, 1037-1053.
- Platt, J.P., 1993. Exhumation of high-pressure rocks: a review of concepts and processes. *Terra Nova* **5**, 119-133.
- Platt, J.P. & England, P.C., 1993. Convective removal of lithosphere beneath mountain belts: Thermal and mechanical consequences. *American Journal of Sciences* **294**, 307-336.
- Platt, J.P., Soto, J.I., Whitehouse, M.J., Hurford, A.J. & Kelley, S.P., 1998. Thermal evolution, rate of exhumation, and tectonic significance of metamorphic rocks from floor of the Alboran extensional basin, western Mediterranean. *Tectonics* **17**, 671-689.
- Raouzaïos, A., Lister, G.S. & Foster, D.A., 1996. Oligocene exhumation and metamorphism of eclogite-blueschists from the island Sifnos, Cyclades, Greece. *Geological Society of Australia Bulletin* **41**, p 358.
- Ravenhurst, C.E. & Donelick, R.A., 1992. fission-track thermochronology. Short course handbook on low-temperature thermochronology. *Mineralogical association of Canada* (eds Zeuhilli, M. & Reynolds, P.H.), 21-42.
- Reddy, S.M., Wheeler, J. & Cliff, R.A., 1999. The geometry and timing of orogenic extension; an example from the Western Italian Alps. *Journal of Metamorphic Geology* **17**, 573-589.
- Reinecke, T., Altherr, R., Hartung, B., Hatzipanagiotou, K., Kreuzer, H., Harre, W., Klein, H., Keller, J., Geenen Elke & Böger, H., 1982. Remnants of a Late Cretaceous High Temperature Belt on the Island of Anáfi (Cyclades, Greece). *Neues Jahrbuch fuer Mineralogie* **145**, 157-182.
- Reiners, P.W. & Farley, K.A., 1999. Helium diffusion and (U-Th)/He thermochronometry of titanite. *Geochimica et Cosmochimica Acta* **63**, 3845-3859.
- Reiners, P.W., Brady, R., Farley, K.A., Fryxell, J.E., Wernicke, B. & Lux, D., 2000. Helium and argon thermochronometry of the Gold Butte block, south Virgin Mountains, Nevada. *Earth and Planetary Science Letters* **178**, 315-326.
- Reiners, P.W., 2002. (U-Th)/He Chronometry Experience a Renaissance. *EOS* **83**, 21-26.

- Reiners, P.W., Farley, K.A. & Hickes, H.J., 2002. He diffusion and (U-Th)/He thermochronometry of zircon: initial results from Fish Canyon Tuff (Colorado) and Gold Butte (Nevada). *Tectonophysics* **349**, 297-308.
- Rey, P., Vanderhaeghe, O. & Teyssier, C., 2001. Gravitational collapse of the continental crust: definition, regimes and modes. *Tectonophysics* **342**, 435-449.
- Ricou, L-E., 1994. Tethys reconstructed: plates, continental fragments and their boundaries since 260 Ma from Central America to South-eastern Asia. *Geodynamica Acta* **7**, 169-218.
- Ridley, J., 1984. Listric normal faulting and the reconstruction of the synmetamorphic structural pile of the Cyclades In: *The geological evolution of the eastern Mediterranean* (Eds Dixon, J.E. & Robertson, A.H.F.). Geological society Special publications **17**, 755-761.
- Ring, U. & Brandon, M.T., 1994a. Kinematic data for the Coast Range fault and implications for Carpholite, sudoite, and chloritoid in low-grade high-pressure metapelites from Crete and the Peloponnese, Greece. *European Journal of Mineralogy* **4**, 487-507.
- Ring, U. & Brandon, M.T., 1994b. Kinematic data for the Coast Range fault and implications for exhumation of the Franciscan subduction complex. *Geology* **22**, 735-738.
- Ring, U., 1995. Horizontal contraction or horizontal extension? Heterogeneous Late Eocene and Early Oligocene general shearing during blueschist and greenschist facies metamorphism at the Pennine-Austroalpine boundary zone in the Western Alps. *Geologische Rundschau* **84**, 843-859.
- Ring, U., Brandon, M.T., Willett, S.D. & Lister, G.S. 1999a. Exhumation processes. In: *Exhumation processes: Normal faulting, ductile flow and erosion* (Eds. Ring, U., et al.). Geological Society of London, Special Publications no. **154**, 1-27.
- Ring, U., Gessner, K., Güngör, T. & Passchier, C.W., 1999b. The Menderes Massif of western Turkey and the Cycladic Massif in the Aegean- do they really correlate? *Journal of the Geological Society* **156**, 3-6.
- Ring, U., Laws, S. & Bernet, M., 1999c. Structural analysis of a complex nappe sequence and late-orogenic basins from the Aegean Island of Samos, Greece. *Journal of Structural Geology* **21**, 1575-1601.
- Ring, U., Brachert, T. & Fassoulas, C., 2001a. Middle Miocene graben development in Crete and its possible relation to large-scale detachment faults in the southern Aegean. *Terra Nova* **13**, 297-304.
- Ring, U., Layer, P.W. & Reischmann, T., 2001b. Miocene high-pressure metamorphism in the Cyclades and Crete, Aegean Sea, Greece: Evidence for large-magnitude displacement on the Cretan detachment. *Geology* **29**, 395-398.
- Ring, U. & Reischmann, T. 2002. The weak and superfast Cretan detachment, Greece: Exhumation at subduction rates in extrusion wedges. *Journal Geological Society London* **159**, 225-28.
- Ring, U. and Layer, P.W., 2003. High-pressure metamorphism in the Aegean, eastern Mediterranean: Underplating and exhumation from the Late Cretaceous until the Miocene to Recent above the retreating Hellenic subduction zone. *Tectonics* **22** (3), 1022, doi: 10.1029/2001ITC001350, 23p.
- Ring, U., Thomson, S.N. & Bröcker, M. 2003. Fast extension but little exhumation: the Vari detachment in the Cyclades, Greece. *Geological Magazine* **140**, 245-252.
- Ring, U., Johnson, C., Hetzel, R. & Gessner, K. 2003a. Tectonic denudation of a Late Cretaceous–Tertiary collisional belt: regionally symmetric cooling patterns and their relation to extensional faults in the Anatolide belt of western Turkey. *Geological Magazine*, **140**, 421-441.
- Robertson, A.H.F. & Dixon, J.E., 1984. Introduction: aspects of the geological evolution of the eastern Mediterranean. In: *the geological evolution of the eastern Mediterranean* (Eds Robertson, A.H.F. & Dixon, J.E.). Geological society of London, special publication **17**, 1-74.
- Robertson, A.H.F., Clift, P., Degnan, P.J. & Jones, G. 1991. Palaeogeographic and palaeotectonic evolution of the Eastern Mediterranean Neotethys. *Palaeogeography, Palaeoclimatology, Palaeoecology* **87**, 289-343.
- Robertson, A.H.F., 1994. Role of the tectonic facies concept in orogenic analysis and its application to Tethys in the Eastern Mediterranean region. *Earth Sciences Review* **37**, 139-213.
- Rolandone, F. & Jaupart, C., 2002. The distributions of slip rate and ductile deformation in a strike-slip shear zone. *Geophysical Journal International* **148**, 179-192.
- Royden, L.H., 1993a. The tectonic expression slab pull at continental convergent boundaries. *Tectonics* **12**, 303-325.
- Royden, L.H., 1993b. The steady state thermal structure of eroding orogenic belts and accretionary prisms. *Journal of Geophysical Research* **98**, 4487-4507.
- Rutherford, E., & Soddy, F., 1903. Radioactive change. *Phil. Mag. Ser.* **65**, 576-591.
- Salemink, J., 1980. On the geology and petrology of Serifos Island (Cyclades, Greece). *Annual Geology Pays Hellenic* **30**, 342-365.
- Sánchez-Gómez, M., Avigad, D. & Heimann, A., 2002. Geochronology of clasts in allochthonous Miocene sedimentary sequences on Mykonos and Paros Islands: implications for back-arc extension in the Aegean Sea. *Journal of the Geological Society* **159**, 45-60.
- Schermer, E.R., 1993. Geometry and kinematics of continental basement deformation during the Alpine orogeny, Mt Olympos region, Greece. *Journal of Structural Geology* **15**, 571-591.
- Schmitz, M.D. & Bowring, S.A., 2001. U-Pb zircon and titanite systematics of the fish Canyon Tuff: an assessment of high-precision U-Pb geochronology and its application to young volcanic rocks. *Geochimica et Cosmochimica Acta* **65**, 2571-2587.
- Seidel, E., Kreuzer, H. & Harre, W., 1982. A late Oligocene/Early Miocene High Pressure Belt in the External Hellenides. *Geologisches Jahrbuch* **23**, 165-206.

- Sengör, A.M.C., 1984. The Cimmeride orogenic system and the tectonics of Eurasia. *Geological Society American Special Paper* **195**, 1-82.
- Sengör, A.M.C., Yilmaz, Y. & Sungurlu, O., 1984. Tectonics of the Mediterranean Cimmerides: nature and evolution of the western termination of Palaeo-Tethys. In: *the geological evolution of the eastern Mediterranean* (eds Robertson, A.H.F. & Dixon, J.E.). Geological society of London, special publication **17**, 77-112.
- Sibson, R.H. 1977. Continental fault structure and the shallow earthquake source. *Journal of Geological Society of London* **140**, 741-767.
- Sibson, R.H. 1977. Fault rocks and fault mechanisms. *Journal of Geological Society of London* **133**, 191-213.
- Sibson, R.H. 1982. Fault zone models, heat flow, and the depth distribution of earthquakes in the continental crust of the United States. *Bulletin of seismological Society of America* **72**, 151-163.
- Silk, E.C.H. & Barnes, R.S., 1959. Examination of fission fragment tracks with an electron microscope. *Phil. Mag.* **4**, 970-971.
- Smith, A.G. & Woodcock, N.H., 1982. Tectonic syntheses of the Alpine-Mediterranean region: a review. In: *Alpine and Mediterranean Geodynamics* (eds Berkheimer, H. & Hsü, K.J.) 15-38.
- Smith, A.G., 1996. Some aspect of the Phanerozoic Palaeogeographic evolution of Europe. *Zeitschrift der Deutschen Geologischen Gesellschaft* **147**, 147-168.
- Sorel, D. 2000. A Pleistocene and still-active detachment fault and the origin of the Corinth-Patras rift, Greece. *Geology* **28**, 83-86.
- Spakman, W., Wortel, M.J.R. & Vlaar, N.J., 1988. The Hellenic Subduction Zone: A tomographic image and its geodynamic implications. *Geophysical Research Letter* **15**, 60-63.
- Spray, J.G. & Roddick, J.C., 1980. Petrology and $^{40}\text{Ar}/^{39}\text{Ar}$ geochronology of some Hellenic sub-ophiolite metamorphic rocks. *Contributions to Mineralogy and Petrology* **72**, 43-55.
- Stockli, D.F., Farley, K.A. & Dumitru, T.A., 2000. Calibration of the apatite (U-Th)/He thermochronometer on an exhumed fault block, White Mountains, California. *Geology* **28**, 983-986.
- Stormer, J.C.Jr., Pierson, M.L. & Tacker, R.C., 1993. Variation of F and Cl x-ray intensity due to anisotropic diffusion in apatite during electron microprobe analysis. *American Mineralogist* **78**, 641-648.
- Streiger, R.H. & Jäger, E., 1977. Subcommittee on geochronology: convention on the use of decay constant in geo- and cosmochronology. *Earth and Planetary Science Letters* **36**, 359-362.
- Summerfield, M.A. & Brown, R.W., 1998. Geomorphic factors in the interpretation of fission-track data In: *Advances in Fission-Track Geochronology*, Kluwer Academic Publishers, 269-284.
- Tagami, T., Carter, A. & Hurford, A.J., 1996. Natural long-term annealing of the zircon fission-track system in Vienna Basin deep borehole samples; constraints upon the partial annealing zone and closure temperature. *Chemical Geology* **130**, 147-157.
- Tagami, T., Galbraith, R.F., Yamada, R. & Laslett, G.M., 1998. Revised annealing kinetics of fission tracks in zircon and geological implications. In: *Advances in fission-track geochronology* (eds Van Den Haute, P. et al.). Kluwer Academic Publishers, 99-112.
- Tagami, T., Farley, K.A. & Stockli, D.F., 2003. (U-Th)/He geochronology of single zircon grains of known Tertiary eruption age. *Earth and Planetary Science Letters* **207**, 57-67.
- Thomson, S.N., Stöckhert, B. & Brix, M.A. 1998. Thermochronology of the high-pressure metamorphic rocks of Crete, Greece: Implications for the speed of tectonic processes. *Geology* **26**, 259-62.
- Thomson, S.N., Stöckhert, B., Rauche, H. & Brix, M.R., 1998. Apatite fission-track thermochronology of the uppermost tectonic unit of Crete, Greece: Implications for the post-eocene tectonic evolution of the Hellenic subduction system In: *Advances fission-track geochronology* (eds Van Den Haute, P., et al.). Kluwer Academic Publishers, 187-205.
- Thomson, S.N., Stöckhert, B. & Brix, M.R., 1999. Miocene high-pressure metamorphic rocks of Crete, Greece: rapid exhumation by buoyant escape In: *Exhumation processes: Normal Faulting, Ductile Flow and Erosion* (eds Ring, U., et al.). Geological society of London, Special Publication **154**, 87-107.
- Tomaschek, F., Kennedy, A., Villa, I.M., Ballhaus, C., 2003. Zircons from Syros, Cyclades, Greece- Recrystallization and mobilisation during high pressure metamorphism. *Journal of Petrology* **44**, 1977-2002.
- Trotet, F., Vidal, O. & Jolivet, L., 2001. Exhumation of Syros and Sifnos metamorphic rocks (Cyclades, Greece). New constraints on the P-T paths. *European Journal of Mineralogy* **13**, 901-920.
- Tsokas, G.N. & Hansen, R.O., 1997. Study of the crustal thickness and the subducting lithosphere in Greece from gravity data. *Journal of Geophysical Research* **102**, 20585-20597.
- Underhill, J.R., 1989. Late Cenozoic deformation of the Hellenide foreland, western Greece. *Geological Society America Bulletin* **101**, 613-634.
- Urai, J.L., Schuiling, R.D. & Jansen, J.B.H., 1990. Alpine deformation on Naxos (Greece). *Geological Society Special Publication* **54**, 509-522.
- Van Den Haute, P., De Corte, F., Jonckheere, R. & Bellemans, F., 1998. The parameters that govern the accuracy of fission-track age determinations: A re-appraisal In: *Advances in Fission-Track Geochronology*, Kluwer Academic Publishers, 33-46.
- Vandenberg, L.C. & Lister, G.S., 1996. Structural analysis of basement tectonites from the Aegean metamorphic core complex of Ios, Cyclades, Greece. *Journal of Structural Geology* **18**, 1437-1454.

- Vanderhaeghe, O & Teyssier, C., 1997. Formation of the Shuswap metamorphic core complex during late-orogenic collapse of the Canadian Cordillera: Role of ductile thinning and partial melting of the mid-to lower crust. *Geodinamica Acta* **10**, 41-58.
- Van Der Maar, P.A., Feenstra, A., Manders, B. & Jansen, J.B.H., 1981. The petrology of the island of Sikinos, Cyclades, Greece, in comparison with that of the adjacent island of Ios. *Neues Jahrbuch fuer Mineralogie* **10**, 459-469.
- Van Der Maar, P.A & Jansen, J.B.H., 1983. The geology of the polymetamorphic complex of Ios, Cyclades, Greece and its significance for the Cycladic Massif. *Geologische Rundschau* **72**, 283-299.
- Villa, I.M. 1998. Isotopic closure. *Terra Nova* **10**, 42-47.
- Wagner, G.A., Reimer, G.M., Carpenter, B.S., Faul, H., Van Der Linden, R. & Gijbels, R., 1975. The spontaneous fission rate of U-238 and fission track dating. *Geochimica et Cosmochimica Acta* **39**, 1279-1286.
- Wagner, G.A. & Van Der Haute, P., 1992. *Fission-track dating*. Published by Ferdinand Enke Verlag and Kluwer Academic Publishers, 285p.
- Walcott, C.R., 1998. The Alpine evolution of Thessalys (NW Greece) and late Tertiary Aegean kinematics. PhD thesis, Utrecht University; *Geologica Ultraiectina* **162**, 176p.
- Walker, R., & Jackson, J., 2002. Offset and evolution of the Gowk Fault, SE Iran; a major intra-continental strike-slip system. *Journal of Structural Geology* **24**, 1677-1698.
- Wallis, S.R., Platt, J.P. & Knott, S.D., 1993. Recognition of syn-convergence extension in accretionary wedges with examples from the Calabrian arc and the eastern Alps. *American Journal of Science* **293**, 463-495.
- Warnock, A.C., Zeitler, P.K., Wolf, R.A. & Bergman, S.C., 1997. An evaluation of low-temperature apatite U-Th/He thermochronometry. *Geochimica et Cosmochimica Acta* **61**, 5371-5377.
- Wawrzenitz N. & Mposkos, E., 1997. First evidence for Lower cretaceous HP/HT-metamorphism in the Eastern Rhodope, North Aegean region, North-East Greece. *European Journal of Mineralogy* **9**, 659-664.
- Weidmann, M., Solounias, N., Drake, R.E. & Curtis, G.H. 1984. Neogene stratigraphy of eastern basin, Samos Island, Greece. *Geobis*, **17**, 477-490.
- Weingartner, H. & Hejl, E., 1994. The relief generation of Thasos and the first attempt of fission-track dating in northern Greece. *Bulletin of the geological Society of Greece*, 307-312.
- Weldon, R.J., II, Fumal, T.E., Powers, R.J., Pezzopane, S.K., Scharer, K.M., Hamilton, J.C. 2002. Structure and earthquake offset on the San Andreas Fault at the Wrightwood, California, palaeoseismic site. *Bulletin of the Seismological Society of America* **92**, 2704-2725.
- Wernicke, B. 1981. Low-angle normal faults in the Basin and Range province: nappe tectonics in an extending orogen. *Nature* **291**, 645-648.
- Wernicke, B., 1985. Uniform sense normal simple shear of the continental lithosphere. *Canadian journal Earth of Sciences* **22**, 108-125.
- Wernicke, B., Axen, G.J. & Snow, J.K., 1988. Basin and range extensional tectonics at the latitude of Las Vegas, Nevada. *Geological Society of America Bulletin* **100**, 1738-1757.
- Wernicke, R.S. & Lippolt, H.J., 1993. Botryoidal hematite from the Schwarzwald (Germany): heterogeneous uranium distributions and their bearing on the helium dating method. *Earth and Planetary Science Letters* **114**, 287-300.
- Westaway, R. 1994. Present-day kinematics of the Middle East and eastern Mediterranean. *Journal of Geophysical Research*, 12071-12090.
- Westaway, R., 2001. The Quaternary evolution of the Gulf of Corinth, central Greece: coupling between surface processes and flow in the continental crust. *Tectonophysics*, 87-88.
- Wheeler, J. & Butler, R.W.H., 1994. Criteria for identifying structures related to true crustal extension in orogens. *Journal of Structural Geology* **16**, 1023-1027.
- Wijbrans, J.R. & McDougall, I. 1986. $^{40}\text{Ar}/^{39}\text{Ar}$ dating of white micas from an Alpine high-pressure metamorphic belt on Naxos (Greece): The resetting of the argon isotopic system. *Contributions to Mineralogy and Petrology* **93**, 187-194.
- Wijbrans, J.R. & McDougall, I. 1988. Metamorphic evolution of the Attic Cycladic metamorphic belt on Naxos (Cyclades, Greece) utilizing $^{40}\text{Ar}/^{39}\text{Ar}$ age spectrum measurements. *Journal of Metamorphic Geology* **6**, 571-594.
- Wijbrans, J.R., Schliestedt, M. & York, D. 1990. Single grain argon laser probe dating of phengites from the blueschist to greenschist transition on Sifnos (Cyclades, Greece). *Contributions to Mineralogy and Petrology* **104**, 582-593.
- Will, T., Okrusch, M., Schmädicke, E. & Chen, G., 1998. Phase relations in the greenschist-blueschist-amphibolite-eclogite facies in the system $\text{Na}_2\text{O}-\text{CaO}-\text{FeO}-\text{MgO}-\text{Al}_2\text{O}_3-\text{SiO}_2-\text{H}_2\text{O}$ (NCFMASH), with application to metamorphic rocks from Samos, Greece. *Contributions to Mineralogy and Petrology* **132**, 85-102.
- Wolf, R.A., 1996. Development of the (U-Th)/He thermochronometer. *PhD thesis*: Pasadena, CA, California Institute of Technology.
- Wolf, R.A., Farley, K.A., & Silver, L.T. 1996a. Assessment of (U-Th)/He thermochronometry: the low-temperature history of the San Jacinto Mountains, California. *Geology* **25**, 65-68.
- Wolf, R.A., Farley, K.A., & Silver, L.T. 1996b. Helium diffusion and low-temperature Thermochronometry of apatite. *Geochimica et Cosmochimica Acta* **60**, 4231-4240.
- Wolf, R.A., Farley, K.A. & Kass, D.M., 1998. Modelling of the temperature sensitivity of the apatite (U-Th)/He thermochronometer. *Chemical Geology* **148**, 105-114.

- Wortel, M.J.R. & Spakman, W., 1992. Structure and dynamics of subducted lithosphere in the Mediterranean region. *Proceedings of the Koninklijke Nederlandse Akademie van Wetenschappen* **95**, 325-347.
- Yamada, R., Tagami, T. & Nishimura, S., 1995. Confined fission-track length measurement of zircon: assessment of factors affecting the paleotemperature estimate. *Chemical geology* **119**, 293-306.
- Yamada, R., Yoshioka, T., Watanabe, K., Tagami, T., Nakamura, H., Hashimoto, T. & Nishimura, S., 1998. Comparison of experimental techniques to increase the number of measurable confined fission track in zircon. *Chemical Geology* **149**, 99-107.
- Yin, A., Rumelhart, P.E., Butler, R., Cowgill, E., Harrison, T.M., Foster, D.A., Ingersoll, R.V., Zhang, Q., Zhou, X., Wang, X., Hanson, A. & Raza, A., 2002. Tectonic history of the Altyn Tagh fault system in northern Tibet inferred from Cenozoic sedimentation. *Geological Society of America Bulletin* **114**, 1257-1295.
- York, D., 1969. Least squares fitting of a straight line with correlated errors. *Earth and Planetary Science letters* **5**, 320-324.
- Yurtmen, S., Guillou, H., Westaway, R., Rowbotham, G., & Tatar, O., 2002. Rate of strike-slip motion on the Amanos Fault (Karasu Valley, southern Turkey) constrained by K-Ar dating and geochemical analysis of Quaternary basalts. *Tectonophysics* **344**, 207-246.
- Zeitler, J.F., 1977. Helium: Stopping power and ranges in all elemental matter. *New York, Pergamon*, 367p.
- Zeitler, P.K., Herczeg, A.L., McDougall, I. & Honda, M., 1987. U-Th-He dating of apatite: a potential thermochronometer. *Geochimica et Cosmochimica Acta* **51**, 2865-2868.
- Zimmerman, J.Jr. & Ross, J.V., 1976. Structural evolution of the Vardar root zone, northern Greece: discussion and reply. *Bulletin of geological Society of America* **90**, 126-128.

Figure Captions

ABSTRACT FOR NON GEOLOGISTS

Fig. A (1) Example of the geometry of fault showing rock locations in the time, the path of the rocks in the crust correlated to the footwall and hangingwall senses of movement related to the fault. **(2)** Enlargement of the boxed zone showing the isotherm in the crust related to the methods of dating used and the distance between the samples of rocks collected (A, B, C) and the fault.

Fig. B Map of the Aegean area showing the studied area and the results obtained from the islands of Samos, Ikaria, Tinos, Mykonos, Naxos, Paros, Serifos and Ios. Ma = Million years.

INTRODUCTION

Fig. 1(a) Simplified tectonic map of the Alpine-Himalaya chain (modified after Dewey et al., 1986 and Lips, 1999) showing the dominant linear elements associated with the development of the Alpine-Himalayan system. Black zones characterize main thrust belts. **(b)** Topographic map of the Aegean region showing the main relative motions which control the present-day extension.

Fig. 2 (a) Generalized tectonic map of the Hellenides showing major tectonic zones, the Cycladic Blueschist Unit, the Cyclades and the subduction zone (modified after Ring et al., 2003). **(b)** Schematic NNW-SSE cross section showing nappe pile and major Miocene detachments in southern Aegean (after Ring et al., 2003); Mountsouna and Mykonos detachment are related top-to-the NNE while the Ios detachment is related top-to-the SSE (Altherr et al., 1982; Buick, 1991; Gautier et al., 1993; Forster & Lister, 1999; Sánchez-Gómez et al., 2002).

Fig. 3 Closure temperatures of the different chronometers used in this study. The combination of the four methods will allow to constrain the thermal histories of the rock from ~500°C to ~40°C. AmAr/ArCT= closure temperature of the amphibole with the $^{40}\text{Ar}/^{39}\text{Ar}$ method (550±50°C); ZFTPAZ= zircon partial annealing zone of fission tracks (~300-200°C); AFTPAZ= apatite partial annealing zone of fission tracks (~110-60°C); HePRZ= partial retention zone of the helium in apatite (~80-40°C).

Table 1 Slip rates of extensional and strike-slip faults from different areas.

CHAPTER I

Fig. I.1 Frantz magnetic separator

Fig. I.2 Separatory funnels

Fig.I.3 Decay scheme for ^{40}K , illustrating the dual decay to ^{40}Ca (85.5%) and the ^{40}Ar (10.5%). Note that the ^{40}K to ^{40}Ar branch is dominated by electron capture (e.c). Adapted from Faure, 1986.

Fig. I.4 Schematic illustration of equipment used during this PhD thesis for Argon measurement at the University of Montpellier II.

Fig. I.5 Cartoon representation (modified from Fleischer et al., 1975) of the ion spike explosion model and the formation of fission tracks in a mineral. **a)** Spontaneous fission of ^{238}U produces two highly charged heavy particles and releases about 200 MeV of energy. The frequency of fission events is low, about 1 for 2×10^6 α -particle decay events. The highly charged particles recoil as a result of coulomb repulsion and interact with other atoms in the lattice initially by electron stripping or ionisation. This lead to further deformation of the lattice as the ionised lattice atoms repel each

other. **b)** As the fission particles capture electrons. They slow down and begin to interact by atomic collisions, leaving a damage trail or fission track.

Fig. I.6 Photomicrograph of a polished and etched prismatic section through an apatite crystal (sample M2 from Mykonos), showing etched surface intersecting tracks and a horizontal confined track (narrow). The acid etchant reached the confined track trough a fracture.

Fig. I.7 Examples of non uniform uranium distribution in grain. **a)** The repartition of the spontaneous tracks in the grain from a Naxos sample (Na2) is clearly not uniform with a higher track concentration in the core of the crystal. **b)** Not uniform repartition of the induced tracks in a sample from Paros (P32) with a higher concentration of tracks on the rim.

Fig. I.8 The external detector method used in this study, after Hurford & Carter (1991). The surface of a given mineral is polished and etched to reveal spontaneous tracks. Confined tracks can also be revealed if there is a pathway for the etchant. Then an uranium-free detector (muscovite mica) is sealed against this surface and this assembly is sent to irradiation, which will induces fission in ^{235}U . During the fission process, some heavy particles cross the interface between the mineral and the mica, producing a mirror image of the original grain. After, only the mica is etched to reveal the induced tracks. By counting the number of induced tracks in the mica, we estimate the uranium (or parent) concentration of the mineral, whereas by counting the number of spontaneous tracks in the mineral, we estimate the concentration of the daughter product.

Fig. I.9 Examples of confined tracks (arrows): **a)** Track-IN-Cleavage or TINCLE; **b)** Track-IN-Track or TINT.

Fig. I.10 Different shapes of fission tracks in apatite crystal according to axis types: **a)** a-crystallographic axis with characteristic fission track shape; **b)** c-crystallographic axis conventionally used for fission track measurement.

Fig. I.11 **(a)** Schematic illustration (modified from Jolivet, 2001) of the sample mount for fission track counting. **(b)** Schematic illustration (modified from Jolivet, 2001) of the preparation of the samples for irradiation. Tube of irradiation: a piece of dosimeter is put on top, middle and bottom to define the fluence cross the tube during irradiation (one dosimeter is put in the middle of the tube because between 30 and 40 samples can be put in the tube use at the Radiation center in Oregon). Samples are for the age determination while standards are put regularly in the tube to determinate the zeta number. Dosimeters, samples and standard are cover with external detector (muscovite). The most important is to compress well this sandwich to obtain a good contact between the mount and the external detector. A bad contact induce an ageing of the dating because a part of the induced tracks revealed in the external detector can be lost.

Fig. I.12 Schematic illustration (modified from Wagner & Van der haute, 1992) of equipment used during this PhD thesis for track counting and track size measurements at the University of Montpellier II and University College of London. (1) Tri-axial joystick for manual control of motorised stage; (2) Controlled unit of motorised stage; (3a) Step motors for movement in X, Y direction; (3b) Step motor for movement in the Z direction (focus); (4) Microscope; (5) Drawing tube attachment; (6) High resolution digitising tablet; (7) Cursor with centred LED; (8) and (9) personal computer and monitor connected to tablet and stage controller.

Fig. I.13 Graph of the zeta evolution (Stéphanie Brichau) for apatite and zircon. Grey lines correspond to the weighted mean, i.e. zeta values used in this study (332.9 ± 9.7 for apatite and 127.3 ± 4.4 for zircon). The zeta was determined on Durango, Fish Canyon and Mont Dromedary

apatite standards and on Fish Canyon, Tardree, Buluk and Mont Dromedary zircon standards (listing of data are given in section A I.3).

Fig. I.14 Examples of problems encountered during fission track counting. **(a)** *Sample P32*: Sometimes crystal defects can be confused with fission tracks. The repartition of the defects is a good indicator to distinguish them from FT because their repartition is random. **(b)** *Sample P34*: fluid inclusions in this apatite does not allow to count the fission tracks. **(c) and (d)** *Sample Na2*: inclusions of zircon in an apatite grain are a problem to count the induced tracks in the mica because the high uranium concentration in the zircon induce a high concentration of tracks (photo d.) and consequently a perturbation of the counting. **(e) and (f)** *Sample IK1*: concerning the zircon the most important problem is the strong zonation of the tracks in the grain (photo f.) and the mica (photo e.) in relation with inhomogeneous uranium distribution. Consequently it is difficult to find good grains and/or a large counting area.

Fig. I.15 Schematic illustration (modified from Farley, 2002) of the effects of long α -stopping distance on He retention. The upper figure illustrates the three relevant possibilities within a schematic crystal: α retention, possible α ejection and possible α implantation. “U” denote the site of the parent U or Th nuclide, and the edge of the shaded sphere labelled He indicates the locus of points where the α particle may come to rest; the arrow indicates possible trajectories. The lower plot shows schematically how α retention changes from rim to core to rim along the path A-A’; exact equations defining the shape of this curve as a function of grain size (Farley et al., 1996).

Fig. I.16 CL pictures from different apatite crystal reveal different types of chemical zoning. **a)** Picture from IK2 sample; **b)** Picture from M4 sample; **c)** Picture from M2 sample.

Fig. I.17 Apatite grain surfaces (a, b) and CL (c, d) images showing different inclusions types. **a)** and **b)** Surface grain picture (a) on apatite from P16 sample reveal several zircon inclusions (arrow), easily recognisable using CL (b and enlargement view). **c)** and **d)** Surface picture (c) on apatite from Na6 sample show feldspar and quartz inclusions, easily recognisable in CL image (d) by black area (arrows).

Fig. I.18 Schematic illustration of equipment used during this PhD thesis for Helium measurement at the Caltech. Q = Quatrupole mass spectrometer; SAES = Gas cleanser; Black boxes = Volumes used for diffusion experiments. The Cryo-pump is used to trap the Helium while the ionic and turbo pump are used to clean the line. ^3He is used to spike the sample and ^4He is used only on standard to know the $^3\text{He}/^4\text{He}$ ratio. The laser heat the sample 2 times (for extract and re-extract measurement) during 5 min at 1050°C . The time of analyse per sample is around 15 min. At Caltech, all the system of floodgates (closing and opening), the lasering process and the sample holder driver are controlled by computer.

Fig. I.19 Helium closure temperature (T_c) as a function of grain size and cooling rate (modified from Farley, 2002). T_c was calculated assuming an activation energy of 33kcal/mol and $D=50\text{cm}^2/\text{sec}$ assuming spherical geometry and including the effects of α -ejection on He diffusion (more details in Farley, 2000).

Fig. I.20 Closure temperatures of the different chronometers used in this study. The method association will allow to constrain the thermal histories of the rock from $\sim 500^\circ\text{C}$ to $\sim 40^\circ\text{C}$. AmAr/ArCT= closure temperature of the amphibole with the $^{40}\text{Ar}/^{39}\text{Ar}$ method ($550\pm 50^\circ\text{C}$); MsAr/ArCT= closure temperature of the muscovite with the $^{40}\text{Ar}/^{39}\text{Ar}$ method ($400\pm 50^\circ\text{C}$); BAr/ArCT= closure temperature of the biotite with the $^{40}\text{Ar}/^{39}\text{Ar}$ method ($300\pm 50^\circ\text{C}$); ZFTPAZ= zircon partial annealing zone of fission tracks ($\sim 300\text{-}200^\circ\text{C}$); AFTPAZ= apatite partial annealing

zone of fission tracks (~110-60°C); HePRZ= partial retention zone of the helium in apatite (~80-40°C).

CHAPTER II

Fig. II.1 (a) Schematic geometry of a detachment zone which formed by simple shear of the entire lithosphere (from Wernicke, 1985). **(b)** Different styles of detachment faults that affect the upper and middle crust: Asymmetric extension accommodated by a single-sense detachment Fault (Gautier & Brun, 1994); Bivergent extension accommodated by two synchronously operating detachment zones with opposite shear senses (Hetzel et al., 1995).

Fig. II.2 Schematic sketch of an extrusion wedge in a subduction setting (modified from Ring & Reischmann, 2002). The wedge is defined by the subduction thrust at the base and a normal fault at the top.

Fig. II.3 Aegean region and surrounding areas showing main tectonic domains, main basins and fault zones (modified from Lips 1998).

Fig. II.4 Spatial distribution of the three proposed HP metamorphic belts in the Aegean region, which are related to the Alpine Orogeny (following data and/or postulations from Bonneau & Kienast, 1982; Seidel et al., 1982; Papanikolaou, 1984; Gautier & Brun, 1994; Jolivet et al., 1996; Okay & Monie, 1997; Okay et al., 2002).

Fig. II.5 Timing of metamorphic and tectonic events recognized in the Aegean from North to South (modified from Lips, 1998; Data from Andriessen et al., 1979; Altherr et al., 1982; Wijbrans & McDougall, 1988; de Wet et al., 1989; Bröcker et al., 1993; Schermer, 1993; Baldwin & Lister, 1994; Harris et al., 1994; Okay et al., 1994; Dinter et al., 1995; Hetzel et al., 1995b; Hetzel & Reischmann, 1996; Jolivet et al., 1996; Okay et al., 1996; Wawrzenitz & Mposkos, 1997; Keay, 1998; Thomson et al., 1998).

Fig. II.6 Idealized tectonostratigraphic columns of the nappe pile in the Aegean (modified from Ring et al., 1999b).

Fig. II.7 Relation between convergence and subduction rates in the distribution of contraction and extensional regimes in the overriding plate (modified from Royden, 1993a).

Fig. II.8 Current kinematics which control the present-day extension in the Aegean region (Jackson, 1994; Le Pichon et al., 1995). Black arrows indicate relative motions, white arrow indicates position and propagation direction of tear in subducted slab (Spakman et al., 1988; Meijer & Wortel, 1997).

Fig. II.9 Schematic presentation on crustal thickness in the Aegean region, based on the Moho depth (Tsokas & Hansen, 1997).

Fig. II.10 Palaeogeographic reconstruction (240-42 Ma from Robertson & Dixon, 1984; 25 to recent from Walcott, 1998, Kissel & Laj, 1988 and Duermeijer et al., 1998) showing reconstructed development of the eastern Mediterranean and the role of continental fragments and secondary basins of the Tethys seaway in the development of the southern Eurasia margin during the African-Eurasian convergence.

- 240 Ma: Proposed location of continental fragments in Triassic;

- 119-95 Ma: reconstruction shows the overall narrowing of Tethys due to N-S convergence of the African and Eurasian plates (position of southern margin of Europe relative to the Africa position has been drawn successively from 119 to 95 Ma);
- 65 Ma: Gradual closure of Tethys and accretion of continental fragments;
- 42 Ma: Collision of most fragments, closure of Pindos basin and formation of Ionian basin;
- 25-3 Ma: Development of the present-day Aegean configuration during extension of the overriding Eurasia plate above the subducting African plate. Clockwise rotation of mainland Greece and northern Cyclades, anticlockwise rotation of southern Cyclades. Development of Mid-Cycladic Lineament;
- 3 Ma to recent: Further outward migration of the overriding plate and associated rotation of individual blocks.

Abbreviations: TTL=Tornquist Teisseyre Line; Rho=Rhodope; Pel=Pelagonian; Kir=Kirsehir; Moe=Moesian; Pon=Pontides; Cau=Caucasus; Pin=Pindos basin; Sak=Sakarya; Ion=Ionian Sea.

Fig. II.11 Reconstruction of the convergence between African and Eurasia plates, based on the movement and pole rotation of Africa-North America versus Eurasia- North America (from Müller & Roest, 1992). This drawing shows the change from oblique to dominant convergence of African and Eurasian plates since ~118 Ma and indicates the differences in overall rates since this time.

Fig. II.12 Simplified geologic map of the Cycladic zone with orientations of tectonic transport of different rock types: granite, greenschist facies and blueschist facies (map modified from Dürr et al., 1978; Altherr et al., 1982; Avigad & Garfunkel, 1991; Faure et al., 1991; Foster & Lister, 1999; Ring et al., 1999b).

CHAPTER III

Fig. III.1 (a) Simplified geologic map of Samos Island and **(b)** WSW-ENE cross section (modified from Ring et al., 1999c); sample locations are indicated.

Fig. III.2 Simplified geological map of Samos (modified from Ring et al., 1999c) showing previous geochronological data from Ring & Layer (2003) and Mezger et al. (1985).

Fig. III.3 Plot of zircon fission-track (ZFT) ages (2σ) against distance in slip direction (2σ) for Selçuk detachment fault; estimated minimum slip rate is 8.1 ± 1.7 km/Myr (2σ).

Fig. III.4 Simplified geologic map of Ikaria Island (modified from Altherr et al., 1982 and Kumerics et al., 2004). Shown are tectonic units, Messaria and Fanari extensional detachments and localities geochronological sample collected during this thesis and by Altherr et al. (1982).

Fig. III.5 T-t diagrams showing cooling rates for the footwall of the Messaria extensional fault system. **(a)** T-t path for Ik1 and Ik2 from the I-type granite. **(b)** T-t path for Ik6 from metasediments of the Ikaria nappe. Boxes represent uncertainties on ages and temperatures (2σ); lines represents cooling path for each samples.

Fig. III.6 Plot of zircon fission-track (ZFT), apatite fission-track (AFT) and apatite (U-Th)/He ages (2σ) against distance in slip direction (2σ) for Messaria extensional fault system; estimated minimum slip rates are 8.5 ± 0.4 km/Myr (ZFT), 8.4 ± 0.9 km/Myr (AFT) and 6 ± 0.2 km/Myr (apatite (U-Th)/He) (2σ). Slip rates were calculated with samples from the I-type granite (Ik1 to Ik4). Samples Ik5 to Ik7 (open symbols) have been also projected following the slip direction; note that the ages from these samples plot along the regression lines calculated for the I-type granite.

Fig. III.7 K-Ar muscovite ages (2σ) from Altherr et al. (1982) plotted along the slip direction; estimated minimum slip rate of 8 ± 0.3 km/Myr (2σ).

Fig. III.8 (a) Simplified geologic map of Tinos Island and **(b)** SW-NE cross section (modified from Gautier & Brun, 1994; Jolivet & Patriat, 1998 and Aubourg et al. 2000); sample locations are indicated.

Fig. III.9 (a) Simplified geological map of Tinos (modified from Bröcker & Franz, 2000) showing a part of previous geochronological data. **(b)** Mineral zone pattern in the contact aureole of the I-type granite of Tinos (modified from Bröcker & Franz, 2000). Abbreviations: FT = Fission Track; hbl = hornblende; m = muscovite; bio = biotite; ph = phengite; pa = paragonite; wr = whole rock; ap = apatite; zr = zircon. All ages are in millions of years and given for 1σ error level excepted dating from Bröcker & Franz, 1998 and Bröcker & Franz, 2000 given for 2σ .

Fig. III.10 $^{40}\text{Ar}/^{39}\text{Ar}$ ages spectra and Ca/K ratio evolution of amphiboles from the I-type granite of Tinos. **(a)** T3 Plateau age of 13.7 ± 0.7 Ma. **(b)** T4 plateau age of 14.4 ± 0.8 Ma. Ages are given for 1σ error level.

Fig. III.11 Temperature/time evolution for samples (T2, T3 and T4) from the Tinos granodiorite, from the hornblende $^{40}\text{Ar}/^{39}\text{Ar}$ closure temperature (Hornb. Ar/Ar), across zircon and apatite fission-track partial annealing zones (Z. PAZ and A. PAZ) and apatite partial retention zone for (U-Th)/He system (A. PRZ); boxes represent uncertainties on ages and temperatures (2σ); lines represents cooling path for each samples.

Fig. III.12 Plot of zircon fission-track (ZFT), apatite fission-track (AFT) and apatite (U-Th)/He ages (2σ) against distance in slip direction (2σ) for the Tinos extensional system; estimated minimum slip rates are 2.5 ± 0.2 km/Myr (ZFT), 3.7 ± 1.5 km/Myr (AFT) and 2.3 ± 0.2 km/Myr (apatite (U-Th)/He). The minimum average slip rate for this detachment is 2.8 ± 0.5 km/Myr (2σ).

Fig. III.13 Plot of hornblende $^{40}\text{Ar}/^{39}\text{Ar}$ ages (2σ) against distance in slip direction (2σ) for Tinos extensional system; estimated minimum slip rate is 1.4 ± 0.2 km/Myr (2σ).

Fig. III.14 (a) Simplified geologic map of Mykonos Island (modified from Altherr et al., 1982 and Sánchez-Gómez et al., 2002) with sample locations. **(b)** WSW-ENE cross section (modified from Faure et al., 1991); sample locations are indicated.

Fig. III.15 Plot of zircon fission-track (ZFT), apatite fission-track (AFT) and apatite (U-Th)/He ages (2σ) against distance in slip direction (2σ) for detachment fault of Mykonos; estimated minimum slip rates are 4.8 ± 0.3 km/Myr (ZFT), 8.6 ± 1.9 km/Myr (AFT) and 7.4 ± 0.6 km/Myr (apatite (U-Th)/He). The minimum average slip rate estimated for this detachment is 6.9 ± 0.7 km/Myr (2σ).

Fig. III.16 Temperature/time evolution for samples (M1, M2, M3 and M4) from the Mykonos monzogranite across zircon and apatite fission-track partial annealing zones (Z. PAZ and A. PAZ) and apatite partial retention zone for (U-Th)/He system (A. PRZ); boxes represent uncertainties on ages and temperatures (2σ); line represents cooling path of each samples.

Fig. III.17 (a) Simplified geologic map of Naxos Island and **(b)** NNE-SSW cross section (modified from Jansen and Schuiling, 1976; Wijbrans and MacDougall, 1988; Buick, 1991; Gautier et al., 1993); sample locations are indicated.

Fig. III.18 (a) Simplified geological map of Naxos showing isograds (modified from Jansen & Schuiling, 1976) and previous geochronological results. Roman numbers indicate metamorphic zones: I = diaspore; II = chlorite-sericite; III = biotite-chloritoid; IV = kyanite; V = kyanite-sillimanite transition; VI = sillimanite; VII = migmatic. **(b)** Table summarizing dating obtained in the different metamorphic zones (Andriessen et al., 1979; Wijbrans & McDougall, 1988). Numbers in brackets=Numbers of dating done.

Abbreviations: FT = Fission Track; hbl = hornblende; wm = white micas; m = muscovite; bio = biotite; ph = phengite; wr = whole rock; ap = apatite; zr = zircon. All ages are in millions of years and given for 1σ error level.

Fig. III.19 Plot of zircon fission-track (ZFT), apatite fission-track (AFT) and apatite (U-Th)/He ages (2σ) against distance in slip direction (2σ) for Mountsouna extensional system; estimated minimum slip rates are 6.5 ± 0.4 km/Myr (ZFT), 8.2 ± 0.5 km/Myr (AFT) and 10.4 ± 0.8 km/Myr (apatite (U-Th)/He). The minimum average slip rate for this detachment is estimated at 8.4 ± 0.3 km/Myr (2σ).

Fig. III.20 Temperature/time evolution for samples (Na3, Na4, Na5 and Na6) from the Naxos granodiorite across zircon and apatite fission-track partial annealing zones and apatite partial retention zone for (U-Th)/He system; boxes represent uncertainties on ages and temperatures (2σ); line represents cooling path of each sample.

Fig. III.22 Plot of zircon fission-track (ZFT) and apatite fission-track (AFT) ages (2σ) against distance in slip direction (2σ) for the detachment fault of Paros; estimated minimum slip rates are 6.8 ± 0.7 km/Myr (ZFT), 6.0 ± 0.9 km/Myr (AFT). The minimum average slip rate for this detachment is estimated at 6.4 ± 0.6 km/Myr (2σ).

Fig. III.22 Plot of zircon fission-track (ZFT) and apatite fission-track (AFT) ages against distance in slip direction for the detachment fault of Paros; estimated minimum slip rates are 13.4 ± 5.5 km/Myr (ZFT), 11.9 ± 8.5 km/Myr (AFT). The minimum average slip rate for this detachment is estimated at 12.7 ± 5.1 km/Myr.

Fig. III.23 (a) Simplified geologic map of Serifos Island and **(b)** NNE-SSW cross section (modified from Altherr et al., 1982); sample locations are indicated.

Fig. III.24 Temperature/time evolution for Se2 from the Serifos granodiorite across zircon and apatite fission-track partial annealing zones and apatite partial retention zone for (U-Th)/He system; white boxes represent uncertainties on ages and temperatures (2σ); black line represents cooling path.

Fig. III.25 Simplified geologic map of Ios Island (modified from Gautier & Brun, 1994 and Vanderberg and Lister, 1996); sample locations are indicated.

Fig. III.26 Temperature/time evolution for two samples from the basement of Ios across zircon and apatite fission-track partial annealing zones and apatite partial retention zone for (U-Th)/He system; boxes represent uncertainties on ages and temperatures (2σ); black line and dotted line represents cooling path of I2 and I8.

Fig. III.27 Plot of zircon fission-track (ZFT), apatite fission-track (AFT) and (U-Th)/He ages (2σ) against distance in slip direction (2σ) for a detachment fault of Ios; estimated minimum slip rates are 6.3 ± 1.5 km/Myr (ZFT), 2.0 ± 0.4 km/Myr (AFT) and 1.9 ± 0.2 km/Myr (apatite (U-Th)/He). The minimum average slip rate for this detachment is estimated at 3.4 ± 0.5 km/Myr (2σ).

Fig. III.28 Cross section interpretation of our data modified from Vanderberg & Lister (1996) and Forster & Lister (1999). Shown the top-to-the south South Cycladic Shear Zone and top-to-the north detachments fault. The main detachment fault can be the André fault described by Forster & Lister (1999) or the Ios detachment fault which has a sense of movement not clearly defined (Forster & Lister, 1999).

Fig. III.29 Cathodoluminescence picture of apatite from Ik6 sample without zoning. The black spot in middle of the grain is an inclusion of feldspar.

Fig. III.30 U/Th versus He diagram and table of U, Th, and He data for samples from Ikaria.

Fig. III.31 REE diagrams of apatites from the Ik2 and Ik6 samples.

Fig. III.32 U/Th versus He diagram of the four aliquots analyzed for (U-Th)/He dating.

Fig. III.33 Thin section photomicrographs. **(a)** Natural light picture of an apatite grain in a big titanite crystal. **(b)** Polaritized light picture of apatites in the vicinity of titanite.

Fig. III.34 U/Th versus He diagram of the four aliquots analyzed for (U-Th)/He dating.

Fig. III.35 Pictures from M3 sample. **(a)** Surface picture of apatite grains showing zircon (light grey) and feldspar (dark grey) inclusions. **(b)** Apatite CL picture does not reveal zonation.

Fig. III.36 Thin section photomicrographs under natural light showing: **(a)** titanite, biotite and zircons; **(b)** monazite grain; **(c)** zircons, biotite and apatites ; **(d)** fluid inclusions in apatite crystal.

Fig. III.37 **(a)** Table of U, Th, and He data for samples from Naxos. **(b)** U/Th versus He diagram and table of U, Th, and He data for samples from Naxos.

Fig. III.38 Thin section photomicrographs under natural light **(a, c)** and polarized light **(b, d)** showing tourmaline associated with undeformed muscovite.

Fig. III.39 Thin section photomicrographs under natural light **(a)** and polarized light **(b)** showing muscovite deformed associated with garnet.

Fig. III.40 Thin section photomicrographs under natural light showing: **(a)** biotite chloritized within rutile crystals and **(b)** apatite crystal within fluid inclusions.

Fig. III.41 U/Th versus He diagram of the four aliquots analyzed for (U-Th)/He dating.

Fig. III.42 Thin section photomicrograph under natural light showing biotite partially chloritized and apatites crystals within fluid inclusions.

Table III.1. Samos fission-track data.

Table III.2. a) Ikaria fission-track and U-Th/He data. **b)** Muscovite K/Ar data (Altherr et al., 1982).

Table III.4. Tinos fission-track and U-Th/He data.

Table III.5. Mykonos fission-track and U-Th/He data.

Table III.6. Naxos fission-track and U-Th/He data.

Table III.7. Paros fission-track data.

Table III.8. Serifos fission-track and (U-Th)/He data.

Table III.9. Ios fission-track and (U-Th)/He data.

Table III.10. (U-Th)/He data for Ik6 sample.

Table III.11. (U-Th)/He data for T2 sample.

Table III.12. (U-Th)/He data for M3 sample.

Table III.13. (U-Th)/He data for Na1 and Na2 samples.

Table III.14. (U-Th)/He data for Se2 sample.

CHAPTER IV

Fig. IV.1 Idealized comparative tectonostratigraphic columns of the nappe piles in the Aegean (modified from Ring et al., 1999b) and in each island studied during this thesis. They are presented in N-S section across the Cycladic zone (Samos, Ikaria, Tinos, Mykonos, Naxos, Paros, Serifos, Ios). The slip rates of detachment are indicated (at 2σ error level). Each color indicate a different timing of movement below $\sim 300^\circ\text{C}$ (ZFT) on the brittle part of extensional fault system or detachment (ages constraining movement at temperature $>300^\circ\text{C}$, i.e. ductile part, are excluded): Blue: ~ 20 Ma; rust: ~ 15 - 14 Ma; red: ~ 13 - 12 Ma; green: ~ 11 - 10 Ma; pink: <10 Ma; black: unconstrained. CBU= Cycladic Blueschist Unit and EFS = Extensional fault system.

Fig. IV.2 (a) Generalized tectonic map of the Hellenides (modified after Ring et al., 2003) showing the Cycladic Blueschist unit and the main extensional fault system correlation (Naxos/Paros and Ikaria/Samos). **(b)** Schematic NNE-SSW cross section across Ikaria and Samos showing fault connections between the Messaria, Fanari and Kallithea detachment.

Fig. IV.3 Aegean map in time slices showing the main events from >21 Ma to ~ 5 Ma:

- >21 Ma: onset of the Selçuk ductile shearing on Samos;
- ~ 21 - 20 Ma: onset of the Tinos and Naxos/Paros ductile extensional shear zone and onset on the Selçuk brittle extensional fault system started to operate;
- ~ 20 - 15 Ma: S- and I-type granite intrusions on Tinos and Naxos; onset of the South Cycladic shear zone on Ios;
- ~ 15 - 10 Ma: Main period of detachment faulting and magmatism;
- ~ 10 - 5 Ma: Kallithea and Fanari detachments started to operate on Ikaria and Samos.

Fig. IV.4 Three stages of the evolution of the extensional deformation on Ios. **(1)** Inception of the South Cycladic shear zone. **(2)** Updoming of the footwall with minor antithetic top-to-the north sense of shear. **(3)** Inception at ~ 15 - 14 Ma of the detachment related top-to-the north.

Fig. IV.5 Pressure-temperature-time history of the Naxos migmatite core (modified after Buick & Holland, 1989) compared to P-T history path (grey dotted line) of other islands studied. Boxes = metamorphic conditions according to Buick & Holland (1989).

Fig. IV.6 Interpretative schematic NNE-SSW cross section showing nappe pile and time constraints (my data) for major Miocene detachments in southern Aegean (modified after Ring et al., 2003); Mountsouna and Mykonos detachment are related top-to-the NNE (Altherr et al., 1982; Buick, 1991; Gautier et al., 1993; Sánchez-Gómez et al., 2002) while the Ios detachment is related top-to-the NNE (my data) and the South Cycladic shear zone is top-to-the SSW (Vandenberg & Lister, 1996).

Fig. IV.7 Simplified pressure-temperature-time (P-T-t) path of blueschist facies rocks of the Cycladic blueschist belt exposed in the studied islands (modified from Avigad et al., 1997) except for the migmatite core of Naxos (see fig. IV.4). Data sources are: Andriessen et al., 1979; Altherr et al., 1982; Wijbrans & McDougall, 1988; Buick & Holland, 1989; Okrusch & Bröcker, 1990; Avigad et al., 1992; Bröcker et al., 1993.

The retrograd path is dominated by isothermal decompression. A major greenschist facies metamorphic overprint affected the blueschists in the Oligo-Miocene when they reached relatively shallow crustal levels corresponding to pressures of ~7-5 kbar. The Oligo-Miocene overprint was coeval with the onset of Aegean back arc extension.

Table IV.1. Data compilation for the extensional fault systems studied.

Table IV.2. Listing of ages obtained in the Cycladic islands.

CONCLUSIONS

Fig. C1 (a) Aegean map showing the time constraints and slip rates for ductile extensional shearing. **(b)** Aegean map showing the time constraints and slip rates for brittle extensional detachments.

Fig. C2 Theoretical model of exhumation of the rocks to the Earth's surface during episodes of faulting. **(a)** Example of the geometry of fault showing rock locations in the time. **(b)** Enlargement of the circled zone showing the isotherms in the crust related to the methods of dating used during this study and the distance in the slip direction related to the actual samples locations on the field (A₂, B₂, C₂).

Appendices

APPENDIX N° I: Deviation of the age equations

1. Decay principles:

Dating principles are based on the natural decay of the radioactive substances. Rutherford and Soddy (1903) demonstrated empirically that the rate of decay of a radioactive substance follows an exponential law, with the activity at any instant proportional to the number of radioactive atoms present. Thus:

$$dN/dt = -\lambda N \quad (1.1)$$

Where: N = number of radioactive atoms present at time t

λ = decay constant, which is the probability of any particular atom decaying per unit time.

The half life ($t_{1/2}$) is the time required for a given number of radioactive atoms to decay to half that number and is related to the decay constant as follows:

$$t_{1/2} = \ln 2 / \lambda = 0.693 / \lambda \quad (1.2)$$

Thus, (1)+(2) yields:

$$N = N_0 e^{-\lambda t}$$

Where : N_0 = number of radioactive atoms present at $t = t_0$, some time in the past.

For a simple decay scheme in which radioactive parent (N) decays to daughter product (D),

$$D = N_0 - N = N_0 e^{-\lambda t} - N = N(e^{\lambda t} - 1) \quad (1.3)$$

$$\text{then } D = D_0 + N(e^{\lambda t} - 1)$$

Where: D = number of daughter atoms present at t

D_0 = number of daughter atoms present at $t = 0$

Rearranging and taking natural logarithms yields the basic equation used in geochronology:

$$t = (1/\lambda) \ln(1+(D/N))$$

These are the basic equations of the majority of isotopic-dating method including $^{40}\text{Ar}/^{39}\text{Ar}$, Fission track and U-Th/He methods.

2. $^{40}\text{Ar}/^{39}\text{Ar}$ equations:

The $^{40}\text{Ar}/^{39}\text{Ar}$ method is derived from the K-Ar technique, involving the formation of 89% and 11% of radiogenic $^{40}\text{Ca}^*$ and $^{40}\text{Ar}^*$ from ^{40}K decay. Deduced from the equation (1.3), equation leading to the calculation of the $^{40}\text{Ar}/^{39}\text{Ar}$ ages can be summarised as follows:

$$\begin{aligned} ^{40}\text{Ca}^* + ^{40}\text{Ar}^* &= ^{40}\text{K} (e^{\lambda t} - 1) \text{ with } \lambda = \lambda_{\beta} + \lambda_{\epsilon} = 5.543 \cdot 10^{-10} \text{ year}^{-1} \\ &\text{then} \\ ^{40}\text{Ar} &= ^{40}\text{K} \lambda_{\epsilon} / (\lambda_{\epsilon} + \lambda_{\beta}) (e^{\lambda t} - 1) \longrightarrow ^{40}\text{Ar} = ^{40}\text{K} \lambda_{\epsilon} / \lambda (e^{\lambda t} - 1) \quad (2.1) \\ &\text{and} \\ t &= 1/\lambda \ln [1 + (\lambda/\lambda_{\epsilon} \cdot ^{40}\text{Ar}/^{40}\text{K})] \end{aligned}$$

The conventional K-Ar method of dating assume that all the $^{40}\text{Ar}^*$ come from the ^{40}K decay and that this radiogenic element has been retained within the crystal lattice. Consequently, loss or excess of $^{40}\text{Ar}^*$ during a thermic and/or tectonic event can not be described.

The $^{40}\text{Ar}/^{39}\text{Ar}$ method does not require to measure the ^{40}K because the sample is submitted to neutronic activation. The sample is put in a reactor under a fast thermic flux of neutron (range between 10^{13} and 10^{14} n/cm²/s), during 2 or 3 days. This irradiation induce the formation of ^{39}Ar (artificial argon isotope) from ^{39}K . Following the derivation of Mitchell (1968a), the amount of ^{39}Ar that is produced in a sample during irradiation with neutrons is given by

$$^{39}\text{Ar}_k = ^{39}\text{K} \Delta T \int \phi_\epsilon \cdot \sigma_\epsilon \cdot d_\epsilon \quad (2.2)$$

Where: $^{39}\text{Ar}_k$ = number of atoms produced from ^{39}K in the sample
 ^{39}K = original number of atoms of ^{39}K present within the sample
 ΔT = duration of irradiation
 ϕ_ϵ = neutron flux at energy E
 σ_ϵ = neutron capture cross section at energy E

Combining equations (2.1) and (2.2) it follows that for an irradiated sample of age t:

$$^{40}\text{Ar}/^{39}\text{Ar} = ^{40}\text{Ar}/^{39}\text{K} \cdot \lambda_\epsilon/\lambda [(e^{\lambda t}-1)/(\Delta T \int \Delta\phi_\epsilon \sigma_\epsilon d_\epsilon)] \quad (2.3)$$

To simplify the calculation Merrihue & Turner (1966) used a standard to calibrated the flux in the reactor. This standard is irradiated with the samples. Thus, it is convenient to define a dimensionless irradiation parameter, J, as follows:

$$J = ^{39}\text{Ar}/^{40}\text{K} \cdot \lambda/\lambda_\epsilon \cdot \Delta T \int \phi_\epsilon \sigma_\epsilon d_\epsilon \quad (2.4)$$

Substituting equation (6) in equation (7) gives

$$J = (e^{\lambda Ts} - 1) / (^{40}\text{Ar}^*/^{39}\text{Ar}^*)_{st}$$

Where: st = standard

Therefore, for any sample:

$$J = (e^{\lambda tsm} - 1) / (^{40}\text{Ar}^*/^{39}\text{Ar}^*)_{sm} = (e^{\lambda Ts} - 1) / (^{40}\text{Ar}^*/^{39}\text{Ar}^*)_{st}$$

Where: sm = sample

This equation induce that if the sample is young, the irradiation duration will be shorter than in a older sample and J will be low for a better age precision. Then, the chronometric equation for the $^{40}\text{Ar}/^{39}\text{Ar}$ method is:

$$t = 1/\lambda \cdot \ln [1 + (^{40}\text{Ar}^*/^{39}\text{Ar}^*)_{sm} / (^{40}\text{Ar}^*/^{39}\text{Ar}^*)_{st} \cdot (e^{\lambda ts} - 1)]$$

This method allows to determinate potassium and argon on the sample and only measurements of $^{40}\text{Ar}^*/^{39}\text{Ar}_k$ are required. Nevertheless, some corrections are necessary to validate the method. For instance, $^{40}\text{Ar}^*$ must be corrected from the ^{40}Ar coming from the atmosphere. Like the ratio $^{40}\text{Ar}/^{36}\text{Ar}$ is constant in the atmosphere at the value of 295.5, $^{40}\text{Ar}^*$ can be expressed as:

$$^{40}\text{Ar}^* = (^{40}\text{Ar})_{total} - 295.5(^{36}\text{Ar})_{atm}$$

$$\text{or } {}^{40}\text{Ar}^*/{}^{39}\text{Ar}_k = ({}^{40}\text{Ar}/{}^{39}\text{Ar})_{\text{measured}} - 295.5({}^{36}\text{Ar}/{}^{39}\text{Ar})_{\text{measured}}$$

Where: atm = atmospheric

This correction could be sufficient assuming that all the ${}^{40}\text{Ar}$ is radiogenic or atmospheric, all the ${}^{36}\text{Ar}$ is atmospheric and that the ${}^{39}\text{Ar}$ is only produced by the neutron flux in the reactor during irradiation. Meanwhile, other corrections are necessary because of interfering reactions created by neutron interactions with the isotopes of calcium, potassium and chlorite during the irradiation of the sample. Dalrymple & Lanphere (1971), proposed a general expression in order to correct these effects:

$${}^{40}\text{Ar}^*/{}^{39}\text{Ar}_k = [({}^{40}\text{Ar}/{}^{39}\text{Ar})_{\text{measured}} - C_1({}^{36}\text{Ar}/{}^{39}\text{Ar})_{\text{measured}} + C_1C_2D - C_3] / [1 - C_4D]$$

Where: $C_1 = {}^{40}\text{Ar}/{}^{36}\text{Ar}$ ratio in the atmosphere

$C_2 = {}^{36}\text{Ar}/{}^{37}\text{Ar}$ ratio produced by interfering neutron reactions with calcium

$C_3 = {}^{40}\text{Ar}/{}^{39}\text{Ar}$ ratio produced by interfering neutron reactions with potassium

$C_4 = {}^{39}\text{Ar}/{}^{37}\text{Ar}$ ratio produced by interfering neutron reactions with calcium

$D = {}^{37}\text{Ar}/{}^{39}\text{Ar}$ ratio in the sample after correcting for decays of ${}^{37}\text{Ar}$

To define these correction parameters, calcium and potassium salt are irradiated regularly. They allow to know the yield of the interfering reactions.

3. Calculation of a Fission Track (FT) age:

In the FT method, it is spontaneous fission tracks instead of daughter isotopes that are measured as a product of the decay of ${}^{238}\text{U}$. This parent not only decays by spontaneous fission but also by α -emission (to ${}^{206}\text{Pb}$). If λ_d , λ_α and λ_f are, respectively the total decay-constant, the decay constant for α -emission, and the decay constant for spontaneous fission, it can be stated that $\lambda_d = \lambda_\alpha + \lambda_f$.

According to equation (1.3), the total number of decayed ${}^{238}\text{U}$ atoms after a time t is given by ${}^{238}\text{N}(e^{\lambda_d t} - 1)$, where ${}^{238}\text{N}$ represents the present number of ${}^{238}\text{U}$ atoms. The number of decays that are due to spontaneous fission stands in fixed proportion (λ_f / λ_d) to the total number of decays of ${}^{238}\text{U}$. Hence, the number of spontaneous tracks N_s that will have accumulated (per unit of volume) is given by:

$$N_s = (\lambda_f / \lambda_d) {}^{238}\text{N}(e^{\lambda_d t} - 1) \quad (3.1)$$

Because the decay constant for spontaneous fission is several orders of magnitude lower than the constant for α -decay, it can be stated that $\lambda_d = \lambda_\alpha = 1.55125 \times 10^{-10} \text{ yr}^{-1}$ (Hurford, 1990b). If equation (3.1) is solved explicitly for t , we then obtain:

$$t = (1 / \lambda_\alpha) \ln [(\lambda_\alpha N_s / \lambda_f {}^{238}\text{N}) + 1] \quad (3.2)$$

In principle, the calculation of a fission track age is thus based on the determination of the number of spontaneous fission tracks and the determination of the number of ${}^{238}\text{U}$ atoms per unit of volume in the sample. For determining the quantity ${}^{238}\text{N}$, a procedure is used which is also based on fission track counting. By irradiating the sample in a nuclear reactor with a fluence (Φ) of thermal neutrons, fission will be induced in the ${}^{235}\text{U}$ atoms, the number N_i of such fissions being given by:

$$N_i = {}^{235}\text{N} \sigma \Phi$$

Where $\sigma = 580.2 \times 10^{-24} \text{ cm}^2$, thermal neutron fission cross section for ${}^{235}\text{U}$ (Hurford, 1990b);

Except for some rare situations, the relative abundances of the uranium isotopes are practically constant in nature. The $^{235}\text{U}/^{238}\text{U}$ ratio can thus also be regarded as a constant and is called I ($I=7.2527 \times 10^{-3}$; Hurford, 1990b). Hence we can write:

$$N_i = {}^{238}\text{N}\sigma I\Phi \quad (3.3)$$

Combination of equations (3.2) and (3.3) finally yields:

$$t = (1/\lambda_\alpha) \ln [(\lambda_\alpha N_s \sigma I\Phi / \lambda_f N_i) + 1] \quad (3.4)$$

This is the fundamental age equation of the fission track method. The measurement of a fission track age is now reduced to the determination of the ratio of spontaneous to an induced track density and the determination of the thermal neutron fluence.

In equation (3.4), both N_s and N_i are expressed as numbers of tracks per unit of volume. In practice, the tracks which are counted are those which cross the investigated sample surface. Using the theoretical relation between the planar and spatial track density (see Wagner and Van der haute, 1992) and taking into account the effects of track etching and the observation factor, for the observed spontaneous and induced track densities, we can write:

$$\left. \begin{aligned} \rho_s &= g_s N_s R_s \eta_s f(t)_s q_s \\ \rho_i &= g_i N_i R_i \eta_i f(t)_i q_i \end{aligned} \right\} \quad (3.5)$$

Where: $g_{s,i}$ = the geometry factor

$R_{s,i}$ = the average etchable range of a fission fragment track in the investigated material

$\eta_{s,i}$ = the etching efficiency factor

$f(t)_{s,i}$ = the etch time factors

$q_{s,i}$ = the observation factor

The geometry factor g refers to the initial geometry of the pre-etched sample surface which is constant and $= 2\pi$ or 0.5 for an external surface (external detector method) and $= 4\pi$ or 1.0 for an internal surface (population method) (Gleadow & Lovering, 1977). In the same material, the etchable ranges of spontaneous and induced tracks are practically equal or $R_s=R_i$ (Bhandari et al., 1971). The values of η , $f(t)$ and q depend upon the techniques that are used for revelation and observation of tracks. Substitution of equations (3.5) in equation (3.4) finally yields:

$$t = (1/\lambda_\alpha) \ln [(\lambda_\alpha \rho_s \sigma I\Phi G Q / \lambda_f \rho_i) + 1] \quad (3.6)$$

This is the practical age equation in which the spatial track densities have been simply replaced by the observed planar track densities. In this equation:

$$G = g_s / g_i \quad \text{and} \quad Q = \eta_i f(t)_i q_i / \eta_s f(t)_s q_s$$

The factor Q can be considered as a procedure factor. If revelation of spontaneous and induced tracks is identical and both types of tracks are counted under identical conditions of observation then it can be stated that $Q=1$.

In past, calculation of a FT age required accurate knowledge of both the total thermal neutron flux in the reactor (which is not readily measurable) and the spontaneous fission decay constant for ^{238}U (a poorly known physical constant) (eq. (3.6)).

The zeta parameter method combined with the use of known age standards (t_{STD}), circumvents this requirement. For each age standard in the package, an estimate of the zeta parameter for the

glass dosimeter used in the capsule is determined (Hurford & Green, 1983). Zeta for the dosimeter glass is defined as:

$$\zeta = \sigma I \Phi / \lambda_f \rho_d \quad (3.7)$$

Where: ρ_d = induced track density for a standard.

Substitution of equations (3.7) in equation (3.6) finally yields:

$$t = (1/\lambda_a) \ln [1 + \lambda_a \cdot \zeta \cdot G \cdot \rho_d \cdot (\rho_s / \rho_i)]$$

Where: ζ = personal mean zeta value

The zeta technique and the use of known age standards puts the FT dating technique on equal footing with other geochronological method (Green, 1985). Furthermore, unlike the J parameter used in $^{40}\text{Ar}/^{39}\text{Ar}$ dating (see previous part about this method), the zeta parameter is not neutron flux dependent. However, large unexplained errors beyond that predicted by conventional error analysis tend to occur in each zeta value determined. Only by averaging zeta parameters from successive irradiations in the same laboratory, measured by the same operator, can a well-defined personal mean zeta value be determined.

Age and zeta calculations, as well as error analysis and the Chi-squared test are carried out by a computer analysis package (the theory and technique of the FT method are extensively described in the book of Wagner & Van der haute, 1992).

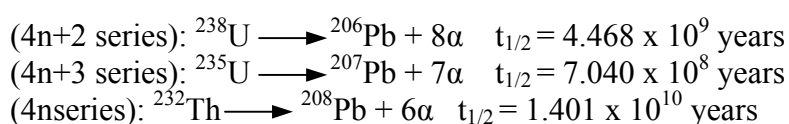
- Details of personal zeta values:

WEIGHTED MEAN ZETA VALUES FOR APATITE						
Standard names	ZETA	ERROR	Z/E2	1/E2	MEANZ	V/E2
Durango	325,9	19,8	0,83	0,00255076	-7,03	0,13
Durango	326,6	20,3	0,79	0,00242665	-6,33	0,10
Durango	321,3	23,5	0,58	0,00181077	-11,63	0,24
Fish Canyon	275,7	18,3	0,82	0,00298606	-57,23	9,78
Fish Canyon	343	24,5	0,57	0,00166597	10,07	0,17
Durango	295,4	35,5	0,23	0,00079349	-37,53	1,12
Fish Canyon	358,9	32,1	0,35	0,00097049	25,97	0,65
Durango	333	28,9	0,40	0,0011973	0,07	0,00
Fish Canyon	327,1	31,1	0,34	0,0010339	-5,83	0,04
Durango	335	48,8	0,14	0,00041991	2,07	0,00
Fish Canyon	409,4	41,4	0,24	0,00058344	76,47	3,41
Fish Canyon	376,3	50,3	0,15	0,00039524	43,37	0,74
Fish Canyon	325,2	40,2	0,20	0,0006188	-7,73	0,04
Durango	474,5	60,7	0,13	0,00027141	141,57	5,44
Mont Dromedary	321,7	23,6	0,58	0,00179546	-11,23	0,23
Mont Dromedary	395,3	20,9	0,90	0,00228932	62,37	8,91
	16	SUM	7,26	0,02180899		30,99
LOWER E TERM:				0,82026934		
WEIGHTED MEAN ZETA:				332,93		
ERROR:				9,70		
CALCULATION FROM HURFORD (PERSONAL COMMUNICATION)						

WEIGHTED MEAN ZETA VALUES FOR ZIRCON						
Standard names	ZETA	ERROR	Z/E2	1/E2	Z-MEANZ	V/E2
Fisch Canyon	129,9	6,2	3,38	0,02601457	2,60	0,18
Fisch Canyon	160,1	8,2	2,38	0,0148721	32,80	16,00
Tardree	119,5	7,02	2,42	0,02029204	-7,80	1,24
Fisch Canyon	114,4	4,5	5,65	0,04938272	-12,90	8,22
Tardree	125,4	6,6	2,88	0,02295684	-1,90	0,08
Fisch Canyon	117,1	4,9	4,88	0,04164931	-10,20	4,34
Tardree	129,3	6	3,59	0,02777778	2,00	0,11
Fisch Canyon	124,1	4,2	7,04	0,05668934	-3,20	0,58
Fisch Canyon	165,3	6	4,59	0,02777778	38,00	40,10
Buluk	110,4	6,2	2,87	0,02601457	-16,90	7,43
Tardree	124,6	5,8	3,70	0,02972652	-2,70	0,22
Buluk	113,9	7,5	2,02	0,01777778	-13,40	3,19
Mont Dromedary	155	7,4	2,83	0,0182615	27,70	14,01
Fisch Canyon	153,4	6,8	3,32	0,0216263	26,10	14,73
Buluk	101,2	6,1	2,72	0,0268745	-26,10	18,31
Fisch Canyon	134,9	6,7	3,01	0,02227668	7,60	1,29
	16	SUM	57,28	0,44997032		130,02
		LOWER E TERM:		6,97845805		
		WEIGHTED MEAN ZETA		127,30		
		ERROR		4,32		
CALCULATION FROM HURFORD (PERSONAL COMMUNICATION)						

4. U-Th/He age calculation:

This method combines the decay schemes of three isotopes:



with alpha particles (${}^4\text{He}$ helium nuclei) being emitted throughout each decay series and trapped within the lattice of the host material.

So the fundamental He ingrowth equation is:

$${}^4\text{He} = 8 {}^{238}\text{U}(\exp(\lambda_{238}t)-1) + 7({}^{238}\text{U}/137.88)(\exp(\lambda_{235}t)-1) + 6 {}^{232}\text{Th}(\exp(\lambda_{232}t)-1) \quad (4.1)$$

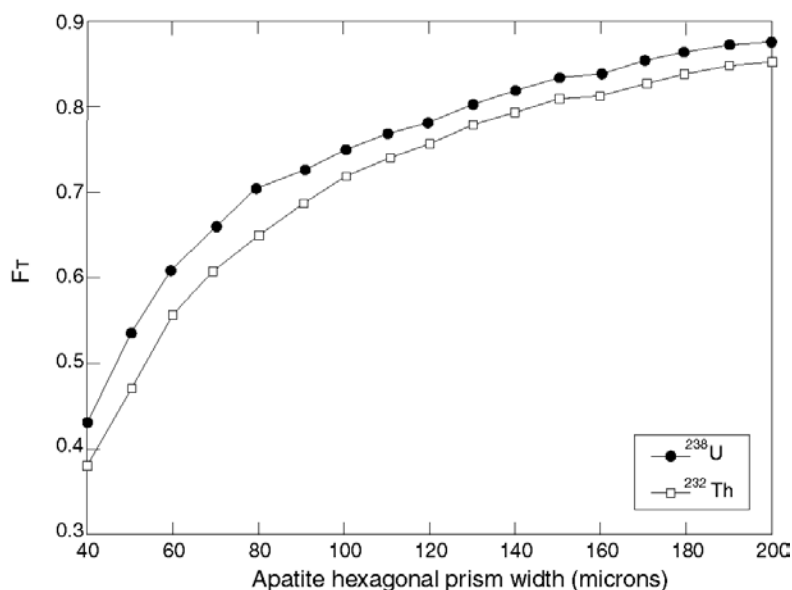
Where ${}^4\text{He}$, U, and Th refer to present day amounts, t is the accumulation time or He age, and λ 's are the decay constant. The coefficients preceding the U and Th abundances account for multiple α particles emitted within each of the decay series, and the factor of (1/137.88) is the present day ${}^{235}\text{U}/{}^{238}\text{U}$ ratio.

This equation (4.1) assumes secular equilibrium among all daughters in the decay chain, a condition guaranteed for crystals formed more than ~ 350 kyr prior to the onset of He accumulation. For most applications this assumption is valid, but in certain cases the effects of secular disequilibrium must be considered (see chapter I.4.1).

In view to solve the problem of the spatial separation between parent and daughter in relation with the α particles travel Farley et al. (1996) developed a quantitative model for correcting He ages: F_T correction model. Based on measurement grain geometry and size, this model shows that

the two most important variables controlling the total fraction of alphas retained in a crystal are the surface to volume ratio (β) of the crystal, and the α stopping distance. Crystals with small β have less “skin” affected by α ejection, and hence require smaller corrections. While each decay in the U and Th chains has a characteristic stopping distance, the mean F_T obtained by modeling each decay separately does not differ substantially from simply using a single mean stopping distance for each parent. However, because stopping distances vary significantly with the density of the stopping medium, it is necessary to use different stopping distances for different minerals. Both analytical and Monte Carlo results were presented that allow computation of F_T from measured dimensions for several simple grain geometries including a sphere, a cylinder, and a cube (Farley et al., 1996).

A typical result of this modeling is shown in the following figure, where F_T is plotted as a function of prism width for an apatite hexagonal prism of length/width ratio of 3:



The effects of α -ejection on He retention in an apatite hexagonal prism. F_T is the total fraction of alphas retained within the crystal, assumed here to have a length/width ratio of 3. The ^{238}U and ^{232}Th series lie on slightly different curves because of differences in decay energy; ^{235}U would plot essentially on top of the ^{232}Th curve.

For relatively large grain widths, F_T values are fairly constant, in the range 0.8 to 0.9, decreasing only slowly with decreasing width. However the curve becomes increasingly steep for widths $<80\mu\text{m}$. The message from this plot is that in general the largest grains will have the least uncertainty on the correction, and that typical corrections for small accessory minerals will be in the range 0.65 to 0.9. This shows that α retentivity is slightly higher for ^{238}U than for ^{232}Th , reflecting the higher mean energy of α decays in the ^{232}Th series. This distinction is relatively subtle but can be accommodated by computing a weighted mean of the F_T values for U and Th, where the weighting factor is the fraction of He derived from each parent. Specifically,

$$\text{mean } F_T = U^{238} F_T + \text{Th}^{232} F_T$$

where F_T for a hexagonal prism of apatite is:

$$F_T = 1 - \left\{ \frac{S}{4} \left[\frac{(2,3L + 2R)}{RL} \right] \right\}$$

where R is half the distance between opposed apices and L is the length.

For more details see Farley et al. 2002.

APPENDIX N° II: Sample characteristics

Name	Rock type	Latitude	Longitude	Altitude (m)	Dating carried out*	Comments
TINOS						
T1	Gabbro	37°31'56"	25°09'38"	15		Low [U] in apatite (no FT) and no zircon
T2	Granite	37°36'39"	25°14'08"	0	Bt Ar/Ar; ZFT; AFT; AHe;	
T3	Granite	37°36'39"	25°12'17"	340	Amp Ar/Ar; Bt Ar/Ar; ZFT; AFT; AHe	
T4	Granite	37°35'46"	25°11'45"	465	Amp Ar/Ar; Bt Ar/Ar; ZFT; AFT; AHe	
T5	S-type granite	37°35'10"	25°10'12"	300	ZFT	No apatite
T6	Schist	37°32'37"	25°09'52"	42		Apatite full of fluid inclusions
T7	Schist	37°34'35"	25°09'09"	250		Apatite full of fluid inclusions
MYKONOS						
M1	Granodiorite	37°25'35"	25°18'04"	10	Bt Ar/Ar; ZFT; AFT; AHe	Only two samples have been dated using the 40Ar/39Ar method, just to constrain the granite emplacement.
M2	Granodiorite	37°25'47"	25°21'43"	145	ZFT; AFT; AHe	
M3	Granodiorite	37°26'47"	25°23'45"	95	ZFT; AFT; AHe	
M4	Granodiorite	37°27'29"	25°25'46"	140	Amp Ar/Ar; Bt Ar/Ar; ZFT; AFT; AHe	
NAXOS						
Na1	S-type granite	37°11'19"	25°32'25"	30	AFT; AHe	Only two samples have been dated using the 40Ar/39Ar method, just to constrain the timing of the S-type and granodiorite emplacements.
Na2	S-type granite	37°09'54"	25°29'44"	175	Bt Ar/Ar; AFT; AHe	
Na3	Granodiorite	37°07'12"	25°24'46"	70	ZFT; AFT; AHe	
Na4	Granodiorite	37°04'23"	25°24'34"	102	Amp Ar/Ar; Bt Ar/Ar; ZFT; AFT; AHe	
Na5	Granodiorite	37°02'18"	25°23'47"	130	ZFT; AFT; AHe	
Na6	Granodiorite	37°00'24"	25°23'19"	2	ZFT; AFT; AHe	
IOS						
I1	Schist	36°39'22"	25°22'45"	40		Low U concentration in apatite: no FT
I2	Gneiss	36°43'24"	25°19'08"	270	ZFT; AFT; AHe	
I3	Schist	36°45'17"	25°18'56"	60		Low U concentration in apatite: no FT
I8	Gneiss	36°40'32"	25°21'23"	70	ZFT; AFT; AHe	
I11	Gneiss	36°44'33"	25°17'27"	200	ZFT	No apatite
PAROS						
P3	Gneiss	37°08'53"	25°13'20"	10	ZFT; AFT	The numerous zircon inclusions in apatite grains did not permit to do He
P16	Gneiss	37°02'47"	25°07'00"	15	ZFT; AFT	
P32	Gneiss	37°04'39"	25°08'15"	8	ZFT; AFT	
SERIFOS						
Se1	Quartzite	37°07'10"	24°30'23"	20		Low U concentration in apatite: no FT
Se2	Granite	37°09'10"	24°30'25"	140	Bt Ar/Ar; ZFT; AFT; AHe	
Se3	Rhyodacite	37°10'50"	24°29'38"	380	ZFT	No apatite
Se4	Schist	37°12'04"	24°30'15"	170		Low U concentration in apatite: no FT
SAMOS						
Sa1	Gabbro	37°39'34"	26°49'15"	450		Low [U] in apatite (no FT) and no zircon
Sa2	Quartzite	37°40'36"	26°48'16"	650	ZFT	No apatite
Sa3	Gneiss	37°48'17"	26°46'13"	80		Low [U] in apatite and no zircon in it
Sa4	Quartzite	37°46'58"	26°51'19"	340	ZFT	No apatite
Sa5	Quartzite	37°45'59"	26°57'35"	0	ZFT	No apatite
Sa6	Quartzite	37°43'48"	26°34'06"	120		No apatite and zircon
Sa7	Granite	37°43'48"	26°34'06"	120	ZFT	Low U concentration in apatite: no FT
Sa8	Quartzite	37°43'51"	26°34'04"	100		No apatite and zircon
Sa9	Quartzite	37°42'52"	26°38'17"	570	ZFT	No apatite
IKARIA						
IK1	Granodiorite	37°38'02"	26°05'09"	20	Bt Ar/Ar; ZFT; AFT; AHe	
IK2	Granodiorite	37°31'11"	26°00'49"	50	Bt Ar/Ar; ZFT; AFT; AHe	
IK3	Granodiorite	37°33'21"	26°02'51"	760	Bt Ar/Ar; ZFT	Low U concentration in apatite: no FT
IK4	Granodiorite	37°36'49"	26°09'07"	60	ZFT	No apatite
IK5	Quartzite	37°35'02"	26°12'13"	880	AFT	No zircon and apatite not good for He
IK6	Quartzite	37°38'31"	26°14'26"	270	ZFT; AFT; AHe	
IK7	S-type granite	37°35'44"	26°15'22"	20	Ms Ar/Ar; Bt Ar/Ar; ZFT; AFT	Apatite not good for He, lot of inclusions

Amp Ar/Ar = 40Ar/39Ar dating on amphibole; Ms Ar/Ar = 40Ar/39Ar dating on muscovite; Bt Ar/Ar = 40Ar/39Ar dating on biotite;

ZFT = zircon fission track dating; AFT = apatite fission track dating; AHe = (U-Th)/He dating on apatite.

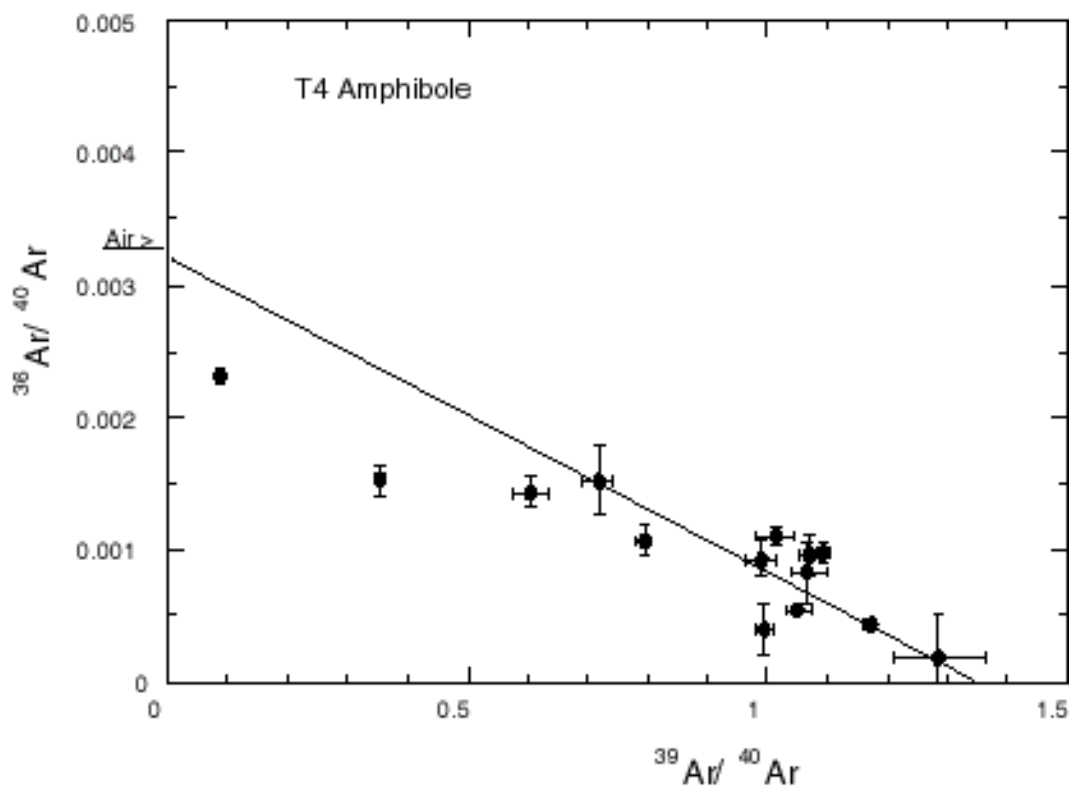
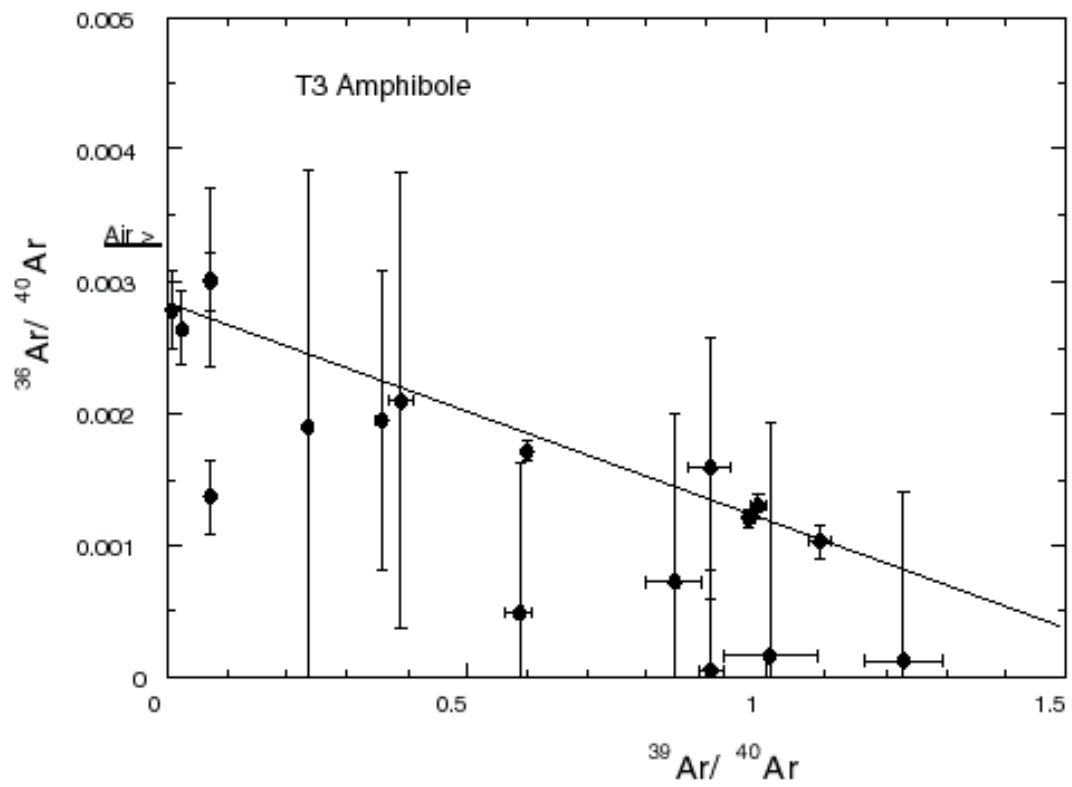
* Only two sample T3 and T4 have been dated on amphibole during this thesis using the Ar/Ar method owing to problems with the spectrometer.

APPENDIX N° III: $^{40}\text{Ar}/^{39}\text{Ar}$ data**1. Data table**

Step number	36Ar/40Ar		39Ar/40Ar	37Ar/39Ar %	39Ar %	Atm.	Age (Ma)	error 1 σ
	40Ar*/39Ar	x 1000						
T3 Amphibole		J=0.011781						
1	17.732	2.789	0.0099	6.911	0,0	82.4	342.28	159.51
2	8.817	2.643	0.0247	2.632	0.1	78.1	178.31	65.1
3	8.28	1.365	0.0719	1.524	0.3	40.3	167.93	23,00
4	1.886	1.888	0.2341	1.031	0.6	55.8	39.66	51.37
5	0.97	2.103	0.3898	1.827	0.9	62.1	20.51	27.46
6	0.932	0.715	0.8456	2.609	1.5	21.1	19.7	9.61
7	1.462	3.022	0.0731	3.253	1.7	89.3	30.82	57.31
8	1.183	1.955	0.3565	4.28	2.1	57.7	24.97	19.86
9	1.46	0.482	0.5871	4.194	2.6	14.2	30.78	12.11
10	0.586	1.584	0.9059	4.296	3.8	46.8	12.43	6.86
11	1.625	3,000	0.0697	2.565	4.6	88.6	34.23	18.86
12	1.078	0.064	0.9091	2.611	6.3	1.9	22.78	5.09
13	0.821	1.717	0.5996	3.006	20.2	50.7	17.36	0.73
14	0.783	0.126	1.2287	3.073	21.3	3.7	16.57	6.54
15	0.941	0.172	1.0086	3.863	22.1	5,0	19.89	10.96
16	0.66	1.209	0.9725	4.5	65.5	35.7	13.98	0.42
17	0.623	1.302	0.9855	4.5	87.2	38.5	13.21	0.56
18	0.637	1.032	1.0901	3.739	100,0	30.5	13.49	0.78
Total age =							15.5 \pm 0.4 Ma	

Step number	36Ar/40Ar		39Ar/40Ar	37Ar/39Ar %	39Ar %	Atm.	Age (Ma)	error 1 σ
	40Ar*/39Ar	x 1000						
T4 amphi		J=0.011781						
1	3.54	2.314	0.0892	1.668	1.6	68.3	73.72	4.16
2	1.544	1.527	0.355	1.083	4.7	45.1	32.54	2.26
3	0.951	1.434	0.6053	0.3	7.5	42.3	20.11	1.93
4	0.765	1.521	0.7187	0.163	9.8	44.9	16.19	2.42
5	0.859	1.074	0.7939	1.017	15.2	31.7	18.18	0.99
6	0.887	0.398	0.9944	1.001	20.6	11.7	18.75	1.3
7	0.706	0.829	1.068	1.611	26.3	24.5	14.96	1.39
8	0.667	0.965	1.07	2.27	35.1	28.5	14.13	0.93
9	0.662	1.106	1.0153	1.806	42.5	32.6	14.03	0.66
10	0.732	0.93	0.99	1.661	48.7	27.4	15.5	1,00
11	0.651	0.971	1.0943	2.257	66.3	28.6	13.79	0.42
12	0.733	0.188	1.2866	2.294	69.1	5.5	15.53	1.86
13	0.743	0.434	1.172	2.547	80.9	12.8	15.73	0.23
14	0.797	0.545	1.0519	2.18	100,0	16.1	16.87	0.39
Total age =							17.1 \pm 0.3 Ma	

2. Isochron correlation plots



APPENDIX N° IV: *Fission track data***1. Data table**

Island Name Sample no.	Mineral	No. of crystals	Track density ($\times 10^6$ tr cm^{-2})			P χ^2 (%)	U (ppm)	FT age (Ma)	Mean		No. of tracks measured
			ρ_d (Nd)	ρ_i (Ni)	ρ_s (Ns)				track length (μm)	StD (μm)	
TINOS											
T2	apatite	30	1.528 [13182]	0.9193 [139]	1.91 [2888]	97.1	15.6	11.9 \pm 1.0	14.75 \pm 0.16	1.19	58
	zircon	11	0.38 [4911]	33.15 [1137]	6.563 [2251]	83.3	633.8	12.2 \pm 0.5			
T3	apatite	21	1.3552 [10618]	0.6369 [100]	1.142 [1793]	98.4	10.5	12.6 \pm 1.3	14.21 \pm 0.19	1.14	37
	zircon	13	0.37 [4911]	43.07 [1710]	7.61 [3021]	96.8	754.8	13.3 \pm 0.4			
T4	apatite	23	1.3472 [10618]	0.8735 [134]	1.529 [2345]	63.8	14.2	12.8 \pm 1.2			
	zircon	15	0.365 [4911]	32.08 [1360]	5.408 [2293]	96.2	543.8	13.8 \pm 0.5			
T5	zircon	12	0.358 [4911]	32.02 [1188]	5.075 [1883]	100	520.3	14.4 \pm 0.6			
MYKONOS											
M1	apatite	28	1.3234 [10618]	3.146 [140]	5.521 [2457]	95.3	52.2	12.5 \pm 1.1			
	zircon	15	0.352 [4911]	41.66 [1837]	7.15 [3153]	94.9	745.4	13.0 \pm 0.4			
M2	apatite	24	1.3075 [10618]	2.975 [318]	6.077 [6496]	89,0	58.1	10.6 \pm 0.6	14.66 \pm 0.09	0.67	62
	zircon	11	0.345 [4911]	58.32 [1493]	11.02 [2820]	90	1171.8	11.6 \pm 0.4			
M3	apatite	25	1.2916 [10618]	2.196 [157]	4.491 [3211]	97.7	43.5	10.5 \pm 0.9			
	zircon	10	0.3394 [4911]	19.42 [767]	3.853 [1522]	97.4	416.6	10.9 \pm 0.5			
M4	apatite	21	1.2836 [10618]	2.148 [151]	4.378 [3078]	98.9	42.6	10.5 \pm 0.9	14.28 \pm 0.14	1.06	56
	zircon	13	0.33568 [4911]	32.18 [1149]	6.434 [2297]	88.2	703.4	10.7 \pm 0.4			
NAXOS											
Na 1	apatite	20	1.2677 [15751]	0.1676 [213]	4.313 [5482]	38.1	42.5	8.2 \pm 0.6			
Na 2	apatite	11	1.2598 [15751]	0.0616 [46]	1.497 [1112]	90.1	14.8	8.7 \pm 1.3	14.53 \pm 0.21	1.21	32
Na 3	apatite	17	1.2439 [15751]	0.1597 [50]	3.562 [1115]	94,0	35.8	9.3 \pm 1.3	14.71 \pm 0.23	1.13	25
	zircon	14	0.321 [4089]	4.421 [1070]	9.343 [2261]	63.6	1068.1	9.7 \pm 0.4			
Na 4	apatite	20	1.2359 [15751]	0.3143 [132]	6.61 [2776]	96.9	66.8	9.8 \pm 0.9			
	zircon	16	0.31756 [4089]	3.883 [1262]	7.388 [2401]	99.4	853.8	10.6 \pm 0.4			
Na 5	apatite	17	1.2041 [15751]	0.2535 [108]	4.763 [2029]	67.7	49.4	10.7 \pm 1.1	14.49 \pm 0.19	1.13	36
	zircon	17	0.307 [4089]	3.814 [1644]	6.71 [2892]	99.8	801.7	11.1 \pm 0.4			
Na 6	apatite	24	1.1882 [15751]	0.1917 [189]	3.368 [3321]	73.4	35.4	11.2 \pm 0.8			
	zircon	14	0.304 [4089]	4.36 [1696]	7.118 [2769]	54.2	860.2	11.8 \pm 0.4			

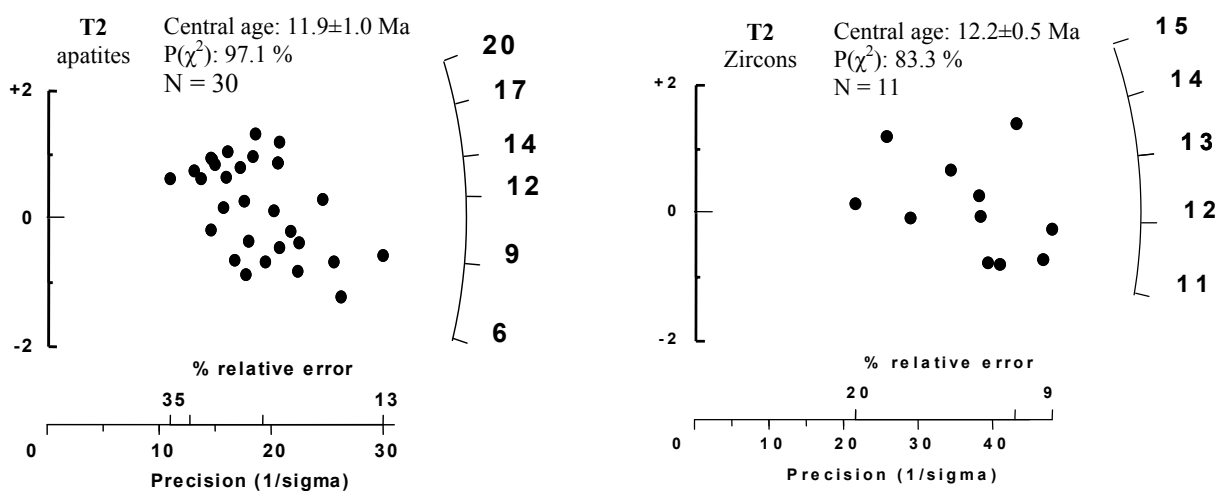
Island Name Sample no.	Mineral	No. of crystals	Track density ($\times 10^6$ tr cm^{-2})			$P\chi^2$ (%)	U (ppm)	FT age (Ma)	Mean		No. of tracks measured
			ρ_d (Nd)	ρ_i (Ni)	ρ_s (Ns)				track length (μm)	StD (μm)	
PAROS											
Ps3	apatite	17	1.2884 [12069]	1.349 [126]	2.734 [2554]	83.6	26.5	10.5 ± 1.0	14.39 ± 0.15	0.83	29
	zircon	11	0.388 [4920]	30.96 [932]	6.904 [2078]	99.7	653	11.1 ± 0.5			
P16	apatite	17	1.8898 [18667]	0.6902 [84]	1.709 [2080]	100	11.3	12.7 ± 1.4	14.73 ± 0.12	1.03	68
	zircon	7	0.374 [4920]	33.02 [591]	5.994 [1073]	100	588.2	13.1 ± 0.7			
P32	apatite	19	1.2721 [12069]	1.201 [196]	2.09 [3411]	97.9	20.5	12.1 ± 0.9	14.97 ± 0.17	1	33
	zircon	8	0.3577 [4920]	23.11 [513]	4.234 [940]	95.3	434.4	12.4 ± 0.7			
IOS											
I2	apatite	24	1.1325 [10618]	2.001 [338]	3.102 [5239]	100	34.2	12.2 ± 0.7	14.73 ± 0.11	0.76	52
	zircon	8	0.296 [4089]	18.29 [620]	2.454 [832]	98.5	304.3	14 ± 0.8			
I8	apatite	23	1.087 [10618]	1.781 [301]	2.939 [4967]	99.6	33.8	11.0 ± 0.7	14.39 ± 0.14	0.92	43
	zircon	12	0.286 [4089]	20.09 [697]	2.769 [961]	97.1	355.4	13.2 ± 0.7			
I11	zircon	10	0.2785 [4089]	29.59 [574]	3.613 [701]	99.9	476.2	14.5 ± 0.8			
IKARIA											
Ik1	apatite	17	1.3077 [13389]	1.392 [60]	4.517 [1947]	93.5	43.2	6.7 ± 0.9	14.14 ± 0.16	0.87	28
	zircon	15	0.386 [5206]	27.64 [1252]	8.15 [3692]	8.4	774.9	8.2 ± 0.4			
Ik2	apatite	22	1.3285 [13389]	1.477 [117]	3.865 [3061]	98.3	36.4	8.4 ± 0.8	14.18 ± 0.12	0.9	52
	zircon	16	0.3593 [5206]	37.36 [1954]	8.264 [4322]	37.3	844.2	10.3 ± 0.3			
Ik3	zircon	10	0.334 [4448]	18.15 [450]	5.121 [1270]	57.0	562.7	7.5 ± 0.4			
IK4	zircon	7	0.3265 [4448]	17.94 [739]	4.539 [1870]	32.4	510.2	8.1 ± 0.4			
Ik5	apatite	24	1.227 [12088]	1.265 [104]	3.808 [3130]	96.7	38.8	6.8 ± 0.7	14.43 ± 0.21	1.02	23
Ik6	apatite	19	1.2179 [12088]	0.7226 [56]	2.374 [1840]	95.5	24.4	6.2 ± 0.8	14.51 ± 0.19	1.12	35
	zircon	3	0.307 [4448]	13.78 [124]	3.111 [280]	95.1	371.9	8.6 ± 0.9			
Ik7	apatite	16	1.1906 [12088]	0.4444 [36]	1.691 [1370]	93.8	17.8	5.2 ± 0.9	14.19 ± 0.18	0.93	26
	zircon	12	0.294 [4448]	16.71 [695]	4.94 [2055]	100	616.6	6.3 ± 0.3			

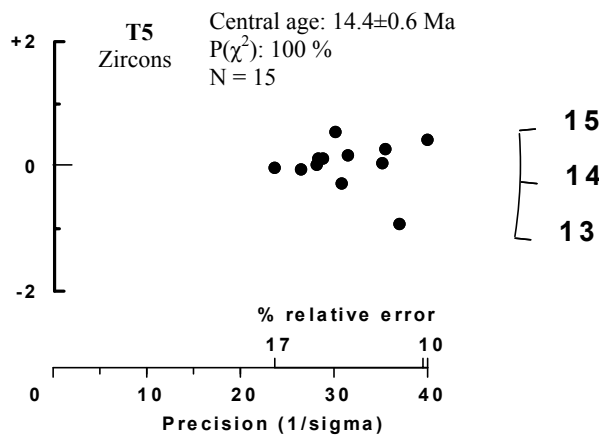
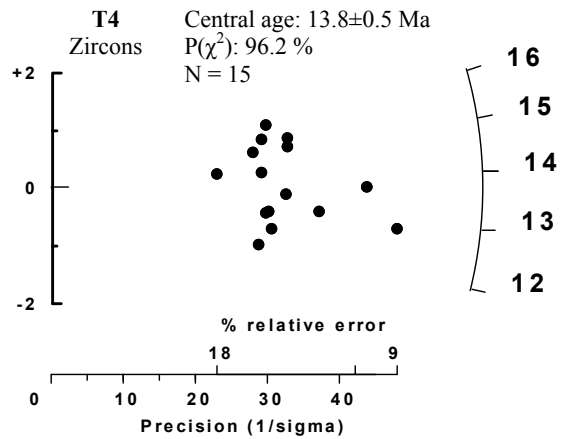
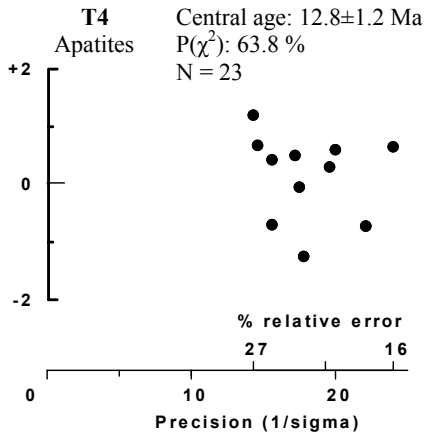
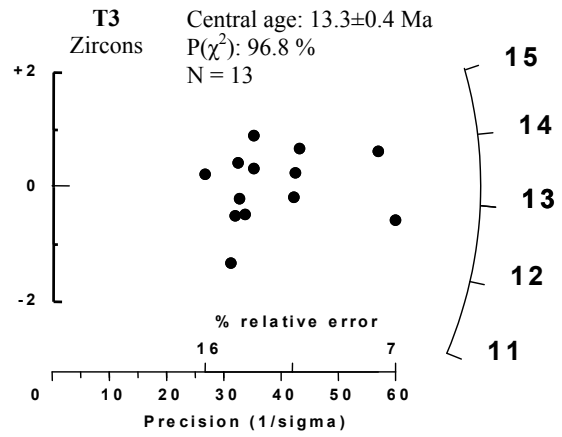
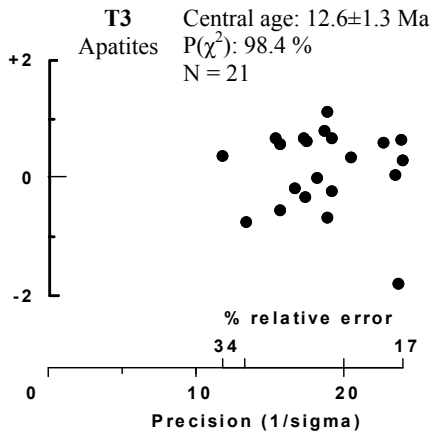
Island Name Sample no.	Mineral	No. of crystals	Track density ($\times 10^6$ tr cm^{-2})			$P\chi^2$ (%)	U (ppm)	FT age (Ma)	Mean		No. of tracks measured
			ρ_d (Nd)	ρ_i (Ni)	ρ_s (Ns)				track length (μm)	StD (μm)	
SERIFOS											
Se2	apatite	19	1.1906 [12069]	0.8722 [71]	1.668 [1358]	97.7	17.5	10.3 ± 1.3	14.95 ± 0.21	1	23
	zircon	9	0.33 [4920]	38.79 [1125]	7.117 [2064]	96.5	791.5	11.4 ± 0.5			
Se3	zircon	7	0.3247 [4920]	17.69 [191]	4.222 [456]	99.2	477.2	8.6 ± 0.8			
SAMOS											
Sa2	zircon	12	0.3 [3836]	27.55 [1102]	2.582 [1033]	72.2	315.9	20.3 ± 0.9			
Sa4	zircon	16	0.291 [3836]	40.97 [2110]	3.928 [2023]	98.5	495.4	19.3 ± 0.7			
Sa5	zircon	12	0.286 [3836]	36.04 [1038]	3.611 [1040]	99.5	463.4	18.1 ± 0.8			
Sa7	zircon	7	0.2629 [3836]	42.05 [328]	9.603 [749]	96.3	1340.5	7.3 ± 0.5			
Sa9	zircon	12	0.245 [3836]	36.24 [1080]	4.003 [1193]	99.6	599.7	14.1 ± 0.6			

These fission track ages have been calculated using a zeta factors of 127.3 ± 4.4 for zircon and 332.9 ± 9.7 for apatite determined by multiple analyses of standards following the recommendations of Hurford (1990) (see section A I.3 and chapter I.3). Central ages are reported. All data are given for 1σ error level.

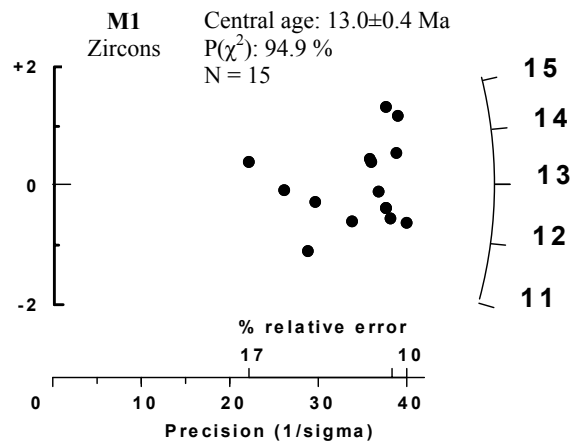
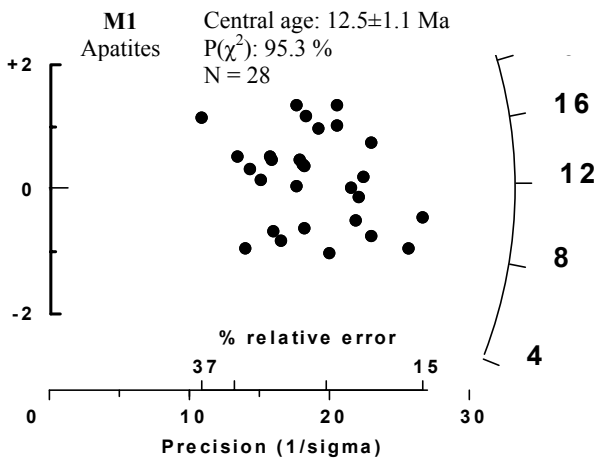
2. Radial plots of ages

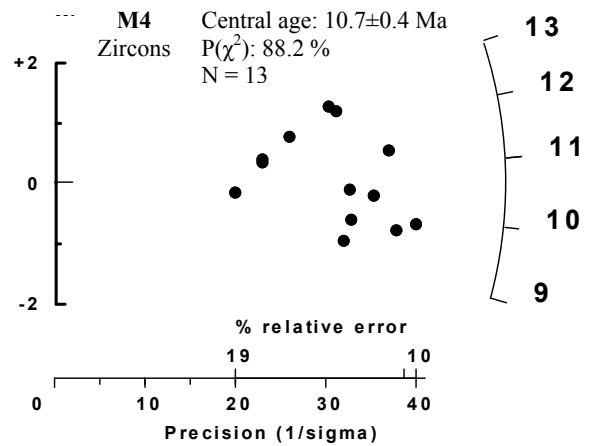
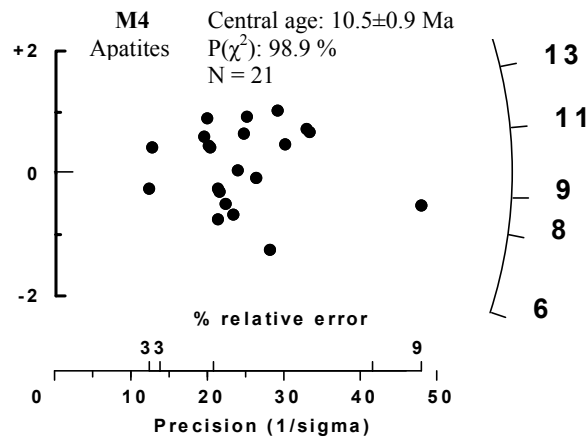
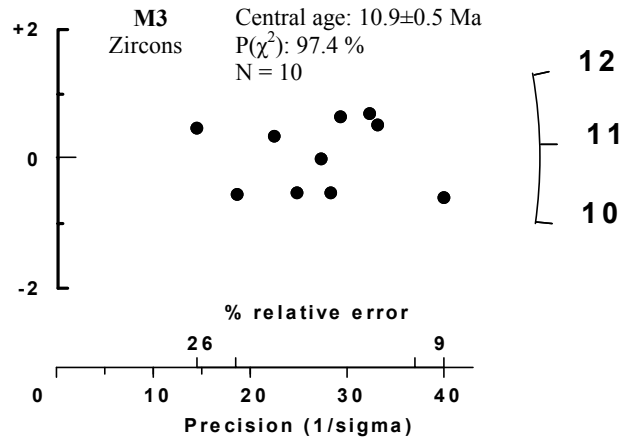
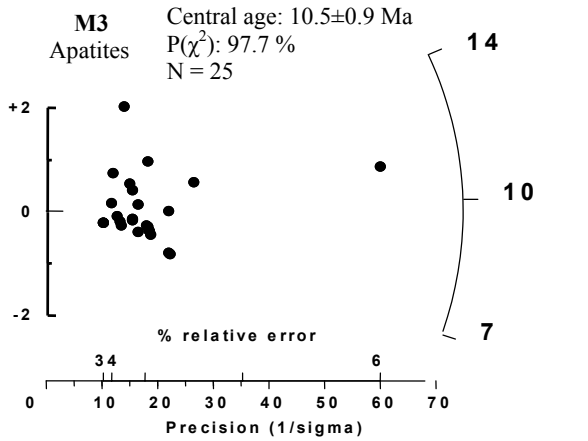
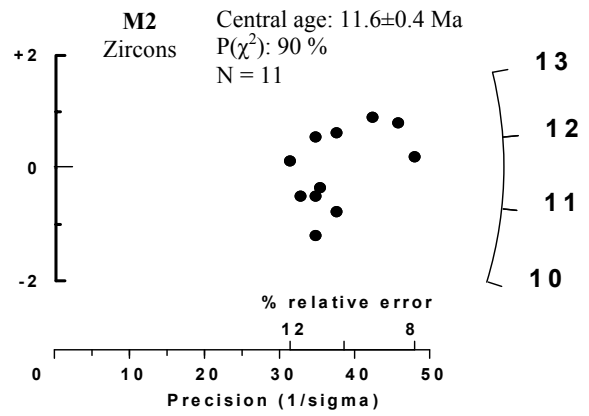
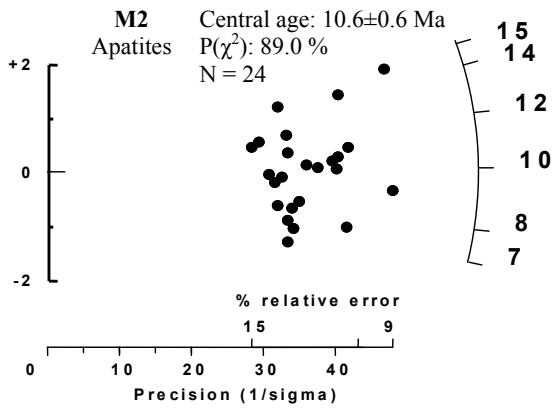
-TINOS



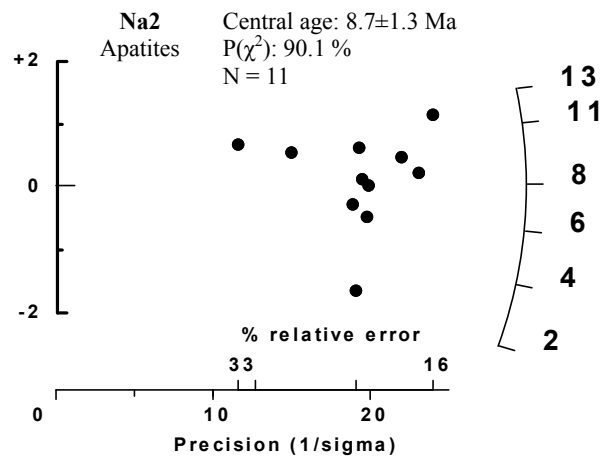
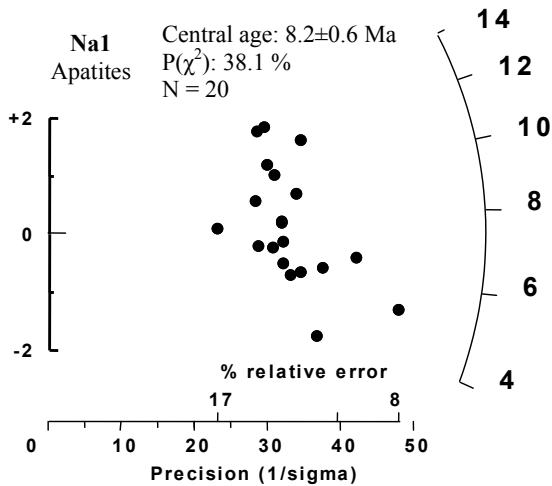


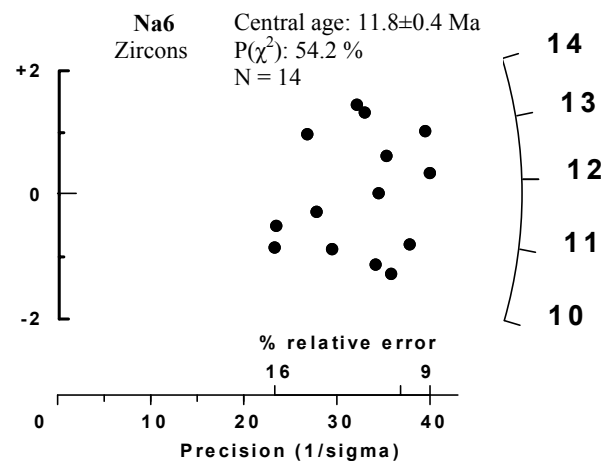
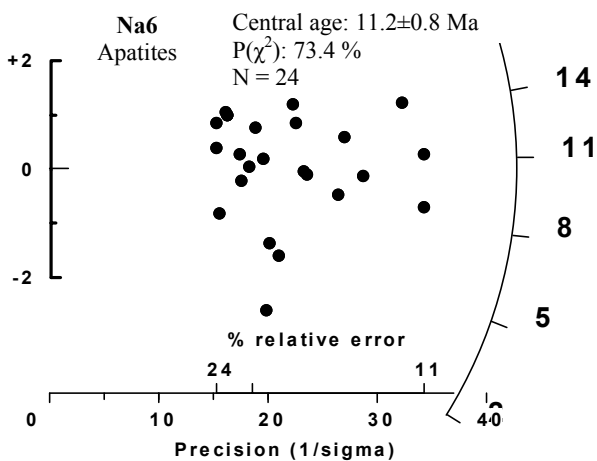
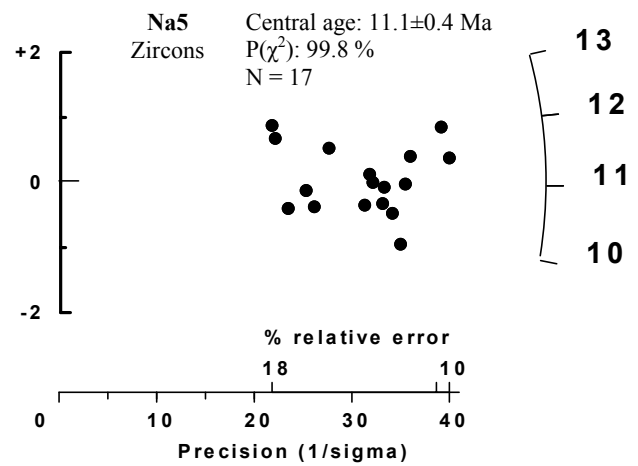
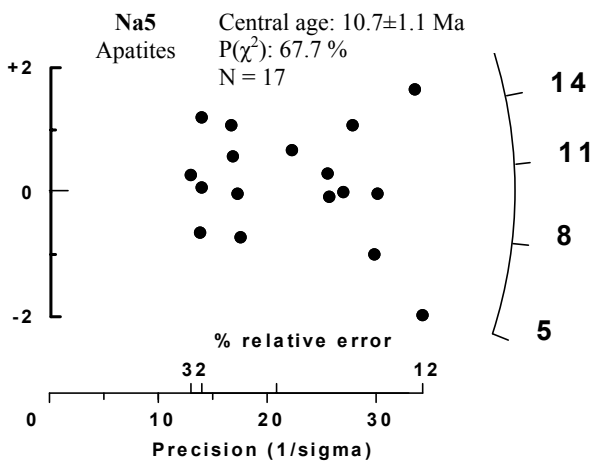
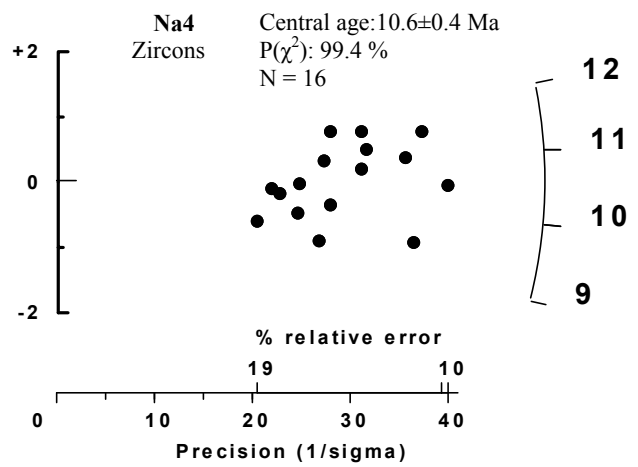
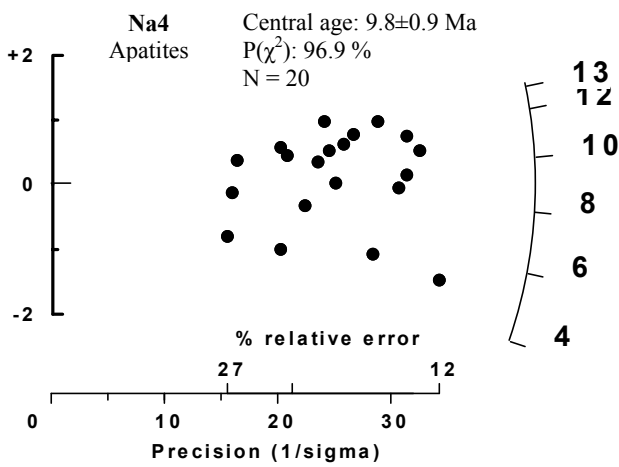
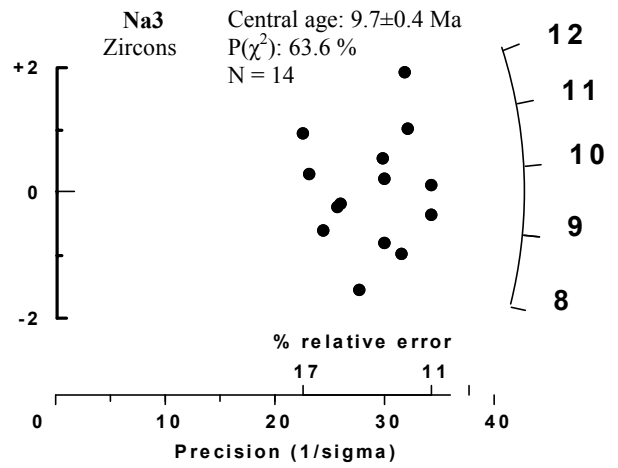
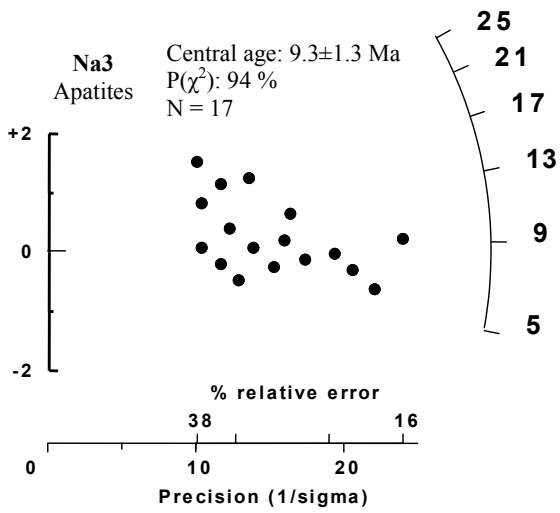
-MYKONOS



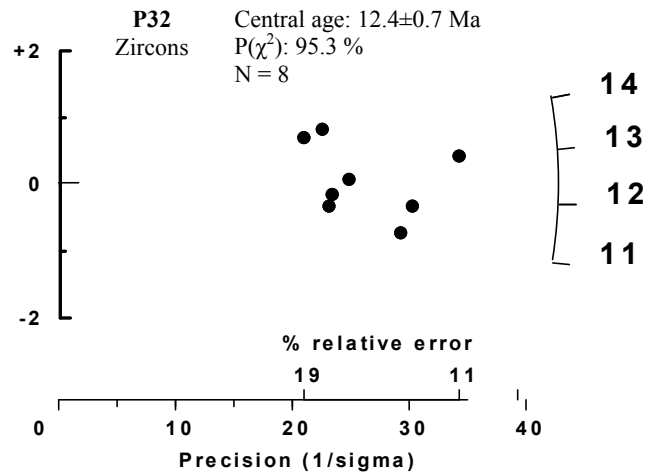
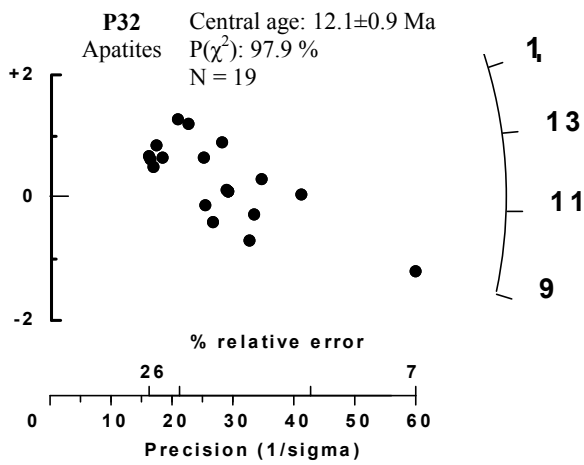
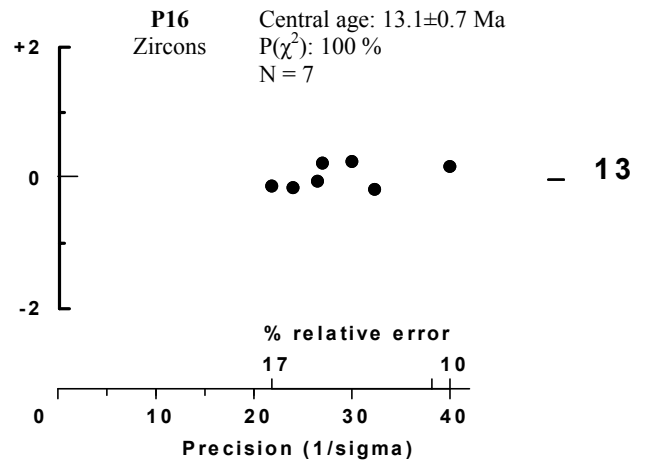
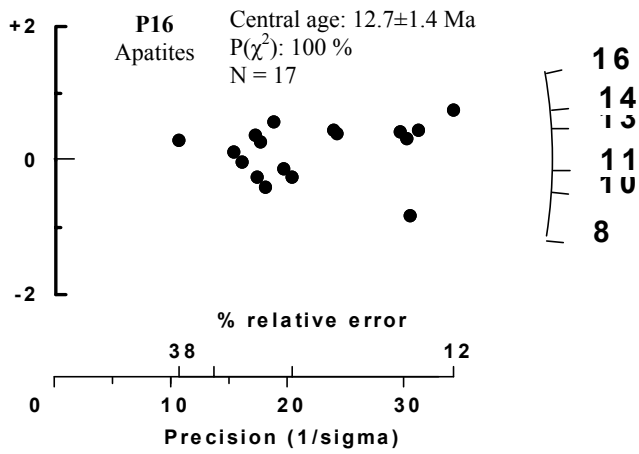
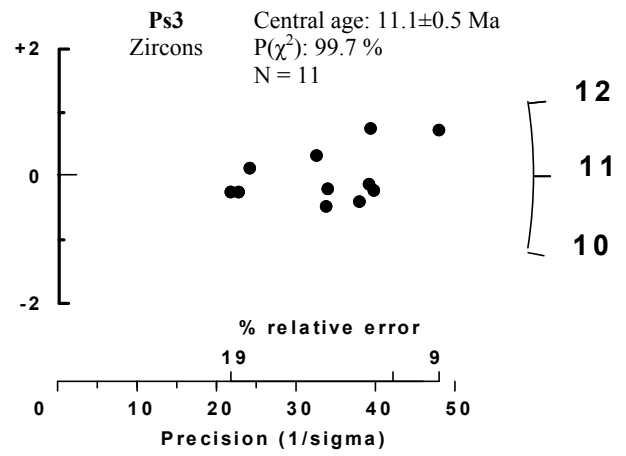
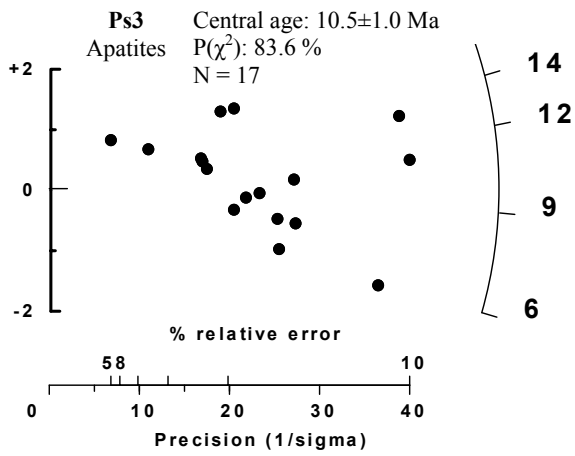


-NAXOS

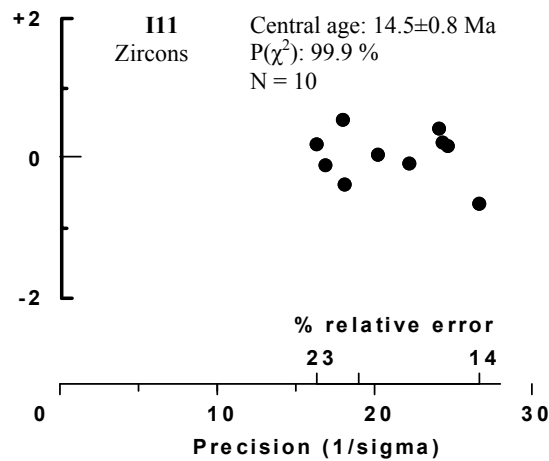
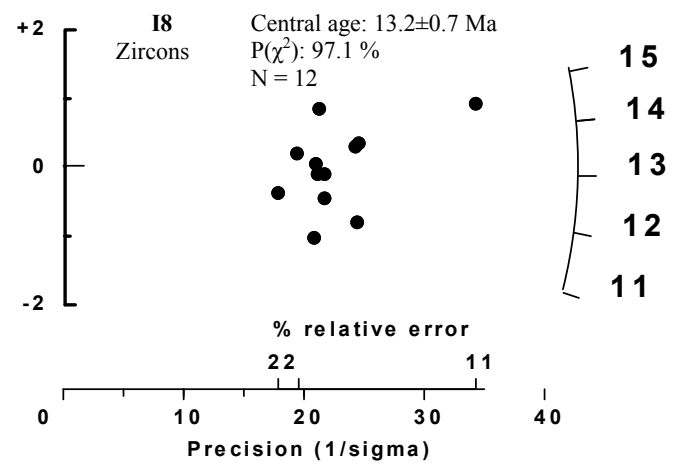
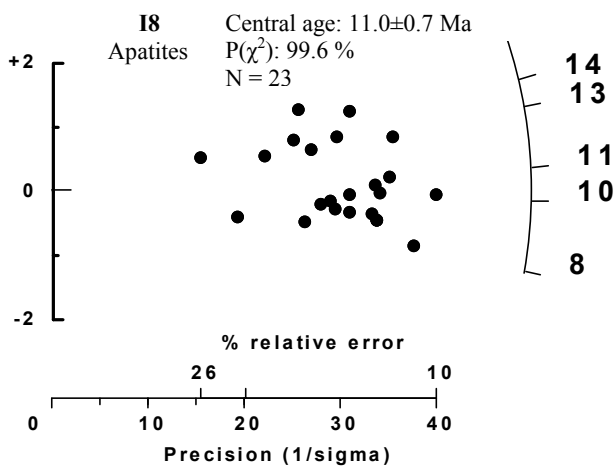
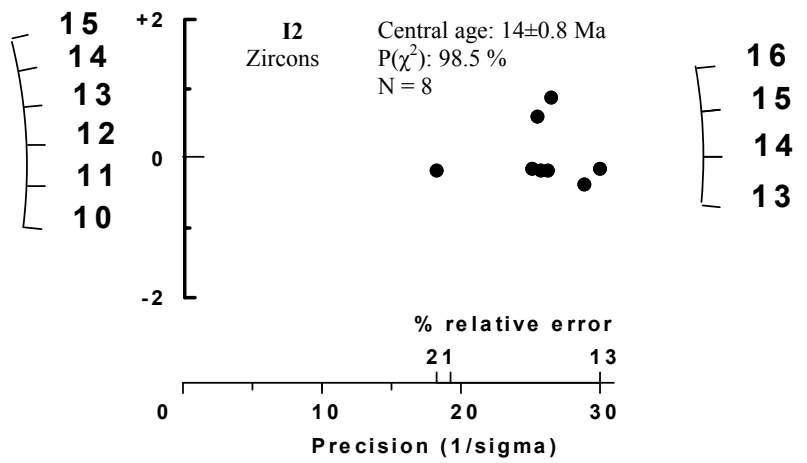
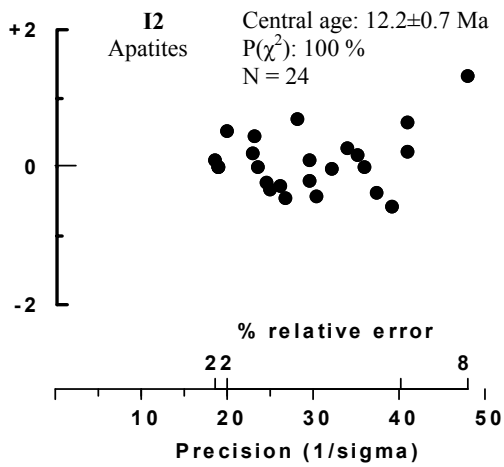




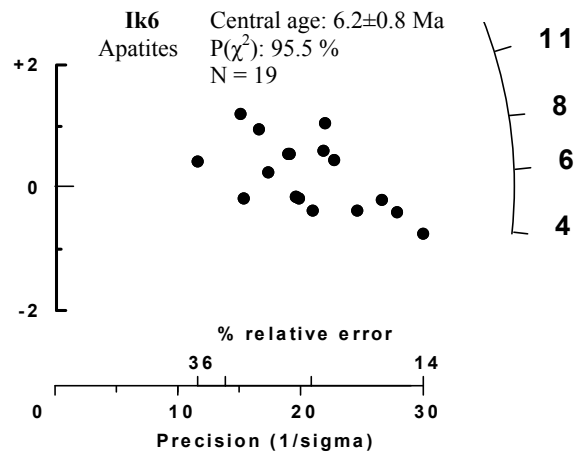
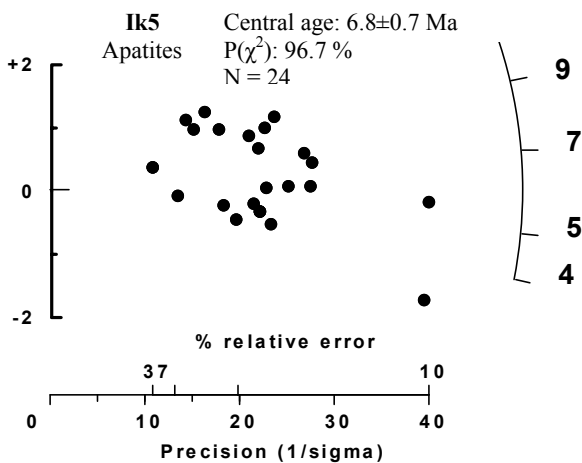
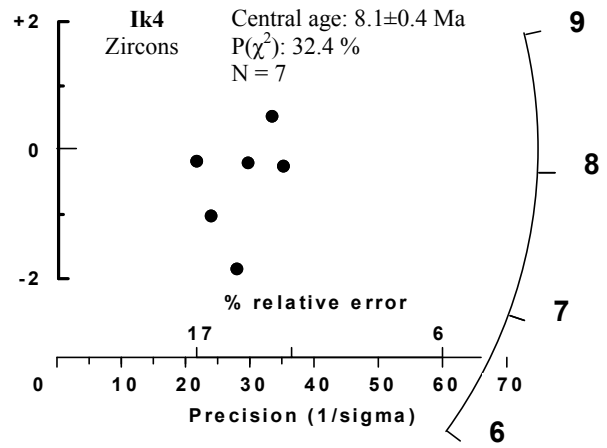
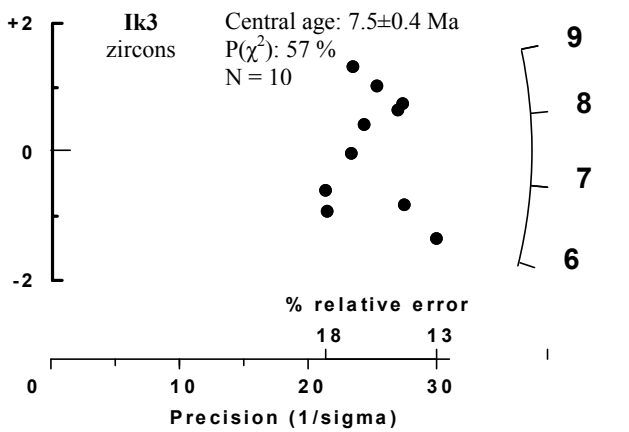
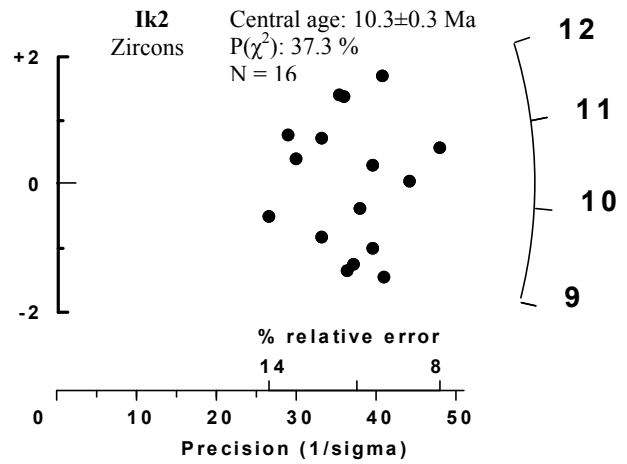
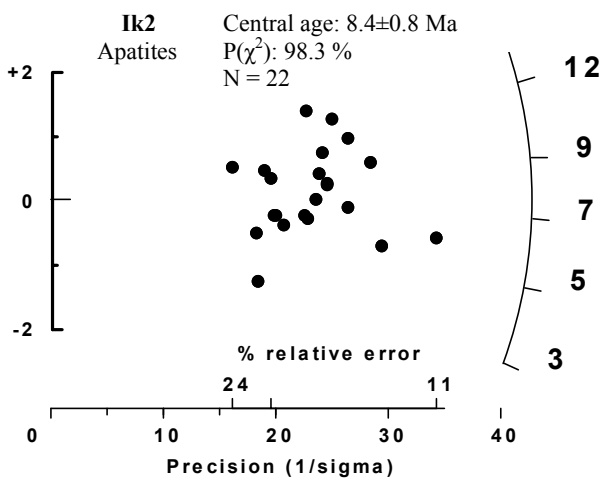
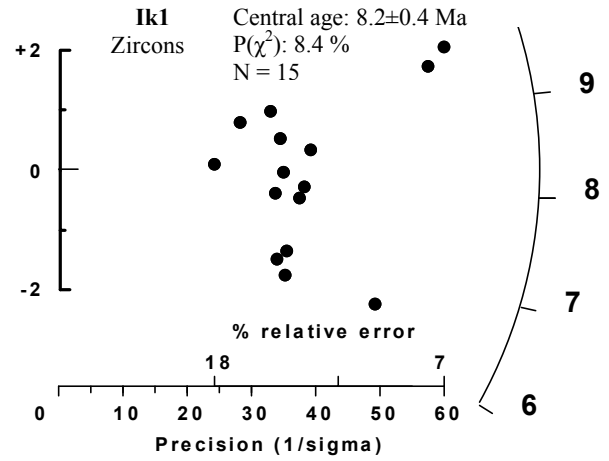
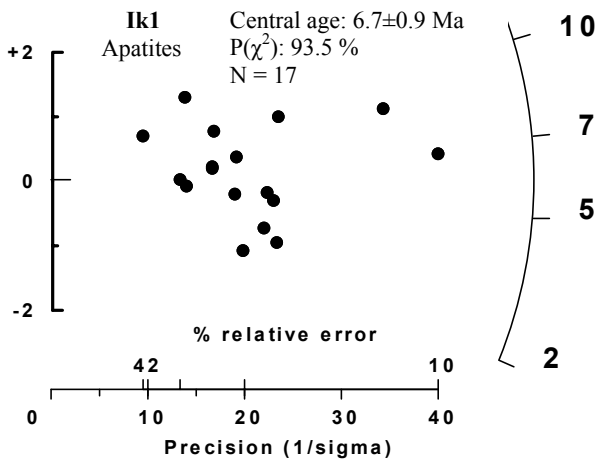
-PAROS

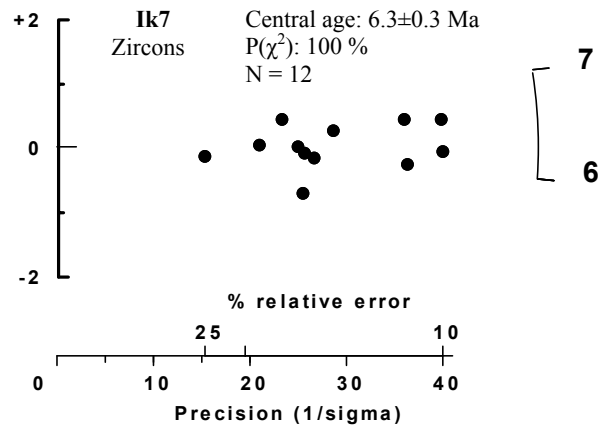
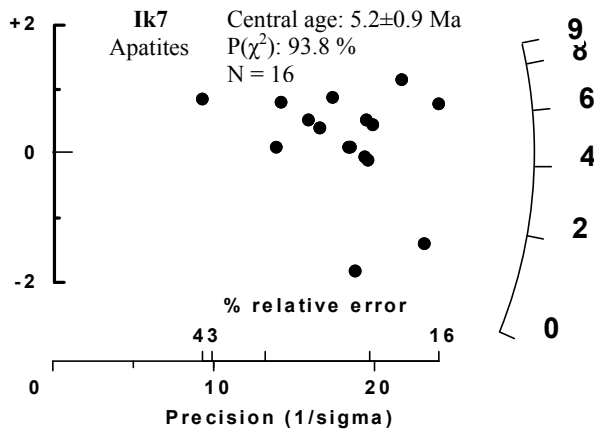


-IOS

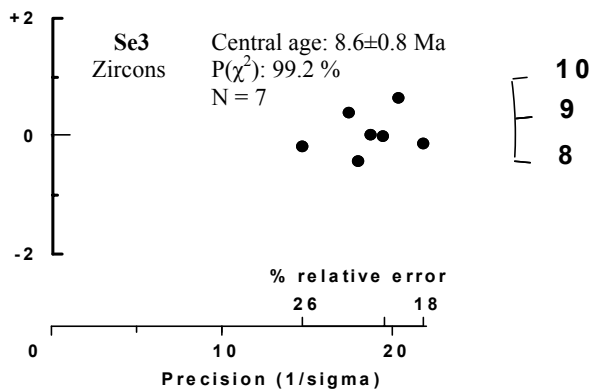
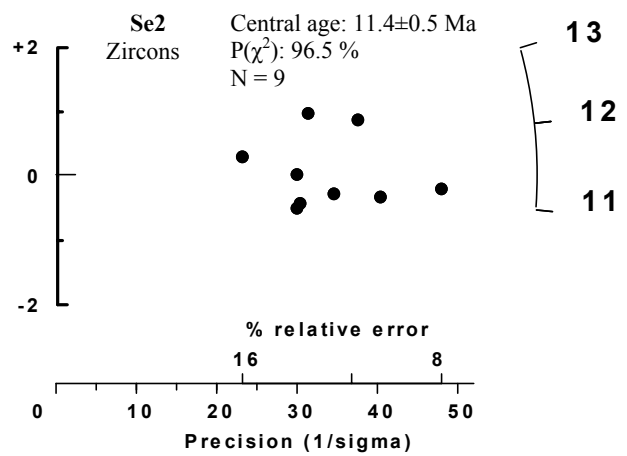
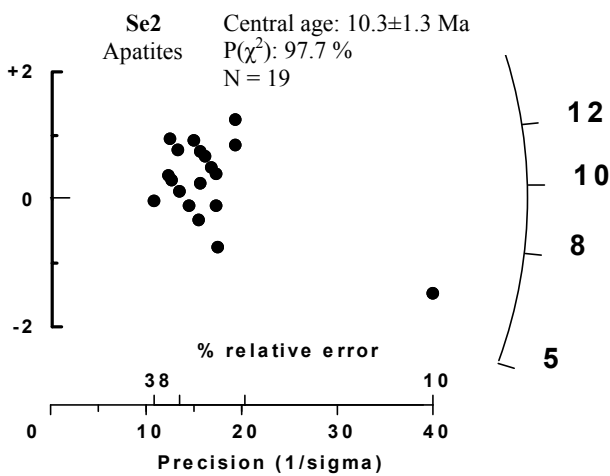


-IKARIA

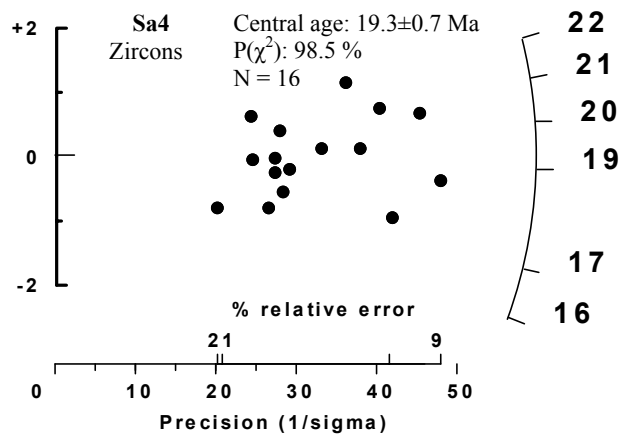
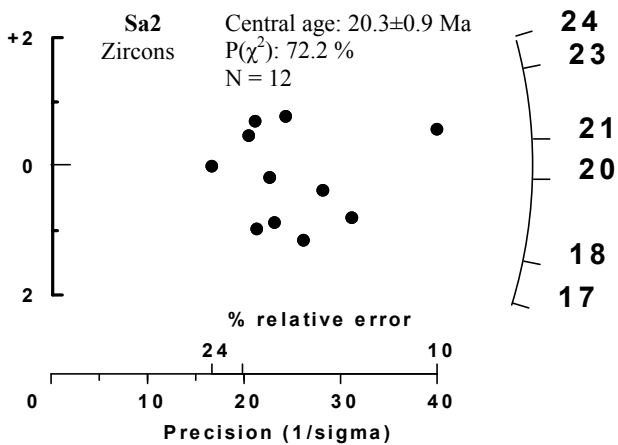


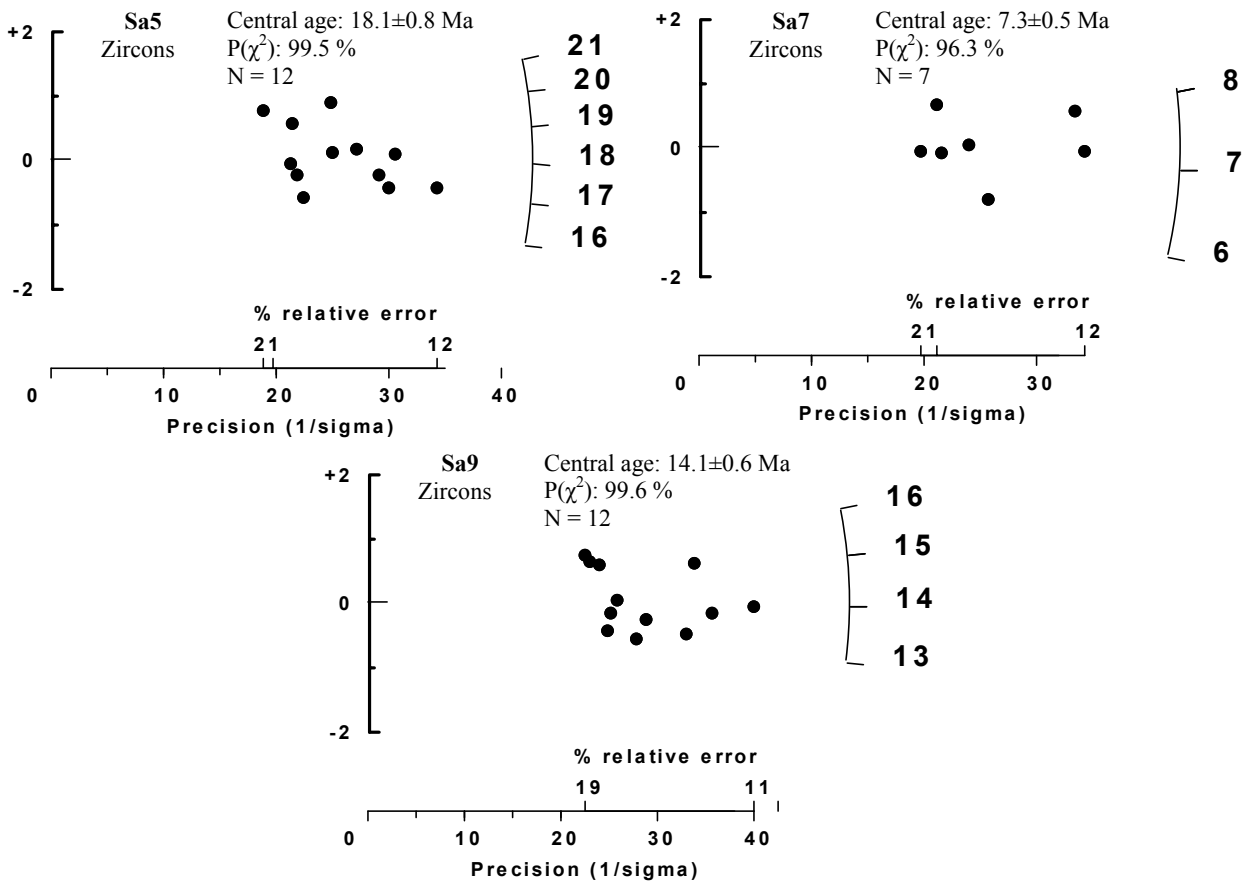


-SERIFOS



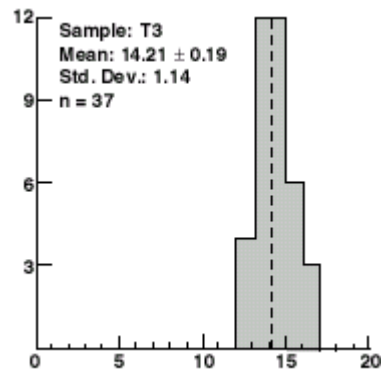
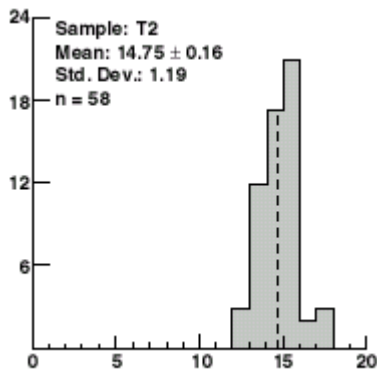
-SAMOS



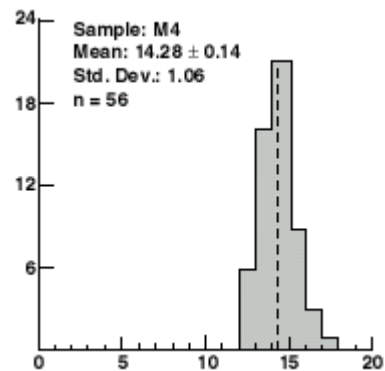
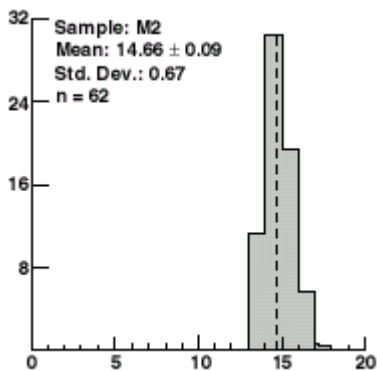


3. Histograms of track lengths

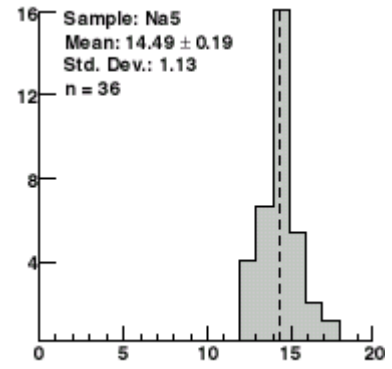
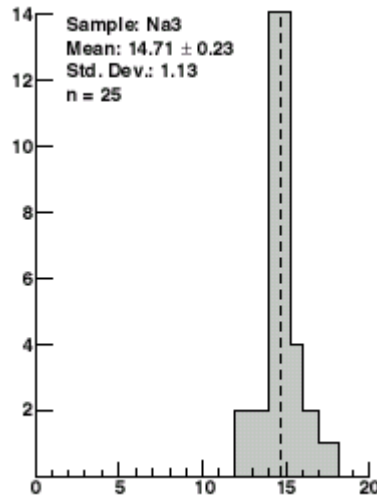
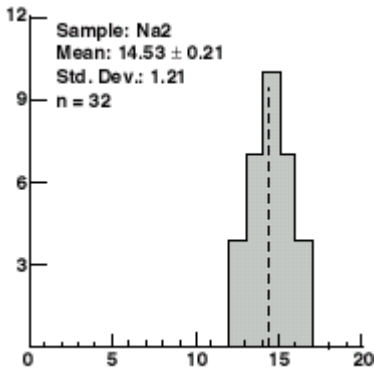
-TINOS



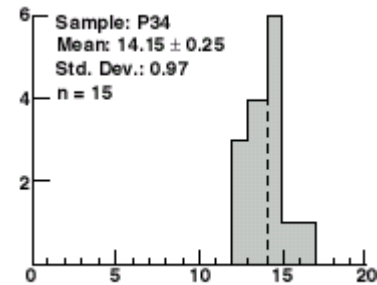
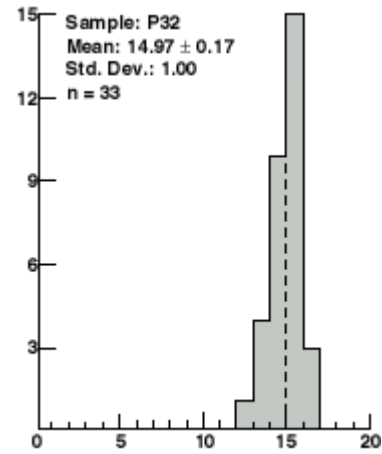
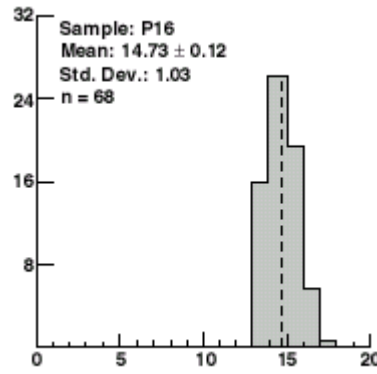
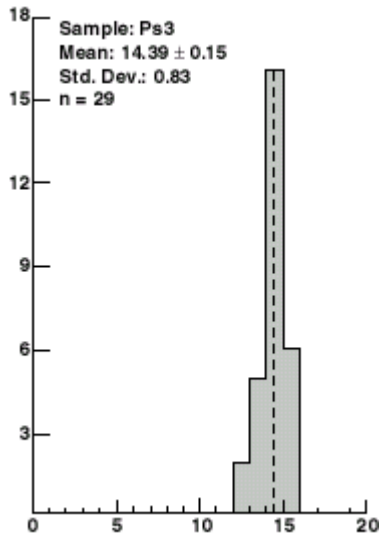
-MYKONOS



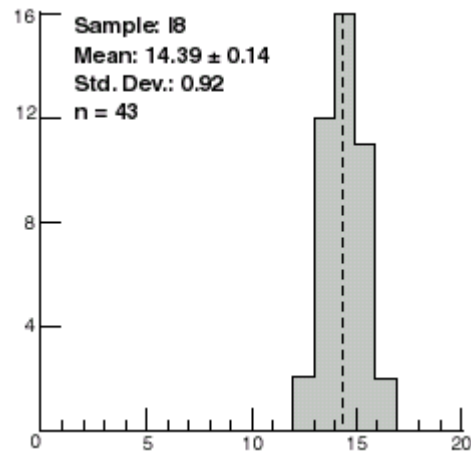
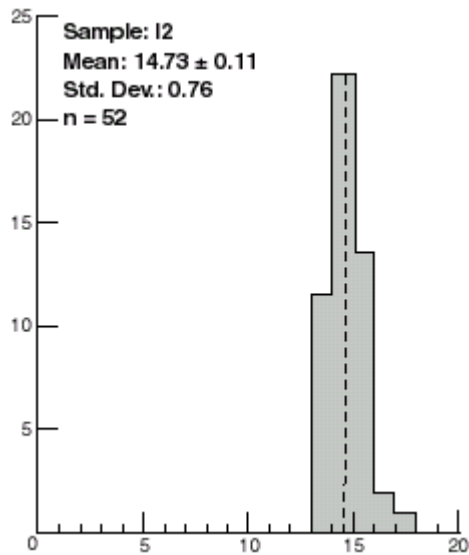
-NAXOS



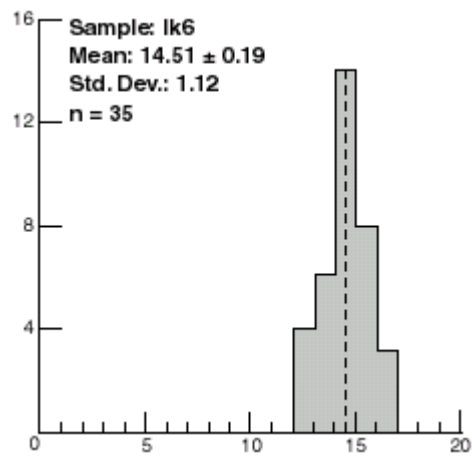
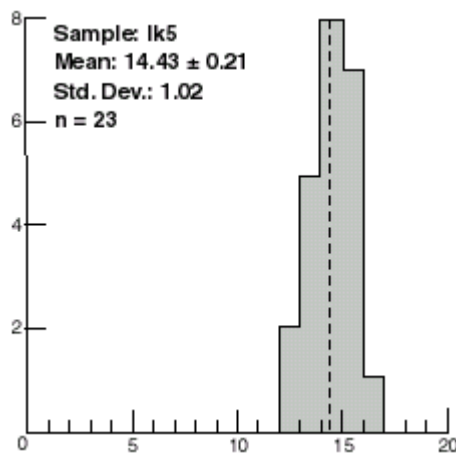
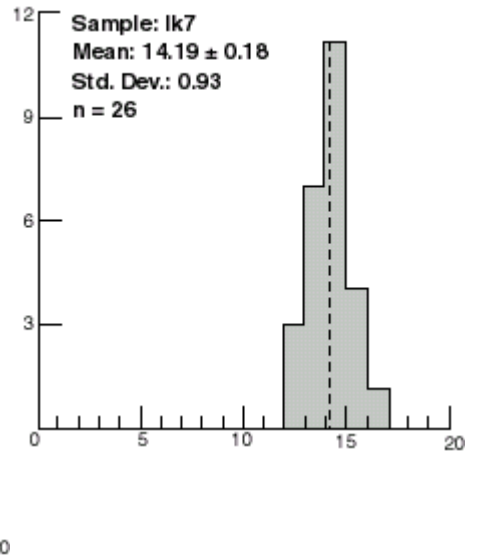
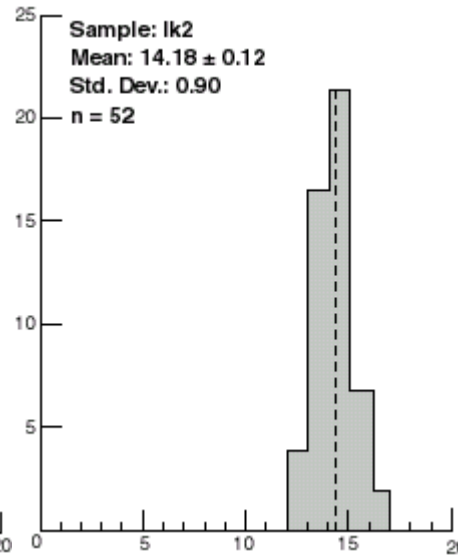
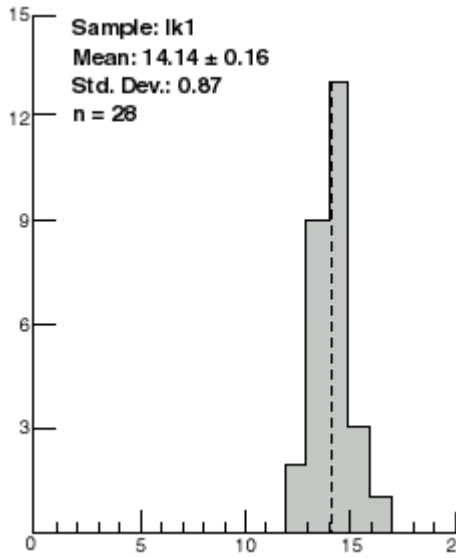
-PAROS



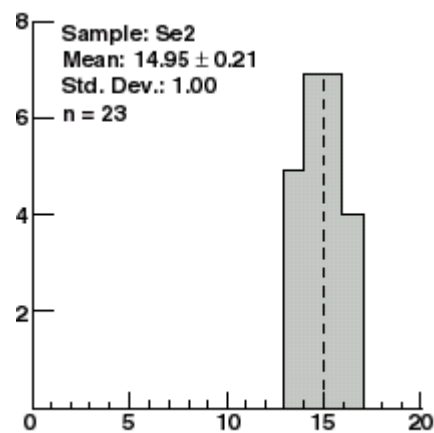
-IOS



-IKARIA



-SERIFOS



APPENDIX N° V: (U-Th)/He data

Name	Raw Age	Corr. Age	Mean Age (1 σ)	U ppm	Th ppm	He nmol/g	Mass ug	Pt um	meanr um	meanl um	RE	F blank	ncc 4He	+/- #	FtU	FtTh	U Ratio	U +/-	Th Ratio	Th +/-
T2-A	5.302	8.088	10 \pm 0.3	11.904	22.278	0.494	5.227	0.655	39.998	152.135	0	0.009	0.058329	0.00007	0.67	0.627	0.0877	0.0015	0.3392	0.0034
T2-B	11.233	16.067	without	10.034	18.616	0.88	9.851	0.699	44.284	239.988	0	0.003	0.194943	0.000114	0.712	0.673	0.1391	0.0034	0.4606	0.0087
T2-C	8.242	11.212	T2-B	11.363	21.982	0.741	12.447	0.735	52.854	205.704	0	0.002	0.206451	0.000194	0.747	0.712	0.1982	0.0025	0.63	0.0142
T2-D	7.228	10.61		16.566	27.666	0.907	7.573	0.681	41.426	205.704	0	0.002	0.153071	0.000136	0.694	0.653	0.1759	0.0046	0.5128	0.0102
T3-A	6.798	9.928	10.4 \pm 0.4	12.142	19.763	0.62	7.912	0.685	41.426	214.275	0	0.003	0.11078	0.000104	0.697	0.657	0.1352	0.0034	0.4116	0.0129
T3-B	6.915	10.787		12.8	21.438	0.671	5.406	0.641	35.713	197.133	0	0.007	0.081984	0.000075	0.655	0.61	0.0975	0.0013	0.3382	0.0083
T4-A	7.462	11.273		11.005	15.649	0.596	5.595	0.662	39.998	162.849	0	0.007	0.075188	0.000103	0.674	0.631	0.0868	0.002	0.2868	0.0038
T4-B	8.725	12.513	11.9 \pm 0.5	11.843	19.06	0.774	9.037	0.697	44.284	218.561	0	0.003	0.15765	0.000118	0.709	0.67	0.1509	0.0034	0.4411	0.01
M1-A	7.015	10.698	11.1 \pm 0.5	224.224	19.624	#	5.268	0.655	37.141	179.991	0	0	#	#	0.658	0.614	1.6406	0.0345	0.3155	0.006
M1-B	7.764	11.42		196.888	16.343	8.473	5.752	0.68	41.426	154.278	0	0	1.092083	0.00071	0.682	0.64	1.5736	0.0281	0.2985	0.0064
M2-A	6.035	8.918	9.3 \pm 0.4	60.219	51.134	2.37	7.068	0.677	39.998	205.704	0	0.001	0.375775	0.000303	0.685	0.643	0.5959	0.0063	0.7835	0.0152
M2-B	6.228	9.736		56.662	51.081	2.325	4.718	0.64	35.713	171.42	0	0.002	0.245823	0.000182	0.649	0.604	0.375	0.0076	0.5651	0.0086
M3-A	7.029	10.145	10.5 \pm 0.4	32.514	28.908	1.502	7.837	0.693	42.855	197.133	0	0.002	0.263173	0.000197	0.701	0.661	0.3575	0.0067	0.5389	0.0129
M3-B	13.969	21.225	without	23.216	14.71	2.027	5.21	0.658	38.569	162.849	0	0.002	0.236572	0.000177	0.665	0.621	0.1701	0.0036	0.267	0.0048
M3-C	10.995	16.138	M3-B	37.363	24.89	2.584	7.73	0.681	39.998	224.989	0	0.001	0.446988	0.000331	0.688	0.647	0.4036	0.0083	0.4815	0.0137
M3-D	7.04	10.794	&M3-C	35.834	16.291	1.518	5.029	0.652	37.141	169.277	0	0.002	0.17102	0.000165	0.658	0.613	0.2523	0.0073	0.2795	0.0083
M4-A	5.753	8.766	8.9 \pm 0.4	19.698	32.962	0.838	5.898	0.656	38.569	186.419	0	0.004	0.113495	0.000092	0.67	0.626	0.1634	0.0016	0.4806	0.0071
M4-B	5.466	8.991		21.406	28.259	0.833	3.389	0.608	33.57	141.421	0	0.007	0.063379	0.000065	0.621	0.572	0.1022	0.0021	0.3017	0.0049
Na1-A	10.249	14.812		30.974	2.673	1.761	5.797	0.692	40.95	211.418	0	0.002	0.228943	0.00017	0.694	0.653	0.2522	0.0034	0.1561	0.004
Na1-B	7.307	11.26	13.4 \pm 0.4	45.419	7.108	1.871	3.576	0.649	36.189	168.563	0	0.003	0.150007	0.000114	0.652	0.606	0.2282	0.0024	0.1741	0.0029
Na1-C	10.9	14.58		30.858	5.776	1.91	13.711	0.747	52.14	231.417	0	0	0.585123	0.000389	0.75	0.716	0.5902	0.0076	0.2745	0.0061
Na1-D	9.129	12.866		41.131	16.008	2.228	9.754	0.709	44.284	231.417	0	0	0.48673	0.000274	0.714	0.675	0.5598	0.0168	0.4152	0.0136
Na2-A	7.615	11.823		8.212	1.991	0.359	4.679	0.644	35.713	171.42	0	0.012	0.037846	0.000046	0.648	0.602	0.0543	0.0015	0.1449	0.0041
Na2-B	9.344	16.201	14.5 \pm 0.4	11.17	3.651	0.611	2.93	0.576	28.57	167.135	0	0.011	0.040242	0.00005	0.582	0.53	0.0463	0.0015	0.1474	0.002
Na2-C	7.781	11.091		10.19	2.552	0.456	7.886	0.701	44.284	186.419	0	0	0.080417	0.000067	0.705	0.666	0.1129	0.002	0.1665	0.0029
Na2-D	12.536	19.059		10.35	2.134	0.74	4.971	0.657	37.855	160.706	0	0	0.082204	0.000084	0.661	0.617	0.0725	0.0026	0.1491	0.0038
Na3-B	5.829	8.867		29.967	38.502	1.236	6.169	0.657	37.141	205.704	0	0.004	0.170932	0.000141	0.669	0.625	0.2588	0.0056	0.564	0.0056
Na3-C	6.167	8.794	8.9 \pm 0.3	24.074	28.527	1.032	8.004	0.701	46.426	173.563	0	0.001	0.184397	0.00017	0.711	0.672	0.2697	0.0037	0.5472	0.008
Na3-D	5.774	8.983		28.301	38.297	1.171	4.891	0.643	36.427	169.277	0	0.002	0.127646	0.00012	0.655	0.61	0.194	0.0044	0.4722	0.0075

Name	Raw Age	Corr. Age	Mean Age (Lo)	U ppm	Th ppm	He nmol/g	Mass ug	Ft um	mean r um	mean l um	RE F blank	ncc 4He +/-	FtU	FtTh	U Ratio	U +/-	Th Ratio	Th +/-		
Na4-A	6.409	9.113	9.1±0.4	39.365	73.202	1.971	8.588	0.703	47.14	179.991	0	0.002	0.37947	0.000251	0.716	0.678	0.4721	0.0134	1.2792	0.0213
Na4-B	6.158	9.138		57.98	113.118	2.831	7.504	0.674	39.998	218.561	0	0.001	0.476653	0.000318	0.688	0.647	0.6068	0.0096	1.6818	0.0119
Na5-A	6.243	9.062	9.2±0.4	36.265	50.561	1.634	7.855	0.689	42.855	199.276	0	0.002	0.288303	0.000207	0.7	0.66	0.3981	0.0085	0.8559	0.0221
Na5-B	6.58	9.361		38.457	58.35	1.866	9.173	0.703	43.569	216.418	0	0.002	0.384175	0.000311	0.714	0.676	0.4925	0.0089	1.1084	0.0279
Na6-A	7.388	10.376	10.7±0.5	42.055	56.805	2.225	9.67	0.712	47.14	201.419	0	0.001	0.482758	0.000381	0.722	0.685	0.5674	0.0094	1.1341	0.0368
Na6-B	7.411	11.002		32.796	44.735	1.745	6.571	0.673	40.712	184.277	0	0.003	0.257379	0.00021	0.685	0.643	0.3015	0.008	0.6672	0.0172
I2-A	7.706	10.192	10.8±0.5	12.875	3.232	0.571	15.278	0.756	55.711	231.417	0	0.005	0.196661	0.000114	0.759	0.726	0.2753	0.0051	0.22	0.0052
I2-B	8.133	11.445		13.108	3.328	0.614	8.347	0.71	46.426	179.991	0	0.008	0.116036	0.000119	0.714	0.676	0.1535	0.003	0.1805	0.0053
I8-A	7.702	9.764	9.5±0.4	35.161	1.323	1.485	21.207	0.789	65.711	222.846	0	0.001	0.706463	0.000442	0.79	0.761	1.0364	0.0181	0.181	0.0057
I8-B	6.804	9.216		38.089	2.589	1.431	12.591	0.738	49.998	235.702	0	0.002	0.404194	0.000224	0.74	0.704	0.6685	0.012	0.1893	0.0062
Se2-A	5.86	8.136	9.2±0.3	10.011	29.587	0.541	14.235	0.72	45.712	308.556	0	0.002	0.172418	0.000154	0.736	0.7	0.1997	0.0052	0.8998	0.026
Se2-B	5.161	7.734	without	13.544	33.994	0.604	6.921	0.667	39.998	201.419	1	0.01	0.092059	0.000068	0.684	0.642	0.1316	0.0026	0.5599	0.02
Se2-C	10.18	14.137	Se2-C	12.653	32.798	1.127	12.701	0.72	47.855	257.13	0	0.001	0.318013	0.000147	0.735	0.698	0.2251	0.0048	0.8914	0.0237
Se2-D	4.741	6.635		9.648	26.404	0.409	9.82	0.714	47.14	197.133	0	0.002	0.090051	0.000071	0.73	0.693	0.133	0.0044	0.6038	0.0116
IK1-A	2.717	3.868	3.6±0.2	31.093	35.868	0.584	9.772	0.702	42.855	244.273	0	0.007	0.128814	0.000111	0.712	0.673	0.4245	0.0053	0.7706	0.023
IK1-B	2.199	3.316		25.936	25.64	0.382	5.663	0.663	39.284	171.42	0	0.019	0.049577	0.000068	0.673	0.629	0.2058	0.0035	0.3952	0.0063
IK2-A	4.371	6.194	6±0.3	44.499	49.096	1.331	10.07	0.706	44.284	239.988	0	0.003	0.301496	0.000225	0.715	0.676	0.6249	0.0145	1.0337	0.0331
IK2-B	3.833	5.827		56.762	50.852	1.432	5.914	0.658	37.141	197.133	0	0.005	0.190919	0.000183	0.667	0.623	0.4688	0.0045	0.6796	0.0101
IK6-A	3.582	5.098	5.6±0.2	11.308	1.004	0.225	7.682	0.703	43.569	184.277	0	0.024	0.039983	0.000058	0.705	0.665	0.122	0.0042	0.1438	0.0037
IK6-B	8.3	11.376	without	10.784	1.528	0.503	9.987	0.729	50.712	179.991	0	0.003	0.112256	0.000135	0.732	0.695	0.1511	0.0027	0.1576	0.0026
IK6-C	4.162	6.127	IK6-B	12.861	1.644	0.3	6.22	0.679	40.712	175.706	1	0.008	0.041056	0.000057	0.682	0.639	0.1124	0.0027	0.1484	0.0052
Dur1	31.324	NaN		-266.4	-4848.346	-239.9	-1	0	0	0	0	0	5.374954	0.003098	#	#	0.3724	0.0108	8.9949	0.1918
Dur	31.696	NaN		-97.452	-1941.154	-95.605	-1	0	0	0	0	0	2.14135	0.001459	#	#	0.1368	0.0057	3.6791	0.097
Dur1LH	30.432	NaN		-226.773	-4884.331	-216.612	-1	0	0	0	0	0	4.852145	0.002799	#	#	0.3172	0.0052	8.531	0.1454
Dur3	26.729	NaN		-62.713	-1121.409	-47.5	-1	0	0	0	0	0	1.064606	0.000552	#	#	0.0884	0.0022	2.1619	0.0211

The He dating method as described in the chapter I.4.1 is an absolute dating technique, based on fundamental measured quantities rather than by reference to independently dated mineral standards. Nevertheless it is useful to have mineral standards to verify both analytical calibrations and the degree to which the system faithfully acts as chronometer. For this reason, Durango standard age is measured regularly with the samples. At Caltech, the mean of several dozen age determinations on Durango apatite is 32.6 Ma, with a standard deviation of the population of 1 Ma (Farley, 2000a). This age is slightly older than, but within error of, the accepted age of this apatite (31.6±1 Ma) (Jonckheere et al., 1993). The accuracy and natural mineral standards of the (U/Th)/He method are extensively described in Farley, 2002.

A sample is heated two times and the measurement procedure is repeated. For inclusion-free samples, this "re-extract" (RE) step will yield He at levels indistinguishable from that of the preceding hot blank. However, a substantial amount of gas in this step has been found to be the telltale signature of mineral inclusions. If such He is found, the analysis is rejected as likely to be compromised by inclusions (see section III.9).

APPENDIX N° VI: Formula listing used for the error calculations of slip and cooling rate and calculation methodology

1. Basic formulas of errors for the four operations:

$$(1) (A \pm a) + (B \pm b) = A + B \pm \sqrt{a^2 + b^2}$$

$$(2) (A \pm a) - (B \pm b) = A - B \pm \sqrt{a^2 + b^2}$$

$$(3) (A \pm a)(B \pm b) = AB \left(1 \pm \sqrt{\left(\frac{a}{A}\right)^2 + \left(\frac{b}{B}\right)^2} \right)$$

$$(4) \frac{(A \pm a)}{(B \pm b)} = \frac{A}{B} \left(1 \pm \sqrt{\left(\frac{a}{A}\right)^2 + \left(\frac{b}{B}\right)^2} \right)$$

2. Formula for the average of n results A_i assigned of a_i errors:

$$(5) \frac{\sum_{i=1}^n A_i \pm a_i}{n} = \frac{\sum_{i=1}^n A_i}{n} \pm \sqrt{\frac{\sum_{i=1}^n a_i^2}{n}}$$

3. Formulas of errors for the inverse of a result “A” assigned of “a” error:

$$(6) \frac{1}{A \pm a} = \frac{1}{A} \pm \frac{a}{A^2}$$

4. Formulas of errors for the slope of regression straight line:

To calculate the error on the slope we have used the ISOPLOT program. We have applied the York regression calculation (1968) using 2σ error level on the ages and on the distance. For the distance we have estimated an average error at 10% considering the error on the measurement and location of the samples on the map and the error related to the position of the samples which are not exactly on the fault but on the erosional surface.

Slip rate is estimated from the inverse slope of mineral ages with distance in the slip direction. For this reason, the error “a” on the slope “A” is calculated first using the York regression calculation (1968) then the error on the inverse slope is calculated using the formula 6.

5. Example of measurement of distance:

For the measurement of the distance in the slip direction we have plotted each sample perpendicularly on the slip direction and we have measured the distance of sample in this slip direction. The origin for the measurement of the distance is chosen arbitrarily, usually at the rim of the island.

NOTE: In some islands, the line indicate for the cross section is not oriented exactly on the slip direction to show more details about the island structure.

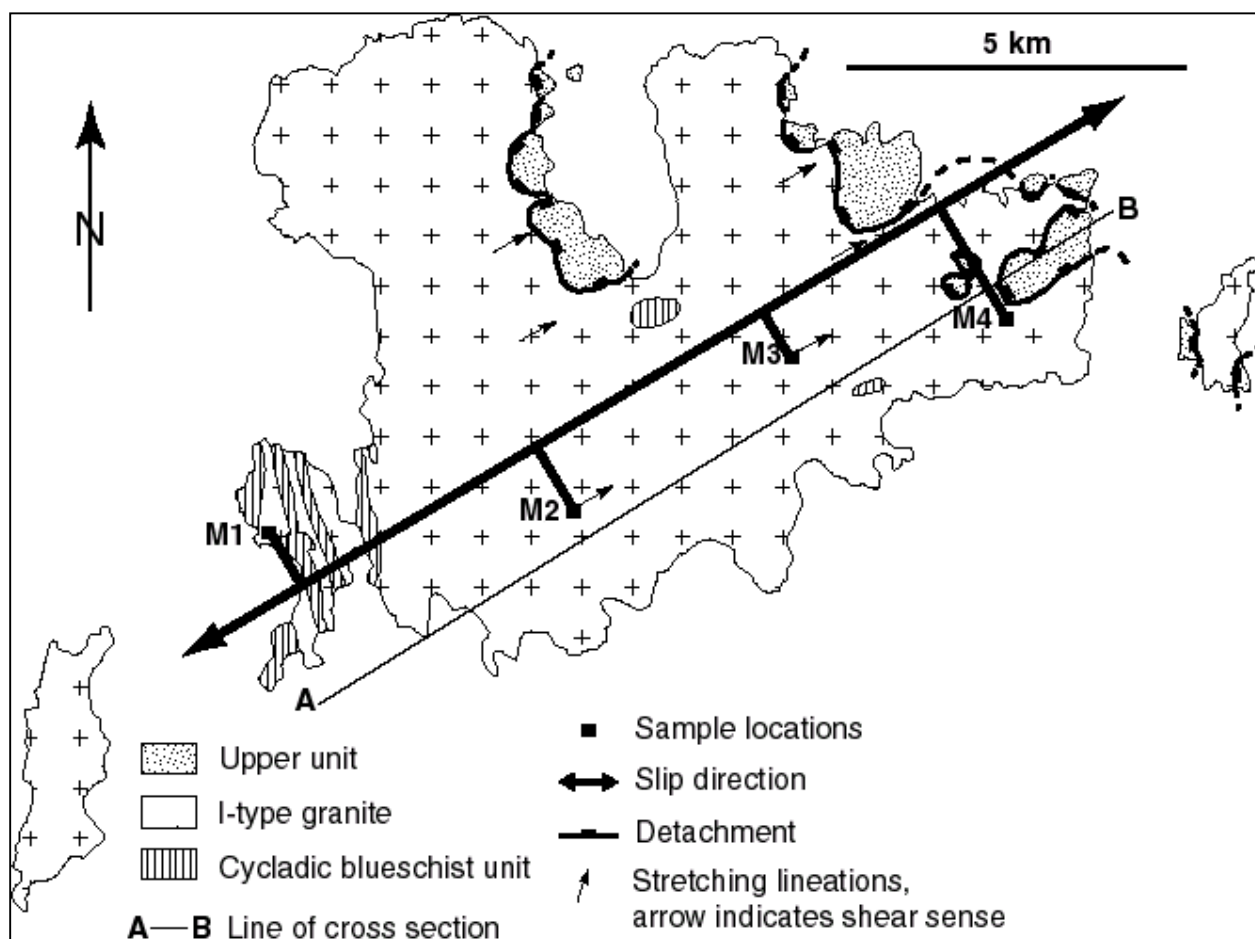


Table III.5. Mykonos fission-track and U-Th/He data

Sample reference (rock type)	Lat. Long.	Elevation (m)	Distance in slip direction (km)	Mineral	Number of crystals	Px2 (%)	FT age (Ma)	Mean track length (μm)	StD (μm)	Number of tracks measured	F_T	Helium age (Ma)
M1 (granodiorite)	37°25'35" 25°18'04"	10	13.90 ± 1.3	apatite	28	95.3	12.5 ± 2.2				0.67	11.1 ± 1
				zircon	15	94.9	13.0 ± 0.8					
M2 (granodiorite)	37°25'47" 25°21'43"	145	9.80 ± 1.0	apatite	24	89.0	10.6 ± 1.2	14.66 ± 0.18	0.67	62	0.689	9.3 ± 0.8
				zircon	11	90.0	11.6 ± 0.8					
M3 (granodiorite)	37°26'47" 25°23'45"	95	6.20 ± 0.6	apatite	25	97.7	10.5 ± 1.8				0.67	10.5 ± 0.8
				zircon	10	97.4	10.9 ± 1.0					
M4 (granodiorite)	37°27'29" 25°25'46"	140	3.02 ± 0.3	apatite	21	98.9	10.5 ± 1.8	14.28 ± 0.28	1.06	56	0.63	8.9 ± 0.8
				zircon	13	88.2	10.7 ± 0.8					

Apatite and zircon FT ages have been calculated using a zeta factors of 127.3 ± 4.4 and 332.9 ± 9.7 determined by multiple analyses of standards following the recommendations of Hurford (1990). Central ages are reported. All data are given for 2σ error level.

6. Minimum average cooling rate calculation

For the granite cooling rate calculations, we have used the mean of zircon and apatite fission track and apatite (U-Th)/He ages (at 2σ) obtained on samples from the granite because of the similar cooling path of the samples.

Example of Mykonos (see table 5):

We use the formula (5) to calculate the mean ages:

Mean zircon fission track age: 11.55 ± 0.43 Ma

Mean apatite fission track age: 11.025 ± 0.89 Ma

Mean apatite (U-Th)/He age: 9.95 ± 0.43 Ma

We assume temperatures from 300°C to 200°C for the zircon partial annealing zone of fission tracks; 110 - 60°C for the apatite partial annealing zone of fission tracks and 80 - 40°C for the apatite partial retention zone of helium. Because the cooling is generally very fast we consider that the ages indicate cooling below 300°C , 110°C and 80°C . For the error on these temperature we have used the errors related to the mid partial annealing and retention zone, therefore the temperatures used are: $300 \pm 50^\circ\text{C}$, $110 \pm 25^\circ\text{C}$ and 80 ± 20 .

We record cooling history of the samples from $300 \pm 50^\circ\text{C}$ to $80 \pm 20^\circ\text{C}$, therefore we calculate the difference in age and temperature from the zircon fission track to the apatite He dating (formula 2):

$$\text{Age: } (11.55 \pm 0.43) - (9.95 \pm 0.43) = 1.6 \pm 0.61$$

$$\text{Temperature: } (300 \pm 50) - (80 \pm 20) = 220 \pm 53.85$$

Thus, in 1.6 ± 0.61 Ma the samples have lost $220 \pm 53.85^\circ\text{C}$, it follow (formula 4):

$$(220 \pm 53.85) / (1.6 \pm 0.3) = 137.5 \pm 62.3$$

The minimum cooling rate for this granite is: $137.5 - 62.3 = 75.2^\circ\text{C/Myr}$

Therefore the minimum average cooling rate for the granodiorite of Mykonos is $\sim 75^\circ\text{C/Myr}$.

Curriculum Vitae

Stéphanie Brichau

Permanent address:

3 plan du Thym, Les Avants 3
34270 S^t Mathieu de Trévièrs
FRANCE
Phone: (+33) (0) 4 67 55 36 83
E-mails : stephanie_brichau@yahoo.fr
Nationality : French
Date of Birth : 09 october 1976
Marital status: Single

EDUCATION

March 2001-June 2004 **PhD thesis in geochronology and tectonic**, University of Mainz (Germany) and University of Montpellier II (France): Constraining the tectonic evolution of extensional fault systems in the Cyclades (Greece) using low-temperature thermochronology.

1999-2000 **DEA (Detailed Studies Degree) of Lithosphere Structure and Evolution (measurements, modelling and applications)**, University of Montpellier II, France. Research thematic: ⁴⁰Ar/³⁹Ar and U/Pb geochronology of Aigoual and Mont Lozère granites (French Massif Central). Geodynamical consequences.

Second semester of **Earth sciences Maîtrise (MSc)**, University of Montpellier II, France. Research thematic: Extensional phase in the Montagne Noire (South French Massif Central): Tectonic and Geochronologic approaches.

1998-1999 First semester of **Earth sciences Maîtrise (MSc)**, University of Montpellier II, France.
End of second semester of **Earth sciences Licence (BSc)**, University of Montpellier II, France.

1997-1998 First and beginning of second semester of **Earth sciences Licence (BSc)**, University of Montpellier II, France.

1996 Second year of **Earth sciences DEUG**, University of Montpellier II.

1994-1995 First year of **Life and Earth sciences DEUG** (University general degree of education), University of Montpellier II, France.

1993-1994 **Baccalaureate D** (options mathematics, physics, biology), Mas de Tesse High school.

- Communications

Kumerics, C., Ring, U., Brichau, S., Glodny, J. And Régnier, J.L. The extensional Ikaria shear zone and associated brittle detachment faults, Aegean Sea, Greece. **submitted**.

Brichau, S., Ring, U., Carter, A. and Brunel, M., 2002. Fission-track and (U-Th)/He studies in the Aegean islands: Constraining the timing of major detachments, their slip rates and their role in the exhumation of the Cycladic blueschists. *Fission track Workshop, Geotemas v. 4, p. 31-33*.

Brichau, S., Ring, U., Carter, A. and Brunel, M., 2003. Slip rate estimation by low temperature thermochronology for major extensional detachments in Cycladic islands. *AGU fall meeting*.

Brichau, S., Ring, U., Carter, A. and Brunel, M. Spatial and long-term evolutions of the slip rate for a major extensional fault system on Naxos and Paros Islands, Greece. **In progress**.

Brichau, S., Respaut, J.P. and Monié, P. ⁴⁰Ar/³⁹Ar and U/Pb geochronology of the Cévennes granites, south French Massif Central. Geodynamical consequences. **In progress**.

TEACHING EXPERIENCE

October 2000-January 2002 **Teaching** at the University of Montpellier II, France.

- Optional module of computing introduction practical work for first year students in Universe and Earth sciences, Life sciences DEUG (Software use: Word, Excel, research on the Internet Web page creation).

MISCELLANEOUS

September 1998 to Jun 1999 Elected student representative of Earth sciences Maîtrise promotion.

September 1997 to Jun 1998 Elected student representative of Earth sciences Licence promotion.

1994-1999 Checkout operator and saleswoman in super market, during week-end and holidays.

Languages: English fluently, Spanish understood.